Stellingen

behorende bij het proefschrift

Turbulence and OH Structures in Flames

van Paul Stroomer

1. Aanzuiging van koude omgevingslucht is een belangrijke destabiliserende factor in het stabilisatieproces van brandstofarme schijfgestabiliseerde voorgemengde vlammen.

   Dit proefschrift.

2. Snelheidsgradiënten en de daaruit voortvloeiende menglaag-ontwikkeling zijn bepalend voor zowel globale grootheden als lokale eigenschappen van niet-voorgemengde straal vlammen.

   Dit proefschrift.

3. Experimentele visualisatie-technieken leveren een wezenlijke bijdrage aan verbetering van het begrip over turbulente verbranding.

   Dit proefschrift.

4. Triplet-doublet magnetische dipool-dipool interacties tussen N-V en P_1 defecten in diamant veroorzaken zijstructuren in de laagveld ODMR spectra van het N-V center.

   Eric van Oort, Paul Stroomer en Max Glasbeek, Low-field optically detected magnetic resonance of a coupled triplet-doublet defect pair in diamond, Physical Review B 42 (1990), 8605-8608.

5. Een samenwerkingsverband krijgt pas een toegevoegde waarde als er een intensieve uitwisseling van informatie tussen de partners plaatsvindt.

6. Het internationale verdrag waar Antarctica het meest bij gebaat is, is het uitroepen tot de laatste mensloze wildernis die dit werelddeel hoort te zijn.

7. Mensen die veel liegen, dienen te beschikken over een goed geheugen.

8. Het grootste verschil tussen toeristen en reizigers is dat voor de laatsten het onderweg zijn belangrijk is.

9. Als het doel van wetenschappelijke publicaties het uitwisselen van kennis is, dienen ook mislukte onderzoeksresultaten gepubliceerd te worden.

10. Moderne ontdekkingsreizigers zouden zich moeten realiseren dat toepassing van fractale analyse op de karthografie leidt tot het kleiner worden van de zogenaamde witte plekken op landkaarten, maar dat hun aantal blijft groeien.

Turbulence and OH Structures in Flames

Turbulence and OH Structures in Flames

Turbulentie en OH Structuren in Vlammen

PROEFSCHRIFT

ter verkrijging van de graad van doctor
aan de Technische Universiteit Delft,
op gezag van de Rector Magnificus Prof. ir. K.F. Wakker,
in het openbaar te verdedigen ten overstaan van een commissie,
door het College van Dekanen aangewezen,
op maandag 26 juni 1995 te 13.30 uur

door

Paul Pieter Johan STROOMER

scheikundig doctorandus
geboren te Alkmaar

Dit proefschrift is goedgekeurd door de promotor:
Prof. ir. C.J. Hoogendoorn

Samenstelling promotiecommissie:
Prof.dr. K. Hanjalić
Prof.dr. K. Hein
Prof.ir. J.K. Nieuwenhuizen
Prof.dr.ir. F.T.M. Nieuwstadt
Prof.dr. D.J.E.M. Roekaerts
Dr.ir. Th.H. van der Meer

Part of this work was performed within SCIENCE project no. SC1-0459, with support of the Commission of the European Communities, aimed at the study of turbulent mixing and extinction phenomena in flames stabilized by recirculation zones.

To scorn all strife and to view all life
With the curious eyes of a child;
From the plangent sea to the prairie,
From the slum to the heart of the Wild.
From the red-rimmed star to the speck of sand,
From the vast to the greatly small;
For I know that the whole for the good is planned,
And I want to see it all.

Uit: *The Collected Poems* van Robert Service

aan mijn ouders

Contents

Chapter 1

General introduction

1.1 Historical overview

One of the oldest symbols of combustion science is Prometheus. With an inflammable blade of grass, he approached the cart of sun god Helios as it passed by, ignited his torch on it and hurried back to earth to bring fire to the people. Mankind created the myths of Prometheus sometime between 1000 and 700 B.C. The Greek heritage of mythology surely must have influenced one of the first true scientists, Aristotle, around 350 B.C., in developing his theory of matter. This theory took the hot-cold and moist-dry qualities of matter and combined them into the four elements: earth, water, air and fire. It was suggested that the theories should be confirmed by means of experiments, which would also contribute to the refinement of theory. It remained for the Arabs, however, around 1000 *A.D.* to reunite these two essentials and to greatly advance the modern science of alchemy. In the decade 1770-1780, experiments by Lavoisier and Priestly were carried out, that would replace alchemy by the science of chemistry. For nearly 100 years of the post-Renaissance period (including most of the eighteenth century) the theory of phlogiston reigned. Fire (phlogiston) was a fundamental substance, and during combustion a material lost phlogiston. When its phlogiston was completely gone, the material could no longer burn. However, as measurements were refined, the theory encountered increasing difficulties.

Ever since, an enormous effort has been put worldwide in solving the problems of fire and flames, and developing theories describing the processes involved. The science of combustion as it is known nowadays, was born near the turn of the nineteenth and twentieth century. It was based on four cornerstones: thermodynamics, chemical kinetics, fluid mechanics and transport processes. The main principles of fluid mechanics and thermodynamics, needed in combustion, had developed over many years already. The sciences of chemical kinetics and molecular transport processes, however, had just begun to flourish. Recent improvements on these fields, and especially on turbulent fluid flow, a feature nearly always accompanying practical combustion situations, added crucial information to the turbulent combustion puzzle.

In the meantime, the use of combustion in both industry and household appliances increased exponentially. Especially in the Netherlands, natural gas as fuel was widely used, after the discovery of major natural gas sources in Slochteren, Groningen (1960). It

is expected that natural gas will remain an important energy carrier for the next 50 years. With the increasingly stringent requirements of provided efficiency and of reduced pollutant emissions, it becomes more and more important to have detailed knowledge of combustion processes. The investigation of turbulent natural gas combustion processes is therefore of practical and fundamental interest.

1.2 Background

The development of theoretical models for turbulent combustion has proven to be difficult due to our limited knowledge about turbulence and its complex interaction with flame chemistry and combustion thermodynamics. Detailed information on the flame-flow interaction is an important key to understand the mixing mechanisms in flames. Flame characteristics as combustion performance and formation and destruction of pollutants are governed by these mixing processes. In nonpremixed geometries, it involves the mixing of fuel and oxidizer. For premixed configurations the mixing between hot combustion products and cold fresh reactants is the governing process. In both cases, combustion is restricted to regions where mixing has been completed on molecular scale and the criteria for flame stabilization have been satisfied. This complexity of combustion chemistry and transport processes in general makes it very difficult to model even the simplest combustion system.

An important property in the mixing process of a turbulent flow is the existence of turbulent eddies of different sizes. In turbulent combustion these eddies transport species, heat and momentum. Knowledge of length scales of the velocity fluctuations, supplemented by knowledge of length scales characterizing the reacting turbulent field, is important to improve combustion models. These scales need not be equal and therefore experimental data are very important in the development, testing and improving of turbulent reacting flow models. Also, the acquisition of spatially resolved velocities, species concentrations and temperatures is necessary to achieve a fundamental, microscopic understanding of combustion systems. The development of advanced laser diagnostics offers the potential of obtaining these data, with less perturbation of the combustion environment than conventional physical probes such as thermocouples or hot wires.

Part of this work is associated with research performed within a European SCIENCE project, focussed on turbulent mixing and flame extinction in flames stabilized by recirculation zones. Within this project, we cooperated with universities of Lisbon (Instituto Superior Técnico), London (Imperial College of Science, Technology and Medicine) and Zaragoza to improve understanding of recirculating flows. The stability of this type of flames is important especially in view of current practice of lean operation to avoid excessive formation of pollutants: the leaner a premixed combustible gas becomes, the lower the rate of pollutant formation. By using excess air, the entire flame zone experiences high fluid velocities which causes a reduction in the residence time for thermal NO to be produced. However, if the ratio of air and fuel exceeds a

critical value, then the flame blows off. As a precursor to global extinction, the flame is believed to extinguish locally, because of stretching of the flame front.

To gain more insight into turbulence-chemistry interactions, within the Section Heat Transfer of the Department of Applied Physics of the Delft University of Technology, a long-term project was defined to study turbulent piloted jet diffusion flames. This project is aimed to construct a database with experimental and numerical results for a large number of relevant quantities in a flow geometry with well-defined initial and boundary conditions. Features of this flame are a central coaxial fuel jet surrounded by an annulus of air. This annular air flow is turbulent and the whole is placed within a low-speed coflowing air stream. This three-flow system with turbulent primary air, differs from flow systems used for nonpremixed jet flames reported in literature. These are mainly jet flows into still air or jet flows in a low-turbulence coflow. The effect of turbulence on chemistry was studied by varying the exit velocities. The flow was designed to have high scalar dissipation rates with resulting localized extinctions, yet to provide overall stability by using pilot flames.

Recently, a dissertation on turbulent fluctuations in this nonpremixed flame has appeared. De Vries (1994) performed a study on turbulent concentration fluctuations in diffusion flames using laser induced fluorescence. Semi-quantitative determination of OH radicals was performed. In addition, NO seeded to the fuel was measured to study the mixing by the shear layer turbulence of a conserved species. The spatial structure of the flames was visualized and length scales of OH and NO concentration fluctuations were derived. A second dissertation by Peeters (1995), reporting the development of numerical models to describe turbulent natural gas diffusion flames, will appear soon. The validity of relatively simple chemistry models will be explored. Important phenomena like radiative heat transfer, turbulent flow and mixing of species, description of chemical reaction and formation of NO_x are incorporated in the numerical code.

1.3 Aims of this study

In the light of the previous discussion on the importance of detailed knowledge of the turbulence structures in turbulent natural gas flames, the principal aims of the study described in this thesis are twofold. Firstly, the performing of experiments should add detailed information on the interaction between turbulence and chemistry in combustion and improve general understanding of flame processes in turbulent flames. Secondly, this work should provide detailed measurements against which computational models of turbulent combustion can be tested.

To provide these data, Laser Doppler Anemometry (LDA), thermocouples and Laser Induced Fluorescence (LIF) setups are used. Applying these experimental techniques, the present study can be divided into two parts. The first part is associated with the study of flame characteristics of a disk-stabilized premixed flame. In the second part of this study, four piloted jet diffusion flames are considered. This division gives rise to the following studies and associated aims:

1. The structure of the disk-stabilized premixed flame has been subject of investigation at Instituto Superior Técnico already. A burner very similar to this one was built. The Reynolds number in our rig, combusting with natural gas, is lower than in the experiments performed in Lisbon, with a premixed propane-air mixture, however. Therefore, measurement of mean velocities and turbulence properties is required in our specific configuration. Mean temperatures in the flame should add information to the overall view of the combustion process. By means of one- and two-dimensional detection of fluorescence of OH radicals, detailed flame chemistry data should be revealed. Estimation of time scales of velocity fluctuations and length scales of concentration fluctuations are required to determine the combustion regime of the flame. Altogether, the measurements should elucidate details of the stabilization process and possible destabilizing factors causing local extinction in this type of flame.
2. The structure of the piloted jet diffusion flames is especially important in view of the long-term research project within our Heat Transfer Group to construct a database for this type of flame. Next to characterization of the velocity field and higher order properties, special attention is paid to resolve the initial conditions of the flow field. This information is very important for modelling applications. Besides, as mentioned in the previous section, determination of the time and length scales of characteristic eddies provides crucial information. A comparison between reacting and nonreacting flows is made to indicate the influence of combustion on the turbulence. Introducing the fuel and primary air velocity as parameters to influence the turbulent mixing in the flame, the interaction between the flame front (marked by the presence of OH radicals and high mean temperature) and turbulence can be investigated. Despite global stability of all flames, they may be extinguished locally. Comparison of different flame properties can help to shed some light on the onset of these local extinctions.

From the studies mentioned above, the influence of turbulence, chemistry and their mutual interaction in combustion should become clear, thereby contributing to the understanding of flame stabilization processes and local extinction phenomena in both flame types.

1.4 Some relevant earlier studies

Disk-stabilized premixed flames and piloted jet diffusion flames have been subjects of intensive research. In literature, reports of experimental and numerical investigations in both geometries have appeared. Until a few years ago, focus was mainly on elucidating the main flame structures and investigating limits of stabilization. These attempts were mainly either experimental or numerical in character. Interactive comparisons of measurements with results of simulations in exactly the same geometry are generally believed to contribute largely to the understanding of combustion processes. Up to now, however, these comparisons have received little attention in literature.

Disk-stabilized premixed flames

After numerous experiments on flames in the near wake of a disk (*e.g.* Longwell *et al.* (1953); Davies and Beér (1970); Ballal and Lefebvre (1979)), knowledge of the governing processes increased drastically as a result of laser Doppler velocity measurements performed by Durão and Whitelaw (1978). These measurements were extended with temperature measurements by Taylor and Whitelaw (1980), while investigating the limits of stability of a confined configuration. Ever since, the mechanism of flame stabilization by a bluff-body has been under intensive investigation for many years. Refinement and improvement of the measurements by Heitor *et al.* (1985, 1987, 1988) resulted in a number of papers. Simultaneous velocity and temperature data were obtained, by coupling a laser Doppler velocimeter with compensated small diameter thermocouples. Mean species concentrations and wall pressures were measured, by means of probes.

From then on, instead of the confined geometry, focus was on unconfined setups (see for example Ferrão and Heitor (1992, 1993)). Simultaneous measurements of temperature with digitally compensated thermocouples or Rayleigh scattering and velocity with a laser velocimeter were used to resolve turbulent transport terms and heat fluxes. The resulting data were used to assess the extent to which turbulent mixing in flames is altered by the accompanying heat release.

Piloted jet diffusion flames

The literature on experiments in atmospheric turbulent diffusion flames is even more abundant. Much of the work on round jets in coflow has been carried out in forced draft, vertical wind tunnels with an axisymmetric fuel jet located at the upstream end of a test section. At first, the experimental data featured velocity measurements (see for example Stårner and Bilger (1980, 1986, 1987) or Schefer *et al.* (1987)). These experiments were extended by exploring the interaction between turbulence and chemistry in turbulent diffusion flames by single-point measurements, using Raman, Rayleigh and LIF methods by for example Dibble *et al.* (1984), Masri *et al.* (1988a, 1988b), Barlow *et al.* (1990b) and Stårner *et al.* (1990, 1991). Although these measurements were highly accurate, the spatial characteristics of the reaction zone could not be explored. Planar imaging of reactive species offers direct spatial information and has recently been used to obtain simultaneous OH, CH and CH_4 images (Schefer *et al.* (1990); Stårner *et al.* (1992); Stårner *et al.* (1993)).

1.5 Outline of this thesis

In Chapter 2 of this thesis, the importance of chemical kinetics and fluid mechanics on the general flame structure will be treated. Next to indicating the importance of OH radicals in the combustion process, some characteristic quantities and dimensionless

numbers will be introduced. Comparison of these properties enables one to distinguish between premixed and nonpremixed combustion and to gain some insight into the interaction between turbulence and chemistry. Understanding these processes is essential to comprehend phenomena as flame stabilization and local extinction.

A description of the flow configurations and the inlet conditions for the disk-stabilized burner and the jet diffusion burner will be given in Chapter 3. Focus in this chapter is on the experimental methods to obtain data on the velocity characteristics (laser Doppler anemometry), mean temperatures (thermocouples) and OH radical distributions (laser induced fluorescence). Also details about the data reduction and the accuracy of the measurements will receive attention.

The structure of the disk-stabilized premixed flame to study the effects of turbulence in a flame that is stabilized by a recirculation zone, will be discussed intensively in Chapter 4. Properties of the reacting and nonreacting velocity field will be presented. Temporal and spectral analysis of fluctuating velocity components will elucidate characteristic time scales and dominant frequencies. Mean temperatures add information on the influence of heat transfer. Visualization of the reaction zone by planar imaging of the OH concentration in the flame, will appear to contribute to the understanding of extinction phenomena and the flame stabilization process. Length scales of concentration fluctuations will be estimated for comparison with scales of the velocity field. From these data not only the influence of combustion on the flow field will be elucidated but also the regime of combustion can be characterized.

The second main configuration of interest is the piloted jet diffusion flame. In Chapter 5, measured data for a number of flow settings (both reacting and nonreacting) will be presented. Variation of the fuel and primary air velocity is used to study flames with different rates of turbulent mixing and turbulence-chemistry interaction. Comparison of mean velocities and higher order moments enables one to quantify these effects. In addition, the mixing behaviour between fuel and air will be addressed, applying a special seeding technique for the laser Doppler measurements. As in Chapter 4, mean temperatures and OH concentrations (both visualized and quantitatively determined) provide information about the zones where chemical reactions occur. Comparing these results with turbulence properties will appear to be useful to resolve the effect of turbulence on the flame front. When characteristic scales of fluctuating velocities and concentration fluctuations are derived, this knowledge can also be used to qualify the combustion regime for nonpremixed flames. Furthermore, a comparison of the turbulent velocity fields in reacting and nonreacting flows will be made. Some attention will be paid to the approach to extinction and lift-off phenomena in the jet diffusion flame. Also an important topic of this study, the comparison of experimental data with results from numerical simulations, will be discussed in Chapter 5.

Finally, in Chapter 6, the main conclusions of the results presented in this thesis will be given.

Chapter 2

Principles of turbulent combustion

2.1 Outline of this chapter

As was mentioned in the introduction of this thesis, flame stabilization and extinction of turbulent flames are important subjects because they affect the operation of combustion devices. In order to comprehend the processes involved, this chapter begins with a review of the general characteristics of turbulent combustion. By means of dimensionless numbers and characteristic properties of chemistry and turbulence, it is possible to distinguish between various types of turbulent combustion. Next to this description, interactions between turbulence and chemistry have great influence on the flame structure. Under certain circumstances, the flame may be locally extinguished or have some problem to stabilize at all. Therefore, a description of possible extinction phenomena and the process of flame stabilization in premixed and nonpremixed flame systems is given in Sections 2.3 and 2.4, respectively. An important part of these sections is associated with disk-stabilized premixed flames and piloted jet diffusion flames, being the explicit topics of investigation in this thesis. The theoretical coverage of the principles of turbulent combustion in this chapter is by no means complete and the reader is referred to more extensive references (see for example Schlichting (1968), Hinze (1975), Gardiner (1984) or Glassman (1987)).

2.2 Introduction

2.2.1 Chemical kinetics

In turbulent flames, as in any chemically reacting flow, reactions take place where reactants are mixed at molecular scale at sufficiently high temperature. The reaction rate constant, given by an Arrhenius type of relation, contains a temperature dependency as well as a steric factor to include the effect of collision terms, because not every collision of reactants will lead to products. Only those molecules which possess greater energy than a certain activation energy E_a will react. The reaction rate constant k is defined as follows

$$k = A \exp\left(\frac{-E_a}{RT}\right), \tag{2.1}$$

where A is the steric factor to include collision terms, R is the universal gas constant and T is the temperature.

In combustion processes of natural gas, the conversion of fuel (mainly methane) with oxygen to carbon dioxide and water does not occur in a single step but through several hundreds of chemical reactions (Westbrook and Dryer (1984)). Modelling of the chemical processes in a flame therefore requires knowledge of all reaction rate constants and of how the reactions interact. The full kinetic mechanism may be reduced to a number of main reactions, in which radical chain reactions play an important role. The initiation step, in which an inert species M is involved, is believed to be either

$$CH_4 + M \rightleftharpoons CH_3 + H + M,$$

or

$$CH_4 + O_2 \rightleftharpoons CH_3 + HO_2,$$

the latter being the more important at lower temperatures. At high temperatures, the H or HO_2 quickly provide a radical pool of chain carriers OH, O and H by the chain mechanisms of the hydrogen-oxygen reaction:

$$\begin{aligned}
H_2 + M &\rightleftharpoons 2\,H + M && \text{(initiation)},\\
H + O_2 &\rightleftharpoons OH + O && \text{(branching)},\\
O + H_2 &\rightleftharpoons OH + H && \text{(branching)},\\
OH + H_2 &\rightleftharpoons H_2O + H && \text{(propagation)},\\
2\,H + M &\rightleftharpoons H_2 + M && \text{(termination)},\\
H + OH + M &\rightleftharpoons H_2O + M && \text{(termination)},\\
H + O_2 + M &\rightleftharpoons HO_2 + M && \text{(termination)}.
\end{aligned}$$

The fuel is attacked by these radicals; for example,

$$CH_4 + OH \rightleftharpoons CH_3 + H_2O.$$

This illustrates the importance of OH radicals in the fuel reduction process. The methyl radicals may undergo the sequence

$$\begin{aligned}
CH_3 + O_2 &\rightleftharpoons CH_3O + O,\\
CH_3O + O_2 &\rightleftharpoons CH_2O + HO_2,
\end{aligned}$$

producing formaldehyde, which is oxidized in steps (again by OH radicals) such as

$$CH_2O + OH \rightleftharpoons HCO + H_2O,$$

followed by

$$HCO + M \rightleftharpoons H + CO + M.$$

The mechanism described here results in H_2O and CO as reaction products. The oxidation of CO to CO_2 occurs largely by

$$OH + CO \rightleftharpoons CO_2 + H.$$

2.2.2 Flame structure

A flame of natural gas is characterized by three zones: a preheat zone, a reaction zone and a recombination zone. Within the preheat zone, on the fresh mixture side, the temperature and species vary due to diffusive and convective processes, mainly without exothermal reactions. Within the reaction zone, diffusion and reactions are acting together. The actual characteristics of the reaction zone and the composition changes throughout the flame are determined by the convective flow of unburnt gases toward the flame zone and the diffusion of radicals from the high-temperature reaction zone against the convective flow into the preheat region. This diffusion is dominated by hydrogen atoms and, consequently, significant amounts of HO_2 form in the lower temperature preheat region. The HO_2 subsequently forms hydrogen peroxide. Since the peroxide does not dissociate at the temperatures in the preheat zone, it is convected into the reaction zone and then forms OH radicals at the higher temperatures that prevail there. Thus, a relatively large OH concentration with respect to that of O and H exists in the early part of the reaction zone and OH is the primary reason for the fuel decay. The latter part of the reaction zone forms the region where the intermediate fuel molecules are consumed and where the CO is converted to CO_2. The CO conversion results in a major heat release in the system and is the reason that the rate of heat release peaks near the maximum temperature. The mean temperature curve falls off quickly because of the rapid disappearance of CO and the remaining fuel intermediates. The recombination zone falls into the burnt gas or post-flame zone.

A very simple theory with constant diffusivities and heat capacities leads, within the flame front, to an exponential decay of the reactant mass fraction and an exponential increase of the temperature from the fresh mixture temperature to T_{ad}, the so-called adiabatic flame temperature. This adiabatic flame temperature is the temperature resulting from a combustion process that takes place adiabatically and with no work, heat exchange or changes in the potential or kinetic energy. This is the maximum temperature that can be achieved for the given reactants, because any heat transfer from the reacting substances and any incomplete combustion would tend to lower the temperature of the products.

A factor complicating the modelling of flames is that in many flow situations there may be an interaction between the character of the flow and the reaction chemistry. If the flow becomes turbulent, there are fluctuating components of velocity, temperature, density, pressure and concentration. The degree that such components affect the chem-

ical reactions, heat release and flame structure, depends upon the relative characteristic times associated with each of the individual elements. The convective and diffusive time scales are in general of the same order of magnitude, but the chemical time scale is much smaller. Therefore, the assumption of fast chemistry, or local equilibrium, is often used. It is an assumption that introduces an important simplification, since it eliminates many parameters associated with chemical kinetics.

2.2.3 Fluid mechanics

The fluid-mechanical aspects of the flow can be represented by a number of characteristic parameters. In terms of the characteristic mean velocity U, the size L of the combustion chamber and kinematic viscosity ν, a Reynolds number Re may be defined as follows

$$\mathrm{Re} = \frac{UL}{\nu}. \tag{2.2}$$

For turbulent fluctuations, there is a relation between a quantity, like temperature, concentration or velocity, at a certain time and location and this same quantity at a different time and or location, provided that the time difference and spatial distance is not too large. If one wants to describe the evolution of for example a fluctuating velocity function $u'(t)$, it should be known how the instantaneous values of u' at different times are related (Tennekes and Lumley (1972); Hinze (1975)). The fluctuating velocity can be obtained from a Reynolds decomposition, which states that an instantaneous velocity u_i can be decomposed into a mean flow velocity $\overline{u}$ and an instantaneous velocity fluctuation u_i', such that

$$u_i = \overline{u} + u_i'. \tag{2.3}$$

The extent to which the fluctuations at different times are correlated, is provided by an autocorrelation function, which is defined as follows

$$\rho_u(\tau) = \frac{\overline{u'(t)\,u'(t+\tau)}}{\overline{u'^2}}. \tag{2.4}$$

Here τ represents a small time difference. The Fourier transform of $\rho_u(\tau)$ is known as the power spectral density or simply power spectrum

$$S_u(\nu) = \int_{-\infty}^{\infty} \rho_u(\tau) e^{2\pi i \nu \tau} d\tau. \tag{2.5}$$

The spectrum $S_u(\nu)$ represents the mean square amplitude of the Fourier coefficient of $u'(t)$ at frequency ν; it may be thought of as the energy in $u'(t)$ at ν. An integral time scale of turbulence $\mathcal{T}_u$ is defined by

$$\mathcal{T}_u = \int_{0}^{\infty} \rho_u(\tau) d\tau. \tag{2.6}$$

The value of $\mathcal{T}_u$ is a rough measure of the longest time interval over which $u'(t)$ is correlated with itself. The integral time scale can be converted into a length scale, according to Taylor's hypothesis. Taylor's hypothesis states that the turbulence is convected by the mean velocity with negligible change of its identity. If Taylor's hypothesis applies, then a relationship between space and time scales can be developed, according to

$$\mathcal{L}_u = \overline{u}\,\mathcal{T}_u. \tag{2.7}$$

This turbulence length scale characterizes the large eddies, those of low frequencies and long wavelengths. Typically, $\mathcal{L}_u$ is less than L, but of the same order of magnitude (Hinze (1975)). The turbulence length scale can be introduced in terms of a representative rate of dissipation of velocity fluctuations, essentially the rate of dissipation of the turbulence kinetic energy. The rate of dissipation is given by

$$\varepsilon \approx \frac{{u'_{\text{rms}}}^3}{\mathcal{L}_u}, \tag{2.8}$$

where u'_{rms} is a representative root mean square velocity. The turbulence kinetic energy per unit mass is defined as

$$k = \frac{1}{2}\left(\overline{u'^2} + \overline{v'^2} + \overline{w'^2}\right), \tag{2.9}$$

where u', v' and w' are three orthogonal fluctuating velocity components.

Together with the integral length scale $\mathcal{L}_u$, a turbulence Reynolds number can be defined

$$\text{Re}_{\mathcal{L}} = \frac{u'_{\text{rms}}\mathcal{L}_u}{\nu}. \tag{2.10}$$

Here, u'_{rms} is used as velocity scale, because it can be interpreted as a turnover velocity of large eddies, thus describing a property of the turbulence. $\text{Re}_{\mathcal{L}}$ has more direct bearing on the structure of turbulence in flows than does Re. In the small eddies, where molecular dissipation occurs, the relevant parameters are the kinematic viscosity, which causes the dissipation, and the rate of dissipation itself. The only length scale that can be constructed from these two parameters through dimensional analysis is the so-called Kolmogorov length l_{K}. The Kolmogorov micro scale is the dissipative scale of turbulence; it represents the smallest scale in a turbulent flow and is given by

$$l_{\text{K}} = \left(\frac{\nu^3}{\varepsilon}\right)^{1/4}, \tag{2.11}$$

or

$$l_{\text{K}} = \frac{\mathcal{L}_u}{\text{Re}_{\mathcal{L}}^{3/4}}. \tag{2.12}$$

The characteristic turning time and velocity of an eddy of the Kolmogorov size are

$$\tau_{\text{K}} = \left(\frac{\nu}{\varepsilon}\right)^{1/2}, \tag{2.13}$$

and

$$v_K = (\nu\,\varepsilon)^{1/4}. \tag{2.14}$$

For large $\mathrm{Re}_{\mathcal{L}}$ there is large spread of the two extreme lengths characterizing turbulence, $\mathcal{L}_u$ and l_K. An additional length, intermediate in size between $\mathcal{L}_u$ and l_K, which often arises in formulations of equations for average quantities in turbulent flows, can be derived from the Taylor micro time scale τ_u. This time scale is defined by the curvature of the autocorrelation coefficient at the origin

$$-\frac{2}{\tau_u^2} = \left.\frac{d^2\rho_u(\tau)}{d\tau^2}\right|_{\tau=0}. \tag{2.15}$$

Expanding $\rho_u(\tau)$ in a Taylor series about the origin, for small τ,

$$\rho_u(\tau) \approx 1 - \frac{\tau^2}{\tau_u^2}. \tag{2.16}$$

The micro time scale is thus the intercept of the parabola that matches $\rho_u(\tau)$ at the origin. Again, by means of Taylor's hypothesis, this time scale can be converted into a Taylor micro length scale of turbulence. With the definition of the turbulence Reynolds number, the Taylor length scale may also be expressed as (Williams (1985))

$$\lambda_u = \mathcal{L}_u\sqrt{\frac{1}{\mathrm{Re}_{\mathcal{L}}}}. \tag{2.17}$$

The parameters introduced thus far, refer to the fluid-mechanical aspects of the flow. As stated before, there are chemical-kinetic aspects, however, that exert an equally strong influence on the determination of combustion regimes. The most fundamental parameter of chemical kinetics is the characteristic time τ_c, required for chemical reaction to occur. In reality, there are many such times, since there are many reactions and, moreover, each of them varies strongly with local conditions. However, from now on a representative τ_c is introduced. The ratio of a characteristic mixing time τ_m to τ_c was introduced by Damköhler, who stated that

$$\mathrm{Da} = \frac{\tau_m}{\tau_c}, \tag{2.18}$$

where the mixing time τ_m can be derived from the integral length scale of velocity fluctuations and the axial rms velocity

$$\tau_m = \frac{\mathcal{L}_u}{u'_{rms}}. \tag{2.19}$$

Qualitatively, large values of Da correspond to conditions of fast chemistry, under which reactions tend to occur in thin, distorted sheets moving in the turbulent flow. On the other hand, for sufficiently small Da, the reactions are relatively slow and

appreciable turbulent mixing occurs prior to reaction, so that conditions of a well-stirred reactor tend to be approached. In a general sense, if the characteristic time τ_c of the chemical reaction is much shorter than a characteristic time τ_m, associated with the fluid-mechanical fluctuations, then the chemistry is essentially not influenced by the flow field. If the contrary condition is true, then the fluid mechanics could have an effect on the chemical reaction rate, energy release rates and flame structure. For example flame stretch may influence the flame surface. A dimensionless number, associated with flame stretch effects is the Karlovitz number Ka, which is defined as

$$\mathrm{Ka} = \frac{\tau_c}{\tau_K}, \tag{2.20}$$

where τ_K is the Kolmogorov time.

By means of these characteristic numbers and time or length scales it is possible to characterize the different regimes of combustion. The most fundamental distinction of combustion types, however, is that of premixed and nonpremixed turbulent combustion. A description of the characteristics of these systems will be the subject of the following two sections.

2.3 Premixed turbulent combustion

2.3.1 General characteristics

Premixed flames arise where fuel and oxidizer are homogeneously mixed prior to combustion. In large combustion devices such as furnaces, premixing is generally avoided because of the explosion hazard. Whenever intense combustion within a small volume is required, however, there are several important applications of turbulent premixed combustion. The principal one is the spark-ignition engine. Other examples are gas-turbine systems and ram jets.

Given a premixed fuel-oxidizer system at room temperature and ambient pressure, the mixture is initially unreactive. However, if an ignition source applied locally raises the temperature substantially, or causes a high concentration of radicals to form, a region of combustion reaction can propagate through the gaseous mixture, provided that the composition of the mixture is within certain limits. There are mixture ratios that will not self-support the flame after the ignition source is removed. These mixture ratios fall at the fuel-lean and rich end of the concentration spectrum. The leanest and richest mixtures, which will just self-support a flame, are called the lean and rich flammability limit, respectively. Essentially what determines the flammability limit is a competition between the rate of heat generation, which is controlled by the rate of reaction and the heat of reaction for the limit mixture rates and the external rate of heat loss by the flame.

The mixture ratio is often defined in terms of an equivalence ratio. It may be defined as the ratio of the actual fuel(F)-oxidizer(O) ratio to the ratio $(F/O)_{st}$ for a stoichiometric process. Stoichiometry is obtained when fuel and oxidizer are mixed on

molecular scale, with exactly the amount of oxidizer to react with all fuel, thus leaving all products in their most stable form.

$$\varphi = \frac{(F/O)}{(F/O)_{st}}. \tag{2.21}$$

For fuel-lean conditions $0 < \varphi < 1$, for stoichiometric conditions $\varphi = 1$ and for fuel-rich conditions $1 < \varphi < \infty$.

An important property of a premixed flame is its ability to propagate normal to itself. The laminar flame speed S_l is defined as the velocity at which unburnt gases move through the combustion wave in the direction normal to the wave surface. The burning velocity and the chemical time scale are linked to each other by the heat conduction process. Therefore,

$$S_l = \sqrt{\frac{\lambda}{\rho c_p \tau_c}}, \tag{2.22}$$

where ρ is the density, λ the thermal conductivity and c_p the heat capacity at constant pressure (Glassman (1987)). Together with an appropriate τ_c, the laminar flame thickness can be defined

$$\delta_l = S_l \tau_c. \tag{2.23}$$

It would be desirable to define a propagation velocity for turbulent flames that would depend only on the fuel-air ratio and some transport properties for laminar flow. However, this is not possible, because the transport properties of turbulent flames are functions of the flow rather than the fluid. A characteristic time for the flame propagation process is the time required for the flame to traverse its own thickness, called the flame time, and equals

$$\tau_f = \frac{l_f}{u_f}, \tag{2.24}$$

where l_f represents a characteristic flame thickness and u_f a flame speed. For premixed flames

$$\tau_f \equiv \tau_c = \frac{\delta_l}{S_l}. \tag{2.25}$$

For scaling purposes it is useful to define a viscosity ν_{ref}, at a reference temperature T_{ref} ($\approx$ 1600-2000 K), as the product of the laminar burning velocity and the flame thickness

$$\nu_{ref} = S_l \delta_l. \tag{2.26}$$

Now the turbulence Reynolds number may be defined

$$\mathrm{Re}_{\mathcal{L}} = \frac{u'_{rms} \mathcal{L}_u}{S_l \delta_l}. \tag{2.27}$$

The turbulence Damköhler number for premixed combustion is given by

$$\mathrm{Da} = \frac{\tau_m}{\tau_c} = \frac{S_l \mathcal{L}_u}{u'_{rms} \delta_l}, \tag{2.28}$$

and the turbulence Karlovitz number

$$\mathrm{Ka} = \frac{\tau_c}{\tau_K} = \gamma \frac{\delta_l}{S_l}, \tag{2.29}$$

where γ is the inverse of the Kolmogorov time τ_K and describes the straining by eddies of the Kolmogorov size l_K, which have a turnover velocity v_K.

2.3.2 Extinction phenomena and combustion regimes

Applying the fast chemistry approach to premixed flows means that complete equilibrium or near equilibrium is maintained everywhere. Once reactions begin, they proceed rapidly to completion and establish an equilibrium state. This approximation is justified if all the chemical-kinetic rates depend strongly on the extent of the reaction, *i.e.*, if the reactions are represented as one-step processes with a value of the overall activation energy large compared with the thermal enthalpy of the burnt gas (Libby and Williams (1981)). As a consequence, premixed flames can be viewed as comprising packets of either unburnt mixture or fully burnt gas, separated by a very thin burning or flamelet zone (Libby (1985); Pope (1987)). This flame surface is convected, bent and strained by the turbulence and propagates at a speed, that depends on a combination of effects of chemical reactions and heat and species molecular diffusion. In most flamelet models, one also assumes that each flamelet behaves like a laminar flame. This is not a necessary assumption: the only important assumption in flamelet modelling is related to the topology of the flow and to the fact that fresh and burnt gases are separated by a relatively thin continuous region where chemical reactions take place (Meneveau and Sreenivasan (1991)). This region may have a laminar flame structure, but it may also be thickened by small-scale turbulence without invalidating the flamelet assumption.

Laminar flamelets in turbulent flows are subjected to strain and develop curvature as consequences of velocity gradient fluctuations. These influences modify the internal structure of the flame and thereby affect its response to the turbulence. The resulting changes are expected to be of negligible consequence, but as turbulence scales approach the laminar flame thickness δ_l, they become important. Under the flamelet assumption, a central parameter for turbulent combustion modelling is flame stretch. A general definition of stretch, a measure of the variations of an arbitrary flame surface A, is defined as the local fractional increase of flame surface area per unit time t (Williams (1985); Law (1988))

$$K = \frac{1}{A}\frac{dA}{dt}. \tag{2.30}$$

Local flame quenching occurs when the flame front is submitted to external perturbations, like heat losses or hydrodynamic stretch, which are sufficiently strong to decrease the reaction rate to a negligible value or in some cases to completely suppress the combustion process. In other words, quenching is reached when the stretch K imposed to the flame equals the critical extinction stretch. A first criterion for flamelet quenching was proposed by Klimov and Williams (Williams (1985)). The Klimov-Williams criterion states that the laminar flame thickness must be smaller than the Kolmogorov

micro scale in order for the flame to be burning. It implicitly assumes that the turbulent strain is completely converted into flame stretch.

The classical theoretical approach to predict quenching in turbulent flames is to assume that flamelets behave like laminar stagnation point flames and are quenched for similar values of stretch. The critical stretch for a planar stagnation point flame is represented as S_l/δ_l. Defining the Karlovitz number by

$$\mathrm{Ka} = \frac{1/A\,(dA/dt)}{S_l/\delta_l}, \tag{2.31}$$

and assuming that the turbulent flame front will be quenched for the stretch value that extinguishes a stagnation point flame, according to the Klimov-Williams criterion, flamelets cannot exist for $\mathrm{Ka} > 1$, because their internal structure is altered by stretching and quenching. The assumption that turbulent flames will extinguish for similar values of strain as laminar stagnation point flames is a crude approximation. In turbulent reacting flows, the stretch is changing with time because vortices are convected by the mean flow and are dissipated by viscous effects. Flamelets are also free to move to escape from regions of high stretch. Moreover, vortices curve the flame front, making the analogy between flamelets and planar stagnation point flames doubtful.

The premixed flame is characterized by the topology of the region in which reaction occurs and the structure or distribution of thermodynamic properties within the reaction region. The flame has different characteristics depending on the relative values of various chemical and turbulence scales. Dimensional analysis reveals a range of premixed combustion modes progressing from flamelets to distributed reaction zones and well-stirred reactors. Based on two characteristic values u'_{rms}/S_l and $\mathcal{L}_u/\delta_l$, Borghi (1984) has given a description of different premixed combustion regimes, as shown in Figure 2.1.

With logarithmic plotting of u'_{rms}/S_l and $\mathcal{L}_u/\delta_l$ constant values of $\mathrm{Re}_{\mathcal{L}}$, Da and Ka are represented by straight lines on the Borghi diagram, thus representing boundaries between different regimes of premixed combustion. Another boundary of interest is the line $u'_{\mathrm{rms}}/S_l = 1$, which separates the wrinkled and corrugated flamelets. The following regimes can be distinguished:

Flamelet regime

The flamelet regime is subdivided into the regimes of wrinkled flamelets and corrugated flamelets. This regime is characterized by $\mathrm{Re}_{\mathcal{L}} > 1$ (turbulence), $\mathrm{Da} > 1$ (fast chemistry) and $\mathrm{Ka} < 1$ (sufficiently weak flame stretch). The $\mathrm{Ka} = 1$ boundary represents the condition that the flame thickness is equal to the Kolmogorov scale according to the Klimov-Williams criterion. Since viscosity as a molecular transport process relates the Kolmogorov velocity, length and time scales to each other in the same way as the velocity, length and time scales are related for flame propagation, the flame time is equal to the Kolmogorov time and the flame velocity is equal to the Kolmogorov velocity. Clearly, if $u'_{\mathrm{rms}} < S_l$ and u'_{rms} is interpreted as the turnover velocity of the large eddies, even those eddies cannot convolute the flame front enough to form multiple connected

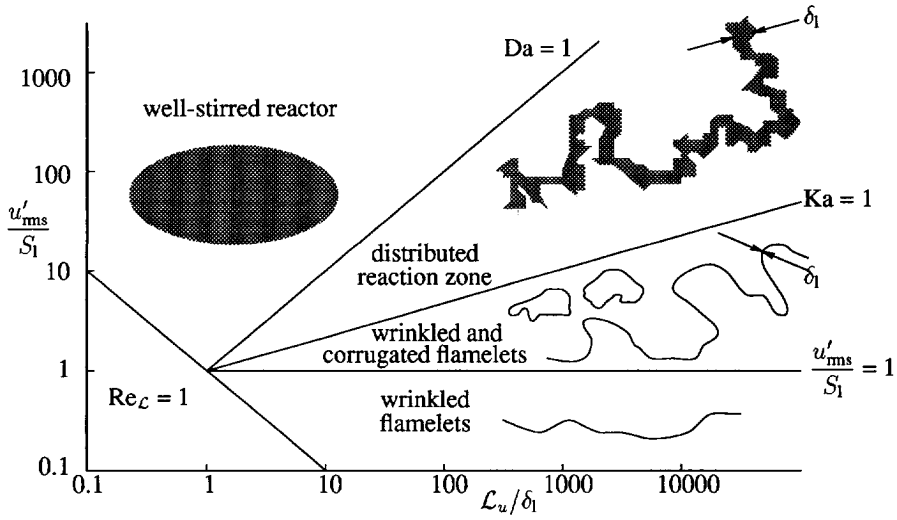

Figure 2.1: Borghi phase diagram for premixed combustion. Based on the ratio of the axial velocity fluctuations u'_{rms} and the laminar flame speed S_l and the ratio of the integral length scale of velocity fluctuations $\mathcal{L}_u$ and the laminar flame thickness δ_l, the combustion regime can be determined.

reaction sheets. In this regime, there is no strong interaction between turbulence and combustion and flame propagation is dominating.

The regime of corrugated flamelets is much more difficult to analyze. With Ka < 1, the laminar flame speed is smaller than u'_{rms} but larger than v_{K} in this regime. Since the velocity of the large eddies is larger than the burning velocity, these eddies will push the flame front around, causing substantial convolution. Conversely, the smallest eddies, having a turnover velocity less than the burning velocity, will not wrinkle the flame front.

Distributed reaction zone regime

The distributed reaction zone regime is characterized by Re$_\mathcal{L} > 1$, Da > 1 and Ka > 1. This last inequality indicates that flame stretch is strong and that the smallest eddies can enter into the flame structure since $l_{\text{K}} < \delta_l$, thereby broadening the flame structure. In this way the smaller eddies may lead to local quenching of the inner reaction zone layer. The notion of a well-defined flame structure and the burning velocity as a relevant velocity scale has no meaning in this regime. The chemical time scale τ_c remains still meaningful, since reactions do also occur independently of flame propagation. In addition, since there is an inner reaction zone thinner than the flame thickness, the quenching of this inner zone by flame stretch is the important physical process. From a physical point of view, the quench time τ_q is the more relevant time scale but, at least

for stoichiometric methane flames, it has been shown that $\tau_q \approx \tau_c$.

A quench scale may be interpreted as the size of the largest eddy within the inertial range that is still able to quench a thin reaction zone

$$\delta_q = \sqrt{\varepsilon \tau_q^3}. \tag{2.32}$$

Smaller eddies, up to δ_q, induce a larger stretch and, thus, will quench the thin reaction layers within the flow field more readily and, thereby, try to homogenize the scalar field locally over a distance up to δ_q. Therefore, δ_q may be interpreted as a correlation length for the reactive scalar field, or in physical terms, as the size of a localized well-stirred reactor.

The well-stirred reactor regime

The well-stirred reactor regime on the upper left of the Borghi diagram is characterized by $Re_{\mathcal{L}} > 1$, $Ka > 1$, but $Da < 1$, indicating that the chemistry is slow compared with turbulence. Now all eddies up to $\mathcal{L}_u$ can quench the inner reaction zones, since $Da < 1$. Turbulence homogenizes the scalar field by rapid mixing, leaving the slow chemistry to be the rate-determining process. Therefore, no specific interaction between turbulence and combustion can occur in this regime and no specific interaction scale is to be defined.

2.3.3 Combustion in disk-stabilized premixed flames

As early as the late 1940's, the stabilization of flames in high-velocity premixed streams received attention because of the relevance to after-burner devices for turbojet engines and rocket combustors. In most cases of flame stabilization, a solid obstacle or bluff body is placed in the flow in order to create a recirculation zone and numerous theories have been proposed to explain and predict the stability limits of bluff-body premixed flames. Stable combustion in bluff-body stabilized configurations refers to the presence of the flame only downstream of the bluff body. There are two types of stability limits for such flames: the first is when the velocity is low and the flame flashes back upstream of the bluff body into the mixture. At small values of the exit velocity U_0, flashback will occur, with the flame attaching to the boundary layer upstream of the baffle. The second, more important stability limit in practice is when the mixture velocity exceeds a critical value and the flame experiences blow-off (*i.e.*, is no longer stabilized at the duct exit). Blow-off conditions for premixed flames are understood to the extent that they can be estimated through suitable balances of flame speed with flow velocity. In Figure 2.2 the main characteristics of a bluff-body stabilized premixed flame with a uniform upstream velocity profile are presented.

The flame stability characteristics of a bluff-body stabilized flame are largely determined by the aerodynamics of the flow around the body. The bluff-body system provides a boundary layer flow, where a combustion wave may propagate, in close proximity to a region of continuously recirculating flow, which acts to provide the boundary layer with a supply of heat and chemically active species carried by the hot

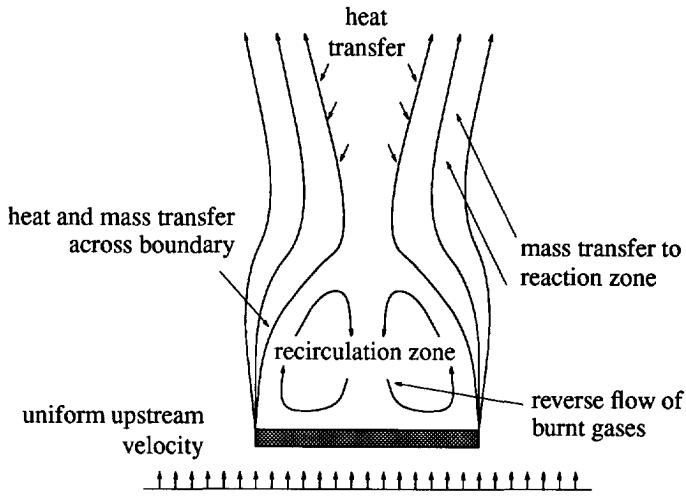

Figure 2.2: Recirculation zone and heat and mass transfer in a flame stabilized behind a bluff body, immersed in a uniform velocity profile.

combustion products (Davies and Beér (1970); Beér and Chigier (1972)). This process involves the recirculation zone which acts as the heat source and the surrounding shear layer, where the heat exchange occurs. This aerodynamic interaction permits a flame to be stabilized over wide ranges of approach flow velocities and mixture ratios.

In the outer regions of the wake, where the flame is anchored, the combustion wave propagates into a flow region with high velocity gradients, where flame stretch occurs. When the flame stretch factor exceeds a critical value, the flame blows off. If flame stabilization could be assumed to be a steady-state process, then the characteristics of the recirculation zone and the surrounding shear layer could be related to the design parameters of the stabilizer. To gap the bridge between aerodynamics and chemical kinetics in bluff-body stabilized flames, several semi-empirical theories were developed according to different understandings of the flame stabilization mechanism. The major differences between these models are:

1. the selection of reaction volume, *i.e.*, either the whole recirculation zone or the mixing layer only.
2. the emphasis on energy and mass balance or characteristic time scales comparison.
3. the emphasis on chemical kinetics or heat transfer.

Stirred-reactor theory

Longwell *et al.* (1953) assumed the recirculation zone behind a bluff body to be a well-stirred reactor. In that case, the flame stability is purely controlled by chemical

kinetics. It was assumed that chemical reaction is initiated and completed inside the recirculation zone, that is uniform in composition and temperature. Extinction was predicted to occur when a chemical time becomes large compared to the residence time in the reactor. Application of this theory may be somewhat doubtful for recirculation zones, because it is evident from measurements that the recirculation zone is a volume of almost inert hot reaction products, in which hardly any chemical reaction takes place.

Based on the stirred-reactor theory, Ballal and Lefebvre (1979) proposed a weak-extinction model. It was assumed that flame extinction occurs when the amount of heat required for igniting the entrained fresh mixture just exceeds the amount of heat generated by combustion in the recirculation zone. The weak-extinction model is insufficient in predicting the peak blow-out velocity for a near-stoichiometric fuel-air ratio due to the limitation of the chemical correlation that was applied. Therefore Ballal and Lefebvre (1981) adopted a different criterion for flame stability. They proposed that flame blow-out occurs when the residence time of unburnt mixture in the recirculation zone is just less than the required combustion time.

Characteristic-time theory

The characteristic-time theory was first proposed by Zukoski and Marble (1956). They described the stabilization mechanism of bluff-body flame holders. The fresh mixture entering the shear layer, surrounding the recirculation zone, is ignited by the hot burnt gases, entrained from the recirculation zone. The burning mixture then flows downstream within the shear layer and, in turn, ignites neighbouring pockets of fresh mixture. When fully burnt gases leave the shear layer, some portion recirculates back into the wake region, thereby providing a continuous source of ignition to the incoming fresh mixture. Accordingly, stable combustion is achieved when the fluid residence time in the shear layer is greater than the ignition delay time. Because the reaction rate is assumed to be very fast, once the mixture has been ignited, the combustion time is equivalent to the ignition delay time. Thus, the Damköhler number in the shear layer controls blow-out, while the function of the recirculation zone is to provide heat and active species to the shear layer.

Following Spaldings' (1970) eddy-breakup model of premixed turbulent flames, Altenkirch and Mellor (1974) suggested that the fluid mechanics time in the shear layer should be characterized as the turbulent mixing time rather than the residence time. The entrained turbulent eddy in the shear layer must be ignited to sustain the flame before being quenched by the oncoming fresh cold mixture.

Plee and Mellor (1979) assumed that the turbulent mixing time is proportional to the ratio of the integral eddy scale to the flow velocity at the flame holder edge. They viewed the large-scale eddy in the shear layer as dissipating when flowing downstream. The initial scale of the large eddy was proportional to the geometric dimension of the flame holder. The discovery of an orderly large-scale coherent structure in the turbulent mixing layer by Brown and Roshko (1974) has changed many aspects of turbulent flow modelling. Their discoveries led to the view that the coherent eddy structure in the mixing layer may persist rather than dissipate when flowing downstream.

Thermal theory

The thermal theory generally assumes that the flow field in the wake region can be described by a simplified heat transfer model to establish energy balance. Lees (1954) first suggested that the wake region behind the flame holder can be divided into two zones:

1. a heat conduction zone adjacent to the flame holder, where the reaction rate is negligible, followed by
2. a combustion zone which resembles a stirred reactor.

An energy balance is established between the two zones and the flame is extinguished when too much cold mixture enters the wake.

Besides these three kinds of theories mentioned above, there are other semi-empirical theories which emphasize different aspects of flame stability in premixed combustion. However, to improve the capability to predict and solve turbulent combustion problems, a great deal of effort has been devoted to the development of turbulent flame theory. Reviews on turbulent premixed flame theories and turbulent reacting flow calculations were given, for example, by Libby and Williams (1981), Jones and Whitelaw (1984), Bray, Libby and Moss (1985), Libby (1985) and Pope (1987).

2.4 Nonpremixed turbulent combustion

2.4.1 General characteristics

The previous section was concerned with flames in which fuel and oxidizer were homogeneously mixed, prior to combustion. Many industrial systems, however, fall in the category of mixing rate controlling and lead to the so-called diffusion flames, in which fuel and oxidizer come together in a reaction zone through molecular and turbulent diffusion. In these flames, the mixing rate is slow compared to the reaction rate of fuel and oxidizer and, thus, the mixing controls the burning rate. For safety reasons, diffusion flames rather than premixed combustors are being used in industrial applications. The distinctive characteristic of a diffusion flame is that the burning (or fuel consumption) rate is determined by the rate at which the fuel and oxidizer are brought together in proper proportions for reaction. Unlike premixed flames, that have a very narrow reaction zone, diffusion flames have a wider region over which the composition changes and chemical reaction can take place. Obviously, these changes are due principally to some inter-diffusion of reactants and products.

The diffusion flame, like the premixed flame, has certain regions of stability beyond which burning cannot occur. These regions are quite similar to those of premixed flames (except for flashback). However, the diffusion flame is more tolerant to changes in flame conditions than a premixed flame. The basic structure of a nonpremixed or diffusion flame is well known (Williams (1985); Borghi (1988)). The case of a steady

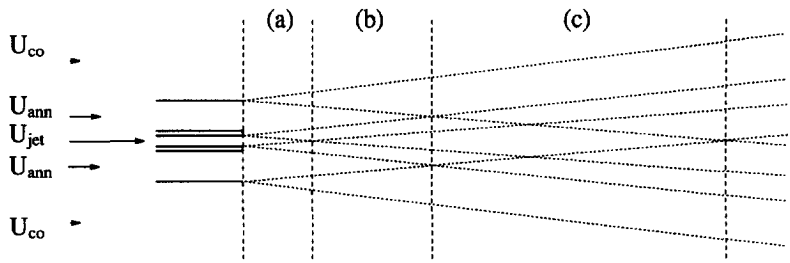

Figure 2.3: Schematic representation of the shear layers present in a three-flow system, featuring the potential core region (a) and the regions of developing (b) and fully developed turbulence (c).

diffusion flame, stabilized at the boundary between two streams, one oxidant rich, the other fuel rich is classical.

When fuel is supplied by a circular jet and the air is obtained from a coflow, because of velocity discontinuities between the jet and the primary air flow, shear stresses are set up and a shear layer originates. The Kelvin-Helmholtz instability is primarily responsible for the formation of vortices. The shear layer becomes turbulent very close to the nozzle and on the inside invades into the uniform velocity jet. On the outer side it penetrates into the ambient air and causes the jet to entrain fluid from its surroundings. The entrainment of ambient air causes the shear layer to grow. The resulting jet spread results in a decreasing centreline velocity. Just downstream of the nozzle, the centreline velocity is not yet influenced by the shear layer and no air is entrained. This region of undiminished velocity has the form of a cone and is known as the potential core. As the jet spreads downstream, the flame zone enters into the boundary region of the intermittent layer and becomes thicker, indicating the transition to a turbulent flame.

In a three-flow system of a fuel jet, with annular primary air and a secondary air coflow, additional to the shear layer between the central jet and the primary flow, a second shear layer exists between the primary and secondary air flows. The boundaries of the shear layers in this three-flow system are shown in Figure 2.3. Again the potential core region (a) can be distinguished. Downstream of the potential core, in region (b), the shear layer with the annular air causes the flow to develop turbulence. In region (c), shear layers of both the primary and secondary air influence the central flow parts and the turbulence becomes fully developed.

Assuming that the chemistry between fuel and air is single-step and very fast, one can show that an infinitely thin reaction sheet separates the fuel and combustion products on one side and oxidizer and combustion products on the other side. This reaction zone will arise near the surface where a stoichiometric mixture of fuel and air

exists. It is accompanied on both sides by narrow diffusion-convection layers in which the major heat release occurs. Across these zones, temperature and concentrations vary and a local flame thickness can be defined at each given abscissa x from the fuel nozzle exit. Roughly speaking, this thickness scales with a Péclet number $Ux/\mathcal{D}$, as follows

$$e_d \propto x/\left(\frac{Ux}{\mathcal{D}}\right)^{1/2}, \tag{2.33}$$

where U is a characteristic velocity at the given distance x and $\mathcal{D}$ is the diffusivity of mass or heat. Here, a difference with premixed flames appears. For a diffusion flame, there is no intrinsic thickness: the local e_d depends on x. The thickness of the flame will also increase continuously in time, because more and more products will be released. The flame will not be steady in this case. If in addition, a flow stretches the flame in such a way that the products can be pulled away in directions parallel to the reaction sheet, then a steady regime is possible. Another difference is that the jet flame may be stabilized in flows with different velocities and there is no intrinsic flame propagation velocity. The quantity equivalent to S_l, the laminar premixed flame velocity, is the volumetric flux per unit surface of each reactant species crossing the flame sheet. This quantity is not a constant along the flame sheet.

The fast reaction limit of nonpremixed combustion is reached when characteristic transport terms of mass diffusion, thermal diffusion and convection are large in comparison to all characteristic times of reaction in the chemical transformation mechanism. In this case, instantaneous equilibrium is maintained at each point in the flow and scalar properties are fixed by diffusion processes at molecular level (Faeth and Samuelsen (1986)). Reviews on the modelling of turbulent nonpremixed combustion have been given by, for example, Jones and Whitelaw (1984), Peters (1986), Borghi (1988) and Bilger (1989). In the modelling of nonpremixed combustion, an essential feature is the introduction of a chemistry-independent conserved scalar variable, called mixture fraction ξ. The mixture fraction is a measure of the degree of mixing between fuel and air and is unity in pure fuel and zero in pure air. All element mass fractions and enthalpy are linearly related to the mixture fraction, under adiabatic conditions. Combustion will take place in a thin layer in the vicinity of a surface where the mixture fraction ξ, equals the stoichiometric mixture fraction ξ_{st}. In case of the combustion of natural gas and air, the stoichiometric mixture fraction is 0.07. The surface of stoichiometric mixture can be determined as a function of time and space from

$$\xi(x_k, t) = \xi_{st}. \tag{2.34}$$

If combustion takes place in this plane, laminar diffusion flamelets are expected to exist there. The influence of the flow field on combustion is introduced by the instantaneous scalar dissipation rate under stoichiometric conditions (Peters (1983, 1984))

$$\chi_{st} = 2\mathcal{D}\left(\frac{\partial \xi}{\partial x_k}\right)^2_{st}, \tag{2.35}$$

where $\mathcal{D}$ represents a molecular diffusion coefficient. χ_{st} has the dimension s^{-1} and may be interpreted as the inverse of a characteristic diffusion time. It incorporates, implicitly, the influence of convection and diffusion normal to the surface of stoichiometric mixture. The scalar dissipation rate increases with flame stretch and decreases due to diffusion.

2.4.2 Extinction phenomena and combustion regimes

The flame stretch required to achieve quenching of premixed flamelets is much larger than for diffusion flamelets. It is noted that, even in a neutrally diffusive, stretchless situation, incomplete reaction, reactant leakage and consequently flame extinction are inherent features of a diffusion flame with finite-rate kinetics. Furthermore, since a diffusion flame does not have a flame speed and, thereby, the extent of flexibility of a premixed flame to adjust its location in the presence of convection, convection always reduces the residence time for reaction. This leads to reduced flame thickness, increased reactant leakage and consequently increased vulnerability to extinction (Law (1988)).

The criterion for extinction conditions, taken from the work of Liñán (1979), defines a maximum instantaneous dissipation rate χ_q, at the surface of stoichiometric mixture for a flamelet to be burning. The maximum temperature will decrease until $\chi_{st} = \chi_q$. Heat conduction to both sides of the flamelet can no longer be balanced by heat production due to chemical reaction then and the flamelet is quenched (Peters (1984)). The parameter χ_q can be interpreted as a global kinetic quantity describing nonequilibrium effects in diffusion flames. It is the critical value where finite-rate kinetics just balance diffusion. In this sense it is equivalent to the flame velocity in premixed flames which also represents a global kinetic quantity (Peters (1984)).

As is the case with premixed flames, diffusion flames can be distinguished in several types. In order to characterize nonpremixed flame types, a modified version of the Borghi diagram has been proposed by Peters (1991). In contrast to premixed combustion, there is no characteristic length scale that is independent of the flow field in nonpremixed combustion. The only quantity that is independent of the flow field is the width of the reaction zone σ_r, which is measured in mixture fraction space. This width depends on the local mixture fraction gradient in a turbulent flow field. The average reaction zone thickness may be estimated from

$$\triangle x = \frac{\sigma_r}{\xi'} \lambda_u. \tag{2.36}$$

In this equation ξ' represents the square of the mixture fraction variance. A phase diagram is proposed for nonpremixed combustion as shown in Figure 2.4. In this diagram, the conditioned mixture fraction variance ξ''_{st} normalized by $\xi_{st}(1 - \xi_{st})$ is plotted over the ratio of the turbulence time τ_m to the chemical time τ_c, which by analogy corresponds to the turbulence Damköhler number. The choice of the vertical and horizontal axes was motivated by the criterion for quenching of diffusion flamelets $\chi_{st} = \chi_q$ (represented in the diagram by the straight line with slope 1/2).

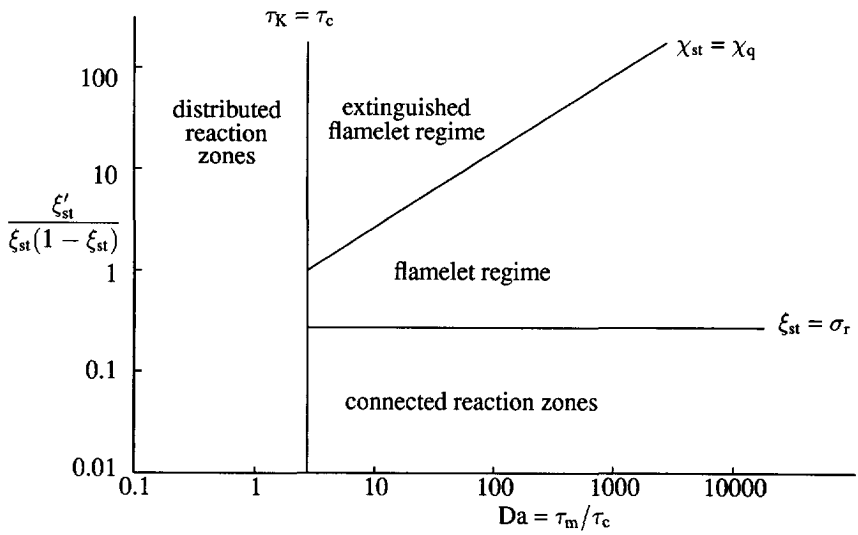

Figure 2.4: Phase diagram showing different regimes in nonpremixed turbulent combustion based on the normalized mixture fraction variation and the Damköhler number.

Analogous to the Klimov-Williams limit in premixed combustion, an additional criterion separating the flamelet regime from the distributed reaction zones regime must be considered. The condition Ka = 1 reduces to $\tau_K = \tau_c$, requiring that the characteristic time for extinction must be smaller than the Kolmogorov time for flamelets to exist. There are four regimes:

Connected reaction zones regime

The regime of the connected reaction zones is defined by $\xi'_{st} < \sigma_r$ and $\tau_K > \tau_c$. This regime is not likely to occur in jet flames, because this type of combustion is more closely related to premixed than nonpremixed combustion.

Flamelet regime

The flamelet regime is defined by $\chi_{st} < \chi_q$, $\tau_K > \tau_c$ and $\xi'_{st} > \sigma_r$. Local quenching of flamelets is possible in this regime and will reduce the probability of burning and thereby the overall heat release rate. However, since the average scalar dissipation rate is lower than χ_q, most flamelets will be burning. In the flamelet regime, the chemical time at extinction τ_c is smaller than the Kolmogorov time. This indicates that burning is faster than perturbations induced by the smallest eddies, which have the shortest turnover time. This is similar to the condition $\tau_c < \tau_K$ for premixed flamelets. A different scaling applies, however, for length scales. Since $\sigma_r < \xi'_{st}$, the average reaction zone thickness is smaller than the Taylor scale in the flamelet regime for nonpremixed

combustion. This differs fundamentally from the condition for premixed flamelets, where the laminar flame thickness is small compared with the Kolmogorov scale.

Extinguishing flamelet regime

The extinguishing flamelet regime is defined by $\chi_{st} > \chi_q$ and $\tau_K > \tau_c$. In this regime, the mean scalar dissipation rate is large due to large mixture fraction fluctuations, while the chemical time scale is smaller than the Kolmogorov time. Flamelets extinguish in this regime due to large mixture fraction gradients. The reaction zone in physical space becomes so narrow that diffusive heat loss will lead to quenching. Because of fluctuations of the scalar dissipation rate, there exists a finite probability for reignition and burning of those flamelets whose instantaneous value of χ_{st} is smaller than χ_q.

Distributed reaction zones regime

The distributed reaction zones regime is defined by $\tau_c > \tau_K$. In this regime, the turnover time of the small eddies is shorter than the chemical time at extinction. Comparable with the premixed case, a quench scale δ_q can be defined, which describes the correlation length of the distributed reaction zones. This regime is likely to occur in flames that are stabilized at the burner nozzle for large turbulence Reynolds numbers. It will occur close to the nozzle rather than downstream, since the Kolmogorov time is considerably smaller upstream than in the downstream portion of the flame.

2.4.3 Combustion in piloted jet diffusion flames

The piloted jet diffusion flame is a burner configuration that is ideally suited to study local extinction phenomena. This flame was designed to have high scalar dissipation rates with resulting localized extinctions, yet to provide overall stability by using pilot flames at the nozzle exit. The possibility of quenching will increase with jet velocity and turbulence levels and decrease with distance from the jet. At downstream locations, where the dissipation rate is smaller, the flame will reignite by hot pockets of reaction products.

Once the pilot flames are shut off, as the velocity of the fuel issuing from the jet is increased, the average flame height changes little. At sufficiently low fuel velocities, the base of the flame extends to the mouth of the duct, where it is stabilized. When a critical exit velocity is exceeded, however, the flame is abruptly detached from the duct and acquires a new configuration of stabilization in which combustion begins a number of duct diameters downstream. This process is referred to as lift-off. The axial distance from the duct exit to the plane at which the flame begins, the lift-off height, increases as the exit velocity is increased further. When the exit velocity exceeds a second critical value, the blow-off velocity, the flame can no longer be stabilized in the mixing region and combustion ceases (blow-off occurs) (Williams (1985)).

Several very different physical mechanisms have been proposed to account for extinction phenomena as well as observed lift-off and blow-out limits.

Premixedness models

Vanquickenborne and Van Tiggelen (1966) suggested that the stabilization of lifted turbulent jet diffusion flames can be understood by assuming that fuel and air are fully premixed at the flame base and that the local flame speed determined by the local turbulence structure of the unignited flow, is associated with this mixture. Flame stabilization occurs at the point where the local time-averaged axial velocity equals the local flame speed. Kalghatgi (1981, 1984) successfully correlated his experimental results by assuming the flame stability model of Vanquickenborne and Van Tiggelen and using dimensional analysis.

Laminar flamelet models

The premixedness model has been challenged by several new theories, which propose that the stabilization of lifted flames results from conditions in the flow where flame extinction processes can no longer occur. Peters and Williams (1983) suggested that the degree of molecular mixing in turbulent jets is insufficient to support the concept of premixed combustion. These authors analyzed the problem in terms of the laminar flamelet model. It was stated that the occurrence of lift-off may be understood in terms of critical strain rates for flamelet extinction. A statistical distribution of the scalar dissipation rate χ exists. When flamelets experience a χ larger than χ_q they will be quenched and therefore not contribute to the overall heat release. As the exit velocity is increased, the average local strain rate increases. An increasing fraction of flamelets then encounters extinction conditions. When too many of the flamelets are extinguished, a network of diffusion flamelets is no longer connected to the burner and lift-off must occur (Janicka and Peters (1982); Donnerhack and Peters (1984)). The behaviour of such randomly distributed networks is described by percolation theory which relates the probability of the burning flamelets to the overall, sudden extinction of the turbulent flame by postulating that the whole flame sheet will disappear if a critical portion of the laminar flamelets has been quenched (Peters (1983)). Stabilization of the flame is believed to occur where combustion extinction and propagation are balanced. This theory was applied successfully to predict the lift-off heights of jet diffusion flames by assuming that lift-off is due to flame extinction at all locations from the nozzle to the flame initiation point.

In this view, any effects of premixing at molecular level are neglected, although time-averaged concentrations will exhibit an apparent mixing through turbulence (Pitts (1988); Bradley *et al.* (1990)). Therefore, Peters (1984, 1993) has extended the flamelet model to the case of partially premixed diffusion flamelets. It was concluded that the extinction of laminar flamelets remains the relevant stabilization mechanism. Experimental and numerical investigations supported this view (Smooke *et al.* (1988)).

Small-scale mixing models

Byggstøyl and Magnussen (1985) also propose that flame stabilization is the result of a balance between combustion extinction and propagation. However, they suggest that the extinction occurs in the smallest scales of the flow. Byggstøyl and Magnussen did

not make particular reference to the exact spatial structure of the small-scale vortices, but assumed that reaction proceeds inside these vortices which were treated as well-stirred reactors. They calculated the volume that these small-scale well-stirred reactors occupy inside turbulent flows and the mass and heat exchange between the reacting vortices with the nonreacting surroundings. It was postulated that extinction occurs when the reactant supply to the Kolmogorov scale reactors is larger than the amount of reactants they can consume.

Lockwood and Megahed (1978) developed a model in which two Kolmogorov scale vortices, one containing burnt and the other unburnt fluid, were assumed to touch. Reaction in the unburnt vortex was supposed to occur only when a flame front propagated into the unreacted vortex. A special characteristic of this model is that the speed at which the flame propagates into the unburnt vortex depends on the vortex rotational speed. The resulting expression for extinction compares the Kolmogorov length scale with a length scale which depends on both the laminar flame speed and the turbulence kinetic energy dissipation rate and which reduces to the laminar flame thickness at the limit of zero turbulence.

Both of these models were developed for premixed combustion to predict diffusion flame extinction with the justification that, because reaction occurs in the small-scale vortices where the reactants are uniformly mixed, the mode of reactant supply in the large scales becomes irrelevant. This is a gross simplification, however, because in diffusion flames the topology of reaction surfaces which follow the diffusive layers between the fuel and air streams is not necessarily the same as the topology of the Kolmogorov scale vortices. It is necessary, therefore, to examine theories for flame extinction developed especially for initially separate reactants.

Large-scale mixing models

Next to small-scale structures, it is believed that the large-scale structures, that develop in the early part of the jet, have an important influence on the distribution of the instantaneous scalar dissipation rate. Two important aspects of large-scale vortices have opposite effects upon flame stabilization (Chen and Goss (1991)):

1. promotion of fuel-air mixing which stabilizes the flame.
2. stretching and penetration of the flame zone which destabilizes the flame.

The weight of these counter effects may be determined by means of associated scales such as the thickness of the combustible mixing zone, the size of the large-scale structure and the thickness of the OH zone which provides a potential source for reignition. Broadwell *et al.* (1984, 1988) propose that flame stabilization results when hot gases, which have been expelled to the edge of the jet by earlier large-scale turbulence structures, are reentrained and ignite noncombusting eddies of the jet. If the mixing time of the reentrained gases is too short, the gases cool rapidly and ignition becomes impossible (Pitts (1988)).

Chapter 3

Experimental methods

3.1 Outline of this chapter

This chapter presents the flow configurations and the experimental methods used to obtain the results shown in Chapters 4 and 5 of this thesis. Details on the operational parameters of the different flames under investigation are given in Section 3.2. Measurements of velocities, mean temperatures and radical concentrations are performed with laser Doppler anemometry, thermocouples and laser induced fluorescence, respectively. The principles of operation, the experimental setups, the reduction of the obtained data and the accuracy of these techniques are described in Sections 3.3 to 3.5.

3.2 Flow configurations

3.2.1 Fuel properties

As fuel, bottled Groningen natural gas is used. Groningen natural gas consists mainly of methane (81.30 %), ethane (2.85 %) and nitrogen (14.35 %) (by volume) (Geerssen (1980)). The net lower calorific value of natural gas is 41.5 MJ/kg. The density of this gas is 0.775 kg/m^3 and its kinematic viscosity is 14.74 $\times$ 10^{-6} m^2/s (at 1 atm and 293 K). Air is supplied from a compressed air line. The density and kinematic viscosity of air are 1.204 kg/m^3 and 15.07 $\times$ 10^{-6} m^2/s, respectively (also at 1 atm and 293 K).

3.2.2 Disk-stabilized premixed flame

Figure 3.1 shows a schematic diagram of the burner arrangement in which a premixed flame is stabilized on a disk with a diameter d = 80 mm, located at the exit section of a contraction with a diameter D = 85 mm. This results in a hydraulic diameter D_h = 5 mm. The blockage ratio, defined as d^2/D^2, is 0.89. Inside the burner, aluminium honeycomb is used as flow-straightener, to ensure a uniform velocity profile upstream of the stabilizing disk. The burner is axisymmetric and is placed vertically upward. The flame is open to the atmosphere and empties into an exhaust hood.

In order to investigate the behaviour of disk-stabilized premixed flames under local extinction conditions, the burner is operated with a fuel-lean mixture. Data are provided for a case where the gas flow rate ϕ_{gas} = 0.54 g/s and the air flow rate

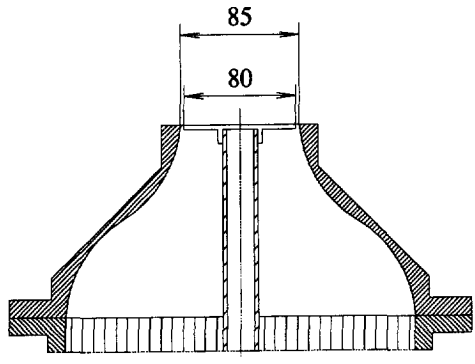

Figure 3.1: Schematic side view representation of the disk-stabilized burner. All measures in mm.

ϕ_{air} = 9.45 g/s, resulting in an equivalence ratio φ = 0.75. This equivalence ratio was selected to provide a stable flame, yet very close to the lean blow-off limit (at φ = 0.7), thus having a high extinction probability. Flow rates are measured with rotameters. The average exit velocity U_0, which is defined as the velocity in the annulus surrounding the stabilizing disk, is 13.2 m/s. Together with the kinematic viscosity of the cold reactants and the hydraulic diameter of the annulus, the Reynolds number becomes 4.4×10^3.

The adiabatic flame temperature for this flame is calculated to be 1898 K. The laminar flame thickness and the laminar flame speed have been derived from numerical and experimental data, known in literature (Gardiner (1984)). The laminar flame speed is calculated to be 0.21 m/s. The kinematic viscosity of the cold reactants mixture ν_c, is 15.04×10^{-6} m^2/s. With a kinematic viscosity of $\nu_h = 3.56 \times 10^{-4}$ m^2/s at the adiabatic flame temperature, the laminar flame thickness becomes 1.7 mm, by means of Equation 2.23. The power of the flame, based on the net calorific value of natural gas, is 22.0 kW.

Also the isothermal flow of this burner with equal exit velocity was investigated. The air flow rate for these measurements was ϕ_{air} = 10.30 g/s.

3.2.3 Piloted jet diffusion flame

A second set of measurements is performed in an axisymmetric nonpremixed jet burner, as presented in Figure 3.2. The burner consists of a round fuel jet with an inner diameter of 8 mm, which is 125 diameters long, sufficiently to establish a fully developed turbulent flow at the nozzle. The burner is operated with primary annular air, introducing the primary air velocity as a parameter, additional to the main fuel jet velocity, for variation of shear and mixing rates near the nozzle. The inner diameter of the annulus is 15 mm and the outer diameter is 45 mm at the exit. The flame is fixed to the nozzle by operation of pilot flames flowing parallel with the main flow. To achieve

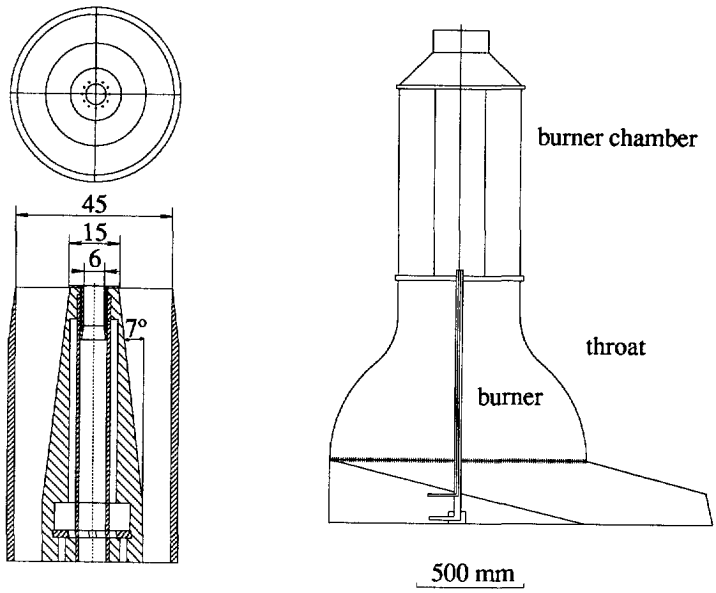

Figure 3.2: Schematic top and side view representation of the axisymmetric non-premixed jet burner and side view representation of the ventilated throat and burner chamber surrounding the burner. All measures in mm.

this an insert with an inner diameter of 6 mm is placed in the fuel jet (D_{jet} = 6 mm), using twelve pilot flames consisting of an acetylene/hydrogen/air mixture, at a ratio chosen to give a C to H ratio equal to that of natural gas (Stårner and Bilger (1985)). This results in combustion products of the same basic composition as those of the main fuel. The pilot flames are located on the burner rim between the fuel jet and the annulus, on a ring 7 mm in diameter. Their Reynolds number is of the order 500 at the nozzle exit and initially laminar. The heat release in the pilot flame is only about 1 % of that in the whole flame. In addition to the stabilizing influence of the pilot flames, there is also a small recirculation zone just above the burner rim, which has a stabilizing effect.

The burner is placed vertically upward and is mounted just above the contraction section of a ventilated throat to avoid an external recirculation zone of combustion products. The throat provides a low velocity (U_{co} = 0.4 m/s), low turbulence intensity, secondary air flow. The Reynolds number of this secondary coflow is 15.1 $\times$ 10^3. In addition, to avoid draught and recirculation, the burner is placed in a windowed burner chamber. The test section consists of an octagonal chamber, 0.9 m high and 0.57 m from side to side. The test section empties into an exhaust hood which also draws air from the room.

Data are provided for the five cases presented in Table 3.1. In this table, the

Table 3.1: Flow settings for the nonpremixed jet flames, featuring flow rate ϕ, exit velocity U and Reynolds number Re of both the gas jet and the primary annular air flow. In addition, the power P of the flames, based on their net calorific value is given.

Flame	$\phi_{gas,jet}$ (g/s)	$U_{gas,jet}$ (m/s)	$Re_{gas,jet}$ (-)	$\phi_{air,ann}$ (g/s)	$U_{air,ann}$ (m/s)	$Re_{air,ann}$ (-)	P (kW)
A	0.25	11.2	4.6×10^3	3.73	2.2	4.4×10^3	10.0
B	0.34	15.5	6.3×10^3	5.20	3.1	6.2×10^3	13.9
C	0.48	21.9	8.9×10^3	7.40	4.3	8.6×10^3	19.6
D	0.48	21.9	8.9×10^3	13.47	7.9	15.7×10^3	19.6
E	0.48	21.9	8.9×10^3	0	0	0	19.6

Table 3.2: Flow settings for the nonreacting jets, featuring flow rate ϕ, exit velocity U and Reynolds number Re of the jet and primary annular air flow.

Jet	$\phi_{air,jet}$ (g/s)	$U_{air,jet}$ (m/s)	$Re_{air,jet}$ (-)	$\phi_{air,ann}$ (g/s)	$U_{air,ann}$ (m/s)	$Re_{air,ann}$ (-)
I	0.74	21.8	8.7×10^3	0	0	0
II	0.75	21.9	8.7×10^3	7.36	4.3	8.6×10^3

gas flow rate $\phi_{gas,jet}$, the average gas jet exit velocity $U_{gas,jet}$, the jet Reynolds number $Re_{gas,jet}$, the air flow rate $\phi_{air,ann}$, the average primary annular air exit velocity $U_{air,ann}$ and the annulus Reynolds number $Re_{air,ann}$ are presented. Flow rates are determined by means of rotameters. The jet Reynolds number is based on the pipe inside diameter, the bulk fuel velocity and the previously referenced density and viscosity. The Reynolds number for the air flow is based on the annular air velocity and the hydraulic diameter of the annulus.

The flames listed in Table 3.1 are designated A,B,C and D in order of increasing Reynolds number. In all cases, the flow is well in the turbulent range. Flames A, B and C have a constant ratio of fuel and primary air flow rate. In these flames, the primary air excess amounts 15 %. In flame D, the fuel flow rate is equal to that of flame C, but the primary air flow rate is 1.8 times larger, resulting in a primary air excess of 112 %. When the pilot flames are shut off, and the primary air flow is decreased to zero, the flame experiences lift-off. This flame is designated as flame E.

Measurements in isothermal jets have been obtained under the circumstances presented in Table 3.2. For jets I and II, the air flow rates for the jet $\phi_{air,jet}$ and the annulus $\phi_{air,ann}$ are given with the respective exit velocities and Reynolds numbers. Jet I represents an air jet into stagnant air. Jet II is an isothermal flow with velocities equal to that of flame C, selected as reference flame.

3.3 Velocity measurements

3.3.1 Laser Doppler anemometry

Laser Doppler anemometry has been widely used and by now is considered state-of-the-art for most combustion research laboratories. The general theory of laser Doppler anemometry is well-known. Therefore, the reader is referred to the works of, for example, Durst *et al.* (1976), Watrasiewicz and Rudd (1976) or Drain (1980). The technique involves the measurement of the frequency of light, scattered from particles moving in the flow, and the linear relationship between this frequency and the particle velocity.

In the differential Doppler technique, two laser beams of equal intensity are focussed and crossed at a point under investigation. Light scattered from the particles in this region, is focussed onto a photo detector. Since light scattered from both beams, reaches the detector simultaneously, a beat is obtained of frequency equal to the difference in Doppler shifts, corresponding to the two angles of scattering. The Doppler frequency is independent of the direction and is given by

$$\nu_D = \frac{2u}{\lambda} \sin(\theta/2). \tag{3.1}$$

Here, u is the velocity component perpendicular to the bisector of the angle of intersection θ of the two crossing laser beams and λ is the wavelength of the laser light.

Instead of the previous description, a so-called fringe model is often used. Although this model contains some physical inaccuracies, it is very useful to explain the principle of laser Doppler anemometry. If one considers the region in the dual-beam system where the two beams overlap, one will realize that in this volume the two beams will interfere with one another and produce a set of fringes. The spacing between these fringes can be defined as follows

$$d_f = \frac{\lambda}{2\sin(\theta/2)}. \tag{3.2}$$

From this equation, it appears that the fringe spacing is dependent on the wavelength of the laser light and the angle of intersection of the crossing laser beams. Now, if a particle is considered crossing these fringes, it will block off much light in a bright fringe and only a little light in a dark fringe. Therefore, if one collects the light which is transmitted, its intensity will fluctuate at the rate at which the particle crosses the fringes. The equation relating the velocity and the Doppler frequency is

$$u = d_f \nu_D. \tag{3.3}$$

3.3.2 Experimental setup

A schematic representation of the laser Doppler configuration is given in Figure 3.3. The 514.5 nm and 488.0 nm laser beams of a 4 W Spectra Physics Ar^+-ion laser are guided through a fibre-optical system to a 2-component OEI backscatter optics, which

form two orthogonal real-fringe measuring volumes. Measurements can be performed at any position of interest in the flows under investigation, by moving a 3-dimensional traversable table on which the optics are mounted. The green beams are aligned with the fringe system perpendicular to the axial direction to measure the axial velocity component directly. Radial velocity components are measured by the blue beams, with the fringe system oriented perpendicular to the radial direction. Directional ambiguity can be overcome through the use of Bragg cells, on each of the beams. The amount of frequency shift is always large (3-6 MHz) compared to the velocities to be measured, so that directional ambiguity is resolved. Because of the accessibility of the LDA optics to the flames, for the measurements in the disk-stabilized premixed burner and the piloted jet diffusion flame two front lenses with a diameter of 80 mm, but with different focal lengths, have been used. This results in differing angles of intersection and fringe spacing, as indicated in Tables 3.3 and 3.4, respectively. The measuring volume is ellipsoidal in shape with an estimated cross diameter of 0.15 mm and a length of 1.9 mm for the measurements in the disk-stabilized premixed flame. For the measurements in the piloted diffusion flames, the measuring volume dimensions are 0.15 mm and 2.1 mm.

The flows are externally seeded with aluminium oxide particles of 1 μm nominal diameter, introduced into the flow with reversed cyclone seeders (Glass and Kennedy (1977)). In the case of the premixed flame, seeding occurs after gas and air are mixed in proper proportions. In the diffusion flame, both the air and gas flows are seeded separately. The concentration of the seeding particles in both flows is (approximately) equal near the nozzle. To accomplish this, the seeding particle concentration was checked just above the burner nozzle in the jet and the primary annular flow by the validated data rate with the laser Doppler system. The outer air surrounding the flame was not seeded. Also conditional seeding measurements are performed in the diffusion flame. These measurements are obtained by seeding the fuel only and the air only, respectively. The purpose of conditional seeding measurements is twofold. Firstly, the velocity measurements in the mixing region of two initially separated flows can be considerably biased due to unequal seeding in the two flows. Thus, by alternately seeding only the jet and only the primary annular air the extremes of potential biasing errors are established. Secondly, conditional seeding provides information on the degree of turbulent mixing since the seed particles act as a marker for fluid originating from the two initially separated inlet flows. Differences in the velocity statistics measured using separate seeding of the inlet streams are indicative of the degree to which small-scale mixing between the inlet streams has occurred.

The scattered laser light, when the seeding particles cross the measuring volume, is collected in the backscatter mode by two separate photo multiplier tubes, one for each velocity component. The photo multiplier signals are input into a TSI, model IFA-750, signal processor. To ensure measurement of both velocity components on one particle simultaneously, a coincidence window of 10 μs is set. Data acquisition and analysis is performed on a personal computer with the commercial TSI FIND-software, extended with self-developed software on a HP-735. For each position either

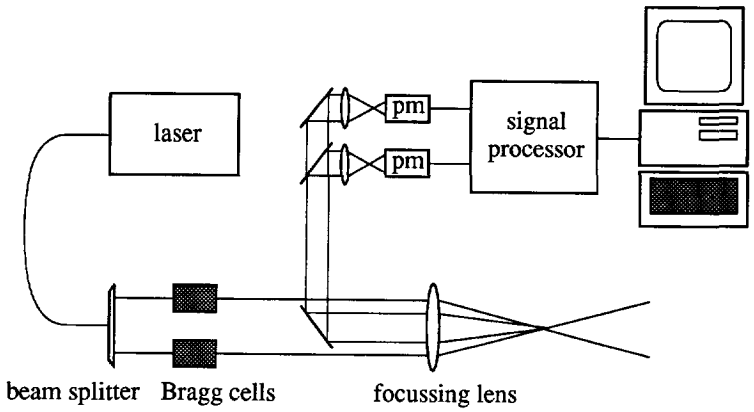

Figure 3.3: Schematic representation of the laser Doppler configuration.

Table 3.3: Characteristics of the LDA configuration for measurements in the disk-stabilized burner.

Focal length of focussing lens (mm)	310	
Wavelength (nm)	514.5	488.0
Half-angle of intersection $\theta/2$ (°)	4.66	4.63
Fringe spacing (μm)	3.165	3.025

Table 3.4: Characteristics of the LDA configuration for measurements in the non-premixed jet burner.

Focal length of focussing lens (mm)	350	
Wavelength (nm)	514.5	488.0
Half-angle of intersection $\theta/2$ (°)	3.99	4.02
Fringe spacing (μm)	3.697	3.480

5,120 or 10,240 data points are collected, depending on the validated data rate. Typical coincidence mode maximum values of the data rate extended from ± 200 Hz in the disk-stabilized premixed flame to ± 500 Hz in the piloted jet diffusion flame. Estimates of the autocorrelation function of axial velocity fluctuations on different positions in the flames are obtained by performing 5 measurements of 19,656 data points and then averaging the results. For these measurements of the axial velocity component only, data rates ranged from approximately 4000 Hz in the disk-stabilized premixed flame to 5000 Hz in the piloted jet diffusion flame.

3.3.3 Data reduction

Performing velocity measurements in the described flows, yields a probability density function (PDF) for the velocity. This PDF is characterized by several moments, the sums of integer powers of the measured values. The following moments can be distinguished:

1. The first moment, or mean velocity

$$\overline{u} = \frac{1}{N}\sum_{i=1}^{N} u_i. \tag{3.4}$$

2. The second moment, or root mean square (rms) velocity, which is a measure of the distribution of measured velocities around the mean velocity

$$u'_{\text{rms}} = \sqrt{\overline{u'^2}} = \sqrt{\frac{1}{N-1}\sum_{i=1}^{N}(u_i - \overline{u})^2}. \tag{3.5}$$

3. The third moment, or skewness, which characterizes the degree of asymmetry of a distribution around its mean

$$S_u = \frac{1}{N}\sum_{i=1}^{N}\left(\frac{u_i - \overline{u}}{u'_{\text{rms}}}\right)^3. \tag{3.6}$$

4. The fourth moment, or kurtosis, is a measure of the peakedness or flatness of a distribution, relative to a normal distribution

$$K_u = \frac{1}{N}\sum_{i=1}^{N}\left(\frac{u_i - \overline{u}}{u'_{\text{rms}}}\right)^4. \tag{3.7}$$

Often the measured skewness and kurtosis values are taken relative to the corresponding values of a Gaussian distribution, being $S_u = 0$ and $K_u = 3$, respectively. The skewness and kurtosis factors are also very sensitive to outliers in the distribution. Therefore, they are ideally-suited to indicate the presence of bad points in the measured data ensembles. These bad data are removed from the data ensemble by means of a sigma-criterion, as described by Meyers (1988), where σ is the standard deviation of the distribution. With this method, first all data points are used to compute a mean and a standard deviation. Next, all data lying outside a window of five times the standard deviation from the

mean are rejected and a new mean and standard deviation are computed, using the remaining data.

In order to calculate autocorrelation functions, a special slotting technique is used (Bell (1982)). The LDA data, consisting of discrete points in time, along with the time between samples, are used to compute an estimate of a correlation function. This is done by forming the product of two data points, determining the time difference (or lag) between them and finding the lagged time slot that best approximates the time difference. The sums of the products at each slot are formed then. The average value of the lagged product within each slot is taken as an estimate of the correlation function at the centre of the lagged time slot (Mossel (1995)). The time slot width τ of the presented results is determined as the inverse of the mean data rate. Estimates of the time scales of the flow have been obtained for the axial velocity component only.

3.3.4 Accuracy

From Equation 3.1 it appeared that once the wavelength of the laser light and the angle of intersection of the crossing beams are known, a linear relation between the Doppler frequency and the particle velocity can be applied. In order to calibrate the LDA system, the angles of intersection have been accurately measured with a theodolite. Applying the LDA technique in our highly turbulent flows, however, may introduce some other sources of error, as reviewed by Durst *et al.* (1976).

Effects as transit broadening (*e.g.* Zhang and Wy (1987)) and non-turbulent Doppler broadening errors (*e.g.* Kreid (1974)) affect mainly the variance of the velocity fluctuations and are estimated to be very small. Apart from preshift, inaccuracies in the Doppler frequency are caused by filtering, the finite resolution of the measurement and optical and electronic noise. Inaccuracies in measurement with an IFA-750 signal processor having a 0.05 % resolution at the highest burst frequencies are neglected.

Since it is the particle velocity that is actually measured with laser anemometry, particle velocity lag is considered. For the particle velocity to correspond with the flow velocity, the particle must be small. Using the estimates of Durst *et al.* (1976) a 1 μm Al_2O_3 particle can follow the flow, with a slip velocity of 1 %, up to a frequency of 3 kHz. This frequency is expected to be sufficient to resolve the frequencies in the flows under investigation.

Once the data are collected, statistical analysis on the ensemble of data points is performed. Generally, the number of rejected samples, as a result of the used 5-σ criterion to calculate the moments of the velocity distribution, is well below 1 % and real outliers are seldomly observed. The statistical uncertainties, with a 95 % confidence interval, are $\pm$ 1 % and $\pm$ 1.5 % for the mean axial and radial velocity, respectively. For the rms values, the statistical uncertainty is $\pm$ 2 % for the axial fluctuations and $\pm$ 2.5 % for the radial fluctuations. Because of the tendency to record preferentially velocities associated with high densities (as these contain more seeding particles), the reported mean and rms velocities are expected to be closer to Favre (density-weighed) averages than to (conventional) time averages. Potential differences between conventional and Favre averages are estimated to be on the order of 10 %. Stårner and Bilger (1981)

report direct measurements of conventionally and Favre averaged velocities in round jet diffusion flames in coflow, yielding differences on the order of 5 % which are well within this limit.

A laser anemometer operates on the signal generated by single particles passing through the measurement volume and produces a measurement of the velocity of the particle while it is in the volume. There are, however, very few circumstances where those realizations can simply be averaged arithmetically to obtain statistical measures of the velocity. The arrival rate of the measurable particles is in general not statistically independent of the flow velocity which brings them to the measurement volume. The result is that the flow statistics are not uniformly sampled and as a consequence, simply averaging of the particle measurements can be, and often is, seriously biased. Two types of bias are assumed to play an important role: velocity bias and seeding bias.

Velocity bias is due to the proportionality of particle flux through the measurement volume and the instantaneous velocity (Edwards (1987); DeOtte *et al.* (1992)). When more faster moving particles than slower moving particles arrive at the probe volume during the measurement time, the mean velocity will be overestimated. It was shown by Razdan and Stevens (1985) that for velocity fluctuations up to 10 % this bias is negligible. As velocity fluctuations increase, however, the velocity statistics are increasingly biased toward higher velocities. A number of techniques have been proposed to eliminate velocity bias. Among the best known are the McLaughlin-Tiedermann weighing technique and weighing with the residence time or the time between data (TBD). The technique of McLaughlin and Tiedermann (1973) weighs each realization by the inverse of the magnitude of the velocity vector. For the residence time weighing method (Buchhave and George (1979)), the amount of time that a particle spends in the measurement region is measured in addition to the particle's velocity. Weighing of each velocity is performed with this residence time. Comparable with residence time weighing, the time between data method (Edwards (1987)) weighs each realization with the time interval between the arrival of the particle triggering the present measurement and the last realization. In all cases, a correction on the arithmetically averaged velocity is obtained, which should result in less weight for the faster moving particles and more weight for the slower moving particles. For both the disk-stabilized premixed flame and the piloted jet diffusion flame a comparison of these correction methods is made.

A bias effect similar to velocity bias occurs in the piloted jet diffusion flame if the seed densities in the fuel jet and the air flow are unequal. In this case, the velocity statistics may be biased toward fluid originating from the more heavily seeded flow. The bias resulting from the origin of LDA seed particles is bounded by measurements of velocity when seed particles are added to the fuel only, followed by measurements when seed particles are added to the primary air flow only. Although seed rates in the fuel jet and the annular air are frequently adjusted to maintain equal seed densities (indicated by the validated data rate), variations up to 30 % in seed density during an experimental run may not be unusual. The difference between these two cases is considered to be the largest source of error (measurements with conditional seeding reveal maximum differences of 20 % of the mean axial velocity, measured in regions

of the highest velocity gradients).

Other, minor, sources of bias are fringe bias and signal amplitude bias. Fringe bias is caused by the fact that processors cannot measure all speeds at all angles (Edwards (1987)). Part of this problem may be solved by using a frequency preshift that is high enough to ensure that a scattering particle crosses a critical number of interference fringes of the measurement volume. Signal amplitude bias occurs when a particle passing through the probe volume does not generate a signal with a large enough amplitude to be validated by the signal processor (Durão *et al.* (1982)). This may be the result of reduced particle visibility associated with higher velocity particles. This can also be alleviated, to some extent, by frequency shifting (Durão and Whitelaw (1979)).

Additional errors can occur as a result of combustion, but are even more difficult to control. For example, high flame temperatures can cause a reduction in the effective scattering cross sections of the seed material. This can result in higher probability of sampling low-temperature fluid elements. Assuming that the ideal gas law applies, the seed density will be proportional to the gas density. This will also result in a higher probability of measuring low-temperature, high-density fluid elements (Goss *et al.* (1988)). Diffraction of the laser beams by the changing refractive index of the gas with temperature will have an effect on the spatial resolution (Bohan *et al.* (1989)). Because of the coincidence criterion for measurements on both velocity components simultaneously, it is believed that when the laser beams are diffracted too much, a measuring volume is no longer existent. Therefore, this effect is disregarded.

The small size of the measuring volume is especially important for determining autocorrelation functions and turbulence spectra. For frequencies related to eddies smaller than the measuring volume the results become ambiguous. In general, this implies that determination of the Taylor micro scales of velocity fluctuations is not very reliable. The positioning of the measuring volume is done by traversing the optical bench on which the optics are mounted. The volume is located with an accuracy of 0.5 mm relative to the burner and the uncertainty in the steps along the traverses is 0.1 mm.

3.4 Temperature measurements

3.4.1 Thermocouples

For an extensive description on the operation of thermocouples, references like Fristrom and Westenberg (1965), Bradley and Matthews (1968) and Benedict (1981) should be consulted. Basically, thermocouples make use of the thermo electrical properties of some materials. If two dissimilar conductors are connected electrically at two junctions maintained at different temperatures, a potential is developed which is dependent on the difference in temperature and the difference in properties of the materials used. As the properties of the materials and the temperature of one junction are known, the temperature at the second junction can be determined, with the aid of a calibration.

3.4.2 Experimental setup

Uncoated thermocouples of Platinum-Rhodium (6 %) / Platinum-Rhodium (30 %) wire are used with a diameter of 50 μm. The thermocouple is attached to 0.3 mm diameter posts, supported in ceramic cladding and oriented horizontally to minimize the effect of the thermocouple holder on the flow. The thermocouple is about 100 diameters long to minimize heat conduction. Calibration of this thermocouple is performed in a high-temperature oven. On every position of interest 200 measurements are performed with a frequency, determined by a Thurlby 1905a digital multimeter, of 3 measurements per second.

3.4.3 Data reduction

In general, the thermocouple does not attain the same temperature as the hot gas. The probe radiates energy and in the steady state this is balanced by convective energy transfer from the gas to the probe. In absence of any heat release by chemical reaction, this means that the wire is at lower temperature than the gas. When there is no thermal conduction along the wire, the value of this temperature difference is called the radiation correction.

Radiation correction is performed according to Bradley and Matthews (1968). For wire temperatures above 1250 K, the gas temperature can be written as

$$T_g = T_\infty + \frac{\sigma_t \epsilon_t T_\infty^4}{h_t}. \tag{3.8}$$

The gas temperature T_g, can be obtained by adding a term to the measured thermocouple temperature T_∞. The Stefan-Boltzmann constant is $\sigma_t = 5.67 \times 10^{-8}$ W/m^{2}K^4. As an expression for the wire emissivity, the following equation is used:

$$\epsilon_t = 9.35 \times 10^{-5} \cdot T_\infty + 0.06. \tag{3.9}$$

Actual values of ϵ_t are therefore in the range 0.20 – 0.24. The convective heat transfer coefficient at the wire surface h_t can only be estimated from the Nusselt relation

$$\mathrm{Nu} = \frac{h_t D_t}{\lambda} = 0.42 \cdot \mathrm{Pr}^{0.20} + 0.57 \cdot \mathrm{Pr}^{0.33} \cdot \mathrm{Re}^{0.50}, \tag{3.10}$$

where D_t is the diameter of the thermocouple. λ is the thermal conductivity coefficient and can be estimated from flue gas properties,

$$\lambda = 3.75 \times 10^{-5} \cdot T_\infty + 0.04. \tag{3.11}$$

Once the dimensionless numbers Pr and Re are known, an equation for h_t can be derived. The Prandtl number is given by

$$\mathrm{Pr} = \frac{\nu}{a}, \tag{3.12}$$

where ν is the kinematic viscosity and a is the thermal diffusivity, estimated by

$$\nu = 2.50 \times 10^{-7} \cdot T_\infty - 1.43 \times 10^{-4}, \tag{3.13}$$

$$a = 2.89 \times 10^{-7} \cdot T_\infty - 1.22 \times 10^{-4}. \tag{3.14}$$

The Reynolds number is introduced in Equation 2.2. In the present situation, it is defined as

$$\mathrm{Re} = \frac{\overline{u} D_t}{\nu}. \tag{3.15}$$

The equation for the convective heat transfer coefficient h_t becomes,

$$h_t = \frac{\lambda}{D_t} 0.42 \left(\frac{\nu}{a}\right)^{0.20} + 0.57 \left(\frac{\nu}{a}\right)^{0.33} \left(\frac{\overline{u} D_t}{\nu}\right)^{0.50} \tag{3.16}$$

With this equation, Equation 3.8 can be solved and the effects of radiation are corrected for.

3.4.4 Accuracy

A temperature sensor immersed in a gas stream will record a temperature differing from the true stream temperature due to several causes. These can be separated into the effects which the probe has on the flame and the direct errors involved with the particular technique employed. The first problem, the effect of the probe on the flame itself, can always be reduced by decreasing the size of the probe. The limit to this approach is set by practical problems of fabrication and wire fragility. Perturbations by the probe can be classified as aerodynamic, thermal or chemical. The principal aerodynamic effect of a probe is the velocity deficient wake behind it. The thermal effect of a probe as a heat sink, is a function of the temperature difference between the stream and the sensor. The principal chemical disturbance of probes is the promotion of catalytic reactions on the thermocouple surface. There will always be some catalytic effect, increasing the reaction rates of the flame chemistry. This effect can be made negligible by coating the thermocouple with non-catalytic silica, but this will introduce additional uncertainties and is therefore not used.

Even if a temperature sensor does not disturb a flame, it will register a temperature which is different from the true stream static temperature because of radiation and conduction losses. Because of the small size of the thermocouple, conduction losses are estimated to be relatively small (about 0.1 %) in the temperature measurements in the disk-stabilized premixed burner. For the piloted jet diffusion flame, however, De Vries (1994) has shown that because of the large temperature gradients, conduction losses may be as large as 150 K for temperatures of 1800 K. Radiation loss remains as the other important factor which has to be corrected for. The radiation corrections for the obtained mean temperatures in both flame types range from 15 K for temperatures of 500 K, to 100 K for temperatures of 1750 K. From the scattering of the data, the remaining experimental accuracy is estimated to be $\pm$ 70 K.

Since temperature measurements must be associated with a position, another source of error is movement or vibration of the thermocouple. This problem is avoided by using heavy and short support wires, held as taut as possible. The thermocouple is located with an accuracy of 0.5 mm relative to the burner.

3.5 Semi-quantitative OH radical concentration measurements

3.5.1 Laser induced fluorescence

Radical concentrations in a flame can be measured with laser induced fluorescence. The principles of laser induced fluorescence are well known, see for example Crosley and Smith (1983), Eckbreth (1988) or De Vries (1994). A laser source is tuned to excite a specific electronic absorption transition of a species of interest. The number of excited molecules is proportional to the Boltzmann factor of the initial energy level and to the total number of molecules of this species in the measuring volume. Here the Boltzmann fraction represents the fraction of molecules belonging to this specific initial energy level. The spontaneous emission (fluorescence), following the excitation, is proportional to the concentration of the species.

In addition to spontaneous emission, processes of collisions tend to reestablish the Boltzmann distribution, which is disturbed by the excitation. Rotational relaxation reestablishes the Boltzmann distribution among rotational levels, vibrational relaxation among vibrational levels and quenching among electronic states. The effects of vibrational relaxation can be diminished by the selection of a proper absorption transition. As shown in Figure 3.4, due to rotational relaxation, molecules are transferred from the rotational level, populated by excitation, to levels in its vicinity. Therefore, spontaneous emission from levels other than the one coupled with the laser field will occur, resulting in a large number of extra lines in the fluorescence spectrum.

The rotational relaxation and quenching rates depend on the temperature and the main species concentrations. In a turbulent flame, these rates can only be estimated when the main species concentrations and the temperature are measured simultaneously with the radical concentration. The need for also measuring main species and temperature can be avoided by making the assumption that the relaxation from the level filled by excitation has the same rate as the relaxation to the level depleted by excitation. This assumption is called balanced cross rate and is proposed by Lucht *et al.* (1980). In this case, the initial and final levels form an isolated two-level system, with a constant population, as illustrated in Figure 3.5.

The rate equation governing the population density of the upper energy level $N_2(t)$ is

$$\frac{dN_2(t)}{dt} = N_1(t)\, B_{12}\, I_\nu - N_2(t)\, (Q_{21} + B_{21}\, I_\nu + A_{21})\,, \qquad (3.17)$$

where $N_1(t)$ is the population density of the lower level, Q_{21} is a collisional coefficient, I_ν is the laser spectral intensity, B_{12} and B_{21} are the Einstein coefficients for stimulated

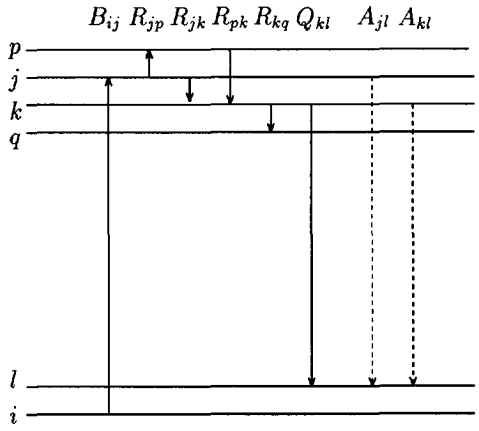

Figure 3.4: Possible transitions between rotational levels in the electronic ground state (i and l) and the first excited electronic state (j, k, p and q). B designates absorption, R rotational relaxation, Q quenching and A spontaneous emission.

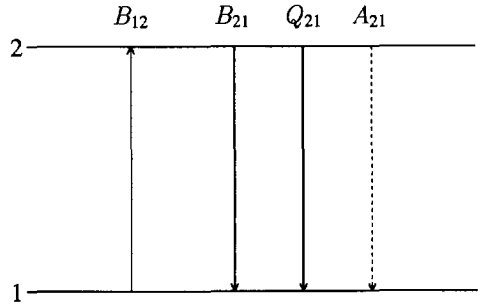

Figure 3.5: Isolated two-level system for modelling of relaxation processes under the assumption of balanced cross rate. B represents absorption and stimulated emission, Q quenching and A spontaneous emission.

absorption and emission and A_{21} is the rate of spontaneous emission, from molecules in the upper energy level.

The steady-state fluorescence rate R_p can be written

$$R_p = N_2 A_{21} = N_1^0 B_{12} I_\nu \frac{A_{21}}{A_{21} + Q_{21}} \frac{1}{1 + I_\nu / I_\nu^{\text{sat}}}. \tag{3.18}$$

The saturation intensity I_ν^{sat} is defined as

$$I_\nu^{sat} = \frac{Q_{21} + A_{21}}{B_{12}(1 + g_1/g_2)}, \tag{3.19}$$

where g_1 and g_2 are degeneracies of the lower and upper level. For a laser intensity smaller than the saturation energy ($I_\nu << I_\nu^{sat}$) this equation can be simplified and it reduces to

$$R_p = N_1^0 B_{12} I_\nu \frac{A_{21}}{A_{21} + Q_{21}}. \tag{3.20}$$

This is the so-called linear fluorescence equation, as the fluorescence is linearly proportional to laser intensity. Furthermore, the fluorescence rate is proportional to the unperturbed lower state population and to a factor $A_{21}/(A_{21} + Q_{21})$, known as the Stern-Vollmer factor or fluorescence yield.

By temporal integration over the laser pulse duration and by inclusion of the collection efficiency of the detection optics, the fluorescence rate is converted to a total fluorescence signal. Assuming the steady-state fluorescence is emitted equally into 4π steradians, the total number of photons S_f striking a detector from the collection volume V_c imaged onto the detector is

$$S_f = \eta \frac{\Omega}{4\pi} f_1(T) \chi_m n V_c B_{12} E_\nu \frac{A_{21}}{A_{21} + Q_{21}}, \tag{3.21}$$

where η is the transmission efficiency of the collection optics and Ω is the collection solid angle. $f_1(T)$ represents the fraction of molecules belonging to the absorber species which are in the specific energy level excited by the laser and is given by the Boltzmann distribution. χ_m is the mole fraction of the absorbing species, n is the total gas number density and E_ν is the laser energy.

From Equation 3.21, the number of absorbed photons is seen to be a relatively simple function of species number density, temperature and incident laser energy. The uncertainty in the fluorescence yield, however, represents the principal difficulty in converting the fluorescence signal to quantitative species concentration. Upper state collisional decay (Q_{21}) processes can change the fluorescence yield. The quenching term Q_{21} can be represented with a kinetic model as

$$Q_{21} = n \sigma \langle v \rangle, \tag{3.22}$$

where n is the total number density of the mixture, $\langle v \rangle$ is an appropriate mean molecular speed, which is proportional to $T^{1/2}$ and σ is a mixture-averaged quenching cross section. When it is assumed that σ is a constant, then Q_{21} is proportional to $n\,T^{1/2}$ and the fluorescence yield is proportional to $(n\,T^{1/2})^{-1}$. In this case, the relationship with the fluorescence signal reduces simply to

$$S_f = C_0 f_1(T) \chi_m n \frac{1}{n\,T^{1/2}}, \tag{3.23}$$

$$= C_0 \chi_m \frac{f_1(T)}{T^{1/2}}, \tag{3.24}$$

where C_0 represents a constant, which contains experimental parameters such as the solid angle, the collection efficiency, etc.

When the selected quantum state is judiciously selected, which means that it should have a reduced temperature-dependence, the temperature does not have to be known exactly. In that case, the measured signal is directly proportional to the species mole fraction. In order to calculate absolute concentrations, a simple calibration with a known mixture from a flat flame burner can be used to provide the missing proportionality constants.

3.5.2 Experimental setup

As appeared in Chapter 2, an important radical in the combustion of natural gas is OH. It is present in regions of the flow where high temperatures occur, especially near the reaction zone. Therefore, concentration measurement of OH provides information on the propagation of combustion reactions and indicates the location of the reaction zone.

The spectroscopic structure of OH is well-known after investigations of for example Dieke and Crosswhite (1962). To excite the OH radicals in the flame, a Quantel International frequency-doubled dye laser, pumped by a frequency-doubled Nd:YAG laser, is used. This laser is tuned to an excitation wavelength, corresponding with a strong absorption band of the OH radical, the $Q_1(8)$ line ($A^2\Sigma$ - $X^2\Pi$, (0,0)), at 309.32 nm. This absorption line shows a very weak dependence on temperature and vibrational relaxation. The laser spectral bandwidth is large compared with that of the absorption line. Therefore, excitation of the entire population of the OH radicals in the electronic ground state may be supposed. Because of the horizontal polarization of the laser light, no Rayleigh scattering is detected. Laser energy is 17 mJ per pulse, the pulse duration is 5 ns and the repetition rate is 10 Hz. During the very short laser pulse, the turbulence is assumed to be frozen and successive measurements are uncorrelated, due to the low repetition rate of the laser.

In order to observe OH serving as an indicator of the flame front and the subsequent effect of fluid motion on the state of the burnt gases, planar LIF imaging is performed (Hanson (1986); Seitzman and Hanson (1992)). For these measurements, the laser shots are focussed at the centreline of the burner with a focussing lens with $f = 1500$ mm. A laser sheet is formed by means of a cylindrical lens with a focal length $f = -12.7$ mm, placed at 0.7 m from the centreline of the burner to ensure a uniform light distribution in the laser sheet. The thickness of the laser sheet in the focus is approximately 0.2-0.5 mm. The OH fluorescence is detected perpendicular to the laser sheet, with an intensified Proxitronic CCD camera, gated at 100 μs. This relatively long gating time causes the images to contain a little bit of direct flame emission. The camera consists of a surface of (768 $\times$ 500) pixels. The frequency of the video-signal from this camera is 25 images per second. A trigger pulse of 8.33 Hz is generated from this frequency to trigger the camera and the laser. The OH fluorescence is focussed on the camera with a UV Nikkor f/4.5 105 mm camera lens and 1,000 instantaneous images are stored on a video. Image processing is possible through the use of a frame grabber and further processing occurs on a HP-735 computer. The experimental setup

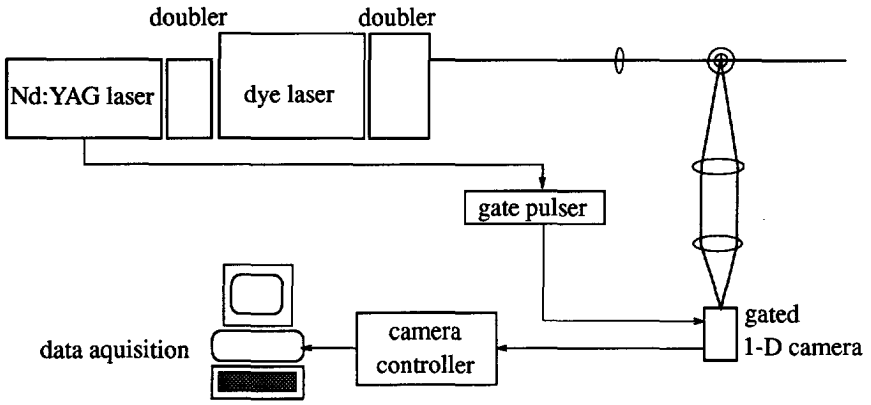

Figure 3.6: Schematic representation of the experimental setup for laser induced fluorescence measurements with broadband detection.

is shown in Figure 3.6. Further details of the setup as well as the spectroscopy of the OH radical are given by De Vries (1994).

Semi-quantitative measurement of OH concentrations and calculation of correlations and gradients of these concentration fluctuations along the laser beam, is performed by one-dimensional detection of the fluorescence profile in a single laser shot. This can be achieved using a diode array camera, as reported by Aldén *et al.* (1982). The laser beam is focussed with a f = 500 mm fused silica lens. The OH fluorescence is detected perpendicular to the laser beam, by projecting the fluorescence with the previously mentioned camera lens on a Princeton Instruments intensified photo diode array, gated at 40 ns and triggered by the laser system. A Schott UG11 coloured glass filter is used to block scattered red fundamental dye laser light. The bandwidth of the UG11 filter is 240 nm to 390 nm. The diode array consisted of 1025 enhanced photo diodes. With this diode array camera instantaneous one-dimensional (radial) concentration profiles can be recorded. Broadband detection, detection of many emission lines of the fluorescence spectrum at once, is used. The measuring volume, is 0.12 mm in radial direction, and about 1.5 mm in the tangential and axial direction, defined by the diameter of the laser beam at the beam waist.

The measurements are temporally stored on a personal computer, connected to the diode array interface and, after transportation, processed on a HP-735 computer. For each measurement 5,000 laser shots are generated and the corresponding broadband fluorescence is collected. The OH concentrations measured in the turbulent flames are put on a quantitative basis by comparing the measurements with a measurement in a laminar, premixed CH_4/air flat flame, from a McKenna porous plug burner (Lucht *et al.* (1984)). This reference flame is placed in the setup at the location of the turbulent flames, preserving optics alignment. As a calibration point, the fluorescence signal is measured

in this flame at 25 mm from the burner surface. At this height, the OH concentration is near equilibrium and gradients are small. The OH concentration, temperature and main species concentration profiles of this flame are calculated with the computer code PREMIX, developed by Kee *et al.* (1985) and performed by Peeters (1995). The calculated concentration for equivalence ratio $\varphi = 0.88$ is 2.13×10^{15} cm^{-3}, a value that is used as reference concentration.

3.5.3 Data reduction

Data processing of the fluorescence signals with one-dimensional detection occurs for each diode, by calculating a representative probability density function and its moments by ensemble averaging the 5,000 stored OH fluorescence signals. Length scales of OH concentration fluctuations are derived by calculating the autocorrelation function, comparable with Equation 2.4 for velocity fluctuations. Now, however, a spatial coordinate δ is used, as described by De Vries *et al.* (1993)

$$\rho_{OH}(x,y,\delta) = \frac{\langle c'_{OH}(x,y-\delta/2,t) \times c'_{OH}(x,y+\delta/2,t)\rangle}{\sqrt{\langle c'^2_{OH}(x,y-\delta/2,t)\rangle \times \langle c'^2_{OH}(x,y+\delta/2,t)\rangle}}, \tag{3.25}$$

where c'_{OH} represents a fluctuating OH concentration, which is obtained for an axial position x and a radial position y at a certain time t. The brackets denote ensemble averaging.

The integral of this autocorrelation function, as with the velocity correlations in Equation 2.6, provides an integral scalar length scale

$$\mathcal{L}_{OH} = \int_0^\infty \rho_{OH}(x,y,\delta)d\delta. \tag{3.26}$$

Analogous to the Taylor micro time scale of turbulence, the Taylor micro length scale of concentration fluctuations λ_{OH} is defined as

$$\left.\frac{d^2\rho_{OH}}{d\delta^2}\right|_{\delta=0} = \frac{-2}{\lambda^2_{OH}}. \tag{3.27}$$

In the case of homogeneous turbulence, the Taylor length scale λ_{OH}, is related to the shape of $\rho_{OH}(x,y,\delta)$, for small δ, by

$$\rho_{OH}(x,y,\delta) \approx 1 - \left(\frac{\delta}{\lambda_{OH}}\right)^2. \tag{3.28}$$

The instantaneous OH profiles as obtained in the disk-stabilized premixed flames are scattered by LDA seeding particles, still present in small amounts in the burner. To remove these spurious data, a sigma-criterion comparable with the processing of the LDA data is used for every value of the instantaneous OH fluorescence signal on each specific diode of the array. The fluorescence signals in the piloted jet diffusion flames

do not suffer from this seeding particle pollution, because measurements are performed in a separate, exact duplicate, configuration.

The original average OH profiles are asymmetrical due to absorption of the laser beam during its path through the flame. This effect is also encountered by Stepowski *et al.* (1989) and Seitzman *et al.* (1990). In case of the piloted jet diffusion flame, the absorption effect is minor because of the narrow zones in which OH is present. In the disk-stabilized premixed flame, however, large amounts of OH are present in relatively large volumes, causing the OH profiles to be significantly asymmetrical. Therefore, a correction for this absorption behaviour is made in this flame. The correction method is based on an iterative computer algorithm, described by Hertz and Aldén (1987), which reconstructs the spatially resolved absorption profile of the laser beam from measurements of the spatially resolved laser induced fluorescence.

The purpose of the iterative reconstruction algorithm is to obtain a 1-D spatially resolved laser-intensity profile, *i.e.*, the laser intensity as a function of position along the beam which passes through the flame. The algorithm is started by calculating the first approximation of the laser-intensity profile from the measured LIF-profile. The 1-D spatially-resolved fluorescence intensity $f(x)$ is described by

$$f(x) \;=\; C_0\,\sigma\,N(x)\,I_0\,I_{\rm rel}(x)\,S, \tag{3.29}$$

where x denotes the spatial position ($0 \leq x \leq$ L), C_0 is a constant which includes experimental parameters, S is the Stern-Vollmer factor, which accounts for the influence of quenching on the fluorescence signal, σ is the absorption cross section and $N(x)$ is the number density of the OH molecules along the laser beam. I_0 is the initial laser intensity and $I_{\rm rel}(x)$ is the relative laser intensity as a function of position ($0 \leq I_{\rm rel}(x) \leq 1$). For simplicity, the factor $C_0 S I_0$ is denoted C in the following.

The LIF-profile is then corrected for the laser absorption by division by the calculated approximation of the laser-intensity profile. It is clear that the absorption of the laser beam influences the laser intensity $I(x)$. For computational reasons, the laser-intensity independent LIF-signal is introduced

$$w(x) \;=\; \frac{f(x)}{I_{\rm rel}(x)} \;=\; C\,\sigma\,N(x). \tag{3.30}$$

The Lambert-Beer law states that the laser beam is attenuated according to

$$I_{\rm rel}(x) \;=\; \exp\left(-\int_0^x \sigma N(x')\,dx'\right). \tag{3.31}$$

The computational procedure is initialized by assuming that $I_{\rm rel}(x)$ equals unity. With this assumption the first approximation of the laser-intensity independent LIF-profile $w_1(x)$ is equal to the recorded spatially resolved LIF-profile $f(x)$ (lower index denotes iteration number). $w_1(x)$ is, thus, approximately equal to $C\sigma N(x)$. The iterative loop is then started by integrating $w_1(x)$ yielding,

$$w_{1,\rm int}(x) \;=\; \int_0^x w_1(x')dx' \approx \int_0^x C\sigma N(x')\,dx'. \tag{3.32}$$

To obtain a first approximation of the relative laser intensity $I_{1,\mathrm{rel}}(x)$ the following equation is used

$$I_{1,\mathrm{rel}}(x) = \exp\left(-\frac{w_{1,\mathrm{int}}(x)}{C_1}\right), \tag{3.33}$$

where C_1, *i.e.*, the first approximation of the experimental constant C, is obtained from the boundary condition $I_{\mathrm{rel}}(L) = T$. With this approximate laser intensity the LIF-profile $f(x)$ is corrected for laser attenuation by division with $I_{\mathrm{rel}}(x)$, yielding the second approximation of the laser-intensity independent LIF-profile $w_2(x)$. This is the end of the first iterative cycle and $w_2(x)$ is then used in the next cycle to obtain better approximations of $I_{i,\mathrm{rel}}(x)$ and $w_i(x)$. The loop is continued until a stable solution is reached. By adjusting the value of the transmission T in this procedure, symmetrical average profiles are obtained.

This estimate of the transmission is then used to correct for absorption along the laser beam for every instantaneously obtained image according to the same procedure. Reperforming the statistical analysis of these corrected images provides profiles of average OH concentration, OH standard deviation and higher moments of the OH concentration distribution by means of probability density functions. Also integral and Taylor length scales of OH concentration fluctuations have been calculated with these corrected instantaneous profiles.

3.5.4 Accuracy

Broadband detection of the fluorescence signal, as described in the previous section, implies that emission of radicals decaying from the excited rotational level and decaying after rotational relaxation is included. The signal is proportional to the radical concentration. However, it is also a function of the quenching and rotational relaxation. These processes are strongly dependent on temperature and composition of the surrounding gas. Despite the fluctuations in temperature and composition in turbulent flames, a constant relation between concentration and signal, as in Equation 3.24, is assumed. Using rotational relaxation and quenching cross sections found in literature, De Vries (1994) found that the broadband fluorescence signal is only a weak function of temperature and composition. It was shown that in the regions with significant amounts of OH, the fluorescence signal per unit concentration does not vary more than 20 %, due to changes in temperature or in composition. Therefore, the random error in the fluorescence signal per unit concentration is estimated to be smaller than 20 %.

The difference between the average fluorescence signal from the turbulent flames and the signal from the laminar calibration flame will result in a systematic calibration error. This error is caused by the differing temperatures and average composition in the turbulent flames and the calibration flame. De Vries (1994) has shown that the combined effect of temperature and composition on the fluorescence signal leads to an overestimation of the concentrations in the turbulent diffusion flame of the order of 35 %, when calibrated with the laminar flat flame. In the disk-stabilized premixed flame, this overestimation is smaller (approximately 30 %), because the quenching

environments of this flame and the laminar flat flame differ less. Because of this rather large systematic bias, the measurements are considered semi-quantitative.

Point measurements, as performed by Stårner *et al.* (1990, 1991), Masri *et al.* (1988b) and Barlow *et al.* (1990b) are much more accurate. The spatial characteristics of the reaction zone, however, could not be explored by their measurements. Determination of length scales of OH concentration fluctuations does not require absolute concentrations. Therefore, the loss of accuracy of 1- and 2-D measurements with broadband detection is accepted because of the additional information that is gathered on the spatial structure.

Chapter 4

Structure of disk-stabilized premixed flame

4.1 Outline of this chapter

In this chapter, detailed measurements are presented that reveal the features of an inert and a reacting flow in the disk-stabilized burner. The effects of turbulence in a premixed flame, stabilized by a recirculation zone will be discussed. Therefore, properties of the nonreacting and reacting flow fields are given in Sections 4.2 and 4.3, respectively. For the isothermal flow, the velocity distributions are measured with Laser Doppler Anemometry (LDA). Additional to a global description of the disk-stabilized premixed flame under investigation (Section 4.3.1), velocity distributions (Section 4.3.2), featuring mean velocities, fluctuations, PDFs and time scales, as well as mean temperatures (Section 4.3.3), are measured in the reacting flow. The OH radical distribution in the flame is visualized in Section 4.3.4, by means of planar Laser Induced Fluorescence (LIF), elucidating the flame stabilization process. Quantitative OH concentrations, examined by one-dimensional detection of the fluorescence signal in Section 4.3.5, provide further information on the overall structure of the flame. Time and length scales of velocity fluctuations and length scales of OH concentration fluctuations are estimated in Section 4.4.1. These data are useful to characterize the regime of combustion and to provide an interpretation of the interaction between turbulence and chemistry. The mutual interaction between combustion and turbulence is discussed in a comparison between the reacting and the nonreacting flow field in Section 4.4.2 and the approach to extinction in Section 4.4.3. The chapter closes with a summary of the main findings.

4.2 Results in nonreacting flow field

4.2.1 Velocity characteristics

To reveal the influence of the flame on turbulence, the properties of a nonreacting flow field in the disk-stabilized burner, are determined. An air flow exits from the annulus between the burner nozzle (outer diameter D = 85 mm) and the stabilizing disk (diameter d = 80 mm), as depicted in Figure 3.1. The air flow rate is selected to have an exit velocity of 13.2 m/s, equal to the exit velocity in the flame.

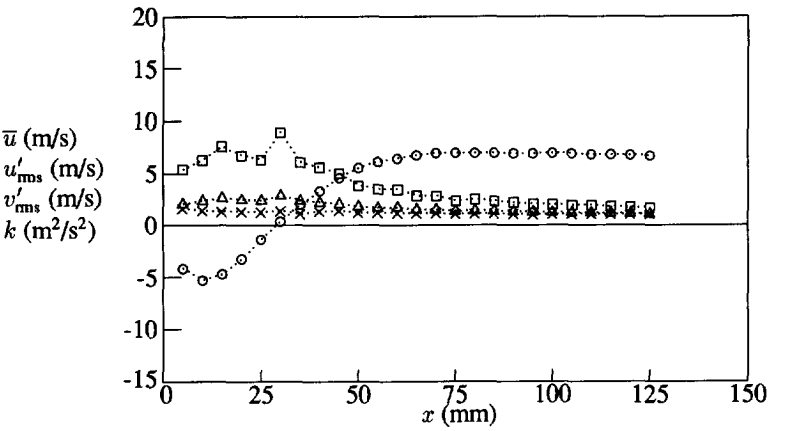

Figure 4.1: Centreline axial profiles in the nonreacting flow of the disk-stabilized burner of the axial mean velocity $\overline{u}$ ($\cdots$ o $\cdots$), axial rms velocity $u'_{\rm rms}$ ($\cdots$ $\times$ $\cdots$), radial rms velocity $v'_{\rm rms}$ ($\cdots$ $\triangle$ $\cdots$) and turbulence kinetic energy k ($\cdots$ $\square$ $\cdots$).

In Figure 4.1, the axial mean velocity, axial rms velocity, radial rms velocity and turbulence kinetic energy profiles are shown in the nonreacting flow, for an axial traverse along the centreline of the disk-stabilized burner. The presence of a characteristic recirculation region, where the axial mean velocity is negative, is revealed. The tip of the recirculation zone, represented by a stagnation zone with an axial and radial mean velocity $\overline{u} = \overline{v} = 0$ m/s, can be found near $x = 30$ mm. Further downstream from the stagnation zone, the flow accelerates upwards and eventually its velocity will decay. In a region around the stagnation zone, the radial velocity fluctuations are much larger than the axial fluctuations, indicating a large anisotropy of the turbulence. The maximum of the fluctuations occurs near the position where the axial mean velocity profile has its inflection point. Only in the immediate vicinity of the disk and far downstream, $u'_{\rm rms}$ and $v'_{\rm rms}$ are similar in magnitude and the turbulence returns to isotropy. At the centreline, the axial turbulence intensity $u'_{\rm rms}/\overline{u}$ has a minimum value of approximately 0.25 within the recirculation zone at the location of largest negative axial mean velocity. At the stagnation point, with zero axial mean velocity, the turbulence intensity attains infinite values. Further downstream, outside of the recirculation zone at $x = 125$ mm, the axial turbulence intensity is constant with a value of approximately 0.15. The turbulence kinetic energy is a measure of the maximum turbulent mixing intensity in the flow. Because the tangential velocity component could not be measured with the present LDA setup, an approximation for the turbulence kinetic energy is made. In our axisymmetric configuration, the tangential velocity fluctuations $w'_{\rm rms}$ are assumed to be equal to the radial velocity fluctuations $v'_{\rm rms}$.

The main characteristics of the flow are further revealed when radial traverses

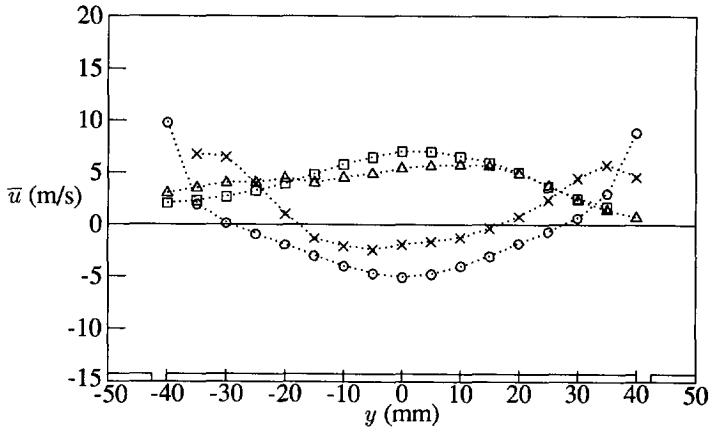

Figure 4.2: Axial mean velocity profiles in the nonreacting flow of the disk-stabilized burner for radial traverses at x = 10 (· · · o · · ·), 25 (· · · × · · ·), 50 (· · · △ · · ·) and 75 mm (· · · □ · · ·).

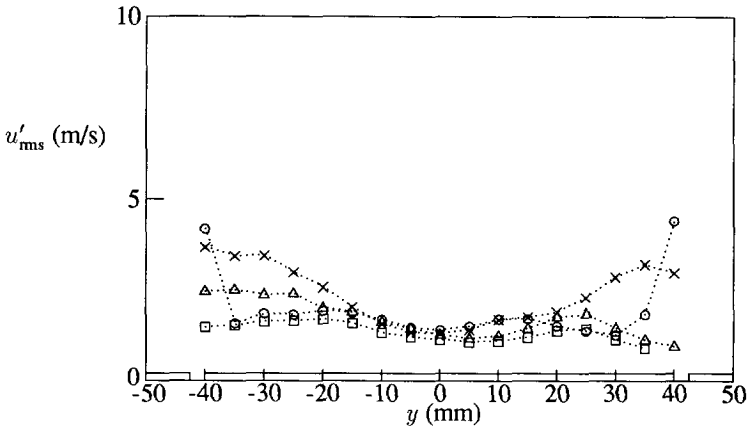

Figure 4.3: Axial rms velocity profiles in the nonreacting flow of the disk-stabilized burner for radial traverses at x = 10 (· · · o · · ·), 25 (· · · × · · ·), 50 (· · · △ · · ·) and 75 mm (· · · □ · · ·).

of the axial mean velocity are studied, as shown in Figure 4.2. As in the sequel, the contours of the burner nozzle and the stabilizing disk are depicted at the bottom of the figure. The radial traverses at x = 10 mm and x = 25 mm elucidate the presence and magnitude of the recirculation zone. In the outer regions of these traverses, high axial mean velocities are found, indicating that the recirculation zone is surrounded by a high velocity layer, originating from the annular exit flow. At x = 25 mm, the radial position where the axial mean velocity has a maximum has moved towards the centreline, when compared with the radial position of maximum axial mean velocity for x = 10 mm, corresponding with the curvature of the flow. Further downstream, the flow is less influenced by the recirculation zone and resembles an undisturbed jet flow.

Axial velocity fluctuation profiles u'_{rms} as a function of the radial position y are presented in Figure 4.3. At the centreline, the axial velocity fluctuations are very similar for all axial positions, which was also seen in Figure 4.1. Moving to positions of large radii, an increase in the u'_{rms} profiles is visible for the traverses at lower axial positions x = 10 mm and x = 25 mm. The high speed annular air flow issues into stagnant air. This velocity difference sets up a shear layer, which grows with downstream position. The turbulence generated by this shear layer is directly reflected in the values of the axial velocity fluctuations.

4.3 Results in reacting flow field

4.3.1 Global flame properties

Although a description of global flame properties of disk-stabilized premixed flames is difficult, some features are revealed by visual inspection of the flame. An instantaneous video image of the flame, given in Figure 4.4, provides a characterization of the flame. Blue flame luminosity is restricted to a rather small area, directly downstream of the stabilizing disk. On the outer edges of the recirculation region, the main reaction zones are revealed. The flame is near the lean blow-out limit and experiences local extinctions very often, which results in visible and audible instabilities.

4.3.2 Velocity characteristics

The mechanism of stabilization of disk-stabilized premixed flames is not well understood. Although the reactants are mixed prior to combustion, modelling of premixed flames is difficult, because it requires knowledge of mixing between fresh reactants and hot combustion products. Once reactants and products are mixed sufficiently, the flame is stabilized. As a consequence of turbulence-chemistry interactions described earlier, however, the flame may be destabilized. To study these interactions, measurements of the chemical flame structure should be supplemented by data on the mean velocity field and turbulence properties in our specific configuration.

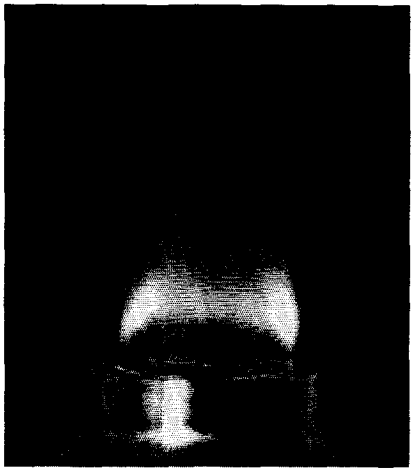

Figure 4.4: Instantaneous video image of disk-stabilized premixed flame with equivalence ratio φ = 0.75, covering x = -35 to 165 mm and y = -90 to 90 mm.

Mean velocities and turbulence properties

In Figure 4.5, general velocity characteristics of the bluff-body stabilized premixed flame are presented by means of an axial traverse along the centreline of the burner. The flame is operated with a fuel-lean mixture with equivalence ratio φ = 0.75. With a disk diameter of 80 mm and an inner nozzle diameter of 85 mm, the exit velocity becomes U_0 = 13.2 m/s. As for its nonreacting equivalent in Section 4.2.1, the presence of the characteristic recirculation region, where the axial mean velocity is negative, is clearly revealed. The axial turbulence intensity $u'_{\mathrm{rms}}/\overline{u}$ attains a minimum value of approximately 0.20 at the centreline, for the largest negative axial mean velocity. Further downstream, outside of the recirculation zone, at x = 100 mm, the axial turbulence intensity has decreased to approximately 0.10. A stagnation zone at the centreline, where the axial mean velocity and the radial mean velocity are zero, can be found near x = 50 mm. This stagnation zone is associated with a pressure maximum as a result of the converging of the streamlines towards the centreline. Further downstream from the stagnation zone, the flow accelerates. Eventually, the centreline axial velocity will decay comparable with a jet flow.

As can be seen from a comparison between the fluctuating velocity components u'_{rms} and v'_{rms}, the turbulent velocity field is substantially anisotropic, except for positions in the immediate vicinity of the disk and far downstream. As for the isothermal flow, in a region around the stagnation zone, the radial velocity fluctuations are much larger than the axial fluctuations. Therefore, there must be a considerable influence of the radial velocity fluctuations on the mixing process of cold reactants and hot products.

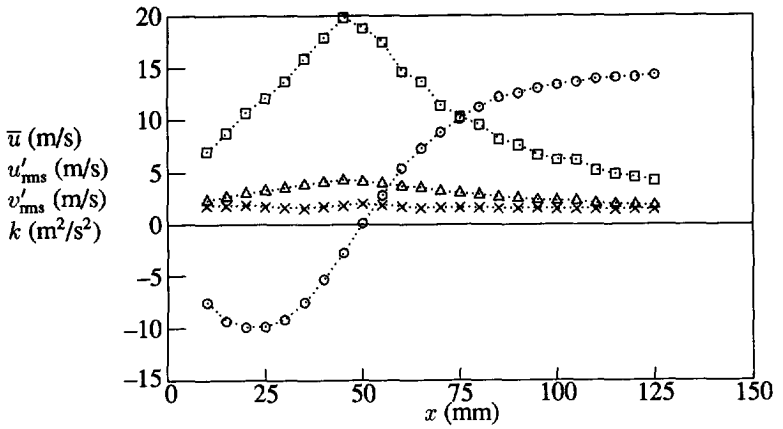

Figure 4.5: Centreline axial profiles in the disk-stabilized premixed flame of the axial mean velocity $\overline{u}$ ($\cdots$ o $\cdots$), axial rms velocity $u'_{\rm rms}$ ($\cdots \times \cdots$), radial rms velocity $v'_{\rm rms}$ ($\cdots \triangle \cdots$) and turbulence kinetic energy k ($\cdots \square \cdots$).

The maximum of the fluctuations occurs near where the axial mean velocity profile has its inflection point, which was also found in confined geometries by Durão and Whitelaw (1978) and Heitor *et al.* (1987).

Radial profiles of axial mean velocities at different axial positions are shown in Figure 4.6. Again, the contours of the burner exit with outer diameter 85 mm and the stabilizing disk of 80 mm diameter are indicated in the lower part of the figures. The traverse at x = 25 mm corresponds with a traverse within the recirculation zone. In the outer regions of this traverse, high axial mean velocities are found, associated with the exit flow from the burner annulus. The traverse at x = 50 mm shows that near the centreline, the flow is severely influenced by the presence of the stagnation zone. Comparing the profiles at x = 25, 50 and 75 mm, the radial position where the axial mean velocity attains its maximum value is shifted towards the centreline. Apparently, the width of the recirculation zone decreases, corresponding with the curvature of the main reaction zone. This so-called necking-down, in which also entrainment of ambient air occurs, will appear to be very important for the stability of the flame, as will be seen in Section 4.3.4. At x = 100 mm, relatively far downstream, the character of the flow resembles that of an undisturbed jet flame.

In Figure 4.7, radial profiles of the radial mean velocity at different axial positions are given. Radial mean velocities $\overline{v}$ are defined positive when moving towards positive values of y and negative when moving towards negative y-values. Within the recirculation zone, at x = 25 mm, for $y = \pm$ 35 mm, the radial velocities reach high mean values. Immediately adjacent to this strong inward movement, zero radial mean velocities are found near $y = \pm$ 25 mm. The axial mean velocity is zero for these

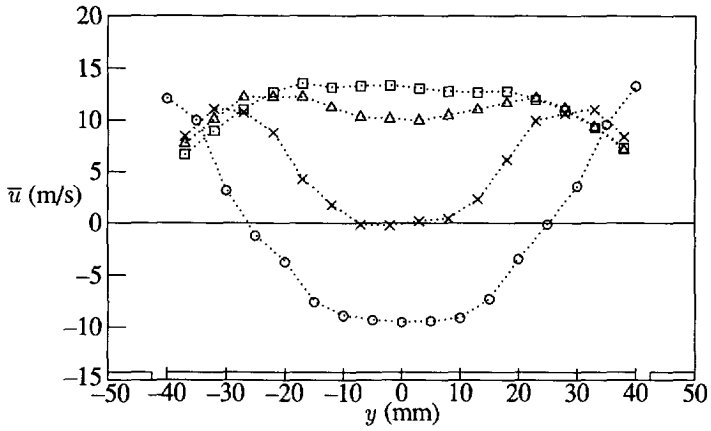

Figure 4.6: Axial mean velocity profiles in the disk-stabilized premixed flame for radial traverses at $x = 25$ (···○···), 50 (···×···), 75 (···△···) and 100 mm (···□···).

positions as well, and thus the core of the toroidal vortex within the recirculation zone is demonstrated. High values of the radial mean velocity are also found for the traverse near the stagnation zone at $x = 50$ mm, indicating the movement of the main flow toward the centreline. Movement in the radial direction is less significant, when moving further downstream. These measurements reveal that the general characteristics of the flow field are in agreement with the general flow structure behind a stabilizing disk, as indicated in Figure 2.2.

By studying radial profiles of the rms velocities u'_{rms} and v'_{rms}, as in Figures 4.8 and 4.9, respectively, the relation between turbulence and the flow field appears. For the traverses at $x = 25$ mm and $x = 50$ mm, increases of the axial velocity fluctuations in the outer regions of the flow are found, compared to values at the centreline. This high degree of turbulence is associated with the velocity difference between the high-speed combustible mixture, issuing from the burner nozzle, and the stagnant ambient air. As for the isothermal flow, a shear layer is generated, which induces turbulence and leads to significant entrainment of ambient air. Entrainment of air also explains the slight increases of u'_{rms} for larger radii at $x = 75$ mm and $x = 100$ mm, compared to centreline values.

In the results of the radial rms velocity profiles, in Figure 4.9, maxima occur for the same positions where u'_{rms} profiles peak. Especially, the large maximum near the centreline stagnation point for $x = 50$ mm is striking. Once again, the importance of radial velocity fluctuations in this region is demonstrated. Contrary to the axial velocity fluctuations, the radial velocity fluctuations attain large values at the centreline as well. The radial velocity fluctuations are also initiated by the shear layer, but they equilibrate more slowly than axial velocity fluctuations. For radial traverses downstream of the

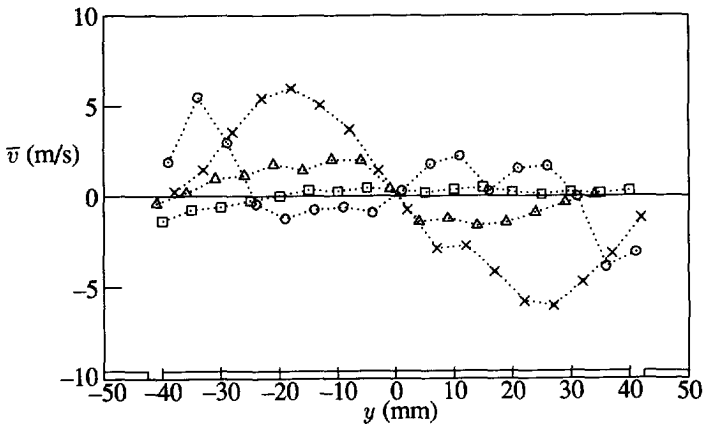

Figure 4.7: Radial mean velocity profiles in the disk-stabilized premixed flame for radial traverses at $x = 25$ ($\cdots\circ\cdots$), 50 ($\cdots\times\cdots$), 75 ($\cdots\triangle\cdots$) and 100 mm ($\cdots\square\cdots$).

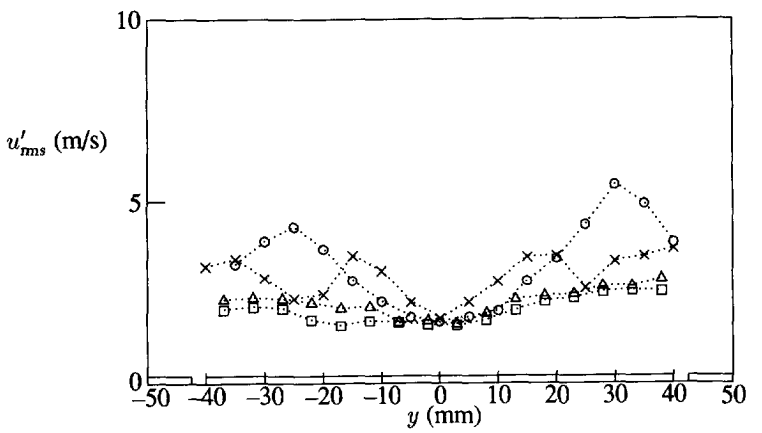

Figure 4.8: Axial rms velocity profiles in the disk-stabilized premixed flame for radial traverses at $x = 25$ ($\cdots\circ\cdots$), 50 ($\cdots\times\cdots$), 75 ($\cdots\triangle\cdots$) and 100 mm ($\cdots\square\cdots$).

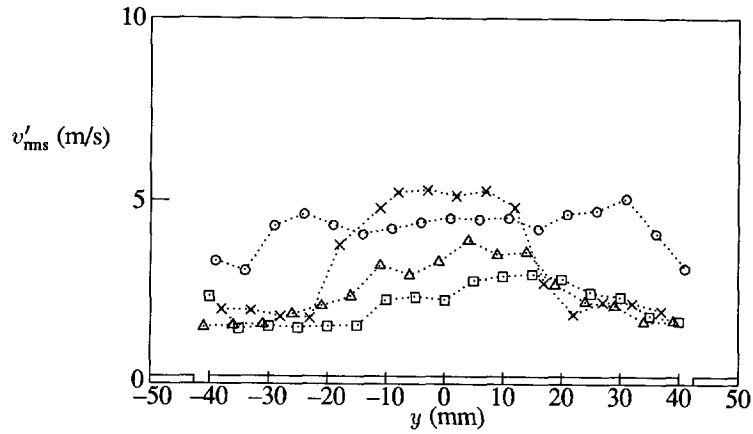

Figure 4.9: Radial rms velocity profiles in the disk-stabilized premixed flame for radial traverses at x = 25 ($\cdots$ o $\cdots$), 50 ($\cdots \times \cdots$), 75 ($\cdots \triangle \cdots$) and 100 mm ($\cdots \square \cdots$).

recirculation zone, the general tendency of both axial and radial rms velocities is to decrease, although their magnitudes differ.

The degree of anisotropy for each of the investigated positions is indicated in Figure 4.10, where the ratio of the axial velocity fluctuations and the radial velocity fluctuations is given as a function of the radial position. For isotropic turbulence this ratio is unity. In general, the axial velocity fluctuations are larger than the radial velocity fluctuations for large radii ($u'_{rms}/v'_{rms} > 1$). Near the centreline, however, the contrary is true: radial rms velocities may be twice as large as the axial rms velocities ($u'_{rms}/v'_{rms} \approx 0.5$). The general anisotropy of the flow suggests the need to consider each of the normal stresses individually in modelling applications.

Reynolds shear stresses can be of importance to the mixing of cold reactants and hot combustion products. The Reynolds shear stress profiles $\overline{u'v'}$, as in Figure 4.11, show evidence of intense mixing at the edges of the recirculation zone, x = 25 mm and $y = \pm$ 30 mm and near the stagnation zone, x = 50 mm and $y = \pm$ 15 mm. Regions of zero shear stress do not, in general, correspond with those of zero axial velocity gradient. This confirms the inability of effective-viscosity turbulence mixing models to represent the flow characteristics. In these models, the hypothesis $\overline{u'v'} = -\nu_t \frac{\partial \overline{u}}{\partial y}$ is used, where ν_t is a scalar turbulence viscosity. Instead, emphasis on the use of Reynolds stress closures should be put.

Effect of velocity bias correction

The velocity statistics of the arithmetically averaged LDA measurements may be biased toward higher velocities, as discussed in Section 3.3.4. To eliminate this velocity bias, a number of post-processing techniques has been used. In order to see the influence

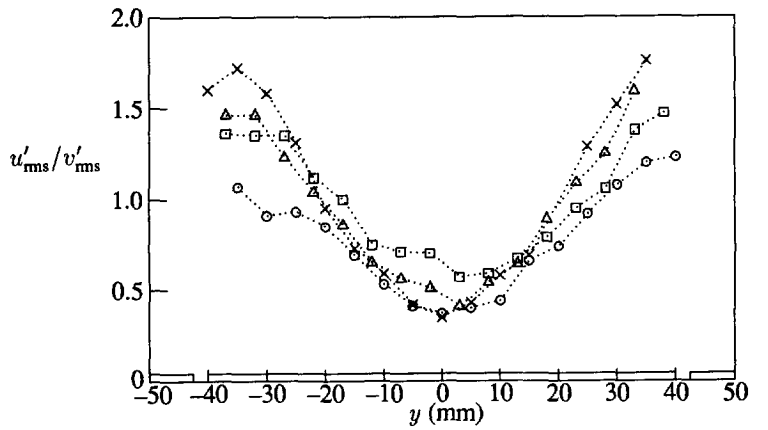

Figure 4.10: Radial profiles of the ratio of axial and radial rms velocities in the disk-stabilized premixed flame at x = 25 (· · · o · · ·), 50 (· · · × · · ·), 75 (· · · △ · · ·) and 100 mm (· · · □ · · ·).

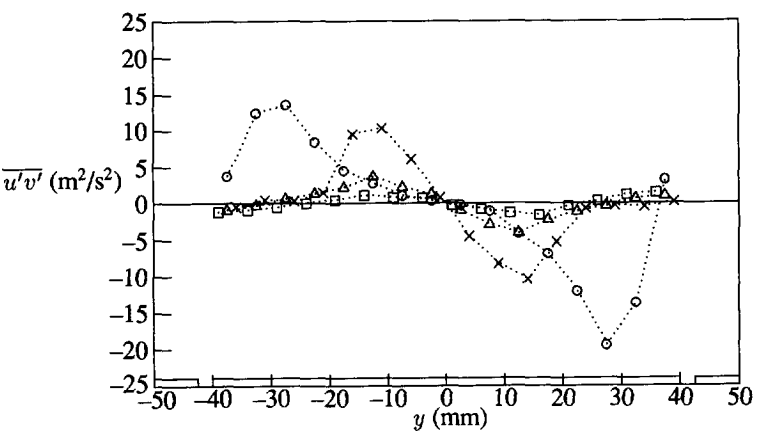

Figure 4.11: Reynolds shear stress profiles in the disk-stabilized premixed flame for radial traverses at x = 25 (· · · o · · ·), 50 (· · · × · · ·), 75 (· · · △ · · ·) and 100 mm (· · · □ · · ·).

of the McLaughlin-Tiedermann weighing technique, weighing with the time-between-data and the residence time, these correction methods have been applied on the data of a radial traverse at x = 50 mm in the disk-stabilized premixed flame. For this particular traverse, the effect of bias correction methods can be studied for all velocity distributions that may occur in the flow; featuring regions of large negative, large positive and near-zero mean velocity and with both high and low turbulence levels. In Figure 4.12, the results of these corrections are depicted for the axial mean and axial rms velocity, as well as the Reynolds shear stress.

In general, all profiles reveal that the effect of correcting for velocity bias is only minor. It is concluded that the presented data can be used without taking into account the effect of velocity biasing. Even within the recirculation zone, with its high turbulence intensities, the arithmetical determination of the moments of the velocity distribution does not differ significantly from the bias corrected values. Apparently, the relatively small validated data rates for each measurement ensure statistical analysis of independent velocity samples and velocity bias does not have to be corrected for.

Probability density functions

An important link between time-dependent velocity changes and the mean velocities is provided by probability density functions (PDFs). Many features of the flame turbulence are shown in joint probability density functions (JPDFs) of the axial versus the radial velocity. In Figures 4.13 and 4.14, JPDFs are presented for various radial positions at axial positions x = 25 mm and x = 50 mm, respectively. Contour lines, in which lines of equal probability $P(u, v)$ are connected, are drawn for joint probabilities of 0.005; 0.015; 0.03 and 0.045. The associated single PDFs of axial and radial velocity are also given.

The anisotropy of the flow near the recirculation zone is shown by the noncircular character of the JPDFs for x = 25 mm and x = 50 mm. In large regions of the flow, the single PDFs show a Gaussian distribution. In general, where deviations from Gaussian behaviour exist, they are greatest in the case of the radial velocity component. For x = 25 mm, moving from the outer regions towards the centreline, the PDFs of the radial velocity become highly skewed. This skewness towards outward moving particles reveals the influence of the turbulent mixing caused by the recirculation behind the disk.

At the centreline, for the traverse at x = 25 mm in Figure 4.13, a broad PDF of the radial velocity is found with some tendency of a bimodal character with maxima on either side of zero velocity. This shape of the PDF suggests that the data have been collected at a position where the flow has had two different mean velocities (and different signs) occurring at different times for that position. One explanation for this observation is that the flow is shifting or bouncing around in this region of the flow on a time scale larger than the turbulence time scale. Also near the stagnation point at x = 50 mm, the radial velocity PDF takes on a broad shape at the centreline and the axial velocity PDF reveals a bimodal appearance outside the centre region, y = 15 mm. Measurements of Durão and Whitelaw (1978) in a similar but confined geometry have

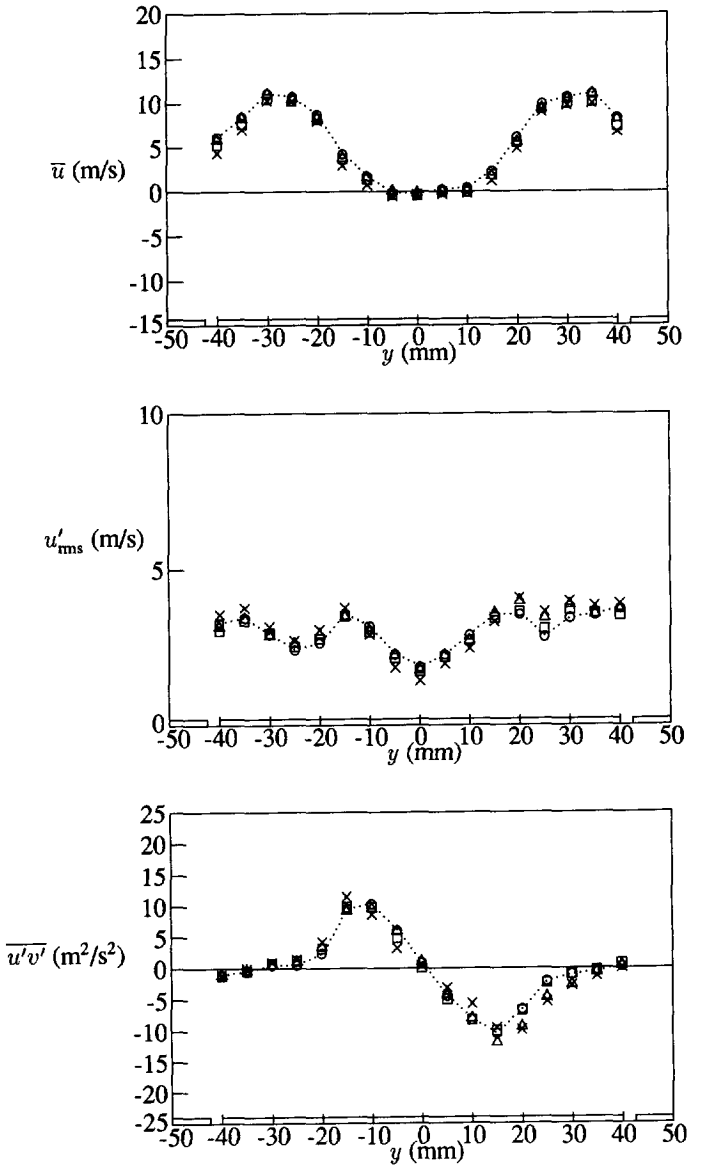

Figure 4.12: Axial mean velocity $\overline{u}$, axial rms velocity u'_{rms} and Reynolds shear stress $\overline{u'v'}$ profiles in the disk-stabilized premixed flame for a radial traverse at $x = 50$ mm with arithmetical averaging ($\cdots$ o $\cdots$), McLaughlin-Tiedermann weighing ($\times$), correction with TBD ($\triangle$) and with residence time ($\square$).

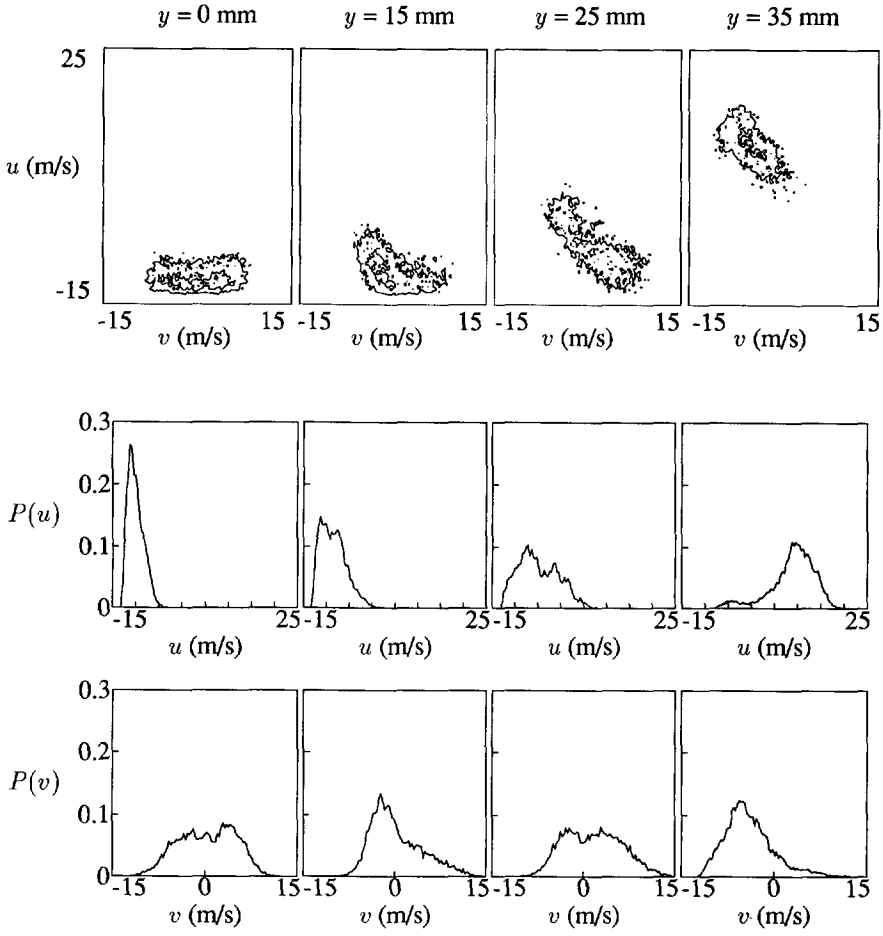

Figure 4.13: Joint probability density functions (top) and single probability density functions of axial (middle) and radial (bottom) velocities in the disk-stabilized premixed flame at $x = 25$ mm and $y = 0$, 15, 25 and 35 mm.

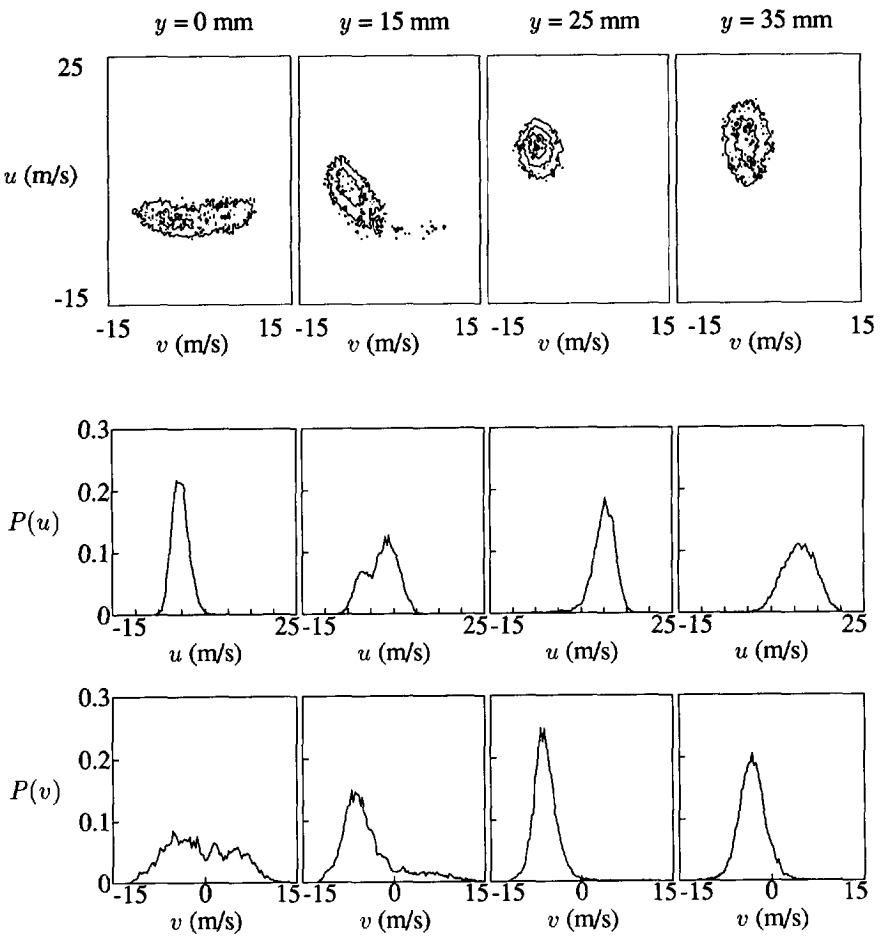

Figure 4.14: Joint probability density functions (top) and single probability density functions of axial (middle) and radial (bottom) velocities in the disk-stabilized premixed flame at $x = 50$ mm and $y = 0$, 15, 25 and 35 mm.

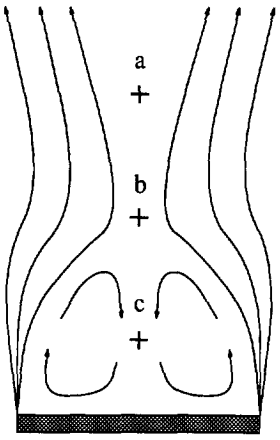

Figure 4.15: Positions for temporal analysis in the disk-stabilized premixed flame, where (a) corresponds with position x = 75 mm, y = 0 mm; (b) with x = 50 mm, y = 0 mm, and (c) with x = 25 mm, y = 0 mm.

also revealed that close to the outer edge of the flame, the PDFs take on a bimodal form. However, their bimodal characteristic did not propagate into the recirculation region.

Temporal analysis

Temporal analysis of axial velocity fluctuations has been performed for three characteristic positions in the disk-stabilized premixed flame. Because of the entirely different flow characteristics at the centreline for positions x = 25, 50 and 75 mm, axial velocity autocorrelation functions have been derived at these three heights as indicated in Figure 4.15. The slot width of the autocorrelation calculation procedure and, thus, the resolution of the autocorrelation function is determined by the inverse of the validated mean data rate. With a typical data rate of approximately 4000 Hz, the slot width used for each correlation function was typically 0.25 ms.

The autocorrelation functions are given in Figure 4.16. All autocorrelation functions show evidence of some periodicity, with the same frequency (as will be illustrated in the results of the spectral analysis). The decay of the autocorrelation functions from $\rho_u(0)$ to zero is not very smooth. Especially for the investigated positions at x = 50 mm and x = 25 mm, a bend in the first time slots catches the eye. It is believed that this correlation of velocity fluctuations results from eddies with two different time scales.

Spectral analysis

Performing a Fourier transformation on the autocorrelation functions, given in Figure 4.16, provides the power spectra depicted in Figure 4.17. All spectra of the axial

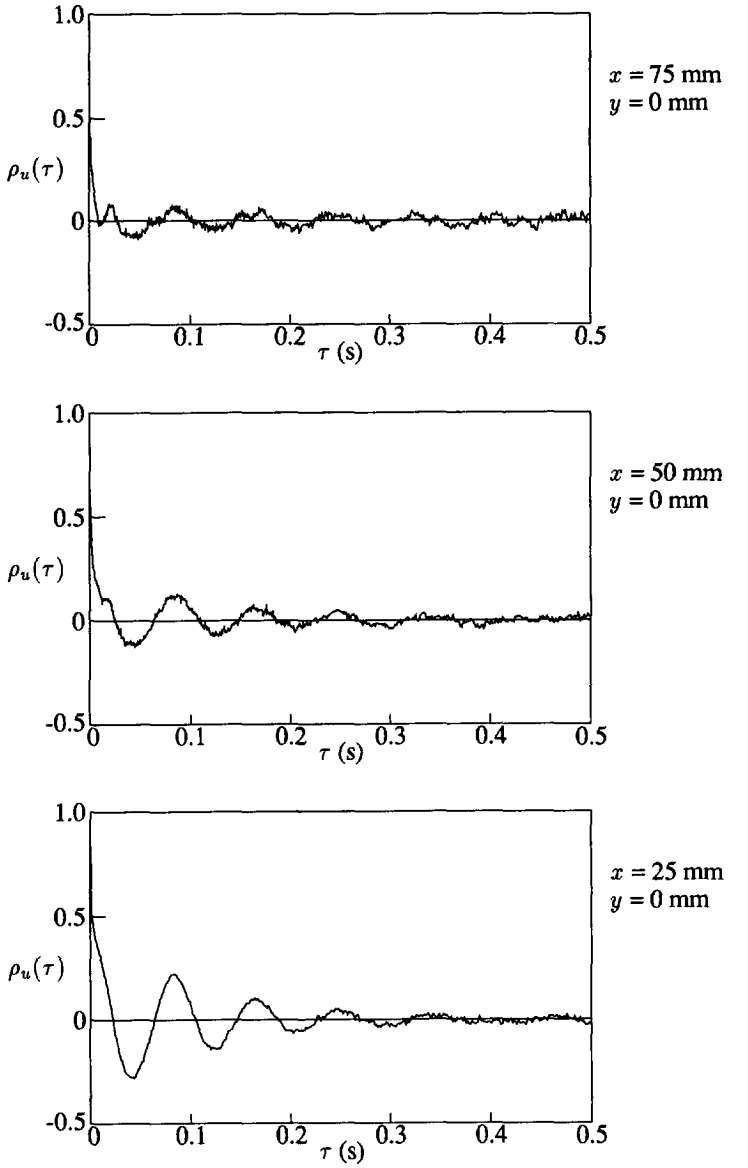

Figure 4.16: Autocorrelation functions of axial velocity fluctuations in the disk-stabilized premixed flame for positions at the centreline at x = 75 mm (top); x = 50 mm (middle) and x = 25 mm (bottom).

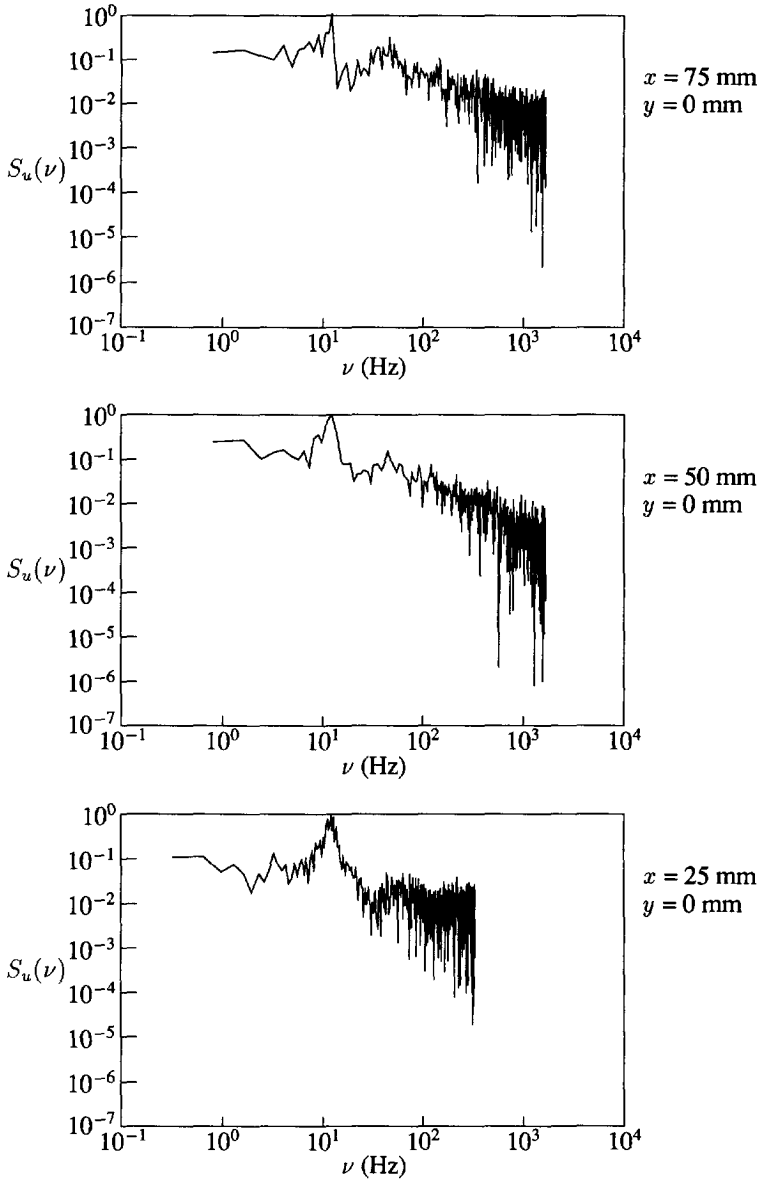

Figure 4.17: Power spectral density functions of axial velocity fluctuations in the disk-stabilized premixed flame for positions at the centreline at x = 75 mm (top); x = 50 mm (middle) and x = 25 mm (bottom).

velocity obtained at the centreline reveal a dominant frequency of 12 Hz. A similar frequency was found by Durão and Whitelaw (1978). It is useful to define a dimensionless Strouhal number St = $\nu D/U$, where ν represents the dominant frequency, D the diameter of the body around which the fluid flows and U is the fluid velocity. The Strouhal number corresponding with a frequency of 12 Hz, in a fluid flowing with U_0 = 13.2 m/s around a body with diameter d = 80 mm is 0.07. For this value of the Strouhal number, a regular periodic shedding, called the Von Kármán vortex street for flows behind a solid obstacle, is known to occur (Schlichting (1968)). The oscillations result from an organized motion with periodic vortices due to the hydrodynamic instability in the shear layer. This instability, caused by the entrainment of ambient fluid, grows in the downstream direction. Because of the presence of a recirculation zone in the present flow, it is transported through almost all regions of the flame.

4.3.3 Mean temperatures

The main purpose of flames is to generate heat. It is therefore quite obvious to measure the temperature in the flame. The goal of our investigation, however, is to study the interaction between turbulence and chemistry. Mean temperature distributions, obtained by uncompensated thermocouples, only provide a global flame property and are therefore not satisfying this aim. However, they can contribute largely in understanding the combustion process in a flame as complex as the disk-stabilized premixed flame.

In Figure 4.18, results of mean temperature measurements in the disk-stabilized premixed flame, using a 50 μm diameter thermocouple, are given for five radial traverses at x = 15, 25, 50, 75 and 100 mm. The temperature profiles within the recirculation zone, at x = 15 mm and x = 25 mm, are rather flat with a value that is approximately 10 % below the adiabatic flame temperature of 1898 K. This indicates that within the recirculation zone nearly 100 % of combustion is completed, which supports the well-stirred reactor model of the recirculation zone, as discussed in Section 2.3.3. Moving downstream, the mean temperature decreases.

At a height of x = 100 mm above the stabilizing disk, the temperatures at the centre of the flame oscillated considerably, accounting for the scattering of the data for this profile. These temperature fluctuations are most probably caused by entrainment of cold ambient air. This cold air decreases the flame temperature, which may influence the formation of hot combustion products. When combustion products of too low temperature are returned towards the burner, they can not ignite the fresh reactants, and the flame is destabilized. Because the entrainment of cold air is a process governed by the hydrodynamic instability in the shear layer between the main reaction zone and the ambient air, flame destabilization will occur at a frequency equal to that for the axial velocity fluctuations, derived in Section 4.4.1. Because of the 3 Hz sampling rate of the temperature, this 12 Hz frequency could not be resolved from the temperature measurements, however.

As mentioned before, the presented mean temperature profiles are useful for a global characterization of the combusting flow field. Complete temperature PDFs are required, however, to resolve the actual flame structure. Therefore, Heitor *et al.* (1985)

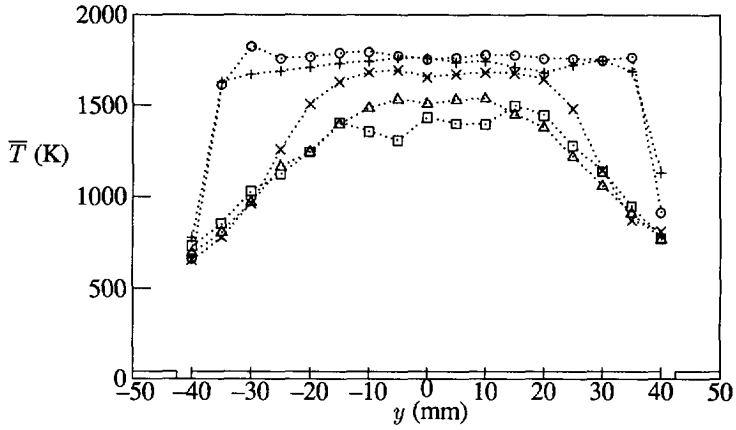

Figure 4.18: Mean temperature profiles in the disk-stabilized premixed flame for radial traverses at x = 15 (· · · + · · ·), 25 (· · · o · · ·), 50 (· · · × · · ·), 75 (· · · △ · · ·) and 100 mm (· · · □ · · ·).

have performed compensated thermocouple measurements in their confined configuration. Nonintrusive temperature distribution measurements are possible by using CARS (Coherent Anti-Stokes Raman Scattering). CARS measurements performed by Pan (1991) provided much insight in the temperature distribution and flame structure for a confined disk-stabilized premixed flame. Both the compensated thermocouple and the CARS measurements revealed that around the maximum width of the recirculation zone, temperature PDFs have a bimodal shape. A high temperature peak, comprising hot products, was centred near the adiabatic flame temperature. The other peak was centred near room temperature, associated with the presence of cold fluid. Also in an unconfined geometry, combined CARS/LDA measurements by Chen *et al.* (1988b) revealed that inside the flame zone, temperature statistics showed distinct bimodal distributions. This illustrates once more that the flame structure is very complex. Detailed knowledge of large-scale structures, entrainment and flame stretching can only be obtained when other techniques are applied.

4.3.4 Visualization of reaction zone

An important tool to collect additional information of flames is visualization. To gain more insight in the detailed flame structure of the disk-stabilized premixed flame, the reaction zone is visualized by means of planar laser induced fluorescence of OH radicals. This provides both spatially and temporally resolved properties of the chemistry in the flame. Besides, the obtained images appear to be helpful in addressing the stabilization process during combustion. Any disruption in this process can be detected. Therefore, phenomena as localized extinctions can also be investigated.

The OH radical is an important flame radical participating in combustion reactions in the flame front, but it is also present as an equilibrium product in the hot burnt gases region. It can, therefore, serve as an indicator of ongoing combustion and of the presence of hot combustion products. In Figure 4.19, three instantaneous images of the OH concentration distribution in the flame, covering x = 0 mm to x = 112 mm, are given.

The upper picture is especially useful to explain the general flame structure. According to the characteristic-time theory, in Section 2.3.3, when the fresh reactants leave the burner annulus, they are mixed with hot combustion products in the shear layer between the high exit velocity and the low-speed region at the edge of the recirculation zone. Within this main reaction zone, the fresh mixture is ignited and large concentrations of OH radicals, as well as hot combustion products are formed. Some portion of these hot combustion products is returned towards the burner, because of the presence of the recirculation zone. The hot combustion products are mixed with pockets of fresh reactants and ignition may occur. This is the main principle of stabilization in this type of flame.

The shear layer surrounding the recirculation zone, leads to entrainment of ambient air and to stretching of the flame front. Collisions of small vortices with the flame front produce small localized flamelets which are responsible for the wrinkled appearance of the flame surface close to the burner nozzle. The vortices grow with downstream position, leading to an increase in the variations of the flame surface. According to Equation 2.30, stretching of the flame surface occurs then, which corresponds with an increase in the Karlovitz number.

The localized stretching of the flame surface, caused by entrainment but also by flame curvature, is believed to invoke finite rate chemistry effects. When the flame stretch is large enough, the flame surface may be locally extinguished, evidenced by holes in the OH zone near the burner nozzle. Further downstream, the presence of holes in the OH zone is rather associated with the entrainment of cold ambient air. The entrained air causes the temperature of the hot combustion products to decrease. When these products enter the wake region and are mixed with the fresh reactants, it is possible that their temperature is too low for ignition to occur. This leads to destabilization of the flame, as described by the thermal theory in Section 2.3.3, which may eventually lead to complete blow-off of the flame. Illustration of these phenomena is given by the two other examples of the instantaneous OH distribution in Figure 4.19. In the middle picture, the combustion process is almost completely interrupted by the excessive amount of entrained cold air. In the bottom picture, a precursor to this situation can be distinguished. The flame still reveals a main reaction zone, but large regions of the flame are extinguished.

4.3.5 OH radical concentrations

Extending the OH visualizations of the previous section, semi-quantitative OH concentration measurements are performed. One-dimensional detection of the fluorescence signal not only enabled us to derive quantitative concentrations, but also to derive

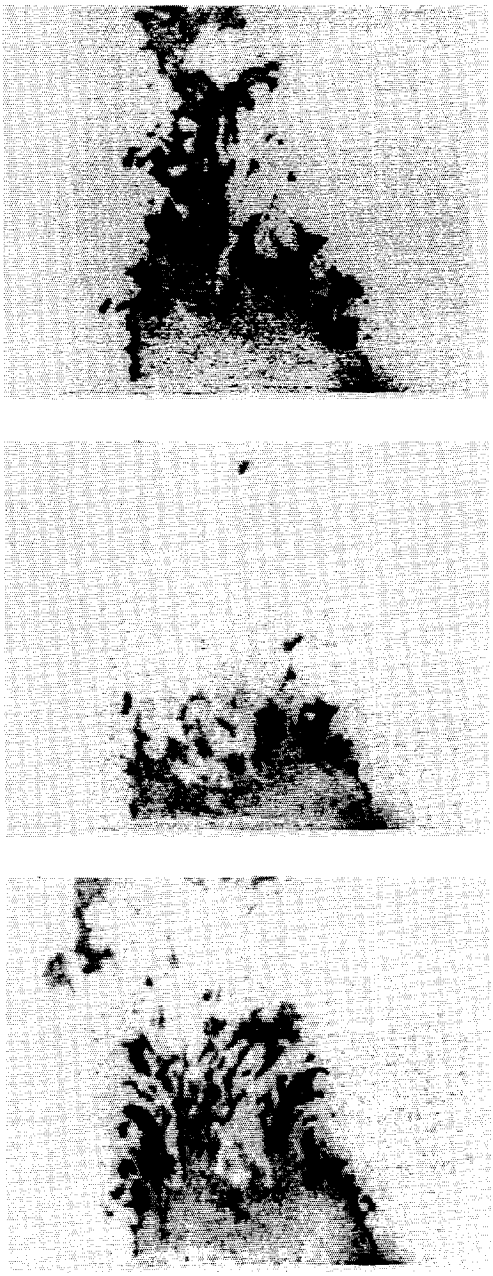

Figure 4.19: Instantaneous images of the OH distribution in the disk-stabilized premixed flame, covering x = 0 to 112 mm and y = -70 to 70 mm

length scales of OH concentration fluctuations. As mentioned in the introduction to this thesis, comparison of these scales with scales of turbulence should add important information on the turbulence-chemistry interactions.

Average OH concentrations and fluctuations

In Figure 4.20, five typical radial profiles of the average OH concentration in the disk-stabilized burner are shown at x = 15, 25, 50, 75 and 100 mm. Within the recirculation zone at x = 15 mm and x = 25 mm, the average OH concentration is almost constant. Because the temperature is constant in this region of the flow as well, it is believed that the recirculation zone is in chemical equilibrium. This is confirmed by numerical simulation by Peeters (1995), who found an equilibrium concentration of OH radicals for a premixed natural gas/air mixture with equivalence ratio $\varphi = 0.75$ of $\overline{c_{OH}} = 4.1 \times 10^{15}$ cm^{-3}, which is only slightly below the measured concentrations.

In contrast, the main reaction zone reveals OH concentrations significantly larger than equilibrium levels and is therefore believed to be in superequilibrium. When the chemical reaction rates are rapid compared to the rates of turbulent mixing (Da >> 1) chemical equilibrium is approached. When the Damköhler number is of the order of unity, mixing rates and reaction rates are competitive, and departures from chemical equilibrium are expected to be sensitive to changes in either τ_c or τ_m (Barlow *et al.* (1990a)). For the OH radical, two Damköhler numbers can be defined: based on a time scale for reactions that produce radicals and one for radical recombination. Superequilibrium results from differences in kinetic rates between these fast 2-body and slow 3-body reactions. Apparently, within the main reaction zone the rapid formation of OH radicals is not equilibrated by OH recombination, leading to high OH concentration levels. Further downstream, due to burnout of the combustible mixture, the OH concentrations decrease.

The average OH concentration profiles in Figure 4.20 are corrected for absorption of the laser beam during its path along the flame by a method adopted from Hertz and Aldén (1987), as described in Section 3.5.3. The algorithm converges after 5-10 iterations. The value of the transmission T in the iterative correction procedure was adjusted to give equal maximum OH concentrations on either side of the centreline. For radial traverses at different heights, values of the transmission as depicted in Figure 4.21 were used. As was to be expected, the general trend in this figure corresponds with the radial integral of the average OH concentration profiles: when the total average OH concentration is high, the laser beam will lose much of its energy across the flame and the transmission is low. Likewise, a low integrated concentration results in high values of T. With the obtained values for the transmission T for every axial location, the instantaneously obtained images were corrected for absorption. This provided corrections of the complete OH concentration distribution. Calculation of the moments of these corrected distributions is then quite straightforward.

The standard deviation profiles of the OH concentration distribution are depicted in Figure 4.22. The profiles of the standard deviation are wider than the average

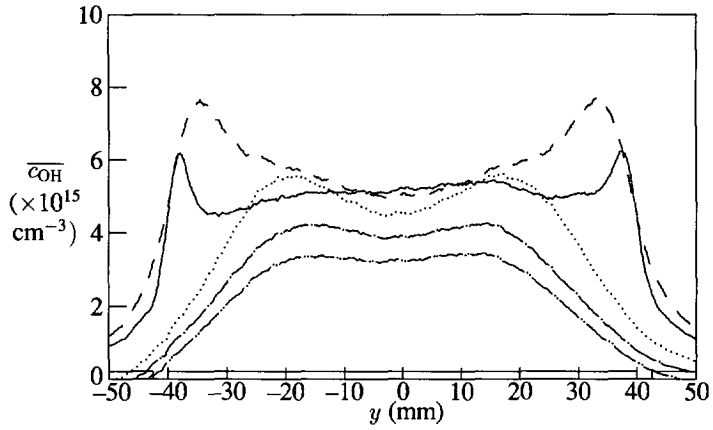

Figure 4.20: Average OH concentration profiles in the disk-stabilized premixed flame for radial traverses at x = 15 (—), 25 (– – –), 50 (· · ·), 75 (– · –) and 100 mm (– · · –).

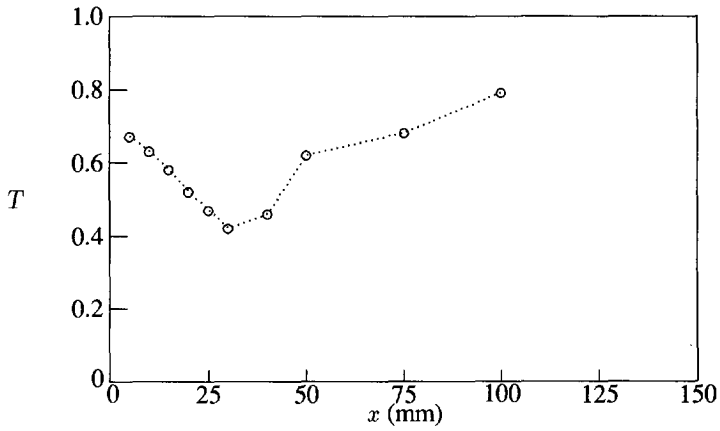

Figure 4.21: Values of the transmission T that provided symmetrical OH profiles for different axial positions in the disk-stabilized premixed flame.

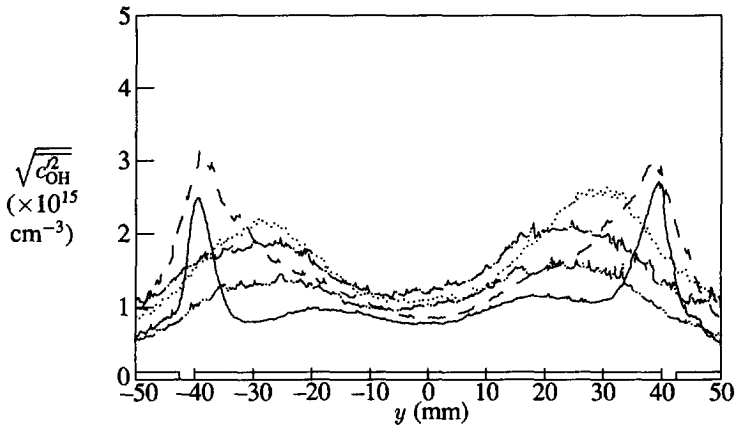

Figure 4.22: OH concentration standard deviation profiles in the disk-stabilized premixed flame for radial traverses at x = 15 (—), 25 (– – –), 50 (· · ·), 75 (– · –) and 100 mm (– · · –).

concentration profiles because the largest fluctuations occur on the slopes of the average concentration profiles. High standard deviations are found near the main reaction zone, where a high concentration gradient exists. Moving to downstream positions, values of the centreline OH standard deviation are increasing. This can be explained by the entrainment of cold air, leading to interruption of the combustion process. In addition to high OH concentrations from the main reaction zone, regions of low OH concentrations are formed by this process. For a certain location, these high OH concentrations may be followed by low OH concentrations, resulting in high standard deviations. These phenomena occur more often for downstream positions, resulting in larger values of the OH standard deviation. Near the heart of the recirculation zone, the relative standard deviation (defined by the ratio of the standard deviation of OH concentration fluctuations and the average OH concentration) is 0.15. This value is comparable with the turbulence intensity of axial velocity fluctuations of 0.20.

Probability density functions

Probability density functions of the OH concentration for various axial and radial positions in the disk-stabilized premixed flame are shown in Figure 4.23. The PDFs obtained at x = 25 mm at the centreline and for y = 20 mm, associated with the heart of the recirculation zone have a Gaussian appearance peaked at $\overline{c_{OH}} = 5 \times 10^{15}$ cm^{-3} up to y = 20 mm. This concentration is referred to as the equilibrium concentration of the recirculation zone. Moving to larger radial positions, the PDFs become broadened and skewed towards high concentrations. In this region of the flow, the main reaction zone is formed, exhibiting high (superequilibrium) OH concentrations.

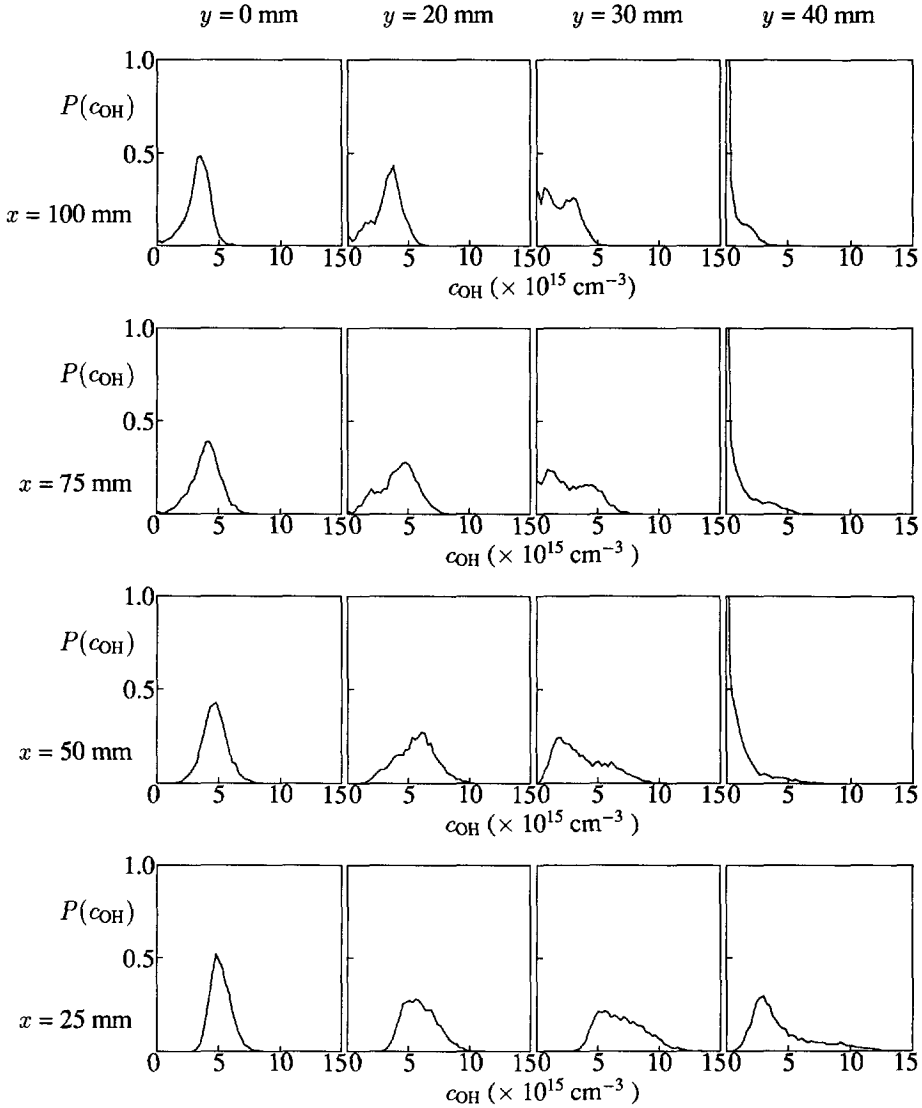

Figure 4.23: Probability density functions of OH concentration in the disk-stabilized premixed flame at x = 25, 50, 75 and 100 mm and radial positions y = 0, 20, 30 and 40 mm.

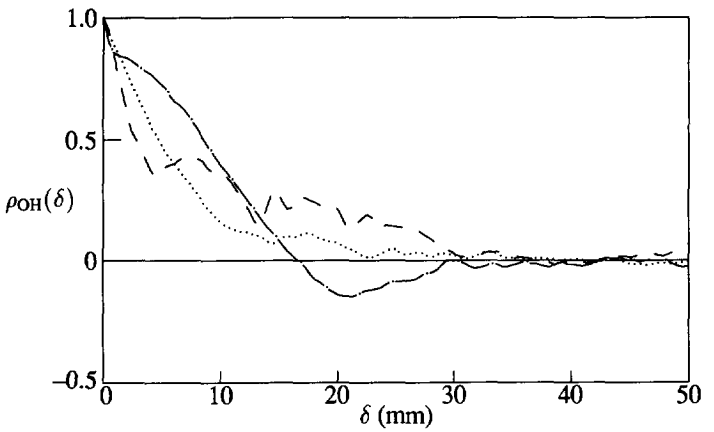

Figure 4.24: Autocorrelation functions of OH concentration fluctuations in the disk-stabilized premixed flame at x = 15 mm for positions near the main reaction zone y = 30 mm (– · –), y = 35 mm (· · ·) and y = 40 mm (– –).

For the traverse near the stagnation zone at x = 50 mm and further downstream, PDFs of the OH concentration lack high values for y = 40 mm. Near-zero OH concentrations are most probable for these positions, outside the flame front. PDFs for smaller values of y at x = 50 mm show evidence of a large spreading of OH concentrations and even some bimodal characteristics for y =30 mm. This prevalence for two OH concentrations also shows up in PDFs at x = 75 mm and x = 100 mm. The higher concentration is associated with the ordinary combustion process. The lower concentration is caused by the entrainment of cold ambient air: the local flame temperature is decreased, thus interrupting the combustion process and leading to formation of relatively little OH radicals.

Spatial analysis

In order to derive integral and Taylor micro length scales of OH concentration fluctuations along a radial profile of the flame, autocorrelation functions have been derived. In Figure 4.24, three typical correlation functions at x = 15 mm in the disk-stabilized premixed flame are given for radial positions near the main reaction zone (y = 30 mm, y = 35 mm and y = 40 mm).

All correlation functions converge towards zero; their slot width is 0.4 mm. Major differences between the correlation functions are elucidated. For y = 40 mm, the correlation function reveals a rapid decay for small δ followed by a transition to a more gradual decay, associated with the presence of two characteristic length scales. For y = 35 mm, the spatial correlation converges smoothly to zero. For y = 30 mm, small negative parts show up. For some other positions (not depicted in Figure 4.24), large

Table 4.1: Integral time and length scales and Taylor micro length scales of the axial velocity fluctuations for three characteristic positions at the centreline of the disk-stabilized premixed flame. Values between parentheses are regarded less significant because Taylor's hypothesis does not apply in regions of zero mean velocity.

x (mm)	$\mathcal{T}_u$ (ms)	$\overline{u}$ (m/s)	$\mathcal{L}_u$ (mm)	λ_u (mm)
25	2.2 ± 0.5	-9.45	21 ± 5	1.9 ± 0.2
50	5.1 ± 0.3	0.54	(2.8 ± 0.2)	(0.68 ± 0.04)
75	1.1 ± 0.3	9.90	11 ± 3	1.5 ± 0.2

negative parts of the spatial correlation functions exist. For these positions (physically irrelevant) near-zero or even negative integral length scales were obtained. De Vries (1994) has shown that this may occur when location fluctuations are the main source of fluctuations at a fixed position. Therefore, integral length scales can only be calculated for positions where large eddies cause deformation of the OH structure, typically for large values of y in the disk-stabilized flame. Unlike the integral scales, Taylor micro length scales are not limited to regions where the interaction of turbulence with OH is very strong, because the Taylor scales are based on local gradients.

4.4 Discussion

4.4.1 Scale estimates and combustion regimes

The data that have been presented in the previous sections can be used to obtain even more important flame characteristics. Both from velocity fluctuations (describing the turbulence) and OH concentration fluctuations (a property of the chemistry), characteristic length scales can be derived. These characteristic scales contain temporal and spatial information of the turbulent flame. Comparison of scales of turbulence and chemistry enables one to distinguish between various regimes of combustion. With this characterization, the governing processes in the flame can be elucidated.

Scales of turbulence in flame

From the autocorrelation functions of axial velocity fluctuations in Section 4.3.2, time scales could be estimated that are characteristic for the flow under investigation, as shown in Table 4.1. The integral of the autocorrelation function provides an estimate of the integral time scale $\mathcal{T}_u$. Near the stagnation point at x = 50 mm, the mean velocities are zero, which explains the rather long residence times of particles in this region, resulting in large values of $\mathcal{T}_u$. When values of $\mathcal{T}_u$ at x = 25 mm and x = 75 mm are compared, they decrease with downstream position, evidencing a decay of the turbulence. It suggests that eddies are broken up into smaller eddies when moving with downstream position, thereby homogenizing the turbulence.

Table 4.2: Estimated rates of dissipation ε and Kolmogorov scales for three axial positions at the centreline of the disk-stabilized premixed flame. Values between parentheses are considered less significant.

x (mm)	u'_{rms} (m/s)	ε (m^2/s^3)	l_K (mm)	τ_K (ms)	v_K (m/s)
25	2.2	512	0.5	0.8	0.7
50	2.2	(3872)	(0.3)	(0.3)	(1.1)
75	1.8	536	0.5	0.8	0.7

Multiplying the integral time scales with the axial mean velocity at each position provides estimates of the integral length scale $\mathcal{L}_u$, according to Taylor's hypothesis. Apparently, the size of the large eddies in the flame is typically of the order of one third to one quarter of the diameter of the stabilizing disk. For situations where the mean velocity approaches zero, or the turbulence intensity becomes very high, Taylor's hypothesis does not apply. Instead, estimates of the length scales can only be obtained then from direct measurement of two-point spatial correlations (Fraser *et al.* (1986)). Despite the fact that Taylor's hypothesis is not valid for $x = 50$ mm at the centreline, length scales have been calculated for this position as well. Taylor length scales of axial velocity fluctuations are estimated by means of Equation 2.17, using a relation with the measured integral length scale, and reveal the same tendency as the integral length scales. The fact that all calculated Taylor length scales are smaller than the measuring volume explains why measurement of these scales (using a parabolic fit on the first points of the autocorrelation function) was not possible.

As described in Section 2.2, the rate of dissipation ε and the Kolmogorov scales l_K, τ_K and v_K can be derived, using the kinematic viscosity of the hot combustion products $\nu_h = 3.56 \times 10^{-4}$ m^2/s. This assumption of constant viscosity is acceptable, since the temperature is almost constant in the flame (and certainly in the recirculation zone). In Table 4.2, results of Kolmogorov scales calculations are given. Again, values between parentheses are expected to be less significant because Taylor's hypothesis does not apply. Remarkable is that the Kolmogorov scales are constant throughout the flame with exception of the stagnation point. This suggests that extinction phenomena are not caused by these smallest scales of turbulence, but rather by larger-scale structures.

The laminar flame thickness for the fuel mixture under investigation is 1.7 mm. Therefore the laminar flame thickness is about 3 times larger than the Kolmogorov micro length scale, which typifies the smallest dissipative eddies. Based on the Klimov-Williams criterion, it is clear that the wrinkled laminar flame structure cannot exist then, because the local structure of the flame is destroyed by these small eddies. As a result a thick wrinkled flame is produced in which small reacting eddies are embedded in an intermediate stage of combustion.

A similar conclusion is drawn when the combustion regime in a Borghi diagram is determined. Based on the characteristic numbers given in Table 4.3, the flame falls into

Table 4.3: Characteristic nondimensional numbers for three axial positions at the centreline of the disk-stabilized premixed flame, comprising turbulence Reynolds number $\mathrm{Re}_{\mathcal{L}}$, Damköhler number Da, Karlovitz number Ka, $u'_{\mathrm{rms}}/S_{\mathrm{l}}$ and $\mathcal{L}_u/\delta_{\mathrm{l}}$. Values between parentheses are considered less significant.

x (mm)	$\mathrm{Re}_{\mathcal{L}}$ (-)	Da (-)	Ka (-)	$u'_{\mathrm{rms}}/S_{\mathrm{l}}$ (-)	$\mathcal{L}_u/\delta_{\mathrm{l}}$ (-)
25	128	1.2	10	10	12
50	(17)	(0.2)	(27)	10	(2)
75	55	0.8	10	9	6

the distributed reaction zone regime. The flame stretch is strong and an estimate of the size of the largest eddy that may quench the reaction zone, obtained by Equation 2.32, is $\delta_{\mathrm{q}} \approx 17$ mm. The stagnation zone, with its large integral time scale and high turbulence intensity can be treated as a well-stirred reactor. The turbulence intensity in this region is so large that no specific interaction between turbulence and combustion will occur.

It should be noted that practical boundaries between combustion regimes are not as sharp as derived from the physical analysis in Chapter 2. The nondimensional numbers Da and Ka, however, show that the flame is in the transition of the distributed reaction zone and the well-stirred reactor regime, because Da ≈ 1 and Ka > 1. Within this combustion regime, thin reaction zones may be generated locally and quenched by flame stretching, thus characterizing a turbulent flame as a thickened-wrinkled flame with possible extinctions.

Scales of chemistry in flame

By calculating the correlation function of OH concentration fluctuations for every location along a radial profile, integral and Taylor micro length scales $\mathcal{L}_{\mathrm{OH}}$ and λ_{OH} can be estimated, given in Figures 4.25 and 4.26. For a number of locations, the integral length scales appeared to be negative due to negative parts in the spatial correlation function as discussed in Section 4.3.5. Therefore, $\mathcal{L}_{\mathrm{OH}}$ is only defined for large values of y, where the interaction between turbulence and chemistry is strong. The integral length scales are smallest for the positions of maximum average concentrations. Near the main reaction zone, the temperature is high and combustion reactions occur rapidly, resulting in small values (minima of approximately 5 mm) of the integral length scale. When moving downstream, burnout of the combustible mixture occurs and the integral length scales increase to values between 15 and 20 mm.

The Taylor micro length scales are derived from the correlation coefficient at the first non-zero value of δ. The parabola from which the Taylor scale is derived therefore consists of only one data point for highest spatial resolution. Only for the centre region of the flame at x =15 mm to x = 50 mm, reliable parabolic fits were possible. The resulting Taylor micro length scales of OH concentration fluctuations are depicted in Figure 4.26. The Taylor micro scales are almost constant over every radial profile,

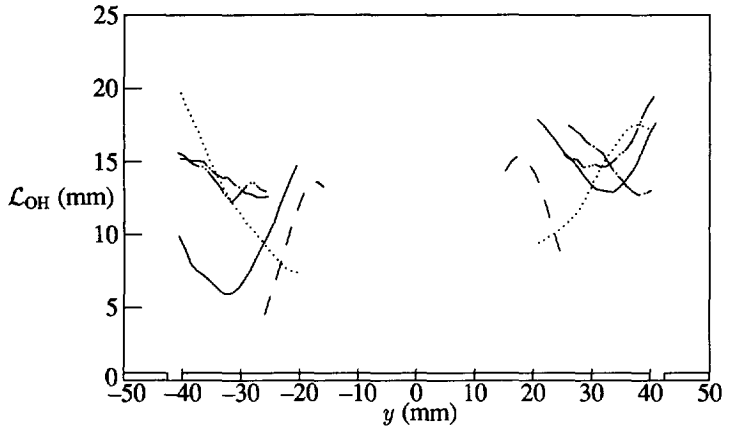

Figure 4.25: Integral length scale profiles of OH concentration fluctuations in the disk-stabilized premixed flame for radial traverses at x = 15 (—), 25 (– – –), 50 (· · ·), 75 (– · –) and 100 mm (– · · –).

evidencing the validity of the stirred-reactor theory. In accord with the tendency of the integral length scales, the Taylor micro length scales increase with downstream position.

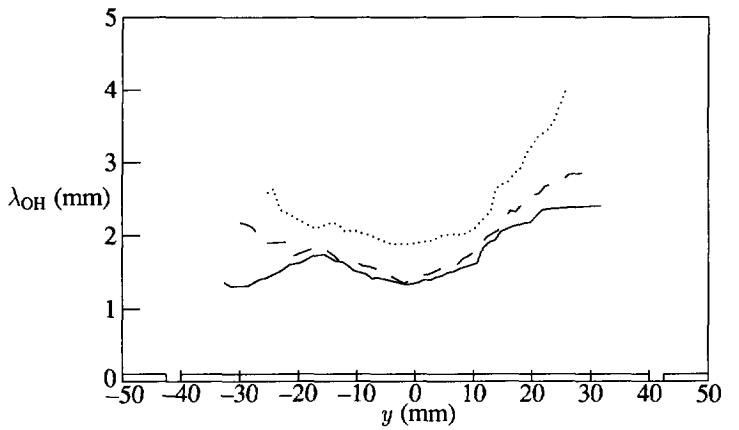

Figure 4.26: Taylor length scale profiles of OH concentration fluctuations in the disk-stabilized premixed flame for radial traverses at x = 15 (—), 25 (– – –) and 50 mm (· · ·).

Table 4.4: Estimates of axial velocity fluctuation and OH concentration fluctuation integral and Taylor micro length scales for three positions at the centreline of the disk-stabilized premixed flame.

x (mm)	$\mathcal{L}_u$ (mm)	λ_u (mm)	$\mathcal{L}_{OH}$ (mm)	λ_{OH} (mm)
25	21 ± 5	1.9 ± 0.2	6 ± 3	1.4 ± 0.3
50	(2.8 ± 0.2)	(0.68 ± 0.04)	10.9 ± 0.3	1.9 ± 0.5
75	11 ± 3	1.5 ± 0.2	12 ± 2	2 ± 2

Comparison of turbulence and chemistry scales in flame

In classical turbulent combustion models, the length scales of concentration fluctuations and of the turbulence kinetic energy are often assumed to be proportional. As shown in Table 4.4, however, the ratio of the two scales is not constant for different positions in the flame. The accuracy of the integral length scales is determined by the convergence of the integrated autocorrelation function (and an error in the axial mean velocity, when using Taylor's hypothesis, for determination of $\mathcal{L}_u$). The accuracy of λ_{OH} is estimated from the scattering of the data in their radial profiles. OH concentration length scales at the centreline for x = 75 mm have not been presented in the previous section, because of their limited accuracy. For completeness, however, they are included in Table 4.4. Looking at this table, the length scales of velocity fluctuations decrease with downstream position, revealing the decay of turbulence. OH concentration length scales, however, increase with downstream position, because burnout of the combustible mixture occurs. It should be noted that a direct comparison between velocity and concentration length scales is not fair, because the velocity scales represent a longitudinal scale, whereas the OH concentration fluctuation scales represent lateral scales.

4.4.2 Comparison of reacting with inert flow

The actual influence of the disk-stabilized premixed flame on turbulence is investigated by comparing velocity characteristics in the flame and its nonreacting equivalent. These results have been presented separately in Sections 4.2.1 and 4.3.1 already. Some of the most striking differences will be discussed in this section.

In Figure 4.27, the centreline axial distributions of the axial mean velocity and the turbulence kinetic energy in the reacting and the nonreacting flow of the disk-stabilized burner are given. The average recirculation zone length, based on the position of the centreline stagnation point, is estimated to be 30 mm in the nonreacting and 50 mm in the reacting case. This approximately 40 % greater length in combustion, as compared to isothermal flow, is also found in confined geometries by Taylor and Whitelaw (1980) and Pan (1991). Actual values of recirculation zones lengths in these investigations can not be compared with our values, because properties that are known to influence the recirculation zone length (exit velocity, reactants and burner geometry) differ.

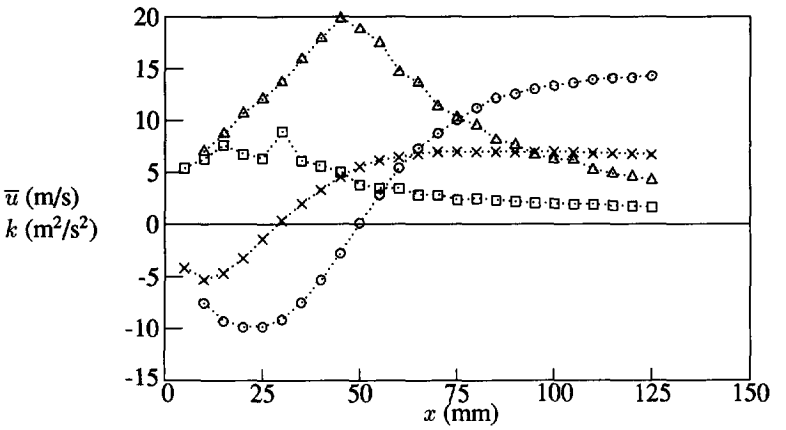

Figure 4.27: Centreline axial profiles of the axial mean velocity (··· ○ ···) and the turbulence kinetic energy (··· △ ···) in the disk-stabilized premixed flame as well as the axial mean velocity (··· × ···) and the turbulence kinetic energy (··· □ ···) in its nonreacting equivalent.

Despite the equal exit velocity U_0 = 13.2 m/s, the maximum velocities in the combusting flow are much larger than in the inert flow. This is caused by thermal expansion due to combustion reactions. As a result, the velocity difference between the annular flow and the surrounding air is larger in the flame. The shear layer in the flame will therefore develop faster, resulting in larger values of the turbulence kinetic energy. The turbulence kinetic energy attains maxima near the stagnation point in both cases. The axial turbulence intensity at the position of maximum negative axial mean velocity and far downstream is smaller in the reacting than in the nonreacting flow. For the reacting flow, $u'_{rms}/\overline{u}$ is 0.20 and 0.10, respectively, whereas for the isothermal flow is attains values of 0.25 and 0.15. Apparently, the increase in velocity fluctuations, because of the larger velocity difference, is smaller than the increase in axial mean velocity, due to thermal expansion.

4.4.3 Approach to extinction

The flame stability characteristics of the bluff-body stabilized premixed flame are largely determined by the aerodynamics of the flow around the body. The flame is anchored in the outer regions of the wake and the combustion wave propagates in a flow region with high velocity gradients, where flame stretch occurs. The turbulent flame structure around the recirculation zone can be characterized into three development stages.

The first stage is a thin flame region. The hot products from the recirculation zone meet the incoming cold reactants and ignite the reactants at the interface through

turbulent heat diffusion and conduction. The resulting flame is a laminar thin flame or a wrinkled laminar flame under the influence of large-scale mainstream turbulence. In this region, turbulence is suppressed by viscous dissipation due to combustion heat release, which causes flow acceleration.

Next, a reacting shear layer with growing coherent structure exists. CARS measurements by Pan (1991) revealed that downstream of the initial thin flame region, a much smaller temperature gradient across the flame exists. This, together with a monotonous growth of the flame zone, suggests the onset of turbulence in the shear layer. Temperature in the recirculation zone remains fairly constant except across the reacting shear layer. Due to entrainment of ambient air, large-scale eddies form as folds around the flame edge. These coherent eddies are squeezed and stretched during travel through the flame and the entrainment process causes their growth downstream, thereby thickening the flame.

Downstream of the maximum recirculation zone width, flame necking down takes place and the entrainment of ambient air dominates, resulting in a thick flame region. The streamlines curve toward the centreline. This large streamline curvature generates higher turbulence which induces flame stretch and breakdown of large eddies. In this third stage, the flame surface may be extinguished locally, when the flame stretch is large enough.

It is evident that the recirculating flame exists at high stretch rates because the recirculation zone is at a sufficiently high temperature. Locally extinguished pockets are transported with the flow toward the stagnation zone. The temperature PDFs acquired by Pan (1991) in the vicinity of the stagnation point showed limited possibility that a cold gas pocket exists. Thus part of the entrained fluid in the thick flame region will be reversed into the recirculation zone, while most of it will be flowing downstream into the propagating flame. However, if the flamelets are extinguished in the thick region due to excess entrainment, which in turn would lower the temperature surrounding the reactants, flame propagation will cease. The flame stabilization process is interrupted, and eventually this will lead to blow-off of the flame.

The disk-stabilized premixed flame under investigation was studied at an equivalence ratio $\varphi = 0.75$. This provided overall flame stability, yet with major extinctions of the flame due to entrainment of ambient air. Visualization of the OH concentration for a fuel/air mixture with an equivalence ratio $\varphi = 0.95$, with the same exit velocity revealed that the entrainment rate is not altered. In this flame, processes similar to that occurring in the flame with $\varphi = 0.75$, where a certain amount of ambient air is entrained and transported into the recirculation zone, occur on a much smaller scale. This leads to an overall more stable combustion process, than for the fuel-leaner mixtures. In contrast, when the equivalence ratio of the flame is reduced to $\varphi = 0.7$ with equal exit velocity, the flame is pushed close to its lean blow-off limit. The amount of ambient air that is entrained and transported into the recirculation zone leads to dilution of the combustible mixture, which becomes too fuel-lean to combust. Slight adjustment of the equivalence ratio towards an even fuel-leaner mixture leads to immediate blow-off.

4.5 Summary of Chapter 4

In this chapter, measurements in a disk-stabilized premixed flame and its nonreacting equivalent are reported. The burner consists of a disk with a diameter of 80 mm, placed in the centre of a contraction with an exit diameter of 85 mm. With a flow exiting from the burner annulus with a velocity of 13.2 m/s, a recirculation zone is formed behind the disk. In a premixed natural gas/air flame, with equivalence ratio $\varphi = 0.75$, the recirculation zone length, based on the position of the centreline stagnation point measured by laser Doppler anemometry, is significantly larger than in the isothermal flow. This is attributed to thermal expansion, due to combustion reactions, leading to high velocities in the flame. As a result, the velocity difference between the annular flow and the stagnant surrounding air is larger in the flame than in the isothermal flow. Because this velocity difference creates a shear layer, which generates turbulence, the higher values of the turbulence kinetic energy in the flame than in the nonreacting flow can be explained. The turbulence kinetic energy is maximum near the centreline stagnation point, where radial velocity fluctuations are much larger than axial velocity fluctuations. This large degree of anisotropy decreases close to the burner and far downstream.

Visualization of OH radicals in the flame by planar laser induced fluorescence revealed the stabilization mechanism of disk-stabilized premixed flames. The main property of this mechanism is the mixing between fresh reactants and hot combustion products. The recirculation zone plays an essential role in bringing products and reactants together. Laser-induced fluorescence with one-dimensional detection on OH radicals elucidated that the average OH concentration is almost constant within the recirculation zone. The mean temperature, obtained by thermocouples, was found to be constant as well. This suggests that the recirculation zone serves as a region of chemical equilibrium, continuously providing the fresh reactants with high temperature combustion products. The shear layer surrounding the recirculation zone, however, can have a destabilizing effect on the flame, because it entrains cold ambient air. A dominant frequency, resulting from this hydrodynamic instability in the shear layer, was revealed by spectral analysis of axial velocity fluctuations. The corresponding dimensionless Strouhal number is in a range where Von Kármán-like vortex streets occur. As a result of this instability, entrained ambient air causes the temperature of the hot combustion products to decrease. When these (relatively cold) products enter the wake region and are mixed with the fresh reactants, it may occur that their temperature is too low for ignition to occur. This introduces destabilization of the flame, which may eventually lead to complete blow-off.

Length scales of axial velocity fluctuations and of OH radical concentration fluctuations were derived. With these scales it was possible to characterize the stagnation zone of the flame as a well-stirred reactor and all other regions of the flame as distributed reaction zones.

Chapter 5

Structure of piloted jet diffusion flame

5.1 Outline of this chapter

In this chapter, the turbulence behaviour of nonpremixed flames under different conditions will be discussed. The flame conditions are determined by the fuel exit velocity and the primary air exit velocity. These parameters influence the turbulent mixing of fuel and air, which will have its effect on both global flame characteristics, like flame length, and local characteristics, like temperature and species concentrations. To reveal the influence of combustion on the turbulence structure of the flow field, in Section 5.2 velocity characteristics of nonreacting jets will be presented. The different flames under investigation will be evaluated based on global flame properties in Section 5.3.1 and on velocity characteristics in Sections 5.3.2 and 5.3.3. Mean temperatures and OH radical distributions will be presented in Sections 5.3.4 and 5.3.5. Estimations of characteristic scales of turbulence add important information to the overall understanding of the flows under investigation, as will be seen in Section 5.4.1. Together with a comparison of a reacting and an isothermal flow in Section 5.4.2, this will enable us to address turbulence-chemistry interactions. In Section 5.4.3, it will be discussed how these interactions can influence the flame structure and how they can contribute to local extinction phenomena. Experimental results obtained for a reference flame are compared with predictions of a conserved-scalar numerical model in Section 5.4.4 Finally, in Section 5.5, a summary of the results presented in this chapter will be given.

5.2 Results in nonreacting flow fields

5.2.1 Velocity characteristics

Nonreacting, isothermal flows of the piloted jet diffusion flame are investigated for two flow settings. Jet I, an axisymmetric air jet issuing into stagnant air, is a standard topic for investigating turbulence in jets. This may be evidenced by the large amount of publications involving experimental data, mathematical analysis and computational modelling on this topic (*e.g.* Hinze (1975), Panchapakesan and Lumley (1993) and Hussein *et al.* (1994)). Jet II, a jet with a co-current primary annular air flow, is the nonreacting equivalent of flame C, which is regarded as a reference flame in this chapter,

and can therefore be useful for comparison with this flame to study the influence of combustion on turbulence.

Axial distributions

Centreline axial profiles of the axial mean velocity, axial and radial rms velocity and the turbulence kinetic energy in nonreacting jets are given in Figures 5.1 and 5.2. The axial mean velocity decays less rapidly in the axial direction for jet II than for jet I. This effect is attributed to the presence of the non-zero primary annular air flow in jet II. Despite the fact that the velocity difference between the central jet flow and the annular flow is smaller in jet II than in jet I, leading to a smaller shear rate (for the present range of Reynolds numbers $\sim 10^4$), values of maximum axial and radial rms velocity are equal in both jets. Initially, both nonreacting jets I and II are highly anisotropic ($u'_{\rm rms}/v'_{\rm rms} \approx 2.5$). Far downstream however, both axial and radial rms velocities attain more equal values in both jets ($u'_{\rm rms}/v'_{\rm rms} \approx 1.2$ at $x = 300$ mm). In order to estimate the turbulence kinetic energy, the tangential velocity fluctuations are assumed to be equal to the radial velocity fluctuations. The axial position where the turbulence kinetic energy attains a maximum differs in both flows: at $x = 50$ mm ($x/D_{\rm jet} = 8.3$) in jet I and at $x = 30$ mm ($x/D_{\rm jet} = 5$) in jet II. Apparently, the contribution of the turbulent primary annular air flow is to cause mixing closer to the burner than in a situation with zero coflow, as in jet I.

The axial turbulence intensity, defined as $u'_{\rm rms}/\overline{u}$, approaches values at $x = 300$ mm ($x/D_{\rm jet} = 50$) of 0.24 in jet I and 0.15 in jet II. With the present definition of the turbulence intensity, the contribution of the primary annular air flow in jet II is not taken into account. For comparison with jet I, the turbulence intensity of jet II should be defined as $u'_{\rm rms}/(\overline{u} - \overline{u}_{\rm ann})$, where $\overline{u}_{\rm ann}$ represents the mean velocity of the primary annular air flow. Because $\overline{u}_{\rm ann}$ is a function of axial position and it is not possible to distinguish between fluid originating from the jet or the primary air flow, this definition can not be applied. As a result, however, with a definition $u'_{\rm rms}/\overline{u}$, the turbulence intensity in jet II will be underestimated. For a self-preserving jet into still air, Wygnanski and Fiedler (1969) obtained values for the axial turbulence intensity of 0.24 at $x/D_{\rm jet} = 20$ and 60, which agrees well with the value found in jet I.

Radial distributions

In Figures 5.3 and 5.4, the axial mean velocity profiles in jet I and jet II are presented for various radial positions y at axial distances from the nozzle $x = 50$, 100, 150, 200 and 250 mm. The spreading of the jet and the decreasing centreline velocity are clearly elucidated. As in the sequel, contours of the burner nozzle with inner diameter $D_{\rm jet} = 6$ mm and an outer diameter of 15 mm, as well as the outer diameter of the annulus of 45 mm are depicted in the lower part of all radial profiles. In Figure 5.4, the presence of the primary air annulus in jet II which forms a wake immediately downstream of the burner rim, results in a minor decrease of the axial mean velocity near $y = \pm 8$ mm, for $x = 50$ mm (indicated by small arrows).

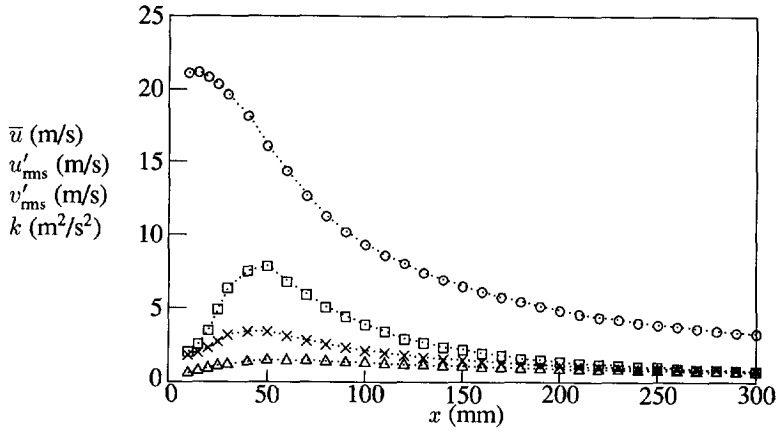

Figure 5.1: Centreline axial profiles in jet I of the axial mean velocity $\overline{u}$ ($\cdots$ o $\cdots$), the axial rms velocity u'_{rms} ($\cdots \times \cdots$), the radial rms velocity v'_{rms} ($\cdots \triangle \cdots$) and the turbulence kinetic energy k ($\cdots \square \cdots$).

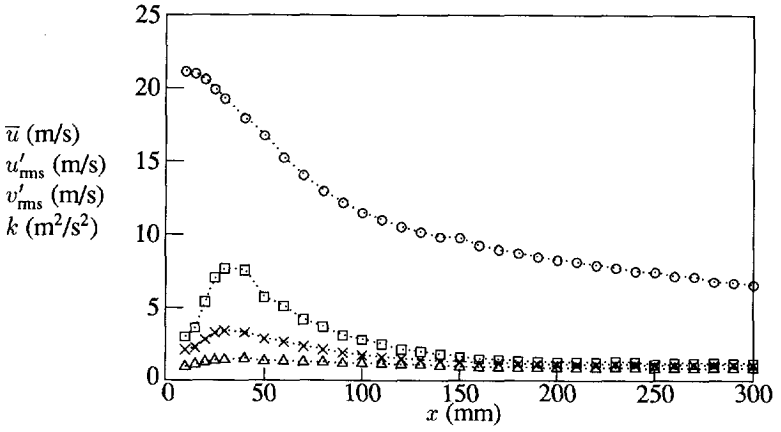

Figure 5.2: Centreline axial profiles in jet II of the axial mean velocity $\overline{u}$ ($\cdots$ o $\cdots$), the axial rms velocity u'_{rms} ($\cdots \times \cdots$), the radial rms velocity v'_{rms} ($\cdots \triangle \cdots$) and the turbulence kinetic energy k ($\cdots \square \cdots$).

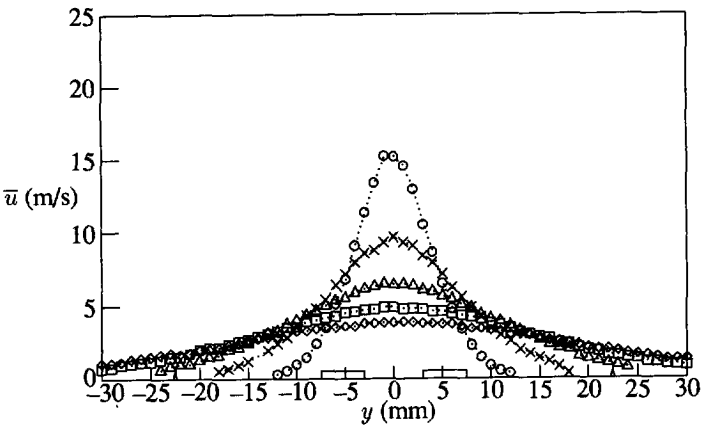

Figure 5.3: Axial mean velocity profiles in jet I for radial traverses at $x = 50$ ($\cdots\circ\cdots$), 100 ($\cdots\times\cdots$), 150 ($\cdots\triangle\cdots$), 200 ($\cdots\square\cdots$) and 250 mm ($\cdots\diamond\cdots$).

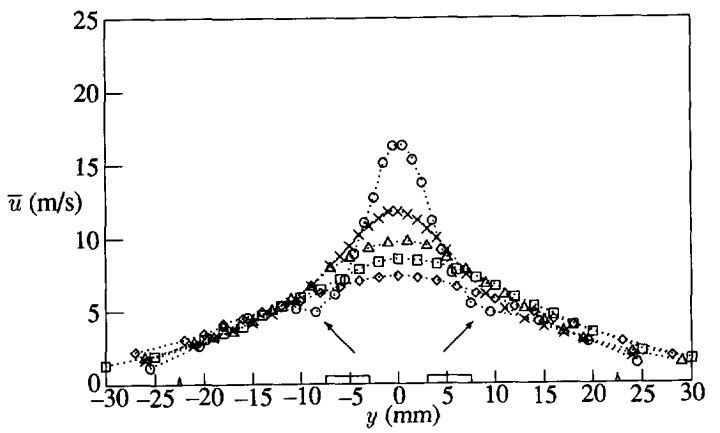

Figure 5.4: Axial mean velocity profiles in jet II for radial traverses at $x = 50$ ($\cdots\circ\cdots$), 100 ($\cdots\times\cdots$), 150 ($\cdots\triangle\cdots$), 200 ($\cdots\square\cdots$) and 250 mm ($\cdots\diamond\cdots$).

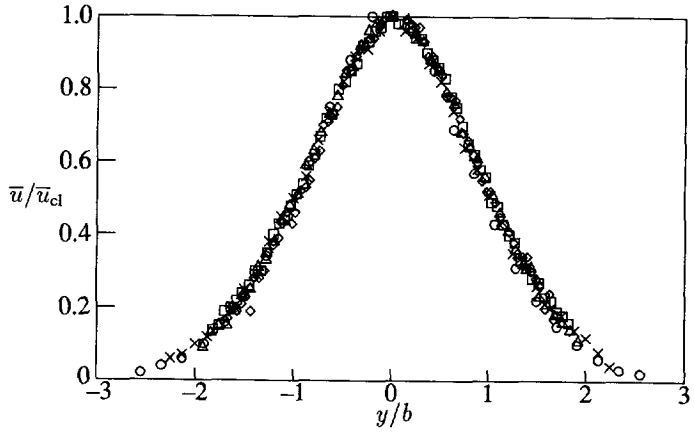

Figure 5.5: Dimensionless axial mean velocity profiles in jet I for x/D_{jet} = 8.3 (○), 16.7 (×), 25 (△), 33.3 (□) and 41.7 (◇). The centreline axial mean velocity $\overline{u}_{cl}$ and the velocity half radius b are used to scale the axial mean velocity and the radial position, respectively.

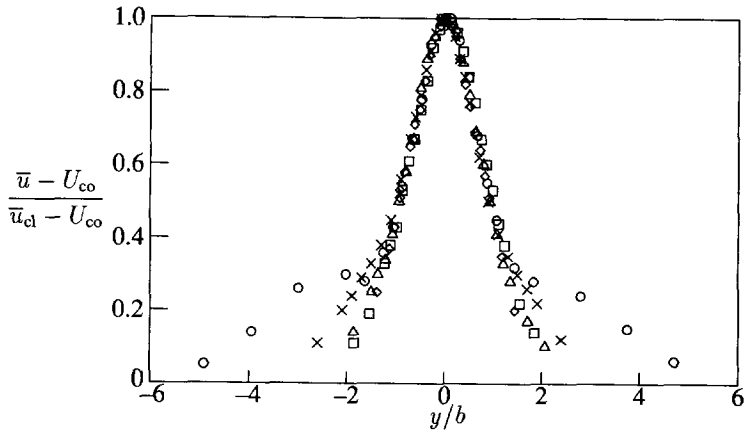

Figure 5.6: Dimensionless axial mean velocity profiles in jet II for x/D_{jet} = 8.3 (○), 16.7 (×), 25 (△), 33.3 (□) and 41.7 (◇). The axial mean excess velocity ($\overline{u}$ - U_{co}) is scaled with an excess centreline velocity ($\overline{u}_{cl}$ − U_{co}) and the radial position is scaled with the excess mean velocity half radius b.

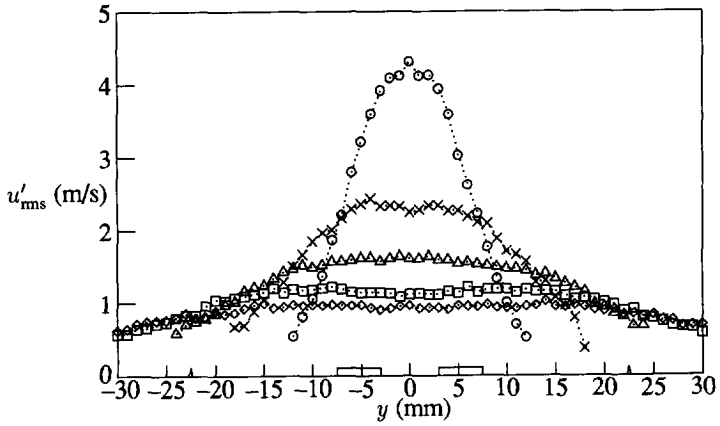

Figure 5.7: Axial rms velocity profiles in jet I for radial traverses at x = 50 (· · · ○ · · ·), 100 (· · · × · · ·), 150 (· · · △ · · ·), 200 (· · · □ · · ·) and 250 mm (· · · ◇ · · ·).

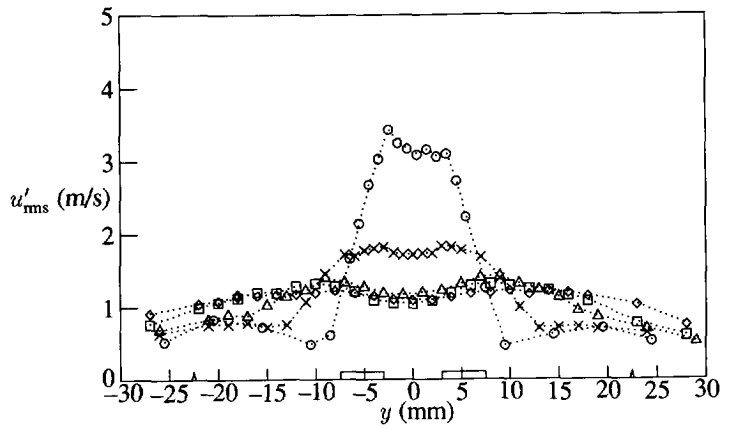

Figure 5.8: Axial rms velocity profiles in jet II for radial traverses at x = 50 (· · · ○ · · ·), 100 (· · · × · · ·), 150 (· · · △ · · ·), 200 (· · · □ · · ·) and 250 mm (· · · ◇ · · ·).

In regions of the fully developed flow, the axial mean velocity distributions of both jet I and II appear to have the same shape. In order to see whether these profiles are truly similar for jet I, in Figure 5.5 $\overline{u}/\overline{u}_{cl}$ is plotted against a dimensionless distance y/b. Here, $\overline{u}_{cl}$ is the centreline axial mean velocity and b is the value of y at $\overline{u} = \overline{u}_{cl}/2$. The profiles indeed appear to be similar, with slight deviations for large radial distances. For jet II, issuing into a coflow with velocity U_{co}, the corresponding similarity law can be visualized by plotting $(\overline{u} - U_{co})/(\overline{u}_{cl} - U_{co})$ versus y/b. Here, the excess mean velocity half radius b represents the value of y at $\overline{u} = (\overline{u}_{cl} - U_{co})/2$. As indicated in Figure 5.6, the velocity profiles of jet II are similar as well, despite the presence of the turbulent primary annular air flow. For the initial traverse at $x = 50$ mm ($x/D_{jet} = 8.3$), however, the development of the turbulent annular flow and the presence of a wake downstream of the burner rim causes the profiles to show large departures from similarity in the outer regions of the flow.

Figure 5.7 contains the measured axial rms velocities u'_{rms} in jet I as a function of radial distance. Production of turbulence energy in this type of flow is primarily due to the mean axial velocity gradient in the radial direction. This gradient is highest near the jet exit and results in high values of the axial velocity fluctuations for $x = 50$ mm and $x = 100$ mm. Further downstream, the mean velocity gradient decreases. Axial velocity fluctuations in jet II have an overall lower value than in jet I, as indicated in Figure 5.8. Because of the presence of the primary annular air flow, the axial velocity gradient at the jet exit is smaller. Thus, a smaller shear rate between the jet and the annular flow exists, leading to less production of turbulence and lower values of u'_{rms} than in jet I (for our Reynolds numbers of order 10^4). Radial profiles of radial rms velocities have not been measured in the nonreacting flows.

Probability density functions

Figures 5.9 and 5.10 present probability density functions of the axial velocity component in jet I and jet II, respectively. Axial velocity PDFs $P(u)$ in jet I are Gaussian-like with some skewness towards higher velocities apparent in the outer regions of the jet and towards lower velocity near the centreline. The PDFs shift to a higher average velocity as the centreline is approached. One should keep in mind that only the central jet flow is seeded with particles in jet I. Due to seeding bias, a skewness toward higher velocities will be present, especially for larger values of the radial position.

In jet II, both the central jet and the annular flow are seeded with particles. As for jet I, the axial velocity PDFs $P(u)$ for jet II are in general characterized by unimodal distributions. In the outer mixing region, $y = 12$ mm, $P(u)$ is relatively narrow, with a mean velocity close to that of the primary annular air velocity. Moving to the centreline, $P(u)$ shows an increasing contribution from high-velocity fluid from the central jet flow.

Temporal analysis

Autocorrelation functions of axial velocity fluctuations derived for various positions

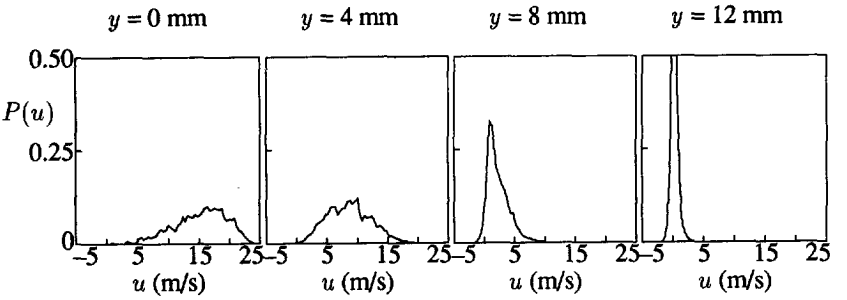

Figure 5.9: Probability density functions of the axial velocity in jet I at $x = 50$ mm, for $y = 0$, 4, 8 and 12 mm.

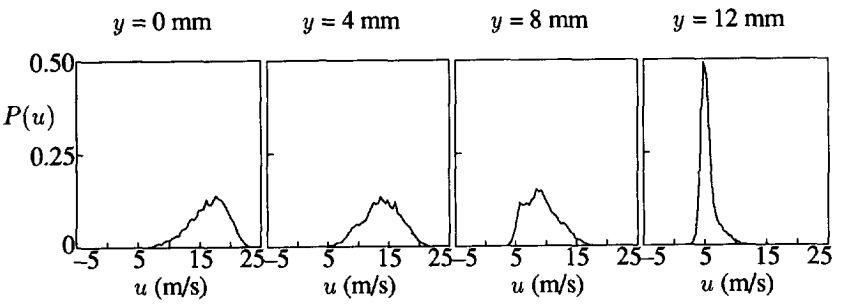

Figure 5.10: Probability density functions of the axial velocity in jet II at $x = 50$ mm, for $y = 0$, 4, 8 and 12 mm.

at the centreline of the burner in jet I and jet II are depicted in Figures 5.11 and 5.12, respectively. All autocorrelation functions that were derived converge towards zero for large τ. With a typical average data rate of 4500 Hz, the slot width of the autocorrelation functions was selected to be 50 μs. The temporal resolution for the first slots is poor for all calculated autocorrelation functions. Therefore, Taylor micro time scales of axial velocity fluctuations were not derived. In order to reveal the differences between the various autocorrelation functions in the first slots, the horizontal scale of the presented profiles extends to 2.5 ms only. As was expected, the autocorrelation functions decay more rapidly with τ for upstream positions than for downstream positions, corresponding with a decrease of the eddy size for larger x. This will also be elucidated when time scales are derived from these autocorrelation functions (see Section 5.4.1).

The decay rate of the centreline autocorrelation functions in jet I and jet II for $x = 50$ mm is almost equal. At the centreline, the primary annular air of jet II has not had sufficient time to mix with the central air jet. The scales of turbulence will therefore only be influenced by the scale of the experiment for this upstream position; in this

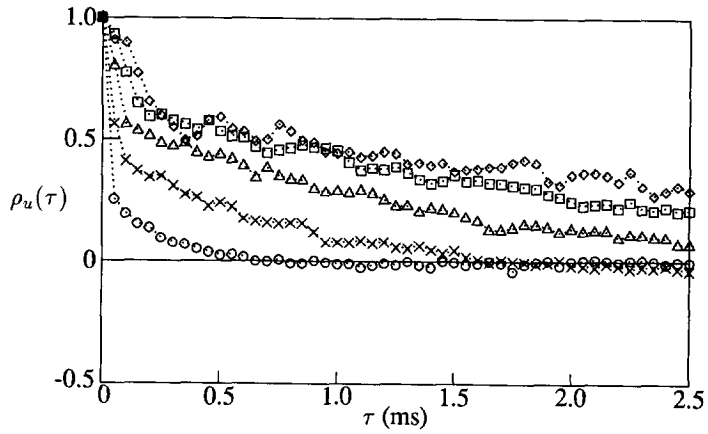

Figure 5.11: Autocorrelation functions of axial velocity fluctuations in jet I for positions at the centreline of the burner at $x = 50$ ($\cdots\circ\cdots$), 100 ($\cdots\times\cdots$), 150 ($\cdots\triangle\cdots$), 200 ($\cdots\square\cdots$) and 250 mm ($\cdots\diamond\cdots$).

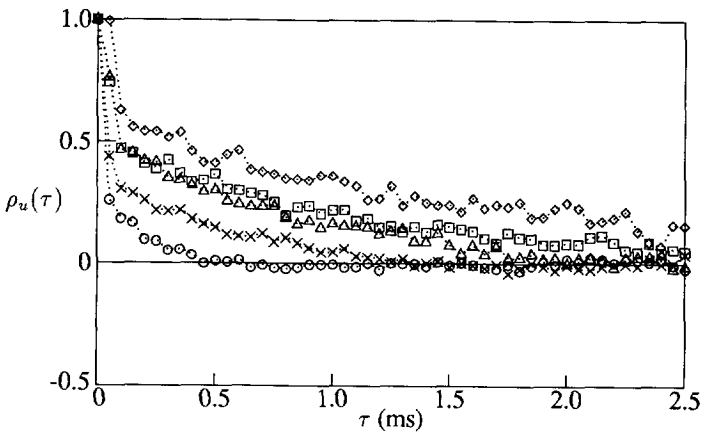

Figure 5.12: Autocorrelation functions of axial velocity fluctuations in jet II for positions at the centreline of the burner at $x = 50$ ($\cdots\circ\cdots$), 100 ($\cdots\times\cdots$), 150 ($\cdots\triangle\cdots$), 200 ($\cdots\square\cdots$) and 250 mm ($\cdots\diamond\cdots$).

case, the diameter of the central jet. Further downstream, however, significant mixing of air from the jet and the annulus in jet II, leads to a higher decay rate than in jet I. This behaviour will be reflected in the integral time scales of Section 5.4.1.

5.3 Results in reacting flow fields

5.3.1 Global flame properties

As stated in Section 3.2.3, the piloted jet diffusion flame can be studied under different rates of shear and mixing, varying the fuel jet velocity and primary annular air velocity. Before going into the detailed measurements of temporally and spatially resolved flame properties, a more global description of the flames can be useful. By means of visual inspection and imaging with video, some basic flame features can be derived.

Video images

Instantaneous pictures, selected from a series of video images, given in Figure 5.13, provide a characterization of the four piloted jet diffusion flames A to D, and the flame at lift-off E. The flow settings for these flames are given in Table 3.1. In flame A, with low Reynolds numbers and low velocities of fuel and air, relatively large residence times enable soot formation to occur, explaining the bright yellow appearance for the entire flame. Flame A suffers from buoyancy-induced instabilities apparent especially near the flame tip. These instabilities appear over a wider range in flame B, with modest Reynolds numbers. Larger velocities in flame B than in flame A decrease the residence times for soot particles in the upstream part of the flame. Therefore, the flame base (up to $x \approx 200$ mm) is blue. The reaction zone in flame B is not strongly curved. In flame C, with high Reynolds numbers, distorsions of the flame front occur very often. Also some local extinctions of the reaction zone are revealed in flame C, indicated in the measurements by near-zero OH mass fractions within the reactive range of mixture fraction (see Section 5.3.4). Flame D, with high Reynolds numbers and with excess primary annular air flow, displays a significant probability of these local extinctions.

Flame length

The flame tip of all flames is yellow due to the presence of soot. Based on the average location of the flame tip, a flame length is determined. The actual flame length, associated with the location of the reaction zone, however, will be smaller because complete burnout of soot may extend to regions downstream of the reaction zone. The flame length is (0.90 ± 0.05) m for flames A to C and (0.70 ± 0.05) m for flame D. In flames A to C the excess of primary air is always 15 %. The primary air excess of 112 % in flame D, decreases the flame length significantly. Apparently, the fuel jet to primary annular air velocity $U_{\text{jet}}/U_{\text{ann}}$ affects the flame length. A higher annular air velocity, with constant fuel jet velocity, will cause a stronger deformation of the reaction zone. This leads to an increase of the reaction zone area of the flame and, thus, to a shorter flame.

Figure 5.13: Instantaneous video images of piloted jet diffusion flames A to D and at lift-off, flame E, covering x = -35 to 400 mm and y = -95 to 95 mm.

The lift-off distance for flame E, the distance from the burner nozzle where stabilization occurs, is approximately (95 $\pm$ 5) mm. The overall flame length of flame E is approximately (1.0 $\pm$ 0.1) m.

OH flame width

De Vries (1994) has derived flame widths w_{OH}, defined as the radial distance between the two maximum average OH concentrations on either side of the flame axis. As a function of the axial distance, these OH flame widths are given in Figure 5.14. OH flame widths of flames A, B and C with a constant fuel jet to primary annular air velocity U_{jet}/U_{ann}, appear to increase with increasing jet velocity. Flame D, with a fuel jet velocity equal to that of flame C, but with a higher annular air velocity, has an overall narrower appearance than flame C. Thus, the most important factor determining the flame width is the difference between the jet exit and primary annular exit velocities. An increase of this velocity difference leads (in our range of Reynolds numbers $\sim 10^4$) to an increased entrainment of air into the fuel jet, resulting in a wider flame.

5.3.2 Velocity characteristics

Detailed experimental information on flame/flow interactions is important to understand the mixing mechanisms in flames. The three-flow system with turbulent primary annular air under investigation differs from widely used nonpremixed systems described in literature, such as jets issuing into still air or low-turbulence coflow. This turbulent primary air flow, in addition to the fuel jet velocity, have been used as parameters for variation of shear and mixing rates near the nozzle. The resulting velocity fields of the four piloted jet diffusion flames and the lifted flame have been investigated. Measurements in comparable configurations have been performed by Glass and Bilger

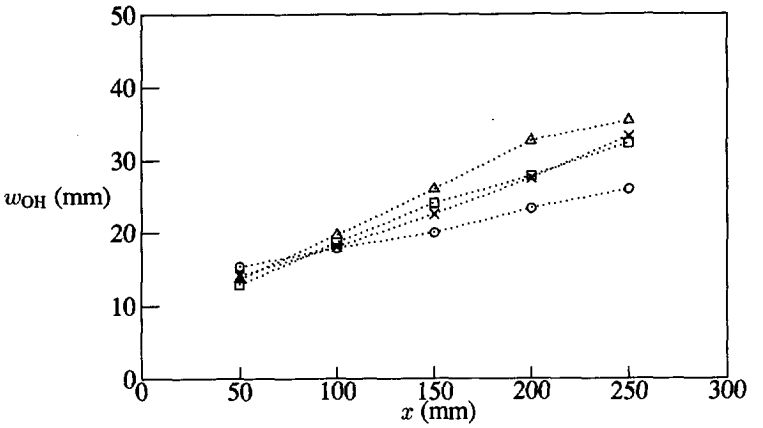

Figure 5.14: Average OH flame widths w_{OH}, determined by the radial distance between maximum average OH concentrations, of flames A ($\cdots\circ\cdots$), B ($\cdots\times\cdots$), C ($\cdots\triangle\cdots$) and D ($\cdots\square\cdots$) as a function of the axial distance x.

(1978) in hydrogen flames, in propane flames by Dibble *et al.* (1984, 1987) and by Sislian *et al.* (1988) in a methane flame. Direct comparison with their results is difficult due to the differences in flow conditions studied.

Axial distributions

In Figures 5.15 and 5.16, results of axial traverses along the centreline of the burner are shown, revealing the axial mean velocity, the fluctuating velocity components in both the axial and radial direction and the turbulence kinetic energy in flames A, B, C and D. Because of the limitations of the seeder capacity and of the vertical travel of the traversing gear, measurements were performed only up to 50 jet diameters ($x = 300$ mm) and the flame tip was never reached. In all flames, an increase of the axial mean velocity at the flame axis for the first diameters of the flow is found. This acceleration is caused by the influence of the high velocity pilot flames, contraction of the central fuel jet and (further downstream) by thermal expansion, due to the combustion reactions.

The radial velocity fluctuations v'_{rms} increase slowly with downstream position and attain an almost constant value at $x = 150$ mm ($x/D_{jet} = 25$). Comparison of the radial rms velocity profiles for flames A (low Reynolds number) to D (high Reynolds number) reveals that the magnitudes of the radial velocity fluctuations differ only slightly in these flames. The axial velocity fluctuations, however, increase with increasing Reynolds number, especially for flames C and D. At the centreline, the axial turbulence intensity $u'_{rms}/\overline{u}$ for $x = 300$ mm ($x/D_{jet} = 50$) attains a value of 0.12 in flames A, B and C and 0.14 in flame D. These values differ little from the axial turbulence intensity of 0.15 for this downstream position in nonreacting jet II. The con-

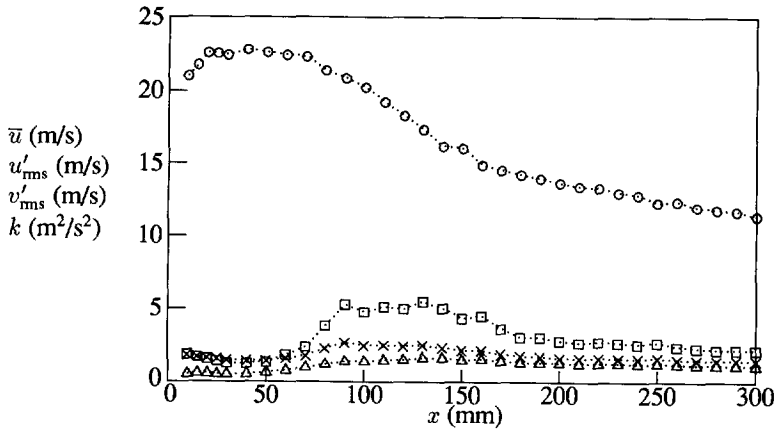

Figure 5.15: Centreline axial profiles in flame C of the axial mean velocity $\overline{u}$ ($\cdots$o$\cdots$), the axial rms velocity u'_{rms} ($\cdots\times\cdots$), the radial rms velocity v'_{rms} ($\cdots\triangle\cdots$) and the turbulence kinetic energy k ($\cdots\square\cdots$).

tribution of tangential velocity fluctuations to the turbulence kinetic energy is assumed to be equal to the radial velocity fluctuations. The region of maximum turbulence kinetic energy k extends roughly from x = 75 to 200 mm ($12.5 < x/D_{jet} < 33.3$) in all flames. With increasing annular air velocity, however, high centreline values of k tend to occur for more upstream positions. In addition to the shear layer between central fuel jet and primary annular air, a second shear layer between primary and secondary air flow plays an important role as discussed in Figure 2.3. Especially in flame D, with high primary annular air velocity, this second shear layer develops close to the burner, leading to high degrees of turbulent mixing for positions relatively close to the burner nozzle.

When the pilot flames are shut off and the primary annular air flow is reduced to zero, the flame lifts off from the burner nozzle, under circumstances described as flame E. The distance from the burner where stabilization occurs is approximately 95 mm. There was a slight oscillation at the stabilization height due to the passage of large eddies. When an axial traverse along the centreline of the burner is made, the axial mean velocity, axial and radial rms velocity and turbulence kinetic energy profiles as depicted in Figure 5.17 are found. The axial mean velocity decays gradually with axial position, comparable with a nonreacting jet. At the position of flame stabilization, little increase in the axial mean velocity was found as was expected because of thermal expansion effects (as in flames A to D). This indicates that at the flame base no combustion products are formed near the centreline (as will also be indicated in Section 5.3.4). The premixed flame concept proposed by Vanquickenborne and Van Tiggelen (1966) does, therefore, certainly not apply to the entire flame base. The axial and radial velocity

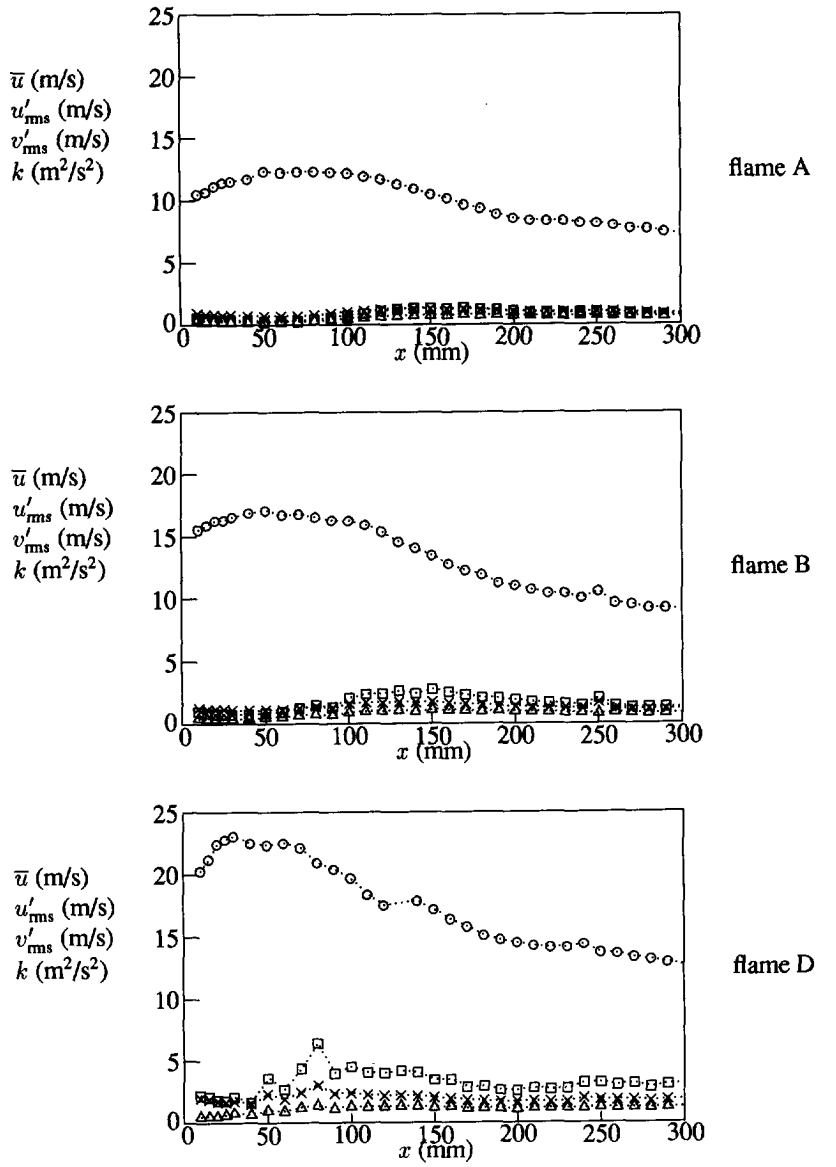

Figure 5.16: Centreline axial profiles in flames A (top), B (middle) and D (bottom) of the axial mean velocity $\overline{u}$ ($\cdots \circ \cdots$), the axial rms velocity u'_{rms} ($\cdots \times \cdots$), the radial rms velocity v'_{rms} ($\cdots \triangle \cdots$) and the turbulence kinetic energy k ($\cdots \square \cdots$).

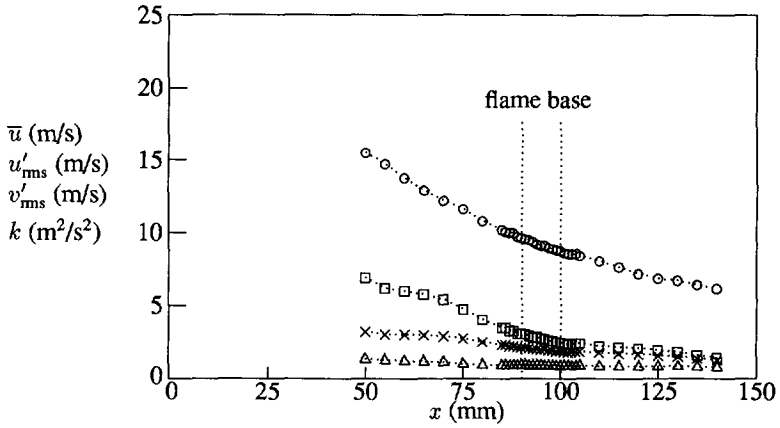

Figure 5.17: Centreline axial profiles in flame E of the axial mean velocity $\overline{u}$ ($\cdots\circ\cdots$), axial rms velocity u'_{rms} ($\cdots\times\cdots$), radial rms velocity v'_{rms} ($\cdots\triangle\cdots$) and turbulence kinetic energy k ($\cdots\square\cdots$).

fluctuations decay gradually with axial position, without an apparent decrease near the flame base. Suppression of turbulence, because of an increased viscosity, is therefore believed to play a negligible role.

Radial distributions of mean velocities

Additional information on the flow fields of flames A, B, C and D has been obtained by performing radial traverses at axial distances x = 50, 100, 150, 200 and 250 mm from the burner nozzle. The initial velocity profiles are very important for the development of the flow further downstream. Therefore, results from radial traverses at x = 3 mm are also given.

Axial mean velocity profiles in reference flame C (with high Reynolds numbers), are presented in Figure 5.18. These profiles show the spreading of the jet with downstream position. For x = 50 mm and x = 100 mm, the central jet flow is accelerated by thermal expansion, resulting in axial mean velocities higher than the initial velocities at x = 3 mm. The velocity profile of the central jet at x = 3 mm is uniform, indicating that this flow may not be regarded as a turbulent developed pipe flow, contrary to the annular air flow. This is attributed to the effect of the pilot flame insert, serving as a contraction for the central flow. For the traverse at x = 3 mm, a region with negative axial mean velocity is found, associated with a recirculation region that is formed behind the broad burner rim. The influence of this wake behind the burner rim is also felt for the traverse at x = 50 mm, featuring a region of low velocity between the central jet and the primary annular air flows. In this wake, jet fuel and primary annular air are mixed, resulting in a some premixed flame character immediately downstream of the

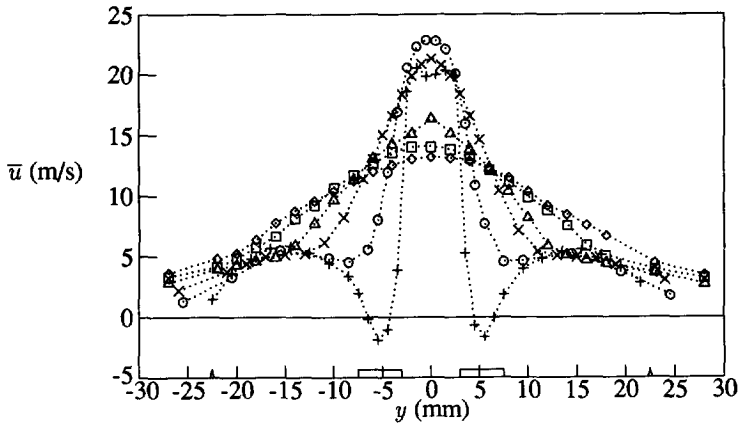

Figure 5.18: Axial mean velocity profiles in flame C for radial traverses at x = 3 ($\cdots + \cdots$), 50 ($\cdots \circ \cdots$), 100 ($\cdots \times \cdots$), 150 ($\cdots \triangle \cdots$), 200 ($\cdots \square \cdots$) and 250 mm ($\cdots \diamond \cdots$).

burner rim. Consequently, the pilot flames are not the only means to stabilize the flame at the burner nozzle; the premixed flame character of the recirculation zone near the burner rim will also have a stabilizing effect.

Radial profiles of the radial mean velocity in flame C are given in Figure 5.19. As required by symmetry, the radial mean velocity is zero at the centreline in all traverses and increases to maxima in the mixing region. Positive radial mean velocities are associated with movement towards positive values of the radial position y. Likewise, negative values correspond to particles moving towards negative values of y. The radial mean velocity profile at x = 3 mm indicates minor movement of the flow towards the centreline for radial positions up to $y = \pm$ 2.5 mm. Immediately next to this low radial mean velocity zone, a region with higher radial mean velocity is present, associated with the presence of the pilot flames and the recirculation zone behind the burner rim. Radial movement in this region is always in the direction towards the centreline, indicating that the composition of the premixed flame near the burner nozzle is mainly determined by the primary annular air flow. The pilot flames, with their high exit velocity, are believed to prevent the fuel jet from leaking into the recirculation zone. The premixed flame will therefore be fuel lean. Thus, the stabilizing effect of this premixed flame character will only be minor. This explains why the flames under investigation could not burn stably without operation of the pilot flames. Downstream profiles of the radial mean velocity reveal that only a small component of the velocity (maxima of $\pm$ 1 m/s at x = 50 mm) is directed outwards.

Radial profiles of the axial mean velocity in flame A, with low Reynolds numbers for both the gas jet and the primary annular air, are given in the top part of Figure 5.20.

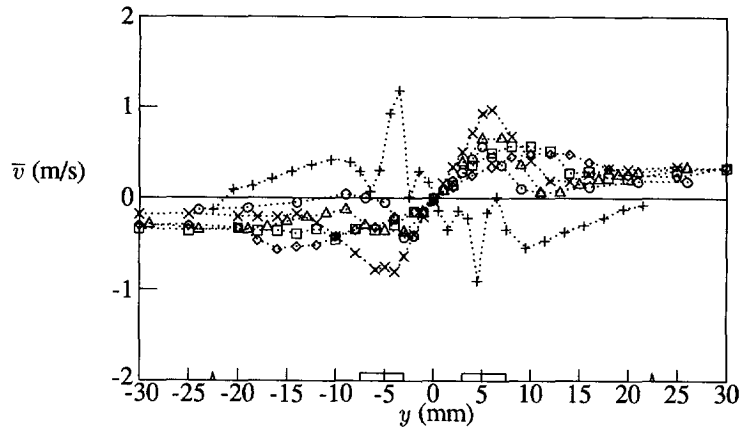

Figure 5.19: Radial mean velocity profiles in flame C for radial traverses at x = 3 ($\cdots + \cdots$), 50 ($\cdots \circ \cdots$), 100 ($\cdots \times \cdots$), 150 ($\cdots \triangle \cdots$), 200 ($\cdots \square \cdots$) and 250 mm ($\cdots \diamond \cdots$).

Due to the relatively low velocities in flame A, the spreading of the flame is small in downstream direction and the influence of the burner rim is only minor. In the middle picture of Figure 5.20, axial mean velocities in flame B with modest Reynolds numbers are given. In flame B, increased flow velocities, compared to flame A, have led to a larger spreading rate with downstream position and a more pronounced presence and influence of the recirculation zone behind the burner rim. For flames A, B and C, the decay rate of axial mean velocity increases with downstream position at the centreline. This decay rate is probably best illustrated comparing the axial mean velocity at the centreline for the traverse at x = 3 mm with the profiles at other axial positions. For flame A, with low Reynolds numbers, the centreline axial mean velocity at x = 3 mm equals the centreline axial mean velocity measured at x = 200 mm (x/D_{jet} = 33.3). For flames B (modest Reynolds numbers) and C (high Reynolds numbers), axial mean velocities equal to the velocity measured at x = 3 mm, occur at x = 150 mm (x/D_{jet} = 25)and x = 100 mm (x/D_{jet} = 16.7), respectively. Not only the fuel flow rate is increased from flames A to C, but the primary annular air flow is increased as well. The velocity difference between central fuel and primary air flow is larger in flame C than in flame B, and larger in flame B than in flame A. In our range of Reynolds numbers, for larger velocity differences the shear layer that is created is stronger, causing a larger spreading rate of the central jet and resulting in a larger centreline axial mean velocity decay.

The axial mean velocity profiles of flame D are given in the bottom part of Figure 5.20. Comparing flames C and D, the gas flow rate is kept constant, but the primary air flow rate is increased to an excess of 112 %, resulting in a primary air velocity of 7.9 m/s. At a position between x = 50 and 100 mm ($8.3 < x/D_{\text{jet}} < 16.7$)

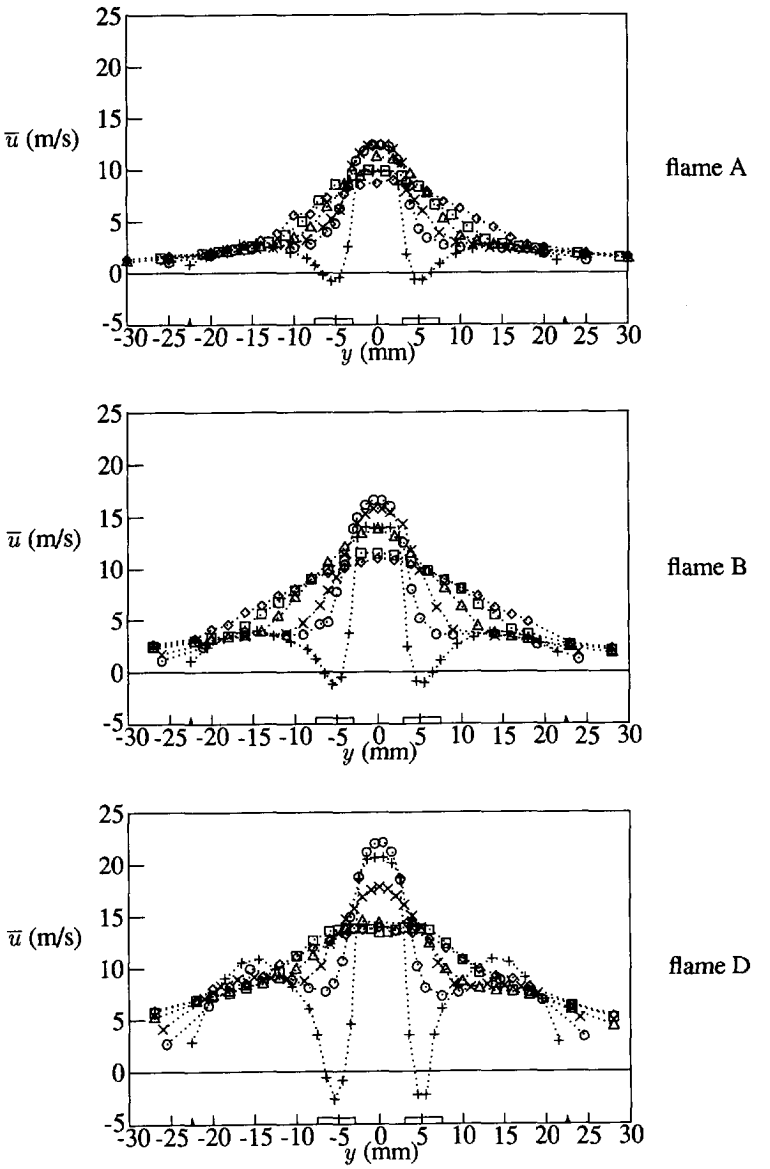

Figure 5.20: Axial mean velocity profiles in flames A (top), B (middle) and D (bottom) for radial traverses at x = 3 ($\cdots + \cdots$), 50 ($\cdots \circ \cdots$), 100 ($\cdots \times \cdots$), 150 ($\cdots \triangle \cdots$), 200 ($\cdots \square \cdots$) and 250 mm ($\cdots \diamond \cdots$).

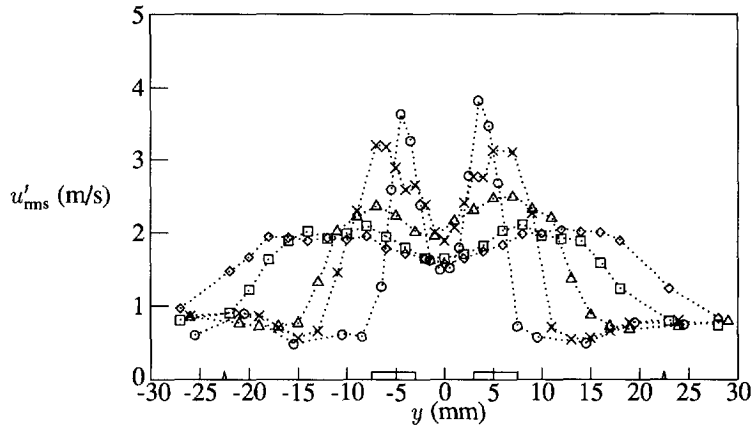

Figure 5.21: Axial rms velocity profiles in flame C for radial traverses at x = 50 ($\cdots$ o $\cdots$), 100 ($\cdots \times \cdots$), 150 ($\cdots \triangle \cdots$), 200 ($\cdots \square \cdots$) and 250 mm ($\cdots \diamond \cdots$).

at the centreline, the axial mean velocity in flame D, equals the axial mean velocity at x = 3 mm. The centreline decay rate of axial mean velocity is therefore larger in flame D than in flame C. The shear layer between central fuel and primary air flow is weaker in flame D than in flame C (because of the smaller velocity difference between these flows). Formation of a strong second shear layer (between primary and secondary air flows) in flame D, however, causes the axial mean velocity to decay rapidly with downstream position.

Radial distributions of turbulence properties

As in jet II, the maxima of the axial rms velocities in high Reynolds number flame C, shown in Figure 5.21, occur at radial positions where the mean axial velocity gradient is largest. This is also illustrated by the interpolated greyscale distributions of the measured axial mean velocities and axial rms velocities in Figure 5.22. At the centreline for $x \leq 150$ mm ($x/D_{jet} \leq 25$) of flame C, significantly lower values of the axial velocity fluctuations appear than the maximum values. In isothermal jet II, the shear layer between primary annular air and central jet penetrates into the jet axis, generating turbulence. In the flame, however, this penetration is delayed, due to flow acceleration in the reaction zone. As a result, a small radial gradient of the axial mean velocity (and therefore small spreading rate of the shear layer) exists in the flame when compared to the nonreacting jet. In addition, the reaction zone of the flame will serve as a region of high viscosity, thereby shielding the central jet from its surroundings. This leads to a decrease in the amount of air entrained into the central jet, when compared with its nonreacting equivalent. In fact, the potential core region in the flame extends further downstream than in the nonreacting flow.

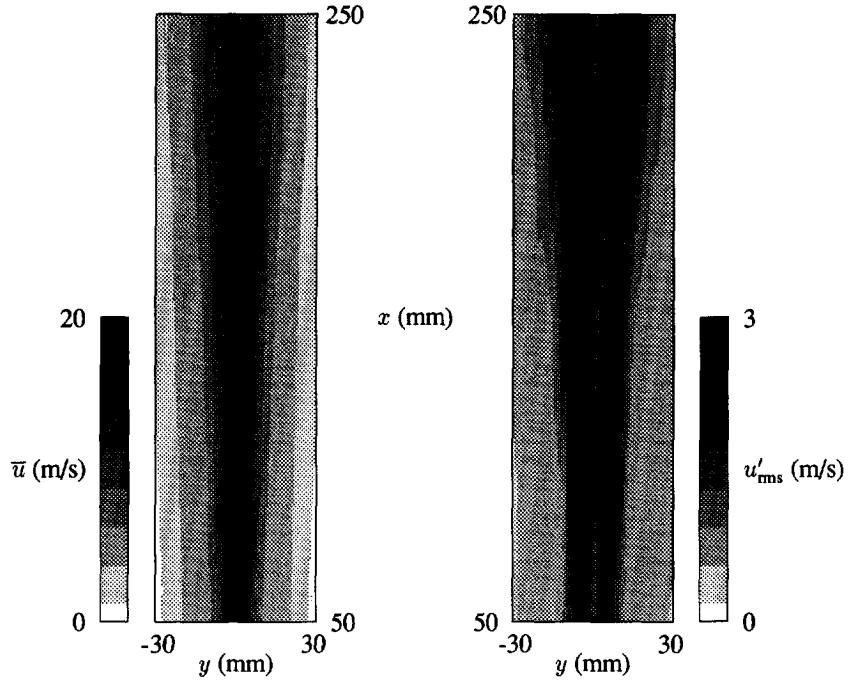

Figure 5.22: Interpolated representation of the axial mean velocity (left) and the axial rms velocity (right) in flame C.

When the axial velocity fluctuations are normalized with the local axial mean velocity, it appears that the increase in velocity fluctuations in the flame is smaller than the increase in axial mean velocity (due to thermal expansion). Profiles of this axial turbulence intensity $u'_{rms}/\overline{u}$ as a function of the radial position for various axial distances from the burner in flame C are given in Figure 5.23. These profiles peak near the maximum mean axial velocity gradient, caused by intermittent mixing of air and fuel, and in the outer regions of the flow, where the axial mean velocity approaches zero.

Radial profiles of the radial velocity fluctuations in flame C are depicted in Figure 5.24. Contrary to axial velocity fluctuations, radial velocity fluctuations increase with increasing axial distance up to x = 150 mm (x/D_{jet} = 25). This is consistent with the observations of Wygnanski and Fiedler (1969) in a self-preserving jet. They found that radial velocity fluctuations tend to equilibrate more slowly than axial velocity fluctuations. These results were explained in terms of a stepwise turbulence energy transfer mechanism in which momentum is transferred directly from the mean flow motion to the axial velocity fluctuations. Subsequent energy transfer to the radial

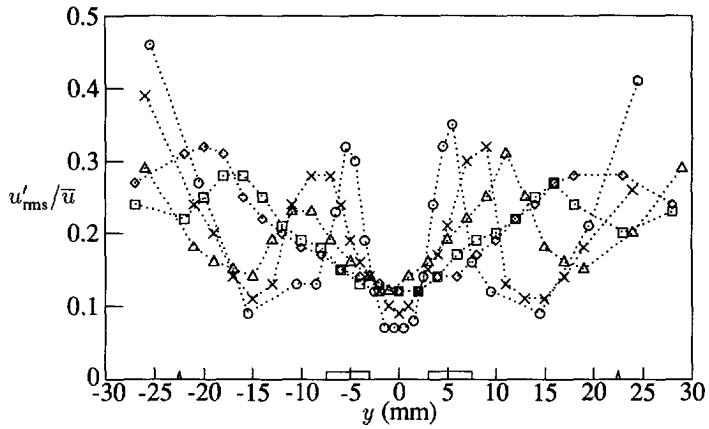

Figure 5.23: Axial turbulence intensity profiles in flame C for radial traverses at x = 50 ($\cdots$ o $\cdots$), 100 ($\cdots$ × $\cdots$), 150 ($\cdots$ △ $\cdots$), 200 ($\cdots$ □ $\cdots$) and 250 mm ($\cdots$ ◇ $\cdots$).

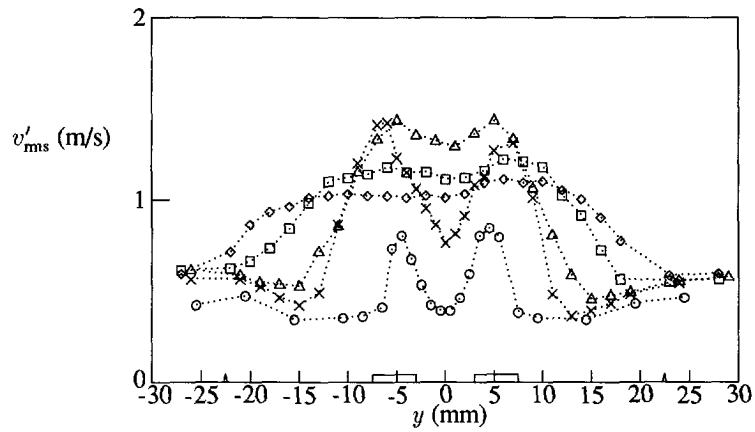

Figure 5.24: Radial rms velocity profiles in flame C for radial traverses at x = 50 ($\cdots$ o $\cdots$), 100 ($\cdots$ × $\cdots$), 150 ($\cdots$ △ $\cdots$), 200 ($\cdots$ □ $\cdots$) and 250 mm ($\cdots$ ◇ $\cdots$).

velocity component occurs through the interaction between pressure and local velocity gradients, which redistributes the energy among the various velocity components only after a balance is reached between the mean and the fluctuating axial velocity. The ratio u'_{rms}/v'_{rms}, depicted in Figure 5.25, attains values mainly between 1.3 and 5, indicating large anisotropy of the turbulence in flame C.

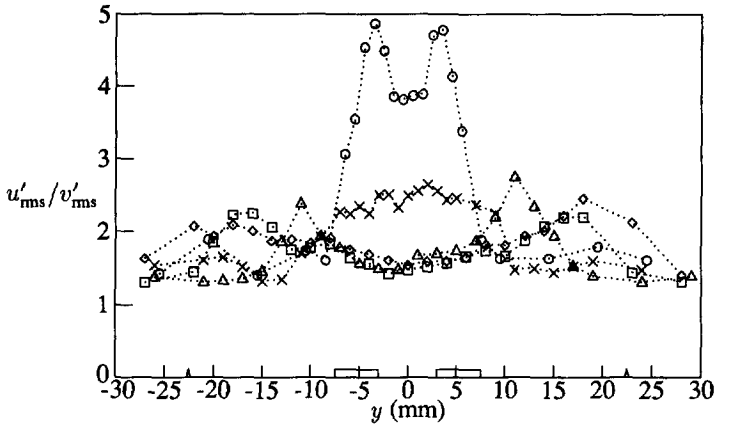

Figure 5.25: Profiles of the ratio u'_{rms}/v'_{rms} in flame C for radial traverses at x = 50 ($\cdots\circ\cdots$), 100 ($\cdots\times\cdots$), 150 ($\cdots\triangle\cdots$), 200 ($\cdots\square\cdots$) and 250 mm ($\cdots\diamond\cdots$).

The turbulence kinetic energy is a measure of the maximum turbulent mixing intensity in the flame. As before, because the tangential velocity component could not be measured with the present LDA setup, an approximation for the turbulence kinetic energy is made. In our axisymmetric configuration, the tangential velocity fluctuations w'_{rms} are assumed to be equal to the radial velocity fluctuations v'_{rms}. Profiles of the turbulence kinetic energy distribution in flame C are presented in Figure 5.26. Production of turbulence energy is primarily due to the mean axial velocity gradient in the radial direction, which is highest near the jet exit and results in a rapid increase in the axial velocity fluctuations (also evidenced in Figure 5.21). Further downstream, the mean velocity gradient decreases, and turbulence energy production is balanced by losses due to viscous dissipation and redistribution of turbulence energy to radial and tangential velocity components. This redistribution occurs through the interaction between pressure and local velocity gradient terms in the turbulence energy transport equation. Thus, the turbulence intensity decreases with axial distance at the centreline and approaches a constant asymptotic downstream value of 0.12 at x = 300 mm (x/D_{jet} = 50) determined by the balance between these production and loss terms. Glass and Bilger (1978) found a flame turbulence intensity of 0.35 at x/D_{jet} = 200. Dibble *et al.* (1984) found a value of 0.34 in a hydrogen jet. In both cases, the difference between fuel jet velocity and coflowing air velocity is much larger than in our investigation. Due to large velocity gradients, entrainment of air into the jet will play a more important role in their flames, leading to larger turbulence intensity than in our investigation.

The correlation between the fluctuating components of radial and axial velocities is directly related to the turbulence transport of momentum. As shown in Figure 5.27, the Reynolds shear stress in flame C is zero on the jet axis and has a peak near the

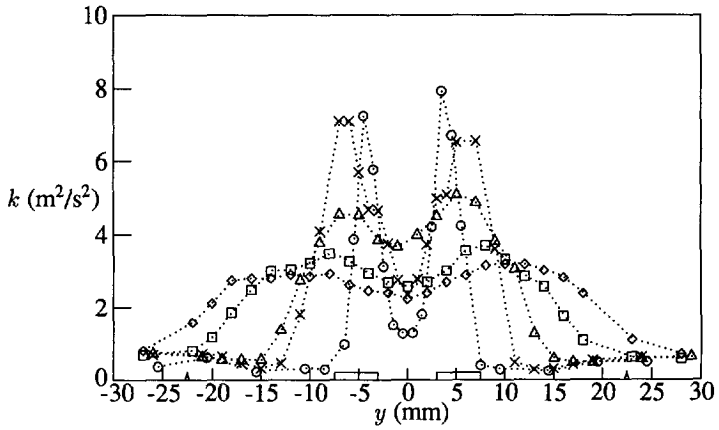

Figure 5.26: Turbulence kinetic energy profiles in flame C for radial traverses at x = 50 ($\cdots\circ\cdots$), 100 ($\cdots\times\cdots$), 150 ($\cdots\triangle\cdots$), 200 ($\cdots\square\cdots$) and 250 mm ($\cdots\diamond\cdots$).

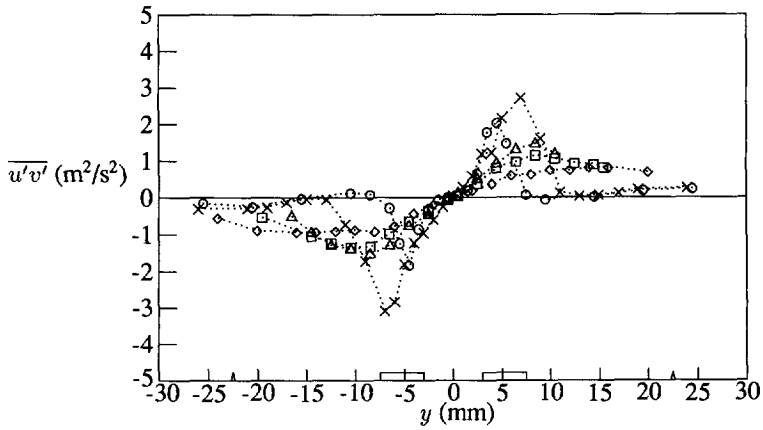

Figure 5.27: Reynolds shear stress profiles in flame C for radial traverses at x = 50 ($\cdots\circ\cdots$), 100 ($\cdots\times\cdots$), 150 ($\cdots\triangle\cdots$), 200 ($\cdots\square\cdots$) and 250 mm ($\cdots\diamond\cdots$).

positions of maximum radial gradients of the corresponding axial mean velocities. In general, the Reynolds shear stresses are appreciably smaller than the corresponding values of the normal stresses.

Radial profiles of the axial rms velocity for various axial positions in flames A, B and D are given in Figure 5.28. With increasing exit velocities and Reynolds numbers

Table 5.1: Initial axial turbulence intensities in flames A to D at $x = 3$ mm in the centre of the fuel jet ($y = 0$ mm) and the centre of the primary annular air flow ($y = \pm 15$ mm).

y (mm)	A	B	C	D
0	0.13	0.10	0.10	0.10
$\pm$ 15	0.16	0.12	0.10	0.07

Table 5.2: Centreline axial turbulence intensities in flames A to D for axial positions $x = 50$, 100, 150, 200 and 250 mm.

x (mm)	A	B	C	D
50	0.08	0.06	0.07	0.08
100	0.05	0.07	0.09	0.13
150	0.14	0.14	0.13	0.13
200	0.15	0.14	0.12	0.15
250	0.14	0.15	0.12	0.15

of the central fuel jet and primary annular air flow, the maxima of the axial rms velocity increase. Next to the effect of the velocity difference between fuel jet and primary air, causing turbulence, the second shear layer between primary and secondary air will influence the flow fields. A higher annular air velocity causes a stronger second shear layer, resulting in a movement of the maximum of the turbulence kinetic energy closer to the burner exit, as indicated in Figures 5.15 and 5.16.

Because of the increasing mean velocities in flames A to D, a comparison between absolute values of u'_{rms} may lead to wrong conclusions about the turbulence level in these flames. A more accurate description can be obtained, normalizing the velocity fluctuations with the local mean velocity. The initial values of this axial turbulence intensity in flames A to D, obtained from the traverses at $x = 3$ mm, for the central part of the fuel jet ($y = 0$ mm) and the central part of the primary annular air flow ($y = \pm 15$ mm) are given in Table 5.1. In all flames, the initial turbulence intensity in both the (not yet reacted) gas jet and the annular air flow is larger than 0.05, a value generally accepted for turbulent developed pipe flows. This shows that even for low Reynolds number flame A the initial jet and annular flows are highly turbulent.

Axial turbulence intensities in flames A to D for positions at the centreline of the flame and their maximum values are presented in Tables 5.2 and 5.3, respectively. For flames A to C, the axial turbulence intensity at the centreline for axial positions $x = 50$ mm and $x = 100$ mm is smaller than their corresponding values at $x = 3$ mm. In these values, the influence of suppressed turbulence caused by changes in velocity gradient near the reaction zone is reflected. Downstream of $x = 100$ mm, combustion reactions have caused increasing turbulence intensities at the centreline in all flames.

Maximum values of the axial turbulence intensity in Table 5.3 increase with downstream position in flames A and B, and are almost constant or even decreasing

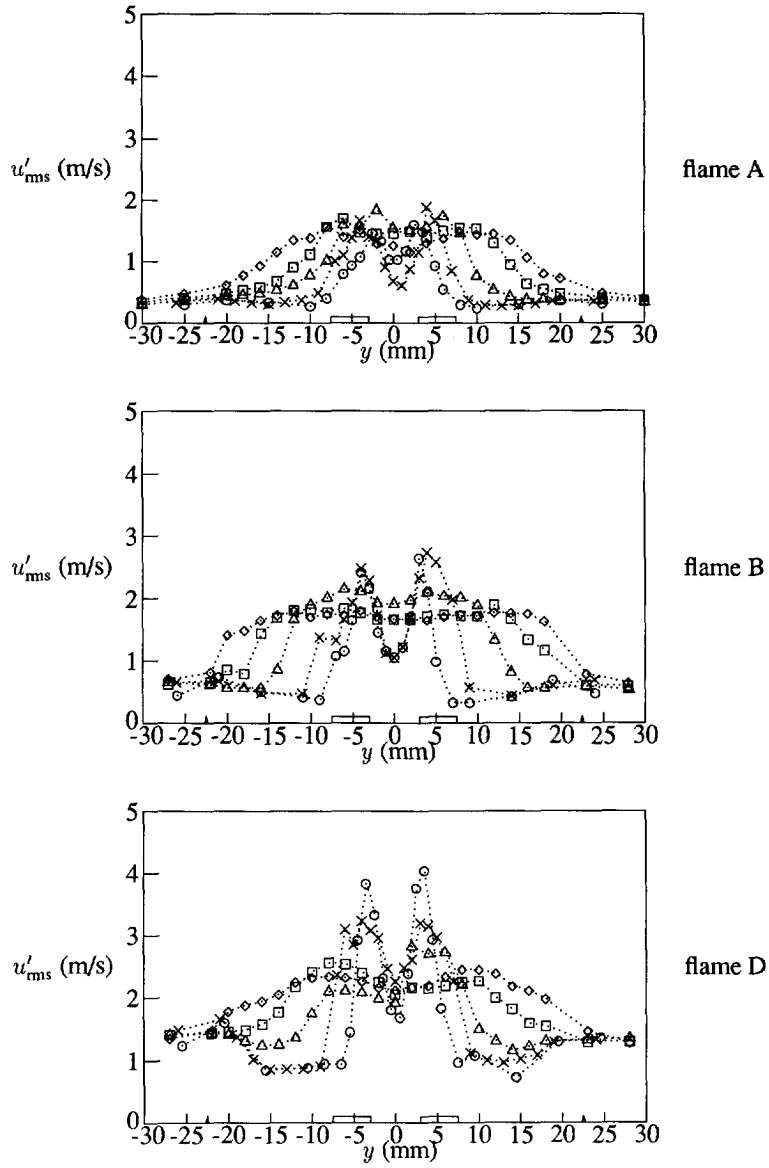

Figure 5.28: Axial rms velocity profiles in flames A (top), B (middle) and D (bottom) for radial traverses at $x = 50$ ($\cdots\circ\cdots$), 100 ($\cdots\times\cdots$), 150 ($\cdots\triangle\cdots$), 200 ($\cdots\square\cdots$) and 250 mm ($\cdots\diamond\cdots$).

Table 5.3: Maximum values of the axial turbulence intensity in flames A to D for axial positions x = 50, 100, 150, 200 and 250 mm.

x (mm)	A	B	C	D
50	0.20	0.20	0.34	0.29
100	0.27	0.26	0.30	0.23
150	0.26	0.28	0.27	0.21
200	0.31	0.33	0.28	0.22
250	0.33	0.33	0.32	0.23

in flames C and D. This behaviour can be explained by the presence of the shear layers in our three-flow system, which generate turbulence. Especially the second shear layer between primary and secondary air is believed to contribute to the differences in turbulence intensities in flames A to D. Because the primary annular air velocity is relatively small in flames A and B, the second shear layer (and thus maximum turbulence intensity) develops slowly with downstream position. In flames C and D, however, the large primary annular air flow generates a strong second shear layer, which is reflected in the large values of the maximum turbulence intensity for x = 50 mm already. The development of the second shear layer and its influence on the maximum turbulence intensity in the flames is further revealed when the largest values of the maximum turbulence intensity are examined. The maximum value of $u'_{\mathrm{rms}}/\overline{u}$ in flame A (for the range of the experiments) is 0.33, occurring at x = 250 mm. In flame B, a somewhat larger primary annular air velocity than in flame A generates a stronger second shear layer, causing the value of $u'_{\mathrm{rms}}/\overline{u}$ = 0.33 to occur at x = 200 mm. In flame C, the primary annular air velocity is larger than in flame B and a turbulence intensity of 0.33 is obtained in the region between x = 50 mm and x = 100 mm. Increasing the primary annular air flow even further, as in flame D, the strong second shear layer has caused the maximum of the turbulence intensity to occur near x = 50 mm.

Effect of velocity bias correction

For the piloted jet diffusion flame configuration, as for the disk-stabilized premixed flame described in Chapter 4, velocity bias may lead to an overestimation of the true flow velocity, which should be corrected for. As discussed in Section 4.3.2, velocity bias correction by means of the residence time weighing technique provided reliable results in the disk-stabilized premixed flame. Applying this technique to piloted jet diffusion flame C leads to the results presented in Figure 5.29. In this figure, results of a radial traverse at x = 50 mm for the axial mean velocity (top), axial rms velocity (middle) and Reynolds shear stress (bottom) are given, comparing arithmetically averaged and residence time weighed velocities.

From the small differences between both averaging methods, the important conclusion may be drawn that even for the radial traverse with the highest velocity gradients, velocity bias does not influence the measured velocities significantly. Apparently, by

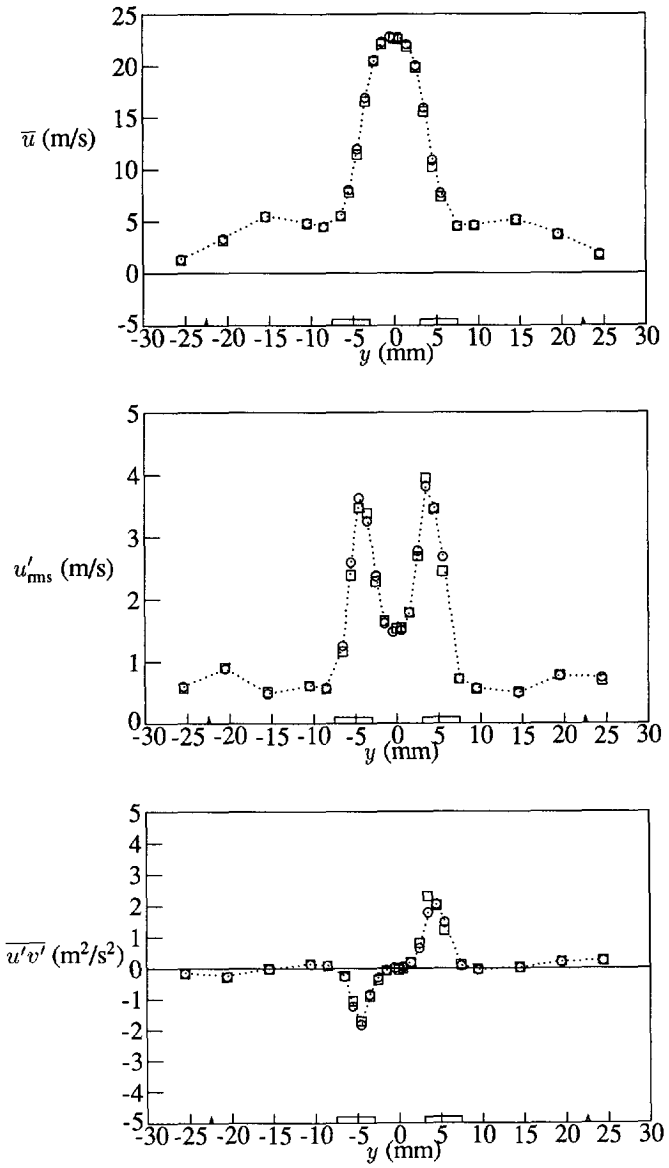

Figure 5.29: Axial mean velocity (top), axial rms velocity (middle) and Reynolds shear stress (bottom) profiles in flame C for a radial traverse at $x = 50$ mm with arithmetical averaging ($\cdots \circ \cdots$) and weighed with the residence time ($\square$).

seeding both the fuel jet and the primary annular air flow with equal seeding particle concentrations, the effect of non-representative sampling of particles originating from the high speed central jet and low-speed primary annular air flow is diminished.

Probability density functions

Some typical probability density functions of axial and radial velocities in flame C at x = 50 mm are shown in Figure 5.30 for various radii in the flame. The radial positions are selected to represent data at the centreline of the flame (y = 0 mm), two positions near the maximum gradient of axial velocity (y = 4 mm and y = 6 mm) and in the primary annular air flow (y = 10 mm). Joint probability density functions (top part of Figure 5.30) of the axial versus the radial velocity are represented by contour lines, connecting points of equal probability $P(u, v)$. Contour lines at $P(u, v)$ = 0.05, 0.1, 0.2 and 0.4 are drawn. Single probability density functions of the axial velocity (middle picture of Figure 5.30) are Gaussian-like with some skewness apparent in regions near the centreline and near the mixing layer between the fuel and the primary air. The intermittent mixing of the streams of reactants causes multimodal histograms in the region of the highest axial velocity gradient. The peaks of the higher and lower velocities correspond to those of the flamelets, primary air and air previously mixed with jet fluid, as will be discussed in Section 5.3.3 . Multimodalities of axial velocity PDFs are encountered in flame C for the traverses at x = 50 mm and x = 100 mm only. Further downstream, fuel and air are well-mixed and the influence of large-scale vortices near the flame front is not visible anymore. The PDFs of the radial velocity (bottom picture of Figure 5.30) have a Gaussian appearance and do not reveal any multimodality. Some skewness towards positive radial velocities (outward movement) for position y = 6 mm is found, however.

Also for flames A (low Reynolds numbers), B (modest Reynolds numbers) and D (high Reynolds numbers) for traverses at x = 50 mm and x = 100 mm, bimodal or trimodal axial velocity PDFs are found near the average position of the flame front. From x = 150 mm and further downstream, the axial velocity PDFs are broad and the contributions of primary annular air, pure jet fluid and flamelets can not be distinguished. Probability density functions of the radial velocity are nearly Gaussian for all positions investigated.

Axial velocity PDFs in flame E, operated at lift-off, for the axial traverse along the centreline of the burner are Gaussian below the stabilization point and reveal bimodalities downstream of the flame base. This is not unexpected, since below the stabilization height, the flow resembles an undisturbed nonreacting jet, and the PDFs will be as in the nonreacting flow. At the flame base, however, pockets of burnt gas are formed that will have an increased velocity because of the thermal expansion effect. Contributions of both cold reactants and burnt products, governed by large-scale vortices, will lead to bimodal PDF shapes. These large-scale vortices are also the reason why the flame base is fluctuating in height.

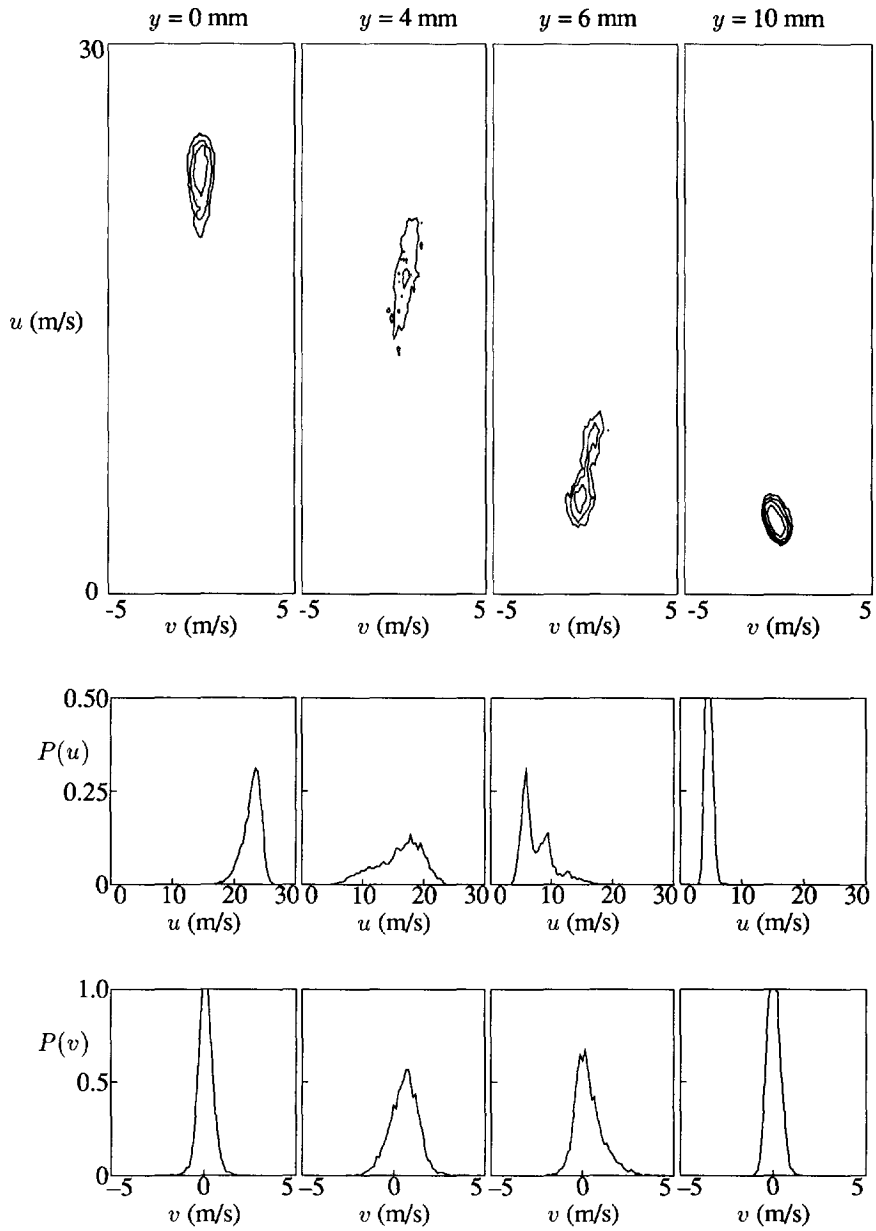

Figure 5.30: Joint probability density functions (top) and single probability density functions of axial (middle) and radial (bottom) velocities in flame C at $x = 50$ mm for $y = 0, 4, 6$ and 10 mm.

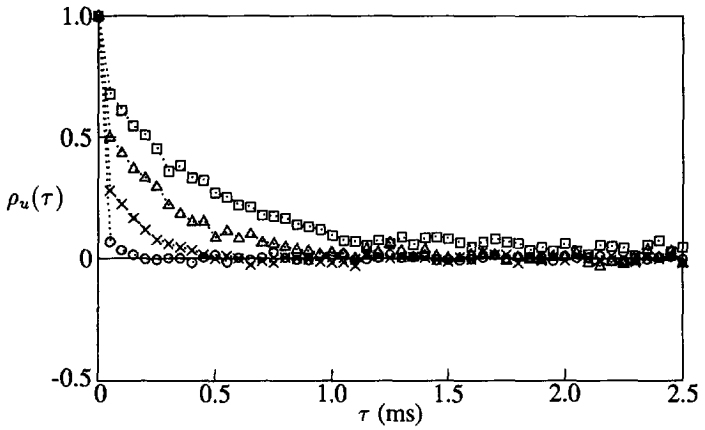

Figure 5.31: Autocorrelation functions of axial velocity fluctuations in flame C for positions at the centreline of the burner at x = 50 ($\cdots$ o $\cdots$), 100 ($\cdots \times \cdots$), 150 ($\cdots \triangle \cdots$) and 200 mm ($\cdots \square \cdots$).

Temporal analysis

The temporal evolution of axial velocity fluctuations is revealed by determining autocorrelation functions. Autocorrelation functions in flames A to E for different positions at the flame axis are given in Figures 5.31 to 5.33. Only the first 2.5 ms of the autocorrelation functions are presented to reveal the differing decay rates with downstream position. Typical data rates in the flames under investigation are in the range from 4000 to 5000 Hz. When slot widths of the autocorrelation functions are selected determined by the inverse of these data rates, resulting in slot widths of approximately 300 μs, resolution in the first slots is very poor. Therefore, a smaller slot width of 50 μs is selected for all flames for high resolution. None of the observed correlation functions reveals evidence of any periodicity. This is confirmed by the calculated power spectra, which lack dominant frequencies.

The temporal correlation between axial velocity fluctuations increases with downstream position, indicating the growing of time scales of turbulent eddies. Characteristic scales of the turbulence in all flames, based on these autocorrelation functions, will be derived in Section 5.4.1. As a consequence of the little amount of data taken immediately after $\rho_u(0)$, a parabolic fit to obtain Taylor micro time scales is not possible with sufficient accuracy. Therefore, these scales were not derived.

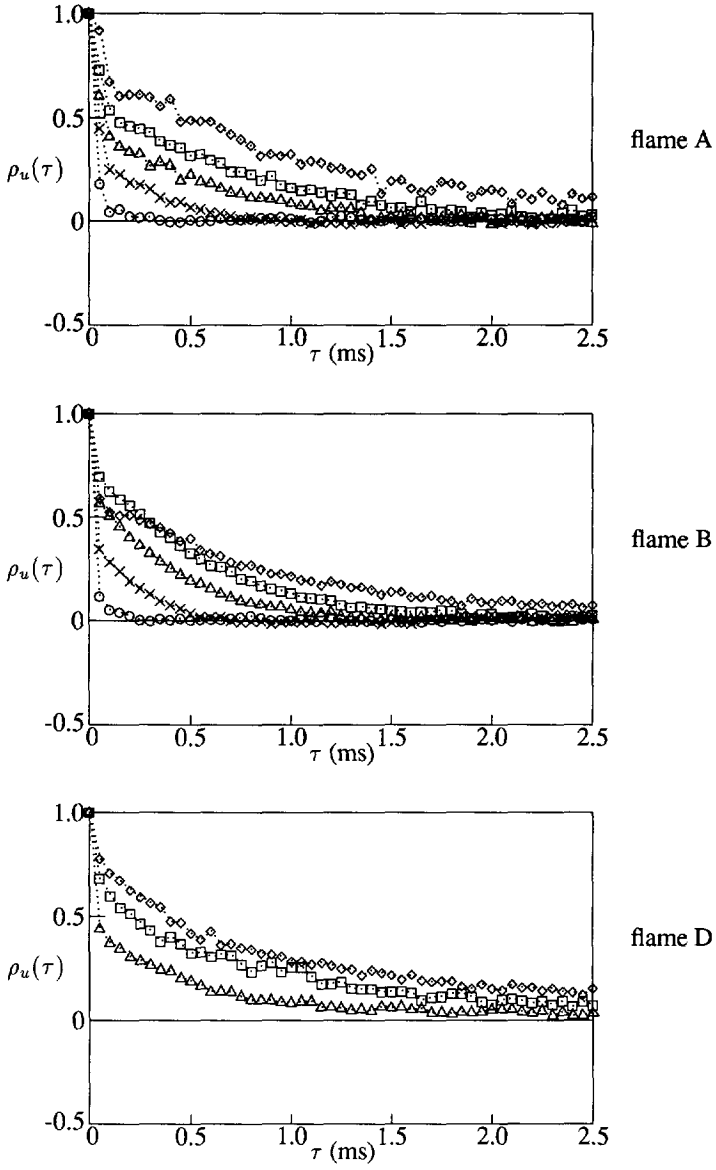

Figure 5.32: Autocorrelation functions of axial velocity fluctuations in flames A (top), B (middle) and D (bottom) for positions at the centreline of the burner at x = 50 ($\cdots\circ\cdots$), 100 ($\cdots\times\cdots$), 150 ($\cdots\triangle\cdots$), 200 ($\cdots\square\cdots$) and 250 mm ($\cdots\diamond\cdots$).

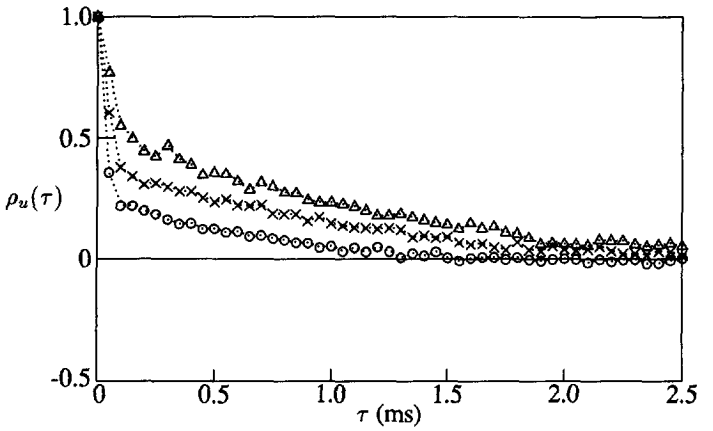

Figure 5.33: Autocorrelation functions of axial velocity fluctuations in flame E for positions at the centreline of the burner at $x = 75$ ($\cdots\circ\cdots$), 100 ($\cdots\times\cdots$) and 125 mm ($\cdots\triangle\cdots$).

5.3.3 Mixing behaviour

Measurements of Labacci *et al.* (1988), Schefer *et al.* (1985, 1987) and Takahashi *et al.* (1990) in diffusion flames indicated that a seeding technique for LDA measurements conditional on the jet fluid and the primary air provides a useful marker for fluid originating from the jet and the coflowing air. Conditional seeding is referred to as adding particles to the central fuel jet flow only and to the primary annular air flow only, respectively. This technique has been applied to our high Reynolds number reference flame C. The resulting conditional velocity statistics provide considerable information on details of the mixing process between fuel and primary air. The maximum differences in conditional statistics can be found in regions of high shear separating the initially unmixed inlet flows. Regions where little difference exists between conditional measurements show that fluid originating from the fuel jet and primary annular air are well-mixed at small turbulence scales. In contrast, the relatively large differences between conditional measurements near the shear layers indicate the intermittent passage of large-scale turbulence structures. This intermittency results in the situation where the fixed measurement volume alternately contains large-scale structures from different flow regions and accounts for the characteristics of the velocity PDFs.

Mean velocities with conditional seeding

Results of the axial mean velocity with conditional seeding of the fuel jet and the primary annular air flow for a radial traverse at $x = 50$ mm are given in Figure 5.34. The conditioned data provide evidence of the fact that for small axial distances from the

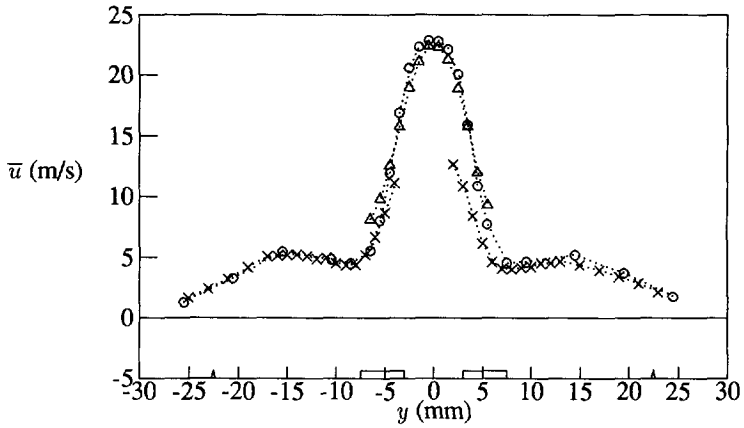

Figure 5.34: Axial mean velocity profiles in flame C for a radial traverse at $x = 50$ mm with equal seeding density for the jet flow and the primary annular flow ($\cdots\circ\cdots$), with conditional seeding of the jet flow ($\cdots\triangle\cdots$) and conditional seeding of the primary annular air flow ($\cdots\times\cdots$).

burner, on average, fluid elements from the jet move faster than those from the primary coflow. For comparison also measurements with equal seeding density of the jet and the annular flow are given. The differences are largest in the mixing region between fuel and primary air. In this region, insufficient time is available for the velocity associated with fluid originating from the annulus to equilibrate fully with the jet fluid. In the mixing zone between fuel and air, differences between jet seeded and annulus seeded axial mean velocity decrease further downstream ($x/D_{\text{jet}} > 25$) because of the high rates of turbulence energy transport relative to the rates of change in the mean flow distribution. This indicates that the jet fluid becomes well mixed with the primary annular air entrained into the jet stream.

The profiles of radial mean velocity, depicted in Figure 5.35, reveal that the fluid elements from the jet are flowing outward (on average) and those from the primary air have zero or even inward velocity. This suggests the existence of large-scale vortical motions, which appears to be consistent with the physical picture of large-scale turbulence structure in the shear layer (Dahm and Dibble (1988)).

Turbulence properties with conditional seeding

In the top part of Figure 5.36, measurements of the axial rms velocity with conditional seeding on the jet and the annulus are presented. For comparison, also the results for equal seeding density of the jet and primary annular flow are given. The profiles of the jet seeded flow and the annular air seeded measurements differ slightly. Each of them reach maxima where the mean axial velocity gradient is largest. Radial velocity

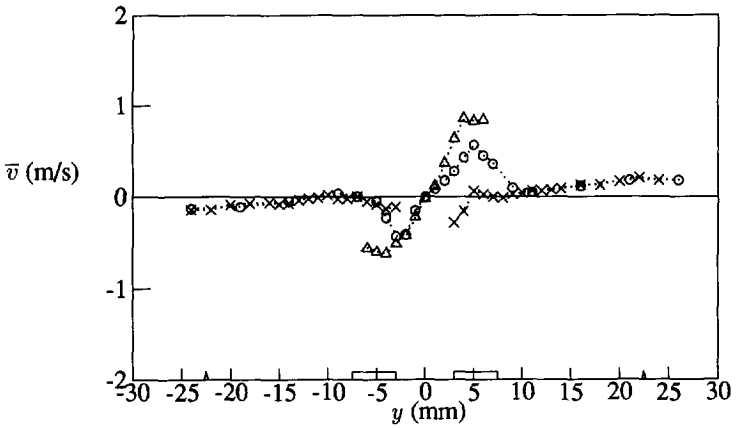

Figure 5.35: Radial mean velocity profiles in flame C for a radial traverse at $x = 50$ mm with equal seeding density for the jet flow and the primary annular flow ($\cdots$ o $\cdots$), with conditional seeding of the jet flow ($\cdots \triangle \cdots$) and with conditional seeding of the primary annular flow ($\cdots \times \cdots$).

fluctuation profiles are depicted in the middle of Figure 5.36. In the mixing zone, profiles of fluctuating velocities obtained with equal seeding density of the jet and the annular flow reveal lower values than for the conditional measurements. Contrary to measurements with equal seeding density, seeding bias will have significant influence on the conditional measurements. Due to this effect, measured rms velocities with conditional seeding can be increased significantly.

Both the Reynolds shear stress profiles conditional on the jet and the air reach a maximum in the mixing region between the fuel jet and the primary coflowing air, as shown in Figure 5.36. The values conditional on the jet are larger than on the primary air for $y > 4$ mm, which emphasizes the role of highly turbulent jet fluid.

Probability density functions with conditional seeding

Statistics, conditional on fluid originating from the primary annular air, consist of contributions from unmixed air, as well as air previously entrained and subsequently mixed with jet fluid. Similarly, statistics conditional on fluid originating from the jet consist of contributions from the unmixed jet fluid and jet fluid that has been mixed with entrained air. The measured differences in conditional quantities thus reflect the extent to which fluid originating from the two inlet streams has mixed at a small-scale level and can be attributed to the presence of larger-scale structures in the flow field.

In Figure 5.37, the axial velocity PDFs conditional on the jet $P(u)_{\text{jet}}$ are in general characterized by a unimodal distribution, which shifts to a higher average velocity as the centreline is approached. In the outer mixing region, PDFs conditional

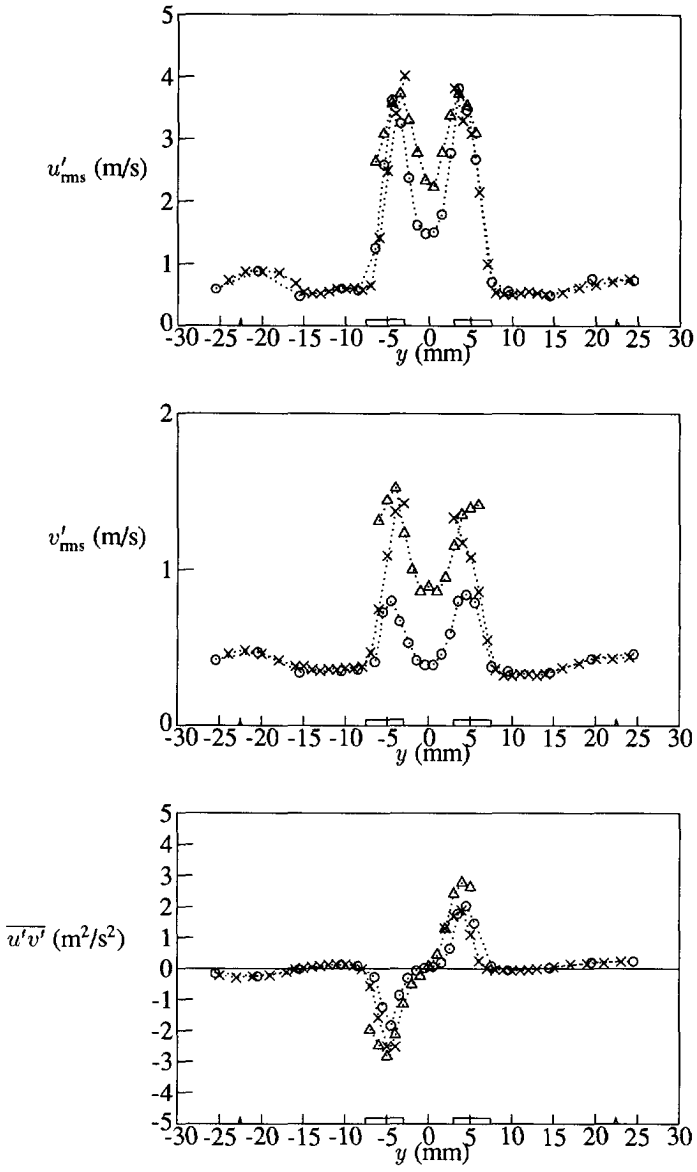

Figure 5.36: Axial rms velocity (top), radial rms velocity (middle) and Reynolds shear stress (bottom) profiles in flame C for a radial traverse at $x = 50$ mm with equal seeding density of the jet flow and the primary annular flow ($\cdots\circ\cdots$), with conditional seeding of the jet flow ($\cdots\triangle\cdots$) and with conditional seeding of the primary annular flow ($\cdots\times\cdots$).

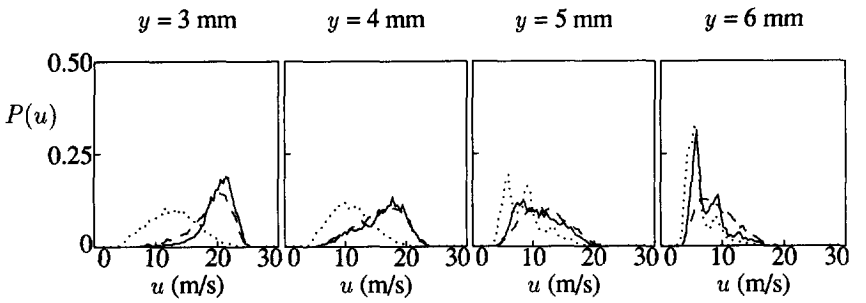

Figure 5.37: Probability density functions of the axial velocity in flame C at $x = 50$ mm for y = 3, 4, 5 and 6 mm with equal seeding density of the jet flow and the primary annular flow (—), conditional seeding of the jet flow (– –) and conditional seeding of the primary annular flow (· · ·).

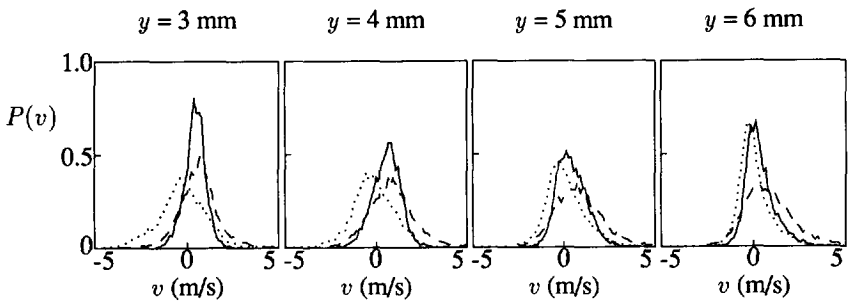

Figure 5.38: Probability density functions of the radial velocity in flame C at $x = 50$ mm for y = 3, 4, 5 and 6 mm with equal seeding density of the jet flow and the primary annular flow (—), conditional seeding of the jet flow (– –) and conditional seeding of the primary annular flow (· · ·).

on the primary annular air $P(u)_{\text{ann}}$ are relatively narrow, with a mean velocity close to that of the primary annular air velocity. In this region, $P(u)_{\text{jet}}$ is clearly skewed toward higher velocities, which accounts for the higher observed mean and fluctuating axial velocities conditional on the jet. Moving to the centreline, $P(u)_{\text{ann}}$ shows an increasing contribution from high-velocity fluid. This high-velocity contribution is due to previously entrained air that has been partially mixed with faster-moving jet fluid originating from near the centreline.

The corresponding radial velocity PDFs are shown in Figure 5.38. In both the jet and the annulus seeded cases, the presence of positive and negative radial velocities corresponds to outward flow from the centreline region and inward flow of mixed fluid originating from both the jet and the primary coflowing air.

5.3.4 Visualization of reaction zones

The presence and position of the reaction zone and the physical width of this reaction zone can be revealed by studying the presence of OH radicals. As described in Section 2.2, OH radicals are formed close to the reaction zone, the layer with a stoichiometric mixture fraction. The presence of OH radicals indicates where burnout is taking place and combustion products are located. The fact that OH is present in a narrow region near the reaction zone enables one to gather information on the interaction between turbulence and the reaction zone. Within the cooperative project in our group to study turbulence-chemistry interactions (as discussed in Chapter 1), De Vries (1994) has performed an extensive study on OH concentration fluctuations in the piloted jet diffusion flames. OH visualizations in flames A to D, presented in Figures 5.39 and 5.40, are taken from his work. In his study, flames A to D are designated flames I to IV.

The images of the OH radical distributions of each flame in Figures 5.39 and 5.40 are built up from three separate images, covering different axial regions of the flames. No temporal correlation exists between any of the images. For both flames A and B, with their relatively low Reynolds numbers, the visualized reaction zone is not very turbulent for the complete range of x that is covered, as can be seen in Figure 5.39. The regions of intense reaction are thin. For larger axial distances, the reaction zone experiences some interaction with the turbulent shear layers between central jet/primary air and primary air/secondary air, however. Due to the low primary annular air velocity, buoyancy-influenced toroidal vortices roll outside the flame surface. As these vortices convect downstream, they interact with the flame and create wrinkles on the flame surface. Chen *et al.* (1988a) have shown that the convective motion of these vortices causes the flame to squeeze at certain locations and to bulge at others, thereby being responsible for the flame flickering. In some of the images of flame A (left part of Figure 5.39), covering x = 100 to 263 mm (x/D_{jet} = 16.7 to 43.8), sharp dark streaks are found outside the reaction zone. They are attributed to laser incandescence of soot.

The pictures on the left of Figure 5.40 reveal that in high Reynolds number flame C, with increased fuel jet velocity, more vortices displace and stretch the OH zone than in flames A and B and the probability increases that eddies penetrate this zone. This penetration may lead to local quenching of the flame zone as the instantaneous flame surface is forced to move outward and stretched due to the engulfment motion of large-scale vortices and the small-scale turbulence of the jet fluid itself. When the flame is stretched to the extent that it is quenched, a localized hole appears in the flame surface. These holes in the OH zone are regarded as evidence for the presence of local extinctions (Chen and Goss (1991)). Locally in the flame front, no OH is produced although the presence of OH near the hole indicates the presence of a stoichiometric mixture of fuel and oxidizer. It is possible that OH is present outside the reaction zone, provided that the temperature is high enough. Therefore, local extinctions will occur more often than based on the observation of holes in the OH structures. The size of the holes in the actual reaction zone can also be larger than of the holes in the OH zone. Further downstream, where the scalar dissipation rates are reduced, reignition may

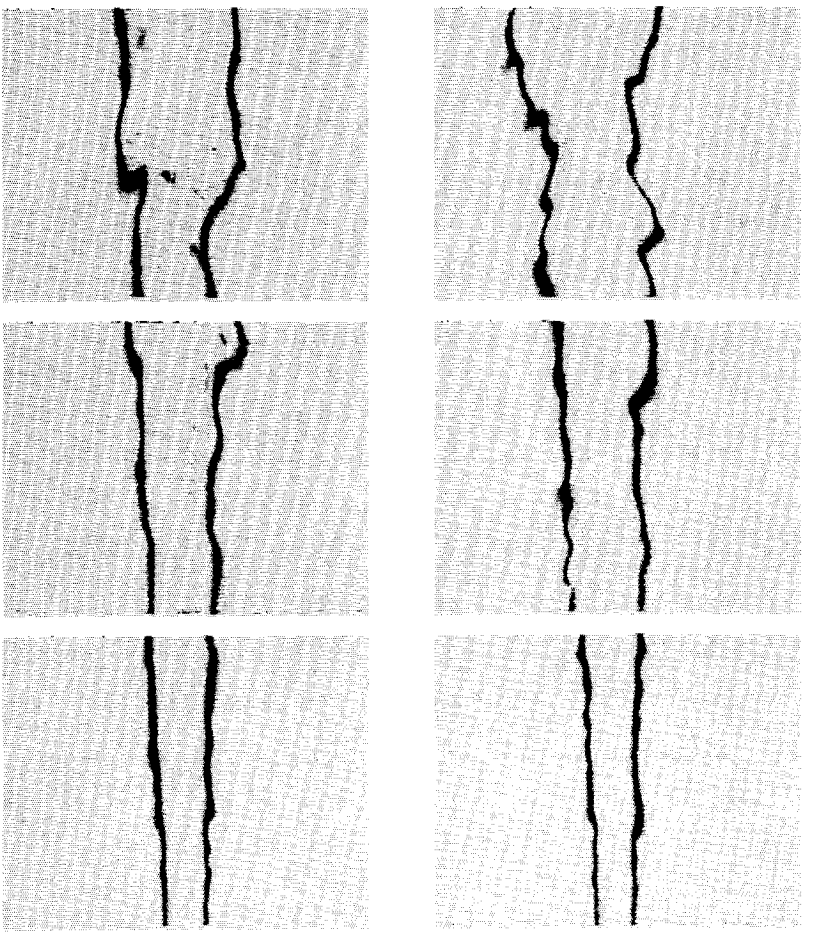

Figure 5.39: Instantaneous images of the OH distribution in flame A (left) and flame B (right), covering x = 15 to 93 mm ($2.5 < x/D_{\text{jet}} < 15.5$), x = 100 to 178 mm ($16.7 < x/D_{\text{jet}} < 29.7$) and x = 185 to 263 mm ($30.8 < x/D_{\text{jet}} < 43.8$).

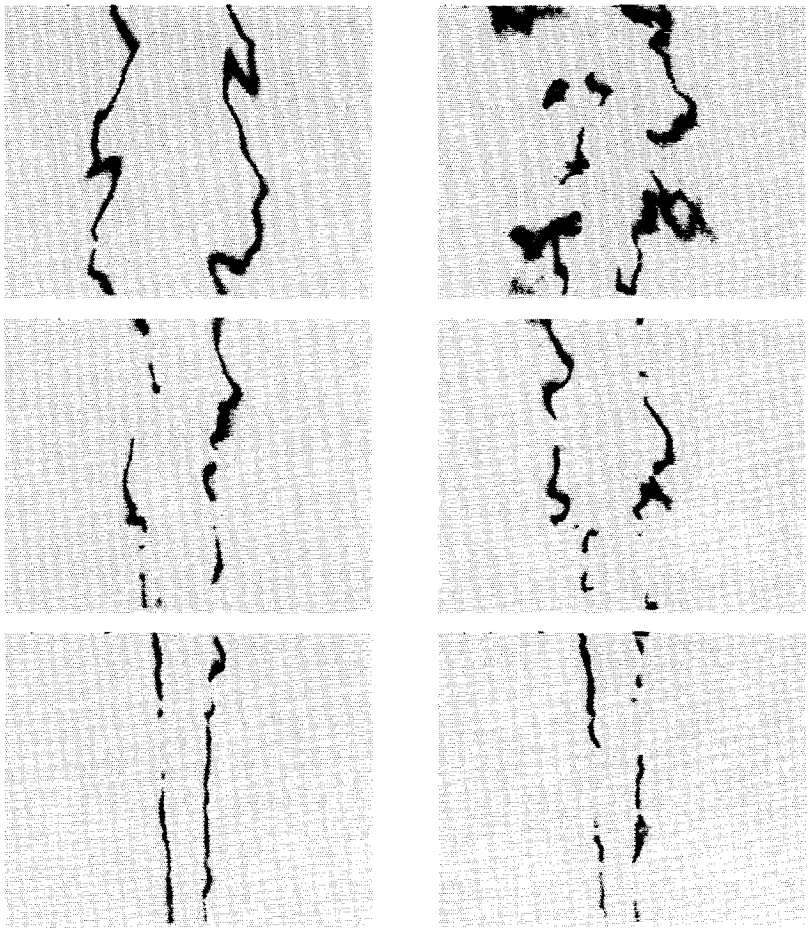

Figure 5.40: Instantaneous images of the OH distribution in flame C (left) and flame D (right), covering x = 15 to 93 mm ($2.5 < x/D_{\text{jet}} < 15.5$), x = 100 to 178 mm ($16.7 < x/D_{\text{jet}} < 29.7$) and x = 185 to 263 mm ($30.8 < x/D_{\text{jet}} < 43.8$).

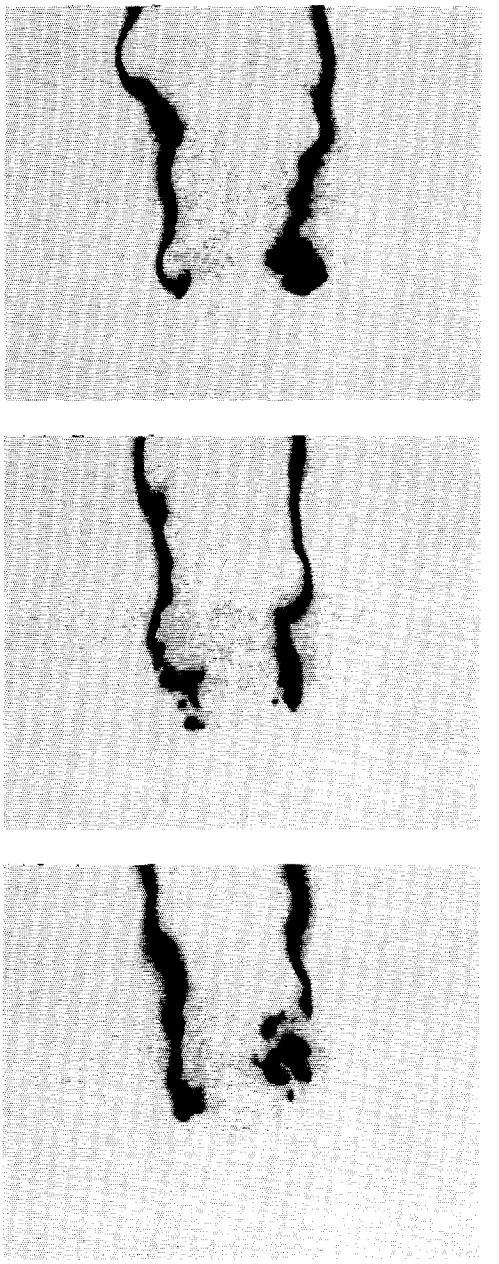

Figure 5.41: Instantaneous images of the OH distribution in flame E, covering x = 72 to 150 mm ($12 < x/D_{\text{jet}} < 25$).

occur, because the surrounding flame reignites the unburnt fuel in the hole. Efficient mixing occurring in these regions also results in thick mixing layers.

In flame D, with high primary air velocity, a lot of holes in the OH structure are found as shown in the right picture of Figure 5.40. As the primary annular air velocity is increased, the interaction between the flame and the vortices becomes stronger, resulting in an increase in the probability that local extinctions (holes) will occur at the flame surface. The OH zone is also more convoluted at larger axial distances. The number of holes is found to decrease with downstream distance.

As the flame reaches lift-off, the interaction between the flame and vortices becomes even stronger. In this case, the flame attempts to stabilize at a downstream location where the interaction is weaker. Figure 5.41 depicts planar OH images taken around the base of the lifted flame E. At the flame base, combustion occurs in a premixed-like zone which is thick in nature and tends to wrap around the vortices. Sometimes distinct islands of combustion are revealed outside the main flame base. At the centreline, however, no OH is found, indicating that the premixed flame concept for the entire flame base is not correct. The fact that the reaction zone is not present at the centreline, explains why the axial mean velocity profile along the centreline of the burner in Figure 5.17 reveals no increase of the axial mean velocity due to thermal expansion.

5.3.5 Mean temperatures and OH radical concentrations

As stated before, in turbulent jet flames, an important source of turbulence is caused by turbulent shear layers. The interaction between turbulent eddies and the reaction zone results in displacement and stretching of the reaction zone. Measurements of the mean temperature and average OH concentration, reported previously by De Vries (1994), provide quantitative information on the position of the reaction zone and influences on the flame structure. Combustion reactions and heat release occur in a thin interfacial region between the fuel and the primary air stream. As suggested by the instantaneous two-dimensional images of OH, the reaction zone is encountered on either side of the flame axis. In the case of combustion of natural gas and air, the stoichiometric mixture fraction is 0.07. This causes the reaction zone to be close to the outer boundary of the shear layer between fuel and primary air, where shear stresses are small. Consequently, close to the nozzle, the turbulence originating from this shear layer does not strongly affect the reaction zone and the flame base appears less turbulent. In this section, effects describing the interaction between turbulence and chemistry, will be addressed more closely for flames A, C and D.

Interpolation of the turbulence kinetic energy profiles of Figure 5.26 and the mean temperature profiles measured by De Vries (1994) in flame C, provides their greyscale distributions, presented in Figure 5.42. Turbulence kinetic energy is produced due to the mean axial velocity gradient in the radial direction, which is highest in the mixing region between central fuel jet and primary annular air flow. Once mixing between the reactants is established sufficiently, combustion reactions and the ensuing heat release occur, resulting in high temperatures.

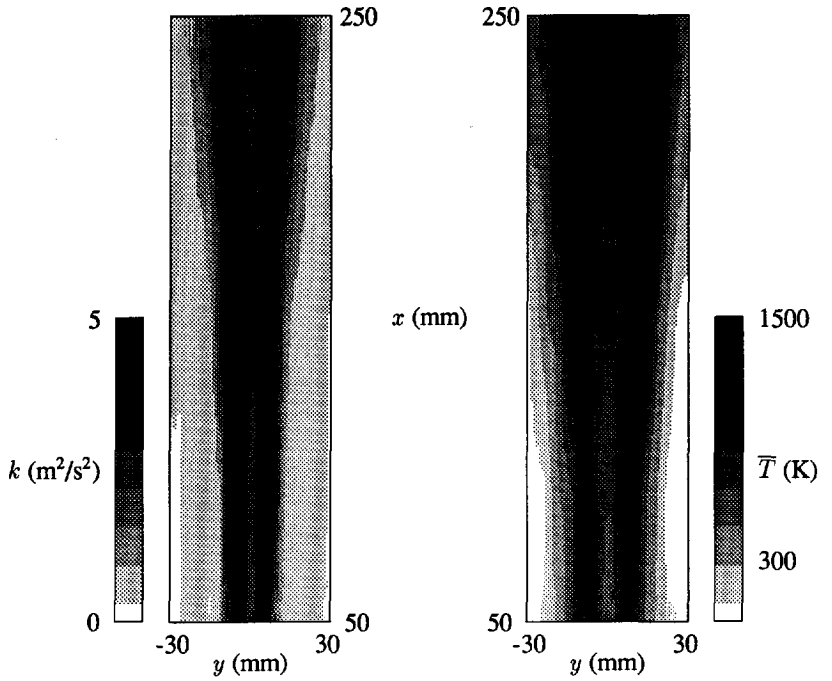

Figure 5.42: Interpolated representation of the turbulence kinetic energy (left) and the mean temperature (right) in flame C.

Results of radial traverses of the mean temperature, average OH concentration and axial turbulence intensity distribution in flames A, C and D are given in Figures 5.43 and 5.44 for axial distances from the burner nozzle x = 50 mm and x = 250 mm, respectively. Generally, the average OH concentrations at positive values of y are somewhat larger than for negative y-values, due to a small effect of laser absorption. This effect was also encountered in the disk-stabilized premixed flame, described in Chapter 4. Because the regions in which OH is found are small for piloted jet diffusion flames, the overall absorption effect will be small as well and therefore no correction procedure for laser absorption, as in Section 4.3.5, is adopted. For all flames, the radial locations of the maximum average OH concentration coincide with the radial locations of the maximum mean temperature. The axial turbulence intensity attains high values for large radial positions, because the axial mean velocity approaches zero for these positions. Also near the flame front, high values of the turbulence intensity are found. These latter high values are referred to as the maximum turbulence intensity in the sequel.

Flame A, with a low Reynolds number for both the gas jet and the primary

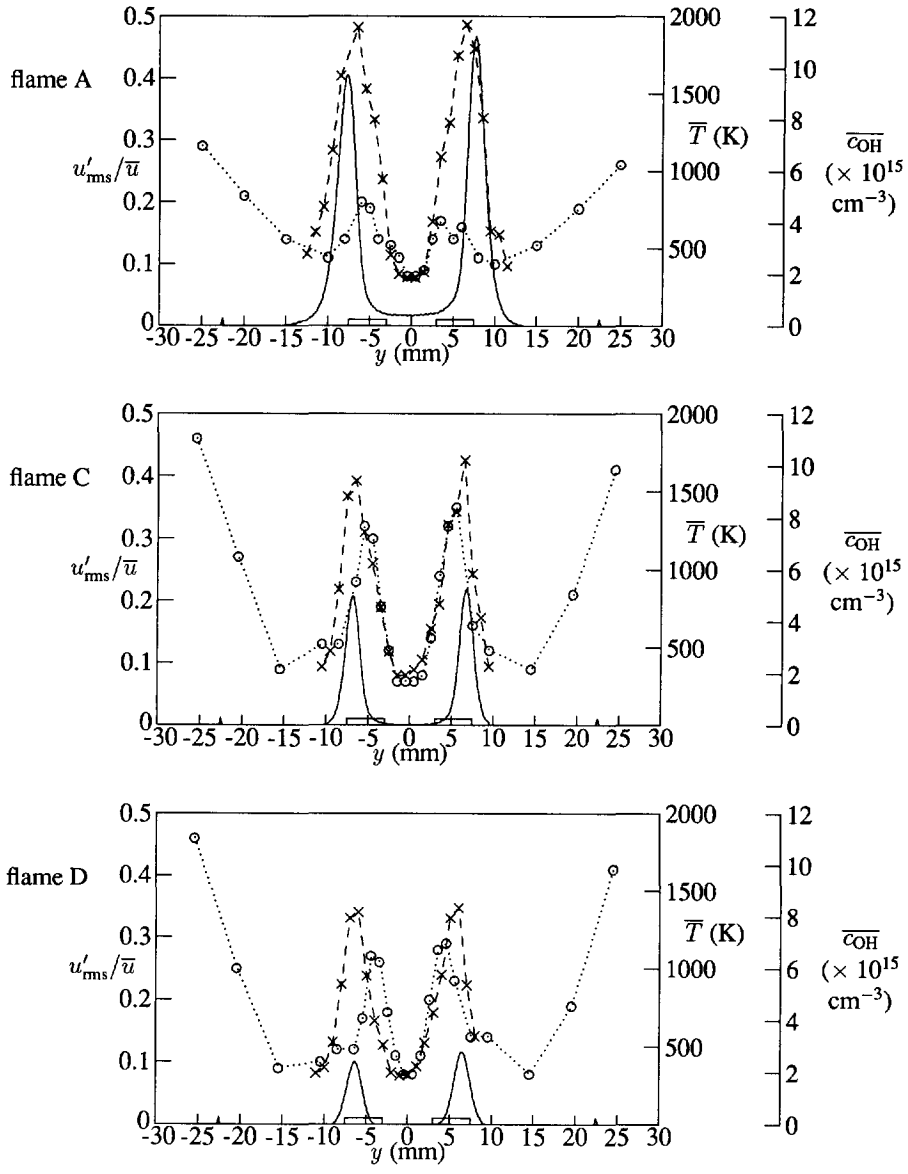

Figure 5.43: Comparison of radial profiles of the axial turbulence intensity (· · · o · · ·), mean temperature (–×–) and average OH concentration (—) at x = 50 mm in flames A (top), C (middle) and D (bottom).

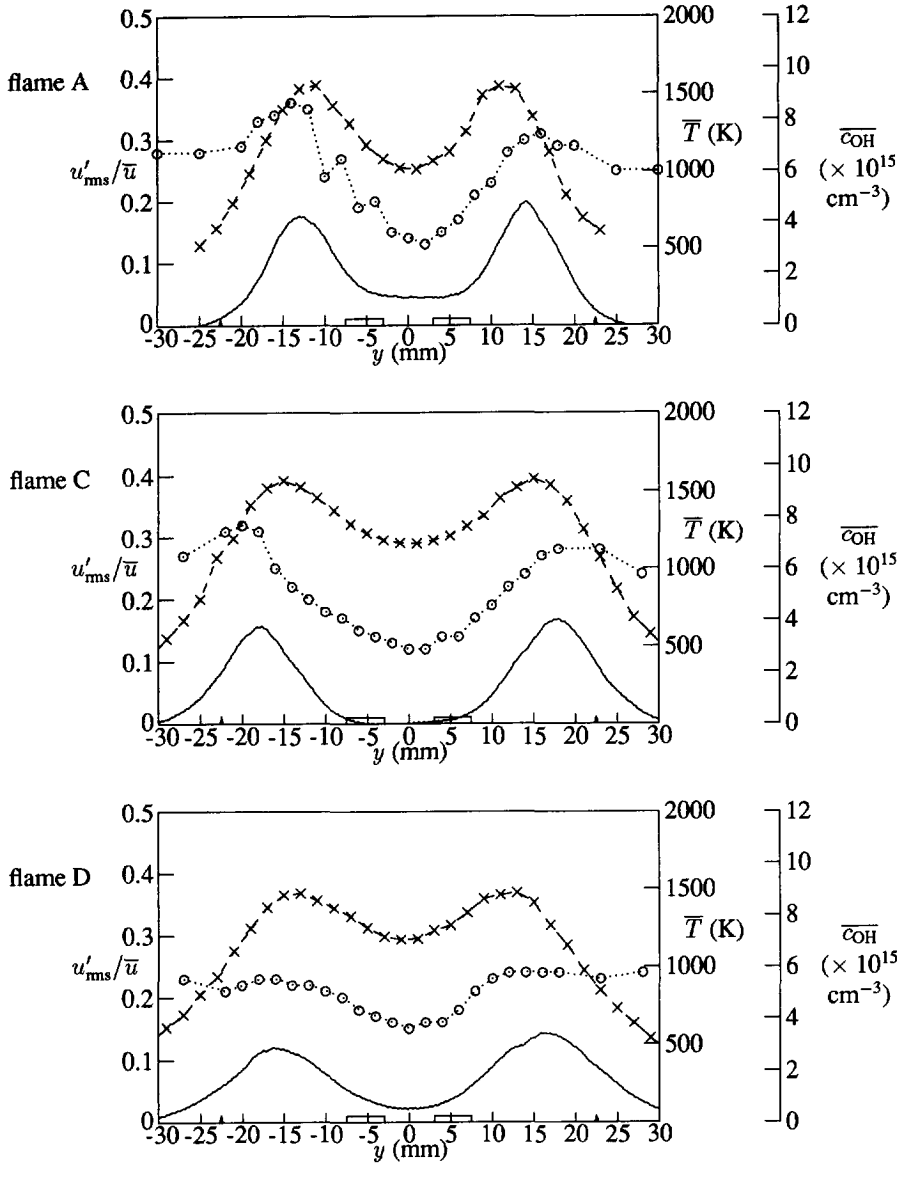

Figure 5.44: Comparison of radial profiles of the axial turbulence intensity (· · · o · · ·), mean temperature (–×–) and average OH concentration (—) at $x = 250$ mm in flames A (top), C (middle) and D (bottom).

annular air flow reveals low axial turbulence intensities in the top part of Figure 5.43. Thus, little cold primary annular air is entrained into the fuel jet flow, explaining the high maximum mean temperatures for $x = 50$ mm. As explained in the previous section, the presence of fluorescence signal at the centreline for flame A does not indicate that the reaction zone reaches the flame axis for this flame. The high centreline values for $x = 250$ mm, however, are attributed to laser incandescence of soot.

For the traverse at $x = 50$ mm, in the top part of Figure 5.43, turbulence in flame A is found to be very low near the flame front (indicated by the maxima of the average OH concentration and the mean temperature). The shear layer between fuel and air is not able to influence the reaction zone. The turbulence that is experienced by the flame front is mainly originating from the pipe flow and the wake behind the burner rim. For more downstream positions in flame A, as $x = 250$ mm (top part of Figure 5.44), maximum turbulence intensities occur closer to the reaction zone. Thus, the flame/flow interaction will be larger, as addressed in Section 5.3.4.

The middle part of Figure 5.43 reveals that in flame C, with Reynolds numbers of fuel and primary air higher than in flame A, the maximum mean temperature and the maximum average OH concentration are lower than in flame A for $x = 50$ mm. This is caused by larger fluctuations and local extinction, as shown in Section 5.3.4. Turbulence from the shear layers stretches the reaction zone, thereby decreasing its temperature and increasing the probability of formation of holes in the OH structure. At the position of the flame front for $x = 50$ mm, the turbulence intensity in flame C is larger than in low Reynolds number flame A. Thus, the reaction zone will experience more influence from the flow field. Still however, we find that the shear layer does not affect the reaction zone very strongly.

At $x = 250$ mm (see Figure 5.44), the maximum average OH concentrations in flames A and C are of the same order of magnitude. As in flame A, flame C elucidates that the peaks in the saddle-type radial distributions of turbulence intensity for $x = 250$ mm gradually approach the radial position of the mean temperature and average OH concentration maxima.

Both for $x = 50$ mm (see Figure 5.43) and $x = 250$ mm (see Figure 5.44), the mean temperatures in flame D are lower than in flame C. The excess of air, used in flame D, does not participate in the combustion process. It is heated by its surroundings, however, leading to an overall lower mean temperature. In addition, the probability of local extinction of the flame front is higher for flame D, which will also result in a lower mean temperature. Thus, the maximum average OH concentration for $x = 50$ mm is low.

Local extinctions near the burner nozzle imply that no combustion occurs. At more downstream positions, however, combustion of these previously noncombusting fuel pockets may occur in a kind of premixed fashion. As appeared from Figure 5.40, OH formed in this way is present near the flame axis. As in flame C, the turbulence intensity in flame D at $x = 50$ mm peaks close to, but not at, the position of the reaction zone. The shear layer between fuel jet and primary air flow in flame D has moved slightly towards the flame front, however, and the interaction between turbulence and

chemistry has led to an increased probability of local extinction, compared to flame C.

5.4 Discussion

5.4.1 Scale estimates and combustion regimes

As pointed out in Section 2.4.1, variation of the fuel and air flow rate does not only influence global flame characteristics (described in Section 5.3.1), but also small-scale turbulence characteristics. Although comparison of overall flame lengths and flame widths as in Section 5.3.1 is useful, information on detailed flame structures can only be obtained when scales of turbulence are compared. The interaction between turbulence and chemistry can be revealed by studying length scales of axial velocity fluctuations and of reacting scalars. This section is focussed on derivation of these detailed flame characteristics.

Scales of turbulence in nonreacting jets

From the autocorrelation functions, given in Section 5.3.2, the integral time scales of turbulence in the nonreacting jets can be derived, according to Equation 2.6. In Tables 5.4 and 5.5, integral time scales for various axial positions at the centreline are given, for jet I and jet II, respectively. The error in the presented values of the integral time scales is estimated from the convergence of the integrated autocorrelation function.

The integral time scales increase with axial position at the jet axis, reflecting the growing temporal correlation for the turbulent eddies. Using Taylor's hypothesis, integral length scales of axial velocity fluctuations can be obtained as well, which also reveal an increase with downstream position. Taylor's hypothesis assumes that the turbulent eddies are convected with the local axial mean velocity. This hypothesis is an approximation which is quite accurate as long as the level of turbulence is not too high. Typical values of $\mathcal{L}_u$ are of the order of the jet diameter $D_{\text{jet}} = 6$ mm. As in the sequel, integral length scales $\mathcal{L}_u$ smaller than the LDA measuring volume (with a length of 2.1 mm), have limited accuracy. Integral scales are larger in jet I than in jet II. Because length scales of velocity fluctuations represent the size of the characteristic eddies in the turbulent flow, it can be concluded that the primary annular air flow in jet II does not only cause less spreading of the jet, but also a smaller size of characteristic eddies. The turbulent annular air flow reduces the formation of large eddies in the shear layer, due to the smaller velocity gradient between the jet flow and its surroundings.

Using Equations 2.10 and 2.17 and a viscosity $\nu = 15.07 \times 10^{-6}$ m^2/s (at 293 K and 1 atm) for air, the Taylor micro length scales of axial velocity fluctuations in jets I and II can be derived. Their values are added in the final column of Tables 5.4 and 5.5 and increase with downstream position. The fact that all calculated Taylor length scales are smaller than the measuring volume explains why measurement of these scales (using a parabolic fit on the first points of the autocorrelation function) was not possible. By means of Equations 2.8 and 2.11 to 2.14, also the rate of dissipation and

Table 5.4: Integral time and length scales and Taylor micro length scales of axial velocity fluctuations in jet I at the centreline.

x (mm)	$\mathcal{T}_u$ (ms)	$\overline{u}$ (m/s)	$\mathcal{L}_u$ (mm)	λ_u (mm)
50	0.24 ± 0.01	17.0	4.1 ± 0.2	0.14 ± 0.01
100	0.32 ± 0.02	9.5	3.0 ± 0.2	0.15 ± 0.01
150	0.60 ± 0.10	6.4	4.0 ± 0.5	0.20 ± 0.02
200	1.20 ± 0.03	4.8	5.8 ± 0.3	0.28 ± 0.02
250	1.90 ± 0.05	3.8	7.3 ± 0.4	0.35 ± 0.02

Table 5.5: Integral time and length scales and Taylor micro length scales of axial velocity fluctuations in jet II at the centreline.

x (mm)	$\mathcal{T}_u$ (ms)	$\overline{u}$ (m/s)	$\mathcal{L}_u$ (mm)	λ_u (mm)
50	0.10 ± 0.01	16.5	1.6 ± 0.2	0.09 ± 0.01
100	0.36 ± 0.01	11.5	4.1 ± 0.2	0.19 ± 0.01
150	0.32 ± 0.01	9.4	3.0 ± 0.1	0.19 ± 0.01
200	0.45 ± 0.03	8.2	3.7 ± 0.3	0.23 ± 0.01
250	0.80 ± 0.02	7.2	5.8 ± 0.3	0.30 ± 0.02

Table 5.6: Estimated rates of dissipation and Kolmogorov scales at the centreline of jet I.

x (mm)	u'_{rms} (m/s)	ε (m^2/s^3)	l_{K} (mm)	τ_{K} (ms)	v_{K} (m/s)
50	3.4	9502	0.02	0.04	0.62
100	2.1	3043	0.03	0.07	0.46
150	1.5	794	0.05	0.14	0.33
200	1.1	229	0.06	0.26	0.24
250	0.9	103	0.08	0.38	0.20

the smallest scales of the turbulent velocity field can be estimated, as in Table 5.6 and 5.7 for jet I and jet II, respectively. In accordance with the other length scales, the Kolmogorov length scales increase with downstream position.

De Vries (1994) has derived length scales of NO concentration fluctuations. NO, serving as a passive scalar, was added to the jet flow (0.7 % by volume) and length scales of NO concentration fluctuations were derived using laser induced fluorescence with one-dimensional detection. Length scales of passive scalars give the size of the small and large eddies that transport this scalar. In Figure 5.45, integral length scales of axial velocity fluctuations and NO concentration fluctuations are presented in jets I

Table 5.7: Estimated rates of dissipation and Kolmogorov scales at the centreline of jet II.

x (mm)	u'_{rms} (m/s)	ε (m^2/s^3)	l_K (mm)	τ_K (ms)	v_K (m/s)
50	2.8	14316	0.02	0.03	0.68
100	1.7	1241	0.04	0.11	0.37
150	1.3	683	0.05	0.15	0.32
200	1.1	322	0.06	0.22	0.26
250	1.0	172	0.07	0.30	0.23

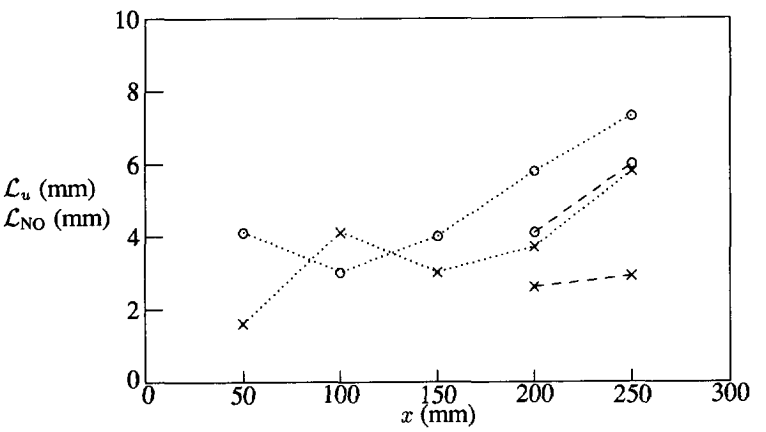

Figure 5.45: Length scales of axial velocity fluctuations (···) and NO concentration fluctuations (– –) in jet I (o) and jet II (×) for positions at the centreline.

and II. $\mathcal{L}_u$ increases gradually with downstream position and is in general larger in jet I than in jet II. Also, the integral length scales of NO concentration fluctuations are larger in jet I than in jet II, and increase with axial position. Once again, the influence of the turbulent annulus on the characteristic eddy size is evidenced.

In both nonreacting jets, integral length scales of axial velocity fluctuations are larger than of NO concentration fluctuations. It should be noted, however, that the velocity scales represent a longitudinal length scale, whereas the NO length scales are obtained from lateral correlations. In jet configurations, it is well-known that longitudinal scales are larger than lateral scales (Wygnanski and Fiedler (1969)) and therefore, from this difference conclusions about the diffusion of mass and momentum may not be drawn.

Table 5.8: Integral time and length scales of axial velocity fluctuations in flame A at the centreline.

x (mm)	$\mathcal{T}_u$ (ms)	$\overline{u}$ (m/s)	$\mathcal{L}_u$ (mm)
50	0.19 ± 0.01	12.8	2.4 ± 0.2
100	0.11 ± 0.02	11.7	1.3 ± 0.2
150	0.27 ± 0.04	9.5	2.6 ± 0.4
200	0.42 ± 0.02	8.5	3.6 ± 0.2
250	0.88 ± 0.03	7.9	6.9 ± 0.4

Scales of turbulence in flames

Based on measurements of autocorrelation functions of the axial velocity component, presented in Section 5.3.2, the turbulence time scales were measured in all flames as well. These measured time scales are given in Tables 5.8 to 5.12. Integral time scales in flame C for x = 250 mm and flame D for x = 50 and 100 mm have not been determined, because for these positions the autocorrelation function did not converge to zero. Because the temperature is not constant over the flame front in diffusion flames, Taylor and Kolmogorov length scales of axial velocity fluctuations could not be derived.

Scales of turbulence have not only been derived at the flame axis but also for the position of maximum axial turbulence intensity. This position is close to the flame front and may therefore be useful for comparison with chemistry scales (as will be discussed in the following section). The characteristic velocity scales in all flames increase with downstream distance and are in general larger in the mixing region than in the central jet. In all flames for x = 50 mm, at the centreline, the integral length scale of velocity fluctuations is approximately one third of the jet exit diameter of 6 mm.

Length scales $\mathcal{L}_u$ in the lifted flame E and nonreacting jet I are comparable at upstream locations up to x = 100 mm. This result is not unexpected since x = 100 mm is near the time-averaged location where the lifted flame is initially stabilized. For axial distances downstream of the flame stabilization point, length scales in the flame become noticeably larger. It is proposed that the reason of the enlargement of the turbulence scale is the expansion of eddies due to the higher temperatures in the flame.

Lateral length scales of NO concentration fluctuations have been derived by De Vries (1994) in flames A to D. Values of $\mathcal{L}_{NO}$ at the flame axes are of the same order of magnitude as the integral length scales of axial velocity fluctuations, as indicated in Figure 5.46. As for the nonreacting jets, a direct comparison of velocity and NO concentration fluctuation length scales may pose problems because they represent longitudinal and lateral scales, respectively. Besides, in the measurements of De Vries (1994) it appeared that NO is not truly conserved. Instead, quenching in the region of the reaction zone and in the region of fresh air, decreases the NO fluorescence signal, thus decreasing the length of correlation.

Table 5.9: Integral time and length scales of axial velocity fluctuations in flame B at the centreline.

x (mm)	$\mathcal{T}_u$ (ms)	$\overline{u}$ (m/s)	$\mathcal{L}_u$ (mm)
50	0.15 ± 0.01	16.4	2.5 ± 0.2
100	0.10 ± 0.02	14.7	1.5 ± 0.3
150	0.10 ± 0.05	12.3	1.0 ± 0.5
200	0.43 ± 0.04	10.5	4.5 ± 0.5
250	0.56 ± 0.03	9.6	5.4 ± 0.4

Table 5.10: Integral time and length scales of axial velocity fluctuations in flame C at the centreline.

x (mm)	$\mathcal{T}_u$ (ms)	$\overline{u}$ (m/s)	$\mathcal{L}_u$ (mm)
50	0.08 ± 0.01	22.9	1.8 ± 0.2
100	0.13 ± 0.01	20.2	2.6 ± 0.2
150	0.24 ± 0.02	16.3	3.9 ± 0.4
200	0.57 ± 0.05	13.8	8.0 ± 1.0
250	–	12.9	–

Table 5.11: Integral time and length scales of axial velocity fluctuations in flame D at the centreline.

x (mm)	$\mathcal{T}_u$ (ms)	$\overline{u}$ (m/s)	$\mathcal{L}_u$ (mm)
50	–	22.3	–
100	–	18.8	–
150	0.20 ± 0.05	14.0	3.0 ± 1.0
200	0.43 ± 0.02	12.2	5.2 ± 0.4
250	0.60 ± 0.05	12.2	7.5 ± 1.0

Table 5.12: Integral time and length scales of axial velocity fluctuations in flame E at the centreline.

x (mm)	$\mathcal{T}_u$ (ms)	$\overline{u}$ (m/s)	$\mathcal{L}_u$ (mm)
75	0.22 ± 0.03	11.0	2.4 ± 0.4
100	0.30 ± 0.03	8.2	2.5 ± 0.3
125	0.90 ± 0.03	6.4	5.8 ± 0.4

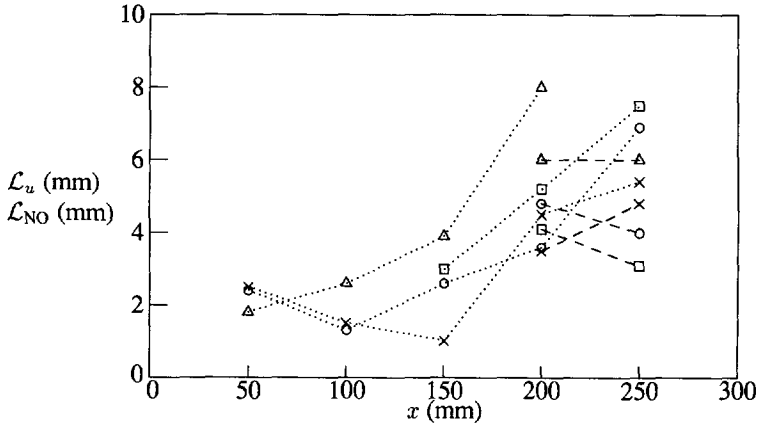

Figure 5.46: Length scales of axial velocity fluctuations (···) and NO concentration fluctuations (– –) in flames A (○), B (×), C (△) and D (□) for positions at the centreline.

Comparison of turbulence and chemistry scales in flames

Next to length scales of nonreacting scalar NO, De Vries (1994) has derived lateral length scales of reacting scalar OH in flame D for $x = 250$ mm. Only in this flame, for the downstream traverses, non-zero OH concentrations are encountered for the entire radial profile and correlation of OH concentration fluctuations provided reliable results. A comparison of integral length scales of axial velocity fluctuations, of NO concentration fluctuations and of OH concentration fluctuations in flame D at $x = 250$ mm is made in Table 5.13. Not only centreline values are given, but also at the position of maximum axial turbulence intensity (which is near the flame front). Once again, it should be noted that the velocity scales represent a longitudinal length scale, whereas the NO and OH length scales are obtained from lateral correlations.

The integral length scale of velocity fluctuations is larger near the mixing region than in the central jet. The increase of $\mathcal{L}_{NO}$ from the centreline to the radial position of maximum turbulence intensity, however, is much larger. Effects of quenching of excited NO and the effect of entrained hot combustion products decreasing the fluid density, are held responsible for this effect.

The integral OH scales are smaller than the velocity and NO integral scales. This is because OH is strongly influenced by chemical reactions. Due to the chemical reactions OH exists in rather narrow regions, and the distance over which OH is transported by turbulent eddies is reduced. This results in small values of the OH integral length scales, especially for the position of maximum turbulence intensity.

Peters' diagram for characterization of nonpremixed combustion, introduced in Section 2.4.1, can not be applied to our results, because no mixture fraction data are

Table 5.13: Integral length scales of axial velocity fluctuations, NO concentration fluctuations and OH concentration fluctuations in flame D at the centreline and at the position of maximum turbulence intensity at $x = 250$ mm.

At the centreline	
$\mathcal{L}_u$ (mm)	7.5 ± 1.0
$\mathcal{L}_{NO}$ (mm)	3.1 ± 0.3
$\mathcal{L}_{OH}$ (mm)	1.90 ± 0.19
At the position of maximum turbulence intensity	
$\mathcal{L}_u$ (mm)	8.5 ± 1.0
$\mathcal{L}_{NO}$ (mm)	8.5 ± 0.2
$\mathcal{L}_{OH}$ (mm)	1.5 ± 0.2

available. De Vries (1994) found that in the outer regions of the flame $\mathcal{L}_{OH}$ attains values of (8 ± 2) mm, which is in good agreement with the values found for $\mathcal{L}_u$. This indicates that momentum and reacting species concentration are transported by eddies of roughly the same size. Further downstream, the length scales of velocity fluctuations become larger than the OH length scales. Chemical reactions, in which OH is involved, occur within the large characteristic eddies of the velocity field. The turbulence is assumed to have less influence on chemistry. Therefore, the flames can be treated as distributed reactors. Under these conditions, the smallest turbulence scales interact with the flame zone, and the bulk of the reaction occurs in small zones where mixing is intense, separated by zones of more limited reaction.

5.4.2 Comparison of reacting with inert flow

The influence of combustion reactions on the flow field and turbulence can only be understood if a well-defined comparison between a reacting flow and its nonreacting equivalent is made. In this section the main differences between reference flame C and jet II will be discussed. Jet II can be regarded as the isothermal equivalent of flame C, despite a minor difference in density between natural gas and air for the jet flow and the fact that no nonreacting equivalent for the pilot flames is used.

Differences between the axial mean velocity and turbulence kinetic energy for axial traverses along the centreline of the burner in flame C and jet II are clearly illustrated in Figure 5.47. Higher centreline axial mean velocities are measured for the flame, due to the presence of high velocity pilot flames and (further downstream) due to the expansion of the flow caused by the temperature rise. Near the burner nozzle of the flame, the magnitude of the turbulence kinetic energy is small and almost constant, whereas in the nonreacting flow k reaches a maximum value and decays rapidly. In jet II, turbulence generated by the shear layer between the central jet and the primary annular air, penetrates into the jet axis and causes a decay of the centreline velocity. In the flame, this penetration is delayed due to the flow acceleration in the reaction zone, lying between the shear layer and the central flow. As a result, less annular air

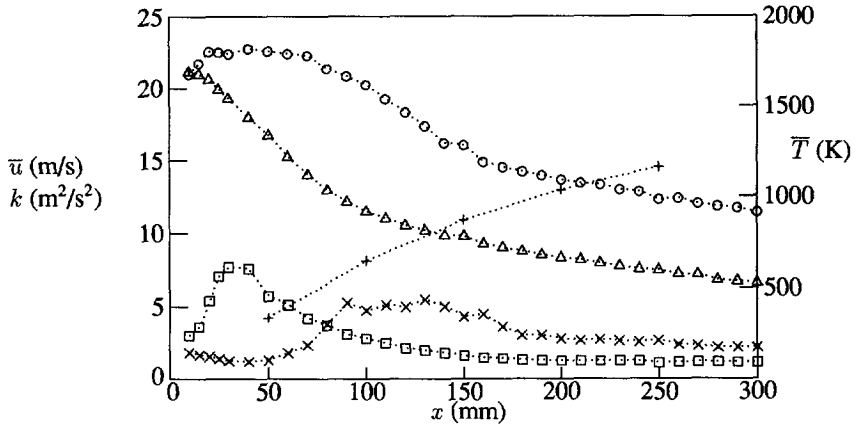

Figure 5.47: Centreline axial profiles of the axial mean velocity (··· o ···), turbulence kinetic energy (··· × ···) and mean temperature (··· + ···) in flame C and the axial mean velocity (··· △ ···) and the turbulence kinetic energy (··· □ ···) in jet II.

is entrained into the central jet and the potential core (characterized by constant mean and fluctuating velocity) extends to $x \approx 50$ mm ($x/D_{\text{jet}} \approx 8.3$). This is confirmed by the NO measurements of De Vries (1994) at x = 50 mm, where (with equal NO concentration at the jet exit) a higher NO concentration is found in flame C than in jet II, illustrating the smaller amount of entrainment into the central jet of the flame.

The turbulence kinetic energy in the flame increases gradually and reaches a relative peak near x = 125 mm (x/D_{jet} = 20.8). The magnitude of this relative peak of k is appreciably less than the maximum value of k in the noncombusting jet. This suppression of turbulence is caused by acceleration of the flow in the flame and the ensuing changes of the velocity gradients (Sislian *et al.* (1988)). The increase of k is accompanied by a temperature rise at the centreline, indicating that eddies with hot combustion products penetrate to the flame axis. This is also in accordance with the decay of the axial mean velocity at the centreline. In the downstream region, the turbulence kinetic energy in the flame changes less rapidly than in the cold flow. Turbulence in the near exit region of jet II (see Figure 5.2) is anisotropic, u'_{rms} being always larger than v'_{rms}, whereas in the same region for the flame (see Figure 5.15), these fluctuations are small and almost equal. Further downstream in the flame, the turbulence becomes more anisotropic than in jet II.

The width of flame C and jet II, based on the velocity jet growth w_u, is determined. In Figure 5.48, the velocity half width as a function of the axial position in flame C and jet II is given. The entrainment of primary annular air is the determining process in the development of the jet growth. The effect of combustion is to generate a high-viscosity layer around the central fuel jet, shielding the jet from its surroundings, thus hindering

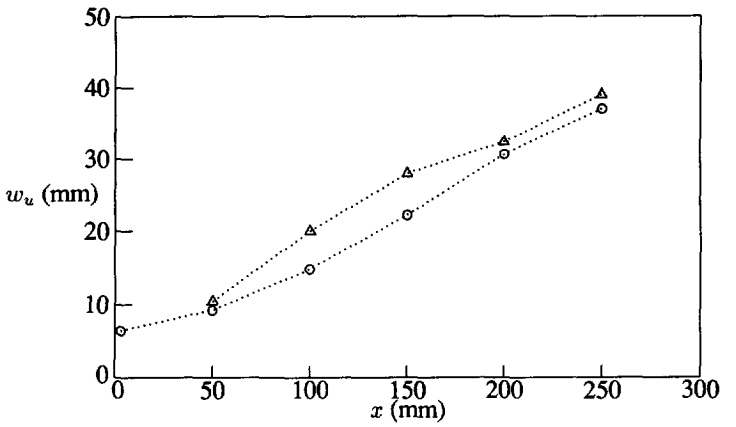

Figure 5.48: Jet growth w_u, determined by the velocity half width, in flame C ($\cdots\circ\cdots$) and jet II ($\cdots\triangle\cdots$) as a function of the axial distance x.

the entrainment of annular air into the jet. This behaviour is reflected in the lower values of w_u in flame C than in jet II.

A comparison of radial profiles of the turbulence intensity $u'_{\text{rms}}/\overline{u}$ at $x = 50$ mm for jet II and flame C is given in Figure 5.49. These profiles peak near the maximum mean axial velocity gradient and in the outer regions of the flow, where the axial mean velocity approaches zero. At the maximum velocity gradient, axial turbulence intensities are approximately equal in jet II and flame C. Near the centreline, however, the flame exhibits the previously mentioned suppression of turbulence, caused by an extension of the potential core. The turbulence intensity of the flame has decreased from 0.19 to 0.07, compared with the jet. Even at higher axial positions this suppression of turbulence at the centreline is quite significant as revealed by the data in Table 5.14. In this table, the centreline axial turbulence intensity is given for jet II and flame C. Maximum values of the turbulence intensity, given in Table 5.15, are only slightly larger in the flame than in the isothermal jet.

The combustion process has been found to have an influence on the turbulence macro scale as well. Axial distributions of $\mathcal{L}_u$, depicted in Figure 5.50 show a monotonic increase along the jet axis in the cold jet. Up to $x = 150$ mm, similar values of the integral length scale are found in the combusting jet. All integral length scales are of the order of the jet exit diameter in both the nonreacting and the reacting flow. At $x = 50$ mm, the integral length scale is typically one third of the jet exit diameter of 6 mm. For $x = 200$ mm, a significantly larger value of $\mathcal{L}_u$ is found in the flame than in the cold jet. This phenomenon is also observed by Sislian *et al.* (1988). The integral length scales of NO concentration fluctuations are constant (within the experimental accuracy) with downstream position. Correlation between NO concentrations in the

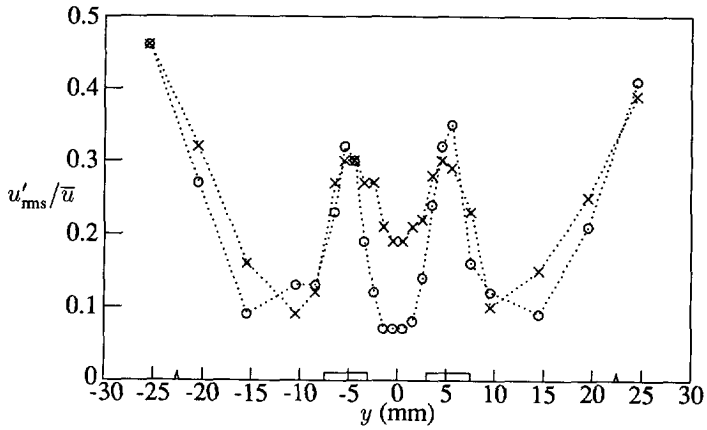

Figure 5.49: Axial turbulence intensity $u'_{rms}/\overline{u}$ profiles for a radial traverse at $x = 50$ mm in jet II ($\cdots \times \cdots$) and flame C ($\cdots \circ \cdots$).

Table 5.14: Centreline axial turbulence intensities $u'_{rms}/\overline{u}$ in jet II and flame C for axial positions $x = 50$, 100, 150, 200 and 250 mm.

x (mm)	jet II	flame C
50	0.19	0.07
100	0.15	0.09
150	0.12	0.13
200	0.12	0.12
250	0.15	0.12

Table 5.15: Maximum values of the axial turbulence intensity $u'_{rms}/\overline{u}$ in jet II and flame C for axial positions $x = 50$, 100, 150, 200 and 250 mm.

x (mm)	jet II	flame C
50	0.30	0.34
100	0.22	0.30
150	0.23	0.27
200	0.27	0.28
250	0.28	0.32

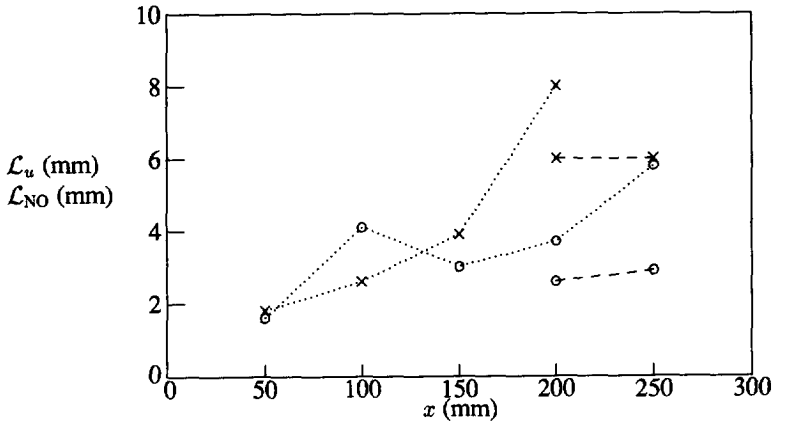

Figure 5.50: Length scales of axial velocity fluctuations (· · ·) and NO concentration fluctuations (– –) in jet II (o) and flame C (×) for positions at the centreline.

radial direction in jet II is smaller than in flame C. As before, a comparison between NO and velocity length scales is obscured by the fact that they represent lateral and longitudinal properties, respectively.

5.4.3 Approach to extinction and lift-off

The diffusion flames described in this chapter represent a range of flames with Reynolds numbers of 4.4×10^3 to flames with fully turbulent characteristics ($\mathrm{Re} \approx 15.7 \times 10^3$). One of the consequences of increased turbulence and axial mean velocity appears to be the development of local extinctions of the flame front. When excessive, these extinctions may lead to lift-off and eventually blow-off of the entire flame. Comparison of turbulence and chemistry scales in the different flames will appear to be useful in the explanation of the processes involved.

During the combustion process, a flame is subjected to regions of high strain, resulting in stretching of the flame front. The stretch rate varies temporally and spatially over the flame surface, depending on local instantaneous velocity gradients at the flame surface. Fluctuations about the mean stretch may cause local extinction of the flame when the stretch rate exceeds a critical value. A global strain rate can be defined as $a = 2V/R$, where V is the approach oxidizer velocity and R the radius of the burner. The critical strain rate varies with fuel type. Numerical simulation of strained laminar diffusion flames, carried out by Peeters (1995), showed that a methane-air flame extinguishes at a critical strain rate $a = 400\ \mathrm{s}^{-1}$. For the flow settings of flames A to D, a is always larger than $400\ \mathrm{s}^{-1}$. This explains why the pilot flames are necessary to stabilize the flame at the burner rim.

The overall stability of the flame is not just influenced by the presence of the

Table 5.16: Estimated Damköhler numbers in flames A to D, based on data obtained at the centreline for $x = 50$ mm.

Flame	$\mathcal{L}_u$ (mm)	u'_{rms} (m/s)	τ_m (ms)	Da (-)
A	2.4	0.66	3.6	1.5
B	2.5	1.11	2.25	0.9
C	1.8	1.38	1.30	0.5
D	-	2.28	-	-

pilot flames. The burner rim between the fuel jet and the primary annular air is quite thick. Therefore, just downstream of the nozzle, a recirculation region is present as indicated in Figures 5.18 and 5.20. Within the recirculation zone a premixed type of combustion reactions will take place. The actual diffusion flame will be connected with this recirculation zone. As the annular air velocity is increased, as in flame C, at a fixed fuel jet velocity, the flux of air coming into the recirculation zone must increase due to the increased convective velocity, while the fuel-flux remains unchanged. Thus, the local equivalence ratio in the recirculation zone must decrease. As reactions cease, because the mixture in the recirculation zone reaches its lean-flammability limit, the flame may become unstable, thereby oscillating locally, leading to local extinction.

According to Peters (1991), the moment of extinction corresponds to a critical value of the scalar dissipation rate. The scalar dissipation rate, which is a parameter of turbulence, is proportional to the local strain rate in the flow. In a conventional turbulent diffusion flame issuing from a round jet, the turbulence mixing rate, as measured by the mean scalar dissipation rate decreases with axial distance from the jet exit at the centreline and approaches an asymptotic level (Namazian *et al.* (1988)). The highest mixing rates and finite rate kinetic effects are thus most significant right near the nozzle due to very steep concentration gradients. Instantaneous levels near the jet exit were found to be sufficient to extinguish flames. The lack of mixture fraction data obtained in our flames, implies that this theory can not be validated by our experiments.

Another popular view of local extinction is introduced by Correa and Gulati (1988), who state that local extinction occurs when chemical reactions are affected by turbulence or, equivalently, when the Damköhler number is of the order of unity. The lower the Damköhler number, the stronger the interaction of turbulence with chemical reactions. In order to calculate Damköhler numbers in our flames, Equation 2.19 is used to determine a characteristic turbulence time scale τ_m. For the scales of chemistry, a numerically obtained value for two-body chemistry $\tau_c = 2.5$ ms, obtained by Peeters (1995), is used. In Table 5.16, estimations of the Damköhler number in flames A to D are given, based on the data obtained at the centreline for $x = 50$ mm.

Comparing Da numbers in flames A to C, Da decreases with increasing primary annular air flow rate. The low values of the Damköhler number confirm that all flames fall into the distributed reaction zone regime, when a characterization with a Peters'

diagram is made. With increasing exit velocity, the turbulence time scales τ_m decrease, leaving less time for chemical reactions to occur. Thus, with increasing exit velocity, the turbulence is affecting the chemistry more and more, resulting in an increased probability of local extinction. Unfortunately, $\mathcal{L}_u$ could not be determined at $x = 50$ mm in flame D. In this flame, the shear layer between primary and secondary air flows, will enhance the mixing rate between fuel and air, compared to flame C. The Damköhler number of flame C will be larger than that of flame D, which corresponds to the much more frequent local extinctions in flame D. This increased influence of turbulence on the chemistry is also indicated in Section 5.3.5, where the radial position of maximum turbulence intensity is closer to the position of the flame front, when the primary annular air flow rate is increased.

Local extinctions must be followed by a certain degree of non-reactive turbulent mixing of fuel and oxidizer. If conditions are favourable, then the mixed reactants will ignite and burn in a premixed fashion. These premixed pockets provide a source of reignition for the flame when the mixing rates become small compared to the chemical kinetics. If too many holes are present, or the probability of burning is too low, on the contour of stoichiometric mixture, where the flame is located instantaneously, the flame cannot be stabilized at the burner rim and lift-off occurs. The physical mechanism that is responsible for the lifting of the flame is once again the competition between flow and chemical effects, characterized by their respective time scales.

5.4.4 Comparison of experimental data with numerical simulations

In this section, experimental results obtained for reference flame C are compared with predictions of a conserved-scalar numerical model. The modelling of this flame is part of the long-term project in our group to develop a database of both experimental and numerical data in a geometry with well-defined initial and boundary conditions, as discussed in Chapter 1. For a description of the mathematical model and the numerical aspects, the reader is referred to the thesis of Peeters (1995), who performed the simulations.

The mathematical model was based upon the Favre-averaged transport equations for mass, momentum (including buoyancy) and enthalpy, in cylindrical coordinates. Turbulence was modelled by a standard k-ε model with a correction for round jet development. No further adjustment of constants was performed for this particular flame. A four-flux radiation model was used to simulate radiative heat losses. In the limit of high Damköhler number, the chemistry attains equilibrium even within the smallest turbulent eddies, before the turbulent mixing process will disturb this chemical equilibrium. By the Shvab-Zel'dovich assumptions (Williams (1985)), all thermo-chemical variables are related to the mixture fraction ξ, which is a conserved scalar. Hence, if the probability density function $\tilde{P}(\xi)$ is known, the mean values of all dependent properties can be determined. In the present model, a β-function PDF was assumed for $\tilde{P}(\xi)$, which is completely determined by the mean $\tilde{\xi}$ and its variance $\widetilde{\xi''^2}$. Transport equations are solved for these moments to calculate the PDF in each grid point.

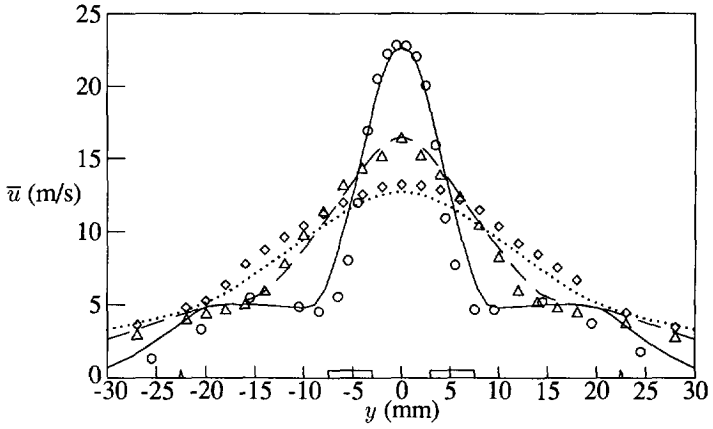

Figure 5.51: Comparison of measured axial mean velocity and numerical results in flame C at x = 50, 150 and 250 mm. Symbols: experiments x = 50 mm (○), x = 150 mm (△), x = 250 mm (◇). Lines: predictions x = 50 mm (—), x = 150 mm (– –), x = 250 mm (· · ·).

The mean axial velocity component for various radial positions on three different heights, is given in Figure 5.51. As in the sequel, the lines correspond to the numerical results whereas the symbols represent measured data. In general, the agreement between observed and predicted values is very good. Only the recirculation zone right above the burner nozzle, is slightly underestimated by the numerical predictions, leading to small discrepancies at x = 50 mm for $y \approx \pm 7$ mm. At x = 150 mm, the correspondence between the numerical and experimental results is particularly good. For x = 250 mm, the mean velocities are somewhat underestimated by the model.

In Figure 5.52, the radial profiles of the axial rms velocity u'_{rms}, are presented at three x-values. For x = 50 mm, the numerical results show lower centreline and peak turbulence than the experiments. The inlet conditions in the model were prescribed at the nozzle exit plane by uniform velocity profiles and a turbulence intensity of 5 %. As discussed in Section 5.3.2, measurements at x = 3 mm revealed a uniform jet velocity profile but a developed pipe flow annular air velocity profile. Besides, the initial turbulence intensities were higher than the assumed 5 %. Of course, these differences are reflected immediately in the predicted axial mean and rms velocity profiles.

For x = 150 mm, the correspondence between the LDA results and the model is fairly good, considering the slight asymmetry of the measurements and the limitations of the k-ε model. At x = 250 mm, the axial rms velocities are slightly overestimated by the model at the centreline, but underpredicted for large radial distances ($y > \pm 15$ mm), which may be due to the simple estimation $\widetilde{u'^2} = \tilde{k}$ which is not generally true. Furthermore, it is still disputable whether the LDA experiments yield Reynolds- or

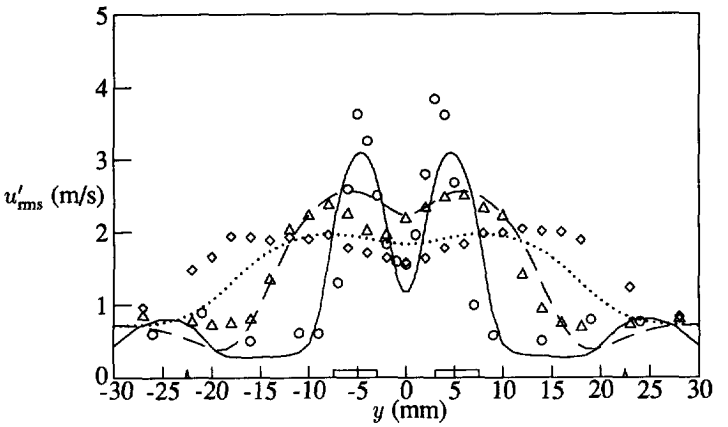

Figure 5.52: Comparison of measured axial rms velocity and numerical results in flame C at $x = 50$, 150 and 250 mm. Symbols: experiments $x = 50$ mm (○), $x = 150$ mm (△), $x = 250$ mm (◇). Lines: predictions $x = 50$ mm (—), $x = 150$ mm (– –), $x = 250$ mm (· · ·).

Favre-averaged velocities. The Reynolds shear stress profiles are shown in Figure 5.53. Correspondence with the numerically obtained results is qualitatively correct.

In Figure 5.54, the mean profiles of the measured temperature are compared with numerical results. Correspondence between the measured and simulated temperatures is excellent, taking into account the experimental accuracy of $\pm$ 70 K. Inspection of the radial location of maximum temperature reveals that the spreading of the reaction zone is predicted accurately by the model. The differences between measured and calculated maximum temperatures are small, but seem to increase slowly with x. This is attributed to soot radiation, which was not included in the present model.

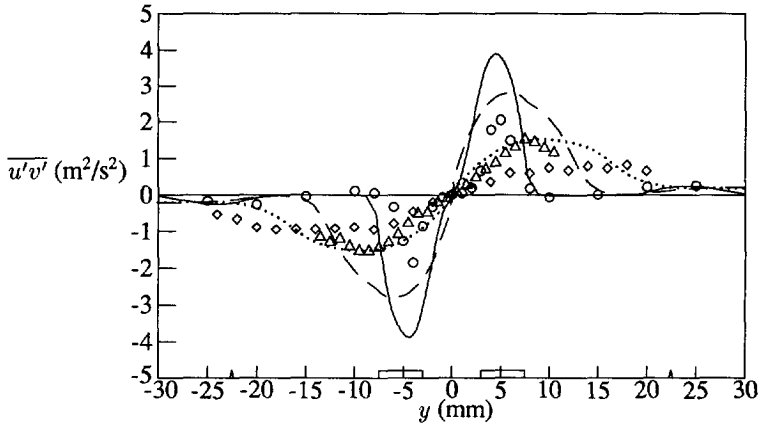

Figure 5.53: Comparison of measured Reynolds shear stress and numerical results in flame C at $x = 50$, 150 and 250 mm. Symbols: experiments $x = 50$ mm (○), $x = 150$ mm (△), $x = 250$ mm (◇). Lines: predictions $x = 50$ mm (—), $x = 150$ mm (– –), $x = 250$ mm (· · ·).

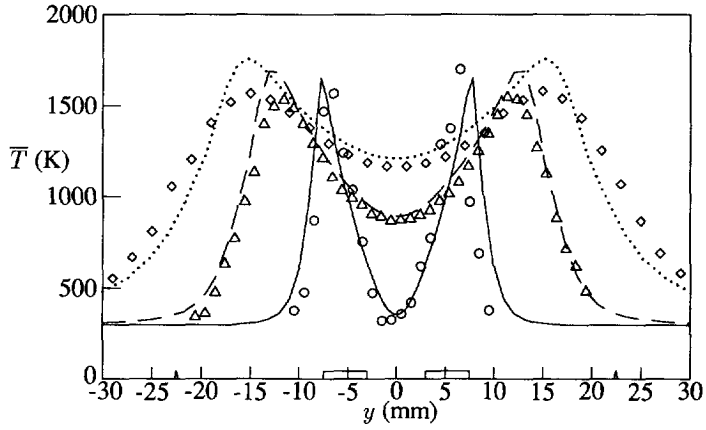

Figure 5.54: Comparison of measured mean temperatures and numerical results in flame C at $x = 50$, 150 and 250 mm. Symbols: experiments $x = 50$ mm (○), $x = 150$ mm (△), $x = 250$ mm (◇). Lines: predictions $x = 50$ mm (—), $x = 150$ mm (– –), $x = 250$ mm (· · ·).

Radial profiles of the average OH concentration $\overline{c_{OH}}$ are shown in Figure 5.55, for $x = 50$, 150 and 250 mm. Predictions of the OH concentrations by the constrained equilibrium model do not take into account super-equilibrium levels of OH. The predicted concentrations therefore are lower than measured OH concentrations. The shape of the predicted profiles does not match with the experiments. To investigate the sensitivity of predictions on the assumed PDF shape, the β-function mixture fraction PDF was replaced by a top-hat distribution. This deteriorated the mean temperature as well as the OH predictions: both the temperature and OH profiles showed lower maximum values, and OH profile shapes deviated even stronger from the experiments. It was concluded that the conserved-scalar model with a β-function PDF performs well for mean temperature predictions, but fails to represent the shape of the measured mean OH profiles. It is unlikely that substituting the β-function PDF by any other PDF shape will significantly improve OH predictions without harming the mean temperature predictions. The observed differences cannot be attributed to the assumed PDF shape, but are inherent to the conserved-scalar chemistry model for OH. Looking at the trend for larger downstream distance x, the experiments show a decay of maximum average OH values, whereas the conserved-scalar model gives a maximum OH level at the flame tip where $\widetilde{\xi} = \xi_{st}$ and fluctuation levels are small. The experiments disagree with such a trend, even for $x > 250$ mm.

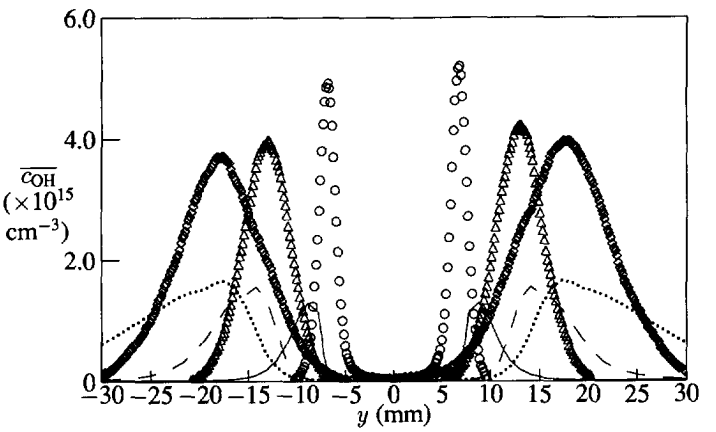

Figure 5.55: Comparison of measured average OH concentration and numerical results in flame C at $x = 50$, 150 and 250 mm. Symbols: experiments $x = 50$ mm (○), $x = 150$ mm (△), $x = 250$ mm (◇). Lines: predictions $x = 50$ mm (—), $x = 150$ mm (– –), $x = 250$ mm (· · ·).

5.5 Summary of Chapter 5

In order to study turbulence-chemistry interactions in combustion, in this chapter measurements on four piloted jet diffusion flames and a jet flame at lift-off are described. The burner configuration consists of a central fuel jet, surrounded by a turbulent primary annular air flow. Overall flame stability is provided by pilot flames. For comparison with numerical simulations and to prevent recirculation, the burner is placed in a low-speed secondary coflow of air. This three-flow system with turbulent primary air differs from widely used nonpremixed combustion systems reported in literature. Therefore, first the influence of the annular air in a nonreacting flow is determined by means of laser Doppler anemometry.

It appeared that the turbulent primary annular flow causes mixing closer to the burner than in a situation with zero coflow. The development of shear layers between central jet flow and annular air, but also between annular and secondary air is held responsible for this effect. The turbulence generated by these shear layers is suppressed in the upstream part of the combusting flows. Due to flow acceleration in the reaction zones, less annular air is entrained into the central jet and the potential core region extends further downstream than in its nonreacting equivalent.

The entrainment of primary annular air is also the determining process in the development of the flame width and flame length. With larger difference between central fuel jet velocity and primary annular air velocity, more air is entrained, leading to wider and shorter flames. In addition, a high primary annular air velocity enhances the interaction between the turbulence and the flame, resulting in an increase in the probability of local extinction of the flame surface. These phenomena are evidenced by visualization of the OH radicals in the flames by planar laser induced fluorescence. A more quantitative evaluation of the occurrence of local flame extinctions due to turbulence-chemistry interactions is performed by comparing average OH concentration, mean temperature and turbulence intensity profiles. One-dimensionally detected laser induced fluorescence and thermocouples were used to determine average OH concentrations and mean temperatures, respectively.

In all flames, the position of the flame front, indicated by the maximum of the average OH concentration, corresponds with the position of maximum mean temperature. The position of the flame front, relative to the maximum in turbulence energy, however, is highly dependent on the primary annular air flow rate. Also a comparison of Damköhler numbers in the flames under investigation revealed a decrease with increasing primary annular air velocity. This indicates a stronger effect of turbulence on the chemistry, evidencing the increased probability of local extinction. Especially the large-scale vortices are believed to play an essential role in this process.

When a flame reaches lift-off, the interaction between the flame and the vortices becomes even stronger. The flame attempts to stabilize at a downstream position where the interaction is weaker. It appeared that at the flame base of a lifted flame combustion occurs in thick premixed-like zones. Increase of the centreline axial mean velocity at the position of flame stabilization, because of thermal expansion effects, was not found.

The combustion process has been found to have an influence on the integral length scales of axial velocity fluctuations as well. Instead of a monotonic increase along the jet axis in the cold flow, in combusting jets the turbulence macro scales are initially equal to those in the nonreacting situation, but larger values were found for more downstream positions. In general, the measured length scales are larger in the mixing region between central jet and primary air flow than in the central jet.

Integral length scales of OH concentration fluctuations were found to be smaller than velocity and (nonreacting scalar) NO concentration fluctuations. This is because OH is strongly influenced by chemical reactions. All scales are of the same order of magnitude, however, indicating that the scales of the turbulence interact with the flame zone. The bulk of the reactions occurs in small zones where mixing is intense, separated by zones of more limited reaction; a combustion regime typified as distributed reactors. This information is important for modelling applications. Comparison of experimental results in a flame with predictions of a numerical model revealed that large progress has been made in this field. Excellent agreement of predicted and observed mean and rms velocities, as well as temperatures was found. Only for the OH concentration differences between numerical and experimental results were found, due to the presence of superequilibrium OH concentrations, which was not included in the model.

Chapter 6

Conclusions

The turbulence and the chemical structure of natural gas flames have been subject of investigation in this thesis. In this chapter, the conclusions of the previous chapters will be summarized and they will be related to the aims of this study, presented in Chapter 1. One aim was to provide experimental data that added information on the interaction between turbulence and chemistry in combustion and to improve general understanding of the major processes in turbulent flames. A second aim was to supply experimental results to validate numerical models of turbulent combustion. First the main conclusions will be drawn regarding the turbulence and OH structures of a disk-stabilized premixed flame. Next, conclusions concerning the flame structure of piloted jet diffusion flames will be discussed.

6.1 Structure of disk-stabilized premixed flame

Both an isothermal and a premixed reacting flow of the disk-stabilized burner were characterized by a recirculation zone downstream of the stabilizing disk of 80 mm diameter. The recirculation zone length was significantly smaller in the nonreacting flow ($L \approx 30$ mm) than in the flame ($L \approx 50$ mm), however. This was attributed to combustion reactions and the ensuing thermal expansion, leading to higher velocities in the flame. The recirculation zone is surrounded by a high-velocity layer, originating from the annular burner exit. Turbulence in the flows is generated by the shear layer between this high-speed flow and the recirculation zone, and especially by the shear layer between the high-speed layer and the stagnant ambient air.

In a large region of the flow, near the centreline stagnation point, radial velocity fluctuations are much larger than axial velocity fluctuations ($u'_{\mathrm{rms}}/v'_{\mathrm{rms}} \approx 0.5$). Radial velocity fluctuations are also initiated by the shear layer between the high-velocity layer and the ambient air, but apparently they equilibrate more slowly than axial velocity fluctuations. The high degree of turbulence anisotropy decreases close to the burner and far downstream, which was also confirmed by the probability density functions of axial and radial velocity. The general anisotropy of the flow suggests the need to consider each of the normal stresses individually in modelling applications. Also the inability of effective viscosity turbulence models for the present configuration was confirmed

by the fact that regions of zero shear stress did not, in general, correspond with those of zero axial velocity gradient. Instead, emphasis should be put on Reynolds stress closures.

As a result of the second shear layer in the flame, ambient air is entrained, which has important influence on the (de)stabilization of the fuel-lean premixed flame. The equivalence ration of $\varphi = 0.75$ was selected to study a flame, exhibiting overall flame stability, yet which was close to extinction. A dominant Strouhal frequency of 12 Hz, encountered in the axial velocity fluctuations of the flame, is characteristic for a flow behind a stabilizing disk, originating from a periodic shedding called the Von Kármán vortex street. It implicitly confirms the entrainment of cold ambient air into the flame, causing a decrease of the flame temperature. The main mechanism for stabilization in this type of flame is the mixing between hot combustion products and fresh reactants. Once, due to entrainment, the temperature of the combustion products is decreased to a certain level, this process is interrupted and the flame is destabilized.

The average OH concentration is constant ($\overline{c_{OH}} \approx 5 \times 10^{15}$ cm^{-3}) within the recirculation zone. The mean temperature is constant in this region as well, some 10 % below the adiabatic flame temperature of 1898 K. Therefore, it was concluded that the recirculation zone must be in some kind of chemical equilibrium, which was confirmed by numerical predictions assuming chemical equilibrium. Entrainment of ambient air disturbs this chemical equilibrium, resulting in lower OH concentrations and temperatures. These lower concentrations were revealed in the probability density functions of OH concentration fluctuations. Unfortunately, because of the low sampling rate of the temperature measurements, instantaneous low temperatures were not elucidated.

Estimation of length scales of axial velocity fluctuations and of OH concentration fluctuations enabled us to characterize the centreline stagnation point of the flame as a well-stirred reactor and all other regions as distributed reaction zones. Characteristic length scales $\mathcal{L}_u$ were in the range 2-25 mm, and $\mathcal{L}_{OH}$ in the range 5-20 mm. Apparently, the size of the large eddies in the flame is typically of the order of one third to one quarter of the diameter of the stabilizing disk. Also based on visualization of the OH radical distribution in the flame, it appeared that the flame can not be modelled by a single flame theory. Around the recirculation zone, the flame structure development comprises three stages: (i) a thin flame just downstream of the flow separation edge where combustion is initiated, (ii) a developed turbulent shear layer with large-scale coherent structure, and (iii) a thick flame downstream of the recirculation zone, around the stagnation zone, where entrainment is the dominant mechanism.

6.2 Structure of piloted jet diffusion flame

A jet configuration (D_{jet} = 6 mm) with turbulent primary annular air and well-defined initial and boundary conditions was investigated. The influence of the primary annular air flow was addressed in nonreacting jets. It appeared that the main effect of the turbulent annular air was to cause mixing closer to the burner nozzle than in a situation

with zero coflow; the maximum of the turbulence kinetic energy k_{max} occurs near x = 40 mm with turbulent primary air and near x = 50 mm in zero coflow. The development of shear layers between the central jet flow and the primary annular air, but also between primary and secondary air, is held responsible for this effect. In the nonpremixed jet flame, the flow is accelerated in the reaction zone. As a result, in the upstream part, less annular air is entrained into the central fuel jet than in its nonreacting equivalent. This explains the measured extension of the potential core and the suppression of centreline turbulence in the flame; $k_{max} \approx 5$ m^2/s^2 in the range x = 100-150 mm in the flame and $k_{max} \approx 8$ m^2/s^2 near x = 40 mm in its nonreacting equivalent.

Variation of shear and mixing rates resulted in the investigation of low-turbulence flames to flames with high probability of local extinction. The ratio of the fuel jet velocity and the primary annular air velocity is of major importance to the flame length. With a smaller ratio U_{jet}/U_{ann}, the reaction zone is deformed stronger, thus increasing the reaction zone area and leading to faster burnout of the reactants and an overall shorter flame. The absolute difference between jet velocity and primary air velocity was found to govern the entrainment rate of air into the fuel jet, and thereby the width of the flames. With a larger difference (U_{jet} - U_{ann}), a stronger shear layer is generated, resulting in increased entrainment of air into the fuel jet and a wider flame.

The initial velocity profiles, measured at x = 3 mm, are very important for the downstream development of the flow and revealed that the annular air flow may be regarded as a developed turbulent pipe flow. The central fuel jet, however, has a uniform velocity characteristic, caused by the pilot flame insert, which significantly reduces the initial pipe jet diameter. Turbulence intensities of the inlet profiles ranged from 7-15 %. Formation of a recirculation region, immediately downstream of the burner rim between the central jet and the annulus was indicated as well. This recirculation zone affects the flame structure. The composition of the resulting premixed flame, however, largely determined by the annular air flow, is such that no stabilization effect, additional to the pilot flames was expected.

The turbulence in all flames is highly anisotropic ($u'_{rms}/v'_{rms} \approx$ 1.5-5) in all flow regions. Radial positions of the maximum turbulence intensity did not correspond to radial positions of the flame front (indicated by maximum mean temperature and average OH concentration) in the upstream part of the flames. Instead, the flame front is located in regions where turbulence levels were low; typically on the fuel-lean side of the shear layer between central fuel and annular air flow. As the flames develop downstream, the peaks of the turbulence energy shift to coincide with the flame front. Comparing the upstream behaviour of the different flames, it appeared that with higher primary annular air velocity, the turbulence at the position of the flame front increased. This explains the larger interaction between (shear layer generated) turbulence and chemistry in the flames with a high annular air velocity, leading to increased probability of local extinction. Especially large-scale vortices, indicated in the probability density functions of velocities and LDA measurements conditional on jet fluid and annular fluid, will influence the upstream flame structure and set up local extinctions. The

occurrence of local extinction is not only evidenced in the visualization of the flame front, but is also reflected in the lower average OH concentration levels and mean temperatures.

The magnitude of time and length scales of axial velocity fluctuations is similar in the flame as in its nonreacting equivalent in the upstream region of the flows. The fact that length scales of velocity fluctuations are of the same order of magnitude for all flames investigated ($\mathcal{L}_u \approx D_{\text{jet}}/3 = 2$ mm at $x = 50$ mm and $\mathcal{L}_u \approx D_{\text{jet}} = 6$ mm at $x = 250$ mm), implies that global differences between these flames are not to be explained by these structures, but rather by the previously mentioned, large-scale shear layer development. Based on a comparison between length scales of turbulence and of OH concentration fluctuations, it was decided that the flames could be characterized as distributed reactors (for the range of the experiments). Together with the flow field data, this provided an important tool for evaluating the validity of turbulence and chemistry models describing turbulent flames.

A comparison of experimental data in a reference flame with numerical predictions showed excellent agreement for axial mean and rms velocities and mean temperature and qualitative correspondence for Reynolds shear stresses. Despite the large anisotropy of turbulence in the flow, the k-ε model performs well. Discrepancies between calculated and observed average OH concentrations suggested that even further improvement of the present chemistry models is possible by inclusion of local extinction (and the ensuing superequilibrium species concentrations).

Principal symbols

a	thermal diffusivity	(m^2/s)
c	concentration	(m^{-3})
c_p	heat capacity at constant pressure	(J/kg mole K)
d	disk diameter	(m)
D	exit diameter	(m)
d_f	fringe separation	(m)
D_h	hydraulic diameter	(m)
D_t	thermocouple diameter	(m)
f	focal length	(m)
$f(x)$	spatially-resolved fluorescence profile	(m^{-3})
h_t	convective heat transfer coefficient	(W/m^2K)
$I^i_{rel}(x)$	relative laser intensity profile	(-)
I_ν	laser spectral intensity	(J)
k	turbulence kinetic energy	(m^2/s^2)
L	characteristic length scale	(m)
l_f	characteristic flame thickness	(m)
l_K	Kolmogorov length scale	(m)
N	number density	(m^{-3})
P	probability density function	(-)
R	universal gas constant	(J/mole K)
S_l	laminar flame speed	(m/s)
$S(\nu)$	power spectral density function	(-)
t	time	(s)
T	temperature	(K)
T_{ad}	adiabatic flame temperature	(K)
T_g	gas temperature	(K)
u	axial velocity	(m/s)
U	characteristic mean velocity	(m/s)
U_0	exit velocity	(m/s)
u_f	characteristic flame velocity	(m/s)
v	radial velocity	(m/s)
v_K	Kolmogorov velocity scale	(m/s)
w	width	(m)
$w(x)$	laser intensity independent signal	(a.u.)

x	axial distance	(m)
y	radial distance	(m)

Greek symbols

δ	spatial difference	(m)
δ_l	laminar flame thickness	(m)
ε	rate of dissipation	(m^2/s^3)
θ	angle of intersection	(°)
λ	thermal conductivity coefficient	(W/m K)
λ	wavelength	(m)
λ	Taylor micro length scale	(m)
ν	frequency	(s^{-1})
ν	kinematic viscosity	(m^2/s)
ν_D	Doppler frequency	(s^{-1})
ξ	mixture fraction	(-)
ρ	density	(kg/m^3)
$\rho(x, y, \delta)$	spatially-resolved autocorrelation function	(-)
$\rho(\tau)$	time-resolved autocorrelation function	(-)
τ	time difference	(s)
τ	Taylor micro time scale	(s)
τ_c	characteristic chemical time scale	(s)
τ_K	Kolmogorov time scale	(s)
τ_m	characteristic mixing time scale	(s)
τ_q	characteristic quenching time	(s)
ϕ	mass flow rate	(kg/s)
φ	equivalence ratio	(-)
χ	dissipation rate	(s^{-1})
χ_q	quenching dissipation rate	(s^{-1})

Calligraphic symbols

$\mathcal{D}$	molecular diffusion coefficient	(m^2/s)
$\mathcal{L}$	integral length scale	(m)
$\mathcal{T}$	integral time scale	(s)

Subscripts

ann	property of annulus
c	property of cold reactants
co	property of coflow
h	property of hot products
jet	property of jet
OH	property of OH concentration
NO	property of NO concentration

u	property of axial velocity field
st	stoichiometric value
rms	root mean square value

Superscripts

$(.)^i$	index
$(.)'$	fluctuating value
$\overline{(.)}$	Reynolds-averaged value
$\widetilde{(.)}$	Favre-averaged value

Non-dimensional numbers

Da	Damköhler number = $\frac{\tau_m}{\tau_c}$
Ka	Karlovitz number = $\frac{\tau_c}{\tau_K}$
Nu	Nusselt number = $\frac{h_t D_t}{\lambda}$
Pr	Prandtl number = $\frac{\nu}{a}$
Re	Reynolds number = $\frac{UL}{\nu}$
$Re_{\mathcal{L}}$	turbulence Reynolds number= $\frac{u'_{rms}\mathcal{L}_u}{\nu}$

Bibliography

Aldén, M., Edner, H., Holmstedt, G., Svanberg, S. and Högberg, T. Single-pulse laser-induced OH fluorescence in an atmospheric flame, spatially resolved with a diode array detector. *Applied Optics*, 21:1236–1240, 1982.

Altenkirch, R.A. and Mellor, A.M. Emissions and performance of continuous flow combustors. In *Proceedings of 15th Symposium (International) on Combustion*, pages 1181–1189. The Combustion Institute, Pittsburgh, 1974.

Ballal, D.R. and Lefebvre, A.H. Weak extinction limits of turbulent flowing mixtures. *Journal of Engineering for Power*, 100:343–348, 1979.

Ballal, D.R. and Lefebvre, A.H. Some fundamental aspects of flame stabilization. In *Proceedings of 5th International Symposium on Airbreathing Engines*, pages 48.1–48.8. ISABE, 1981.

Barlow, R.S., Dibble, R.W., Chen, J.Y. and Lucht, R.P. Effect of Damköhler number on superequilibrium OH concentration in turbulent nonpremixed jet flames. *Combustion and Flame*, 82:235–251, 1990.

Barlow, R.S., Dibble, R.W., Stårner, S.H. and Bilger, R.W. Piloted diffusion flames of nitrogen-diluted methane near extinction: OH measurements. In *Proceedings of 23rd Symposium (International) on Combustion*, pages 583–589. The Combustion Institute, Pittsburgh, 1990.

Beér, J.M. and Chigier, N.A. *Combustion Aerodynamics*. Applied Science, Essex, 1972.

Bell, W.A. Spectral analysis algorithms for the laser velocimeter: a comparative study. *AIAA Journal*, 21:714–731, 1982.

Benedict, R.P. Manual on the use of thermocouples in temperature measurement. Technical report, American Society for Testing and Materials, Philadelphia, 1981.

Bilger, R.W. Turbulent diffusion flames. *Annual Review on Fluid Mechanics*, 21:101–135, 1989.

Bohan, M., Claypole, T.C., Jones, L.M. and Rollings, H. Velocity measurements in gas flames. In *3rd International Conference on Laser Anemometry - Advances and Applications*, pages 5.1–5.10, 1989.

Borghi, R. On the structure of turbulent premixed flames. In Bruno, C. and Casci, C., editors, *Recent Advances in Aeronautical Science*. Pergamon, 1984.

Borghi, R. Turbulent combustion modelling. *Progress in Energy and Combustion Science*, 14:245–292, 1988.

Bradley, D. and Matthews, K.J. Measurement of high gas temperatures with fine wire thermocouples. *Journal of Mechanical Engineering Science*, 10:299–305, 1968.

Bradley, D., Gaskell, P.H. and Lau, A.K.C. A mixedness-reactedness flamelet model for turbulent diffusion flames. In *Proceedings of 23rd Symposium (International) on Combustion*, pages 685–692. The Combustion Institute, Pittsburgh, 1990.

Bray, K.N.C., Libby, P.A. and Moss, J.B. Unified modeling approach for premixed turbulent combustion - Part I: General formulation. *Combustion and Flame*, 61:87–102, 1985.

Broadwell, J.E. and Mungal, M.G. Molecular mixing and chemical reactions in turbulent shear layers. In *Proceedings of 22nd Symposium (International) on Combustion*, pages 579–587. The Combustion Institute, Pittsburgh, 1988.

Broadwell, J.E., Dahm, W.J.A. and Mungal, M.G. Blowout of turbulent diffusion flames. In *Proceedings of 20th Symposium (International) on Combustion*, pages 303–310. The Combustion Institute, Pittsburgh, 1984.

Brown, G.L. and Roshko, A. On density effects and large structure in turbulent mixing layers. *Journal of Fluid Mechanics*, 64:775–816, 1974.

Buchhave, P. and George, W.K. Bias correction in turbulence measurements. In Thompson, H. and Stevenson, W., editors, *Laser Velocimetry and Particle Sizing*. Hemisphere Publishing Corporation, 1979.

Byggstøyl, S. and Magnussen, B.F. A model for flame extinction in turbulent flow. In Bradbury, L., editor, *Turbulent Shear Flows*, volume 4, pages 381–395. Springer Verlag, 1985.

Chen, T.H. and Goss, L.P. Statistical OH-zone structures of turbulent jet flames from liftoff to near-blowout. *Combustion Science and Technology*, 79:311–324, 1991.

Chen, L.D., Seaba, J.P., Roquemore, W.M. and Goss, L.P. Buoyant diffusion flames. In *Proceedings of 22nd Symposium (International) on Combustion*, pages 677–684. The Combustion Institute, Pittsburgh, 1988.

Chen, T.H., Goss, L.P., Trump, D.D. and Schmoll, W.J. Studies of a turbulent premixed flame using CARS-LDV diagnostics. In *24th Joint Propulsion Conference*, pages 1–9. AIAA, 1988.

Correa, S.M. and Gulati, A. Nonpremixed turbulent CO_2/H_2 flames at local extinction conditions. In *Proceedings of 22nd Symposium (International) on Combustion*, pages 599–606. The Combustion Institute, Pittsburgh, 1988.

Crosley, D.R. and Smith, G.P. Laser-induced fluorescence spectroscopy for combustion diagnostics. *Optical Engineering*, 22:545–553, 1983.

Dahm, W.J.A. and Dibble, R.W. Coflowing turbulent jet diffusion flame blowout. In *Proceedings of 22nd Symposium (International) on Combustion*, pages 801–808. The Combustion Institute, Pittsburgh, 1988.

Davies, T.W. and Beér, J.M. Flow in the wake of bluff-body flame stabilizers. In *Proceedings of 13th Symposium (International) on Combustion*, pages 631–638. The Combustion Institute, Pittsburgh, 1970.

DeOtte, R.E., Morrison, G.L. and Wiedner, B.G. Considerations on the velocity bias in laser Doppler velocimetry. In *Proceedings of 6th International Symposium on Applications of Laser Technology to Fluid Mechanics*, pages 5.3.1–5.3.4, 1992.

Dibble, R.W., Kollmann, W. and Schefer, R.W. Conserved scalar fluxes measured in a turbulent nonpremixed flame by combined laser Doppler velocimetry and laser Raman scattering. *Combustion and Flame*, 55:307–321, 1984.

Dibble, R.W., Hartmann, V., Schefer, R.W. and Kollmann, W. Conditional sampling of velocity and scalars in turbulent flames using simultaneous LDV-Raman scattering. *Experiments in Fluids*, 5:103–113, 1987.

Dieke, G.H. and Crosswhite, H.M. The ultraviolet bands of OH. *Journal of Quantitative and Radiation Transfer*, 2:97–199, 1962.

Donnerhack, S. and Peters, N. Stabilization heights in lifted methane-air jet diffusion flames diluted with nitrogen. *Combustion Science and Technology*, 41:101–108, 1984.

Drain, L.E. *The Laser Doppler Technique*. John Wiley & sons, Chichester, 1980.

Durão, D.F.G. and Whitelaw, J.H. Velocity characteristics of the flow in the near wake of a disk. *Journal of Fluid Mechanics*, 85:369–385, 1978.

Durão, D.F.G. and Whitelaw, J.H. Relationship between velocity and signal quality in laser Doppler anemometry. *Journal of Physics E: Scientific Instrumentation*, 12:47–50, 1979.

Durão, D.F.G., Pita, G., Velho, A., Founti, M.A., Laker, J. and Whitelaw, J. Some consequences of bias effects. In *Proceedings of 1st International Symposium on Applications of Laser Doppler Techniques to Fluid Mechanics*, pages 381–391, 1982.

Durst, F., Melling, A. and Whitelaw, J.H. *Principles and Practice of Laser Doppler Anemometry*. Academic Press, London, 1976.

Eckbreth, A.C. *Laser Diagnostics for Combustion Temperature and Species*. Abacus Press, Cambridge Massachusetts, 1988.

Edwards, R.V. Report on the special panel on statistical particle bias in laser anemometry. *Journal of Fluids Engineering*, 109:89–93, 1987.

Faeth, G.M. and Samuelsen, G.S. Fast reaction nonpremixed combustion. *Progress in Energy and Combustion Science*, 12:305–372, 1986.

Ferrão, P.M.C. and Heitor, M.V. Probe and optical techniques for simultaneous scalar-velocity measurements. In Durão, D.F.G., Heitor, M.V., Whitelaw, J.H. and Witze, P.O., editors, *Combusting Flow Diagnostics*, pages 169–231. Kluwer Academic Publishers, 1992.

Ferrão, P.M.C. and Heitor, M.V. On the analysis of turbulent mixing in recirculating flames. In *Joint Meeting of the British and German Sections of the Combustion Institute*, pages 80–83. The Combustion Institute, Cambridge, 1993.

Fraser, R., Pack, C.J. and Santavicca, D.A. A LDV system for turbulence length scale measurements. *Experiments in Fluids*, 4:150–152, 1986.

Fristrom, R.M. and Westenberg, A.A. *Flame Structure*. McGraw-Hill Book Company, New York, 1965.

Gardiner, W.C. *Combustion Theory*. Springer Verlag, New York, 1984.

Geerssen, T.M. *Physical Properties of Natural Gases*. N.V. Nederlandse Gasunie, Groningen, 1980.

Glass, M. and Bilger, R.W. The turbulent jet diffusion flame in a co-flowing stream - Some velocity measurements. *Combustion Science and Technology*, 18:165–177, 1978.

Glass, M. and Kennedy, I.M. An improved seeding method for high temperature laser Doppler velocimetry. *Combustion and Flame*, 29:333–335, 1977.

Glassman, I. *Combustion*. Academic Press, London, 1987.

Goss, L.P., Trump, D.D. and Roquemore, W.M. Combined CARS/LDA instrument for simultaneous temperature and velocity measurements. *Experiments in Fluids*, 6:189–198, 1988.

Hanson, R.K. Combustion diagnostics: Planar imaging techniques. In *Proceedings of 21st Symposium (International) on Combustion*, pages 1677–1691. The Combustion Institute, Pittsburgh, 1986.

Heitor, M.V., Taylor, A.M.K.P. and Whitelaw, J.H. Simultaneous velocity and temperature measurements in a premixed flame. *Experiments in Fluid*, 3:323–339, 1985.

Heitor, M.V., Taylor, A.M.K.P. and Whitelaw, J.H. The interaction of turbulence and pressure gradients in a baffle-stabilized premixed flame. *Journal of Fluid Mechanics*, 181:387–413, 1987.

Heitor, M.V., Taylor, A.M.K.P. and Whitelaw, J.H. Velocity and scalar characteristics of turbulent premixed flames stabilized on confined axisymmetric baffles. *Combustion Science and Technology*, 62:97–126, 1988.

Hertz, H.M. and Aldén, M. Calibration of imaging laser-induced fluorescence measurements in highly absorbing flames. *Applied Physics B*, 42:97–102, 1987.

Hinze, J.O. *Turbulence*. McGraw-Hill, Inc., New York, 1975.

Hussein, H.J., Capp, S.P. and George, W.K. Velocity measurements in a high-Reynolds-number momentum-conserving, axisymmetric, turbulent jet. *Journal of Fluid Mechanics*, 258:31–75, 1994.

Janicka, J. and Peters, N. Prediction of turbulent jet diffusion flame lift-off using a pdf transport equation. In *Proceedings of 19th Symposium (International) on Combustion*, pages 367–374. The Combustion Institute, Pittsburgh, 1982.

Jones, W.P. and Whitelaw, J.H. Modelling and measurements in turbulent combustion. In *Proceedings of 20th Symposium (International) on Combustion*, pages 233–249. The Combustion Institute, Pittsburgh, 1984.

Kalghatgi, G.T. Blow-out stability of gaseous jet diffusion flames. Part I: In still air. *Combustion Science and Technology*, 26:233–239, 1981.

Kalghatgi, G.T. Liftoff heights and visible lengths of vertical turbulent jet diffusion flames in still air. *Combustion Science and Technology*, 41:17–29, 1984.

Kee, R.J., Grcar, J.F., Smooke, M.D. and Miller, J.A. A Fortran program for modeling steady laminar one-dimensional premixed flames. Technical report, SANDIA, Livermore, 1985.

Kreid, D.K. Laser Doppler velocimeter measurements in nonuniform flow: Error estimates. *Applied Optics*, 13(8):1872–1881, 1974.

Labacci, K., Stepowski, D., Cabot, G. and Trinite, M. Conditional LDV in turbulent diffusion flame. In *Proceedings of 4th International Symposium on Applications of Laser anemometry to Fluid Mechanics*, page 5.9, 1988.

Law, C.K. Dynamics of stretched flames. In *Proceedings of 22nd Symposium (International) on Combustion*, pages 1381–1402. The Combustion Institute, Pittsburgh, 1988.

Lees, L. Fluid-mechanical aspects of flame stabilization. *ARS Jet Propulsion*, 24:234–236, 1954.

Liñán, A. The asymptotic structure of counterflow diffusion flames for large activation energies. *Acta Astronautica*, 1:1007–1039, 1979.

Libby, P.A. and Williams, F.A. Some implications of recent theoretical studies in turbulent combustion. *AIAA Journal*, 19:261–274, 1981.

Libby, P.A. Theory of normal premixed turbulent flames revisited. *Progress in Energy Combustion and Science*, 11:83–96, 1985.

Lockwood, F.C. and Megahed, I.E.A. Extinction in turbulent reacting flows. *Combustion Science and Technology*, 19:77–80, 1978.

Longwell, J.P., Frost, E.E. and Weiss, M.E. Flame stability in bluff body recirculation zones. *Industrial and Engineering Chemistry*, 45:1629–1633, 1953.

Lucht, R.P., Sweeney, D.W. and Laurendeau, N.M. Balanced cross-rate model for saturated molecular fluorescence in flames using a nanosecond pulse length laser. *Applied Optics*, 19:3295–3300, 1980.

Lucht, R.P., Sweeney, D.W., Laurendeau, N.M., Drake, M.C., Lapp, M. and Pitz, R.W. Single-pulse laser-saturated fluorescence measurements of OH in turbulent nonpremixed flames. *Optics Letters*, 9:90–92, 1984.

Masri, A.R., Bilger, R.W. and Dibble, R.W. Turbulent nonpremixed flames of methane near extinction: Mean structure from Raman measurements. *Combustion and Flame*, 71:245–266, 1988.

Masri, A.R., Bilger, R.W. and Dibble, R.W. Turbulent nonpremixed flames of methane near extinction: Probability density functions. *Combustion and Flame*, 73:261–285, 1988.

McLaughlin, D.K. and Tiederman, W.G. Biasing correction for individual realization of laser anemometer measurements in turbulent flows. *Physics in Fluids*, 16:2082–2087, 1973.

Meneveau, C. and Sreenivasan, K.R. The multifractal nature of turbulent energy dissipation. *Journal of Fluid Mechanics*, 224:429–484, 1991.

Meyers, J.F. Laser velocimeter data acquisition and real time processing using a microcomputer. In *Proceedings of 4th International Symposium on Applications of Laser Techniques to Fluid Mechanics*, 1988.

Mossel, M.D. *Thermal Stratification of Turbulent Air Flows in a Rectangular Channel.* PhD thesis, Delft University of Technology, 1995.

Namazian, M., Schefer, R.W. and Kelly, J. Scalar dissipation measurements in the developing region of a jet. *Combustion and Flame*, 74:147–160, 1988.

Pan, C.P. *Laser-Diagnostic Studies of Confined Turbulent Premixed Flames Stabilized by Conical Bluff Bodies.* PhD thesis, University of Dayton, 1991.

Panchapakesan, N.R. and Lumley, J.L. Turbulence measurements in axisymmetric jets of air and helium. Part I. Air jet. *Journal of Fluid Mechanics*, 246:197–223, 1993.

Peeters, T.W.J. *Modeling of Turbulent Natural Gas Diffusion Flames.* PhD thesis, Delft University of Technology, 1995.

Peters, N. and Williams, F.A. Liftoff characteristics of turbulent jet diffusion flames. *AIAA Journal*, 21:423–429, 1983.

Peters, N. Local quenching due to flame stretch and nonpremixed turbulent combustion. *Combustion Science and Technology*, 30:1–17, 1983.

Peters, N. Laminar diffusion flamelet models in nonpremixed turbulent combustion. *Progress in Energy and Combustion Science*, 10:319–339, 1984.

Peters, N. Laminar flamelet concepts in turbulent combustion. In *Proceedings of 21st Symposium (International) on Combustion*, pages 1231–1250. The Combustion Institute, Pittsburgh, 1986.

Peters, N. Length scales in laminar and turbulent flames. *Progress in Astronautics and Aeronautics*, 135:155–182, 1991.

Peters, N. Premixed, non-premixed and partially premixed turbulent combustion with fast chemistry. In *Joint Meeting of the British and German Sections of the Combustion Institute*, pages 26–33. The Combustion Institute, Cambridge, 1993.

Pitts, W.M. Assessment of theories for the behavior and blowout of lifted turbulent jet diffusion flames. In *Proceedings of 22nd Symposium (International) on Combustion*, pages 809–816. The Combustion Institute, Pittsburgh, 1988.

Plee, S.L. and Mellor, A.M. Characteristic time correlation for lean blowoff of bluff-body-stabilized flames. *Combustion and Flame*, 35:61–80, 1979.

Pope, S.B. Turbulent premixed flames. *Annual Review on Fluid Mechanics*, 19:237–270, 1987.

Razdan, M.K. and Stevens, J.G. CO/air turbulent diffusion flame: Measurements and modeling. *Combustion and Flame*, 59:289–301, 1985.

Schefer, R.W. and Dibble, R.W. Simultaneous measurements of velocity and density in a turbulent nonpremixed flame. *AIAA Journal*, 23:1070–1078, 1985.

Schefer, R.W., Hartmann, V. and Dibble, R.W. Conditional sampling of velocity in a turbulent nonpremixed propane jet. *AIAA Journal*, 25:1318–1320, 1987.

Schefer, R.W., Namazian, M. and Kelly, J. Structural characteristics of lifted turbulent-jet flame. In *Proceedings of 22nd Symposium (International) on Combustion*, pages 833–842. The Combustion Institute, Pittsburgh, 1988.

Schefer, R.W., Namazian, M. and Kelly, J. CH, OH and CH_4 concentration measurements in a lifted turbulent-jet flame. In *Proceedings of 23rd Symposium (International) on Combustion*, pages 669–676. The Combustion Institute, Pittsburgh, 1990.

Schlichting, H. *Boundary-Layer Theory*. McGraw-Hill Book Company, New York, 1968.

Seitzman, J.M. and Hanson, R.K. Planar fluorescence imaging: Basic concepts for scalar and velocity measurements. In Durão, D.F.G., Heitor, M.V., Whitelaw, J.H. and Witze, P.O., editors, *Combusting Flow Diagnostics*, pages 137–157. Kluwer Academic Publishers, 1992.

Seitzman, J.M., Üngüt, A., Paul, P.H. and Hanson, R.K. Imaging and characterization of OH structures in a turbulent nonpremixed flame. In *Proceedings of 23rd Symposium (International) on Combustion*, pages 637–644. The Combustion Institute, Pittsburgh, 1990.

Sislian, J.P., Jiang, L.Y. and Cusworth, R.A. Laser Doppler velocimetry investigation of the turbulence structure of axisymmetric diffusion flames. *Progress in Energy and Combustion Science*, 14:99–146, 1988.

Smooke, M.D., Seshadri, K. and Puri, I.K. The structure and extinction of partially premixed flames burning methane in air. In *Proceedings of 22nd Symposium (International) on Combustion*, pages 1555–1563. The Combustion Institute, Pittsburgh, 1988.

Spalding, D.B. Mixing and chemical reaction in steady confined turbulent flames. In *Proceedings of 13th Symposium (International) on Combustion*, pages 649–657. The Combustion Institute, Pittsburgh, 1970.

Stårner, S.H. and Bilger, R.W. LDA measurements in a turbulent diffusion flame with axial pressure gradient. *Combustion Science and Technology*, 21:259–276, 1980.

Stårner, S.H. and Bilger, R.W. Measurements of scalar-velocity correlations in a turbulent diffusion flame. In *Proceedings of 18th Symposium (International) on Combustion*, pages 921–930. The Combustion Institute, Pittsburgh, 1981.

Stårner, S.H. and Bilger, R.W. Characteristics of a piloted diffusion flame designed for study of combustion turbulence interactions. *Combustion and Flame*, 61:29–38, 1985.

Stårner, S.H. and Bilger, R.W. Some budgets of turbulent stresses in round jets and diffusion flames. *Combustion Science and Technology*, 53:377–398, 1987.

Stårner, S.H., Bilger, R.W., Dibble, R.W. and Barlow, R.S. Piloted diffusion flames of diluted methane near extinction: Detailed structure from laser measurements. *Combustion Science and Technology*, 72:255–269, 1990.

Stårner, S.H., Bilger, R.W. and Barlow, R.S. Raman/LIF measurements in a lifted hydrocarbon jet flame. In *Proceedings of 8th Symposium on Turbulent Shear Flows*, pages 1–3, 1991.

Stårner, S.H., Bilger, R.W., Dibble, R.W., Barlow, R.S., Fourguette, D.C. and Long, M.B. Joint planar CH and OH LIF imaging in piloted turbulent diffusion flames near extinction. In *Proceedings of 24th Symposium (International) on Combustion*, pages 341–349. The Combustion Institute, Pittsburgh, 1992.

Stårner, S.H., Kelman, J.B., Masri, A.R. and Bilger, R.W. Simultaneous multi-species imaging in turbulent flames. preprint, 1993.

Stårner, S.H. Some triple correlation measurements of velocity and scalars in a turbulent diffusion flame. *Combustion Science and Technology*, 48:99–105, 1986.

Stepowski, D., Labacci, K. and Borghi, R. Instantaneous radial profiles of OH fluorescence and Rayleigh scattering through a turbulent H_2-air diffusion flame. In Borghi, R. and Murthy, S.N.B., editors, *Lecture Notes in Engineering - Turbulent Reactive Shear Flows*. Springer Verlag, 1989.

Takahashi, F. and Schmoll, W.J. Lifting criteria of jet diffusion flames. In *Proceedings of 23rd Symposium (International) on Combustion*, pages 677–683. The Combustion Institute, Pittsburgh, 1990.

Taylor, A.M.K.P. and Whitelaw, J.H. Velocity and temperature measurements in a premixed flame within an axisymmetric combustor. In *Testing and Measurement Techniques in Heat Transfer and Combustion*, pages 14.1–14.11. AGARD, 1980.

Tennekes, H. and Lumley, J.L. *A First Course in Turbulence*. The MIT Press, Cambridge, Massachusetts, 1972.

Vanquickenborne, L. and Tiggelen, A. van. The stabilization mechanism of lifted diffusion flames. *Combustion and Flame*, 10:59–69, 1966.

Vries, J.E. de, Meer, Th.H. van der, Roeckaerts, D. and Hoogendoorn, C.J. OH radical concentration fluctuations and length scales in turbulent diffusion flames. In *Joint Meeting of the British and German Sections of the Combustion Institute*, pages 307–310. The Combustion Institute, Cambridge, 1993.

Vries, J.E. de. *Study on Turbulent Fluctuations in Diffusion Flames Using Laser-Induced Fluorescence*. PhD thesis, Delft University of Technology, 1994.

Watrasiewicz, B.M. and Rudd, M.J. *Laser Doppler Measurements*. Butterworths, London, 1976.

Westbrook, C.K. and Dryer, F.L. Chemical kinetic modeling of hydrocarbon combustion. *Progress in Energy and Combustion Science*, 10:1–57, 1984.

Williams, F.A. *Combustion Theory-The Fundamental Theory of Chemically Reacting Flow Systems*. Addison-Wesley Publishing Company, Inc., Redwood City, 1985.

Wygnanski, I. and Fiedler, H. Some measurements in the self-preserving jet. *Journal of Fluid Mechanics*, 38:577–612, 1969.

Zhang, Z. and Wu, J. On principal noise of the laser Doppler velocimeter. *Experiments in Fluids*, 5:193–196, 1987.

Zukoski, E.E. and Marble, F.E. Experiments concerning the mechanism of flame blowoff from bluff bodies. In *Proceedings of Gas Dynamics Symposium on Aerothermochemistry*, pages 205–210. Northwestern University, 1956.

Summary

Combustion of natural gas is an important means to supply energy for both industrial and domestic applications in modern society. Knowledge of the governing processes is limited, however, because of the complex interactions between flame chemistry and turbulence. To gain insight in the fundamentals of the combustion process, in this thesis, the turbulence and chemical structure of laboratory-scale flames have been studied. The principal aim of this study was to provide experimental data to comprehend the combustion process in these flames. In addition, the measurements should be able to validate numerical combustion models.

With these experimental data, characteristic dimensionless numbers and properties of the chemistry and turbulence in the flames under investigation could be derived. In this way, it was possible to distinguish between various types of turbulent combustion and develop theories that describe the observed phenomena. Drawbacks of existing models appear immediately, when trying to apply them to practical combustion situations, where flame destabilization and local extinctions occur as a result of interactions between turbulence and chemistry.

The main aspects of turbulence-chemistry interactions have been investigated in two completely different burner configurations. In the first part of this thesis, the flame structure of a disk-stabilized premixed flame has been evaluated, as a contribution to a European SCIENCE project. The second part of this thesis is associated with combustion in piloted jet diffusion flames. For this configuration, our Heat Transfer Group aims to construct an extensive data base with experimental and numerical results.

In order to resolve the time-dependent turbulent velocity field of the flames under investigation, Laser Doppler Anemometry (LDA) measurements have been performed. With this technique, velocity characteristics of the flows, the degree of turbulent mixing and estimates of characteristic time scales of turbulent eddies were obtained. The mutual interaction between turbulence and chemistry was addressed by measuring properties of the important combustion radical OH with Laser Induced Fluorescence (LIF). Results obtained in a one-dimensional premixed flat flame, whose OH concentration could be calculated by means of a numerical code, served as calibration. The laser induced fluorescence from points along a radial cross section of the flame was recorded using a diode line array camera. This enabled us to measure not only average and fluctuating properties, but also spatial correlations, from which length scales could be derived. In order to evaluate the spatial structure of the flames, planar LIF measurements were performed to obtain 2-dimensional images of the OH radical distribution in the flames.

Also mean temperatures, measured by thermocouples, added important information on the general flame structures.

In the first part of this thesis, experiments in a disk-stabilized premixed flame were reported. The burner consists of a disk with a diameter of 80 mm, located at the centre of an exit section of a contraction with a diameter of 85 mm. With a flow issuing from this burner annulus with a velocity of 13.2 m/s ($Re \approx 4.4 \times 10^3$), a recirculation zone is formed downstream of the stabilizing disk. The magnitude of this recirculation zone was investigated in both an isothermal flow and a fuel-lean (equivalence ratio $\varphi = 0.75$) premixed natural gas/air flame.

Additionally to the mean velocity fields, turbulence properties have been measured in the cold flow and the flame. Turbulence in these flows is mainly generated by shear layers: one shear layer between the recirculation zone and its surrounding high-velocity layer and a second between the high-velocity layer and the stagnant ambient air. The first shear layer is of importance for stabilization of the flame. It causes a continuous mixing of hot combustion products and fresh reactants. The influence of the second shear layer is mainly to introduce destabilization of the flame, because it decreases the local flame temperature due to entrainment of cold ambient air into the main reaction zone. This important phenomenon was elucidated by visualization of the OH radical distribution in the flame. It also explains the presence of a dominant frequency in the axial velocity fluctuations throughout the flame.

Despite these local and instantaneous interruptions of the combustion process, a constant mean temperature within the recirculation zone was measured. The average OH concentration was constant as well, enabling us to identify the recirculation zone as a region of chemical equilibrium. Derivation of time and length scales of velocity fluctuations and OH concentration fluctuations, respectively, provided a characterization of the regime of combustion for the flame under investigation. Altogether, not only the main combustion process (featuring stabilizing and destabilizing factors) was revealed, but also all conditions were fulfilled to validate numerical models, describing the disk-stabilized premixed flame.

In the second part of the research described in this thesis, turbulence and OH structures in piloted jet diffusion flames are dealt with. A round fuel jet, with an exit diameter of 6 mm is surrounded by an annulus of primary air with a 15 mm inner diameter and 45 mm outer diameter. Flame stabilization is ensured using pilot flames. The burner was placed in a burner chamber with a coflowing secondary air stream. The primary air velocity and the fuel jet velocity were used for variation of shear and mixing rates near the burner nozzle. As a result, flames ranging from fully connected flames ($Re \approx 4 \times 10^3$) to flames with a high probability of local extinction ($Re \approx 10 \times 10^3$) and even a flame at lift-off could be investigated.

The initial and boundary conditions of these three-flow flames are well-defined. The influence of the turbulent primary annular air flow on the central jet was first addressed in nonreacting jets. Next to mean velocities, turbulence properties and time

scales were derived in nonreacting and reacting flows. The development of a second shear layer (between primary and seondary air flows), additionally to the shear layer between the central jet and the primary air flow, is of major importance for flame length and flame width. Also on a more detailed local scale, shear layer turbulence affects the flame structure, for example in the onset of local extinction of the flame front.

Comparison of the position of maximum turbulence intensity with the location of the flame front (indicated by the maxima of the mean temperature and average OH concentration) in various flames, appeared useful in addressing turbulence-chemistry interactions. Length scales of velocity fluctuations and scalar concentration fluctuations helped us to identify these interactions even further. In general, these scales were of the same order of magnitude, indicating that momentum and species are transported by eddies of roughly the same size. Even small-scale turbulence structures interact with the flame zone, explaining the importance of detailed turbulence and chemistry models in numerical predictions. Comparison between experimental mean velocities, turbulent rms velocities and mean temperatures with numerical model calculations revealed an excellent agreement. For the Reynolds shear stresses and the average OH concentrations, a qualitative agreement was found.

It is concluded that entrainment of cold ambient air is an important destabilizing factor in the stabilization process of fuel-lean disk-stabilized premixed flames. Application of turbulent primary annular air in the piloted jet diffusion flame influences the flame structure. Not only global properties (such as flame length and flame width) but also local properties (for example the probability of local extinction of the flame front) are determined by the annular air velocity. Especially velocity gradients and the ensuing shear layer development play an important role in this process. For both investigated geometries, experimental results have become available to validate numerical model predictions. As such, the detailed measurements in this thesis contribute to solving a part of the puzzle that turbulent combustion still is.

Samenvatting

Verbranding van aardgas speelt in de huidige samenleving een belangrijke rol als middel om energie te voorzien in zowel industriële als huishoudelijke toepassingen. Kennis van de bepalende processen is echter beperkt vanwege de complexe interacties tussen vlamchemie en turbulentie. Om inzicht te krijgen in de grondbeginselen van het verbrandingsproces zijn in dit proefschrift de turbulente en chemische structuur van vlammen op laboratoriumschaal bestudeerd. Het hoofddoel van deze studie was het verkrijgen van experimentele gegevens om het verbrandingsproces in deze vlammen te begrijpen. Bovendien moesten de metingen in staat zijn om numerieke verbrandingsmodellen te valideren.

Met deze experimentele gegevens kunnen karakteristieke dimensieloze kentallen en eigenschappen van de chemie en de turbulentie in de onderzochte vlammen worden afgeleid. Op deze wijze is het mogelijk verschillende typen turbulente verbranding te onderscheiden en theorieën te ontwikkelen die de waargenomen verschijnselen verklaren. Nadelen van bestaande modellen blijken onmiddellijk wanneer ze worden toegepast op praktische verbrandingssituaties, waar vlamdestabilisatie en lokale uitdovingen plaatsvinden als gevolg van interacties tussen turbulentie en chemie.

De belangrijkste aspecten van turbulentie-chemie interacties zijn onderzocht in twee totaal verschillende branderconfiguraties. In het eerste deel van dit proefschrift is de vlamstructuur van een schijfgestabiliseerde voorgemengde vlam beschreven als bijdrage aan een Europees SCIENCE project. Het tweede deel van dit proefschrift is gerelateerd aan verbranding in diffusievlammen met stabilisatievlammetjes. Voor deze configuratie heeft onze Sectie Warmtetransport zich tot doel gesteld een uitgebreid bestand met experimentele en numerieke resultaten samen te stellen.

Om het tijdsafhankelijke turbulente snelheidsveld van de onderzochte vlammen op te lossen zijn laser Doppler anemometrie (LDA) metingen verricht. Met deze techniek zijn snelheidskarakteristieken van de stromingen, de turbulente menggraad en schattingen van karakteristieke tijdschalen van turbulente wervels verkregen. De onderlinge interactie tussen turbulentie en chemie is beschreven door eigenschappen van het belangrijke verbrandingsradicaal OH te meten met behulp van lasergeïnduceerde fluorescentie (LIF). Resultaten verkregen in een één-dimensionale voorgemengde vlakke vlam, waarvan de OH concentratie werd berekend met een numerieke code, dienden hierbij ter calibratie. De lasergeïnduceerde fluorescentie van punten langs een radiële dwarsdoorsnede van de vlam werd opgenomen met een diode lijncamera. Hierdoor zijn niet alleen gemiddelde en fluctuerende eigenschappen gemeten, maar ook ruimtelijke

correlaties waaruit lengteschalen konden worden afgeleid. Om de ruimtelijke structuur van de vlammen te bestuderen, zijn planaire LIF metingen uitgevoerd om tweedimensionale beelden van de OH radicaal verdeling in de vlammen te bepalen. Ook gemiddelde temperaturen, gemeten met thermokoppels, voegden belangrijke informatie toe over de algemene vlamstructuren.

In het eerste deel van dit proefschrift zijn experimenten aan een schijfgestabiliseerde voorgemengde vlam beschreven. De brander bestaat uit een schijf met een diameter van 80 mm, die geplaatst is in het midden van de uitstroomsectie van een contractie met een diameter van 85 mm. Met een uitstroomsnelheid van 13.2 m/s ($Re \approx 4.4 \times 10^3$) wordt een recirculatiegebied gevormd stroomafwaarts van de stabiliserende schijf. De grootte van dit recirculatiegebied is zowel in een isotherme stroming als een brandstofarme (equivalentieverhouding $\varphi = 0.75$) voorgemengde aardgas/lucht vlam onderzocht.

Naast de gemiddelde snelheidsvelden zijn turbulentie-eigenschappen gemeten in de koude stroming en de vlam. Turbulentie in deze stromingen wordt hoofdzakelijk veroorzaakt door menglagen: een menglaag tussen het recirculatiegebied en de haar omgevende hoge-snelheidslaag en een tweede tussen de hoge-snelheidslaag en de stilstaande omgevingslucht. De eerste menglaag is van belang voor stabilisatie van de vlam. Zij veroorzaakt een continue menging van verbrandingsprodukten en verse reactanten. De invloed van de tweede menglaag is hoofdzakelijk dat zij destabilisatie van de vlam introduceert, doordat zij de lokale vlamtemperatuur verlaagd door aanzuiging van koude omgevingslucht in de hoofdreactiezone. Dit belangrijke fenomeen is opgehelderd door visualisatie van de OH radicaalverdeling in de vlam. Het verklaart ook de aanwezigheid van een dominante frequentie in de axiale snelheidsfluctuaties in de hele vlam.

Ondanks deze lokale en momentane onderbrekingen van het verbrandingsproces werd een constante gemiddelde temperatuur in het recirculatiegebied gemeten. De gemiddelde OH concentratie was ook constant, waardoor wij het recirculatiegebied als een zone van chemisch evenwicht konden identificeren. Afleiding van tijd- en lengteschalen van respectievelijk snelheidsfluctuaties en OH concentratiefluctuaties droeg bij tot een karakterisatie van de verbrandingsstructuur van de onderzochte vlam. Op deze wijze werd niet alleen het verbrandingsproces (gekenmerkt door stabiliserende en destabiliserende factoren) opgelost, maar zijn ook de condities geschapen om numerieke modellen te valideren, die schijfgestabiliseerde voorgemengde vlammen beschrijven.

In het tweede deel van het onderzoek, beschreven in dit proefschrift, worden turbulentie en OH structuren in straaldiffusievlammen behandeld. Een ronde brandstofstraal met een uitstroomdiameter van 6 mm is omgeven door een ring met primaire lucht met een binnendiameter van 15 mm en een buitendiameter van 45 mm. Vlamstabilisatie is verzekerd door het gebruik van stabilisatievlammetjes. De brander werd in een branderkast geplaatst met een meestromende secundaire luchtstroom. De primaire luchtsnelheid en de brandstofstraalsnelheid werden gebruikt voor variatie van

mengsnelheden dichtbij de uitstroomopening van de brander. Het gevolg is dat vlammen in een bereik van volledig aaneengesloten vlammen (Re $\approx 4 \times 10^3$) tot vlammen met een hoge waarschijnlijk van lokale uitdoving (Re $\approx 10 \times 10^3$) en zelfs een vlam die stroomafwaarts van de brandermond is gestabiliseerd konden worden onderzocht.

De begin- en randvoorwaarden van deze drie-strooms vlammen zijn goed gedefinieerd. De invloed van de turbulente primaire luchtstroom op de centrale straal is eerst beschreven in niet-reagerende stromingen. Naast gemiddelde snelheden, zijn turbulente grootheden en tijdschalen afgeleid in niet-reagerende en reagerende stromingen. De ontwikkeling van een tweede menglaag (tussen primaire en secundaire luchtstromen), naast de menglaag tussen de centrale straal en de primaire luchtstroom, is van groot belang voor de vlamlengte en vlambreedte. Ook op een meer gedetailleerde, lokale schaal beïnvloedt de menglaag-turbulentie de vlamstructuur, bijvoorbeeld bij het optreden van lokale uitdoving van het vlamfront.

Vergelijking van de positie van maximale turbulentie-intensiteit met de plaats van het vlamfront (aangetoond door de maxima in gemiddelde temperatuur en gemiddelde OH concentratie) in verschillende vlammen bleek nuttig in het beschrijven van turbulentie-chemie interacties. Lengteschalen van snelheidsfluctuaties en scalaire concentratiefluctuaties hebben ons geholpen om deze interacties nog verder te identificeren. Over het algemeen waren deze schalen van dezelfde orde-grootte, hetgeen aantoont dat impuls- en stoftransport plaatsvindt door wervels van ongeveer gelijke grootte. Ook kleinschalige structuren interageren met de vlamzone, waaruit het belang blijkt van gedetailleerde turbulentie- en chemie-modellen in numerieke modellen. Vergelijking tussen experimentele gemiddelde snelheden, turbulente rms snelheden en gemiddelde temperaturen met modelberekeningen lieten een uitstekende overeenkomst zien. Voor de Reynolds schuifspanningen en de gemiddelde OH concentraties werd een kwalitatieve overeenkomst gevonden.

Er wordt geconcludeerd dat aanzuiging van koude buitenlucht een belangrijke destabiliserende factor is in het stabilisatieproces van brandstofarme schijfgestabiliseerde voorgemengde vlammen. Toepassing van turbulente primaire lucht in straaldiffusievlammen met stabilisatievlammetjes beïnvloedt de vlamstructuur. Niet alleen globale grootheden (zoals vlamlengte en vlambreedte) maar ook lokale eigenschappen (bijvoorbeeld de waarschijnlijkheid van lokale uitdoving van het vlamfront) worden bepaald door de primaire luchtsnelheid. Vooral snelheidsgradiënten en de daaruit voortvloeiende menglaag-ontwikkeling spelen een belangrijke rol in dit proces. Voor beide onderzochte geometrieën zijn experimentele resultaten verkregen om numerieke modellen te valideren. Als zodanig dragen de gedetailleerde metingen in dit proefschrift bij tot het oplossen van een deel van de puzzel die turbulente verbranding nog steeds is.

Nawoord

Zo'n tien jaar geleden was het voor mij ondenkbaar dat ik nog eens een proefschrift zou schrijven. Het verschijnen ervan is dan ook vooral het resultaat van de invloed die een groot aantal mensen op mij heeft uitgeoefend. Een aantal van hen speelde de afgelopen jaren een bijzondere rol en wil ik daarom met naam noemen.

Mijn promotor, professor Hoogendoorn, wil ik bedanken voor de geboden mogelijkheid een boeiend promotie-onderzoek te verrichten. Zijn open en kritische houding bij de bespreking van meetresultaten en conceptversies van mijn proefschrift hebben mij ('Je bent natuurlijk wel chemicus' (?)) snel de hoofd- en bijzaken van experimenteren aan turbulente verbranding doen inzien. Bij de planning en ontwikkeling van de experimentele opstelling in een (achteraf bezien) ondermaatse ruimte heb ik vooral in de moeilijke beginjaren veel hulp gehad van Theo. In een later stadium waren het vooral zijn suggesties voor interpretatie van de metingen die ik zeer op prijs heb gesteld.

Het tot stand komen van de opstelling was slechts mogelijk door de samenwerking met en de hulp van Rimmert. Door zijn slagvaardigheid en enthousiasme verdwenen ogenschijnlijk onoplosbare problemen als sneeuw voor de zon. Het feit dat Leo (IM) en Peter (TB) altijd klaar stonden om snel en professioneel te assisteren bij de constructie van onze (soms minder professionele) ontwerpen, leidde er toe dat de experimenten nooit lang onderbroken hoefden te worden. Door de mogelijkheden van WT's computerpark werd het verwerken van gemeten data in feite kinderspel. Vooral als er weer eens een tape met al mijn gemeten data onleesbaar was geworden, kwam Jaap mij als een reddende engel te hulp.

Als er één ding als een paal boven water staat, is het de vriendschap met collega's die de afgelopen vier jaar voor mij gezellig, succesvol en onvergetelijk hebben gemaakt. Met Jorrit, Ivo, Rob en Peter bleek ik niet alleen Noordhollands bloed, maar ook een aantal hobbies gemeen te hebben. Door hun bereidheid altijd te luisteren naar mijn vreemde gedachtenkronkels en te discussiëren over allerlei (niet alleen wetenschappelijke) zaken, heb ik 'het vak' (en nog veel meer) geleerd. Dat ook met collega's van beneden de grote rivieren goed viel samen te werken, bleek bij Tim en Robert. De goede sfeer bij WT was een belangrijke reden om in tijden van tegenslag toch maar weer 'een dagje' aan het werk te gaan.

Al vanaf mijn eerste dag als promovendus werd ik geconfronteerd met de begeleiding van studenten. Pieter, Peter, Simon, Erik en Frank voerden een aantal experimenten uit en verwerkten deze op een manier die ik vrijwel direct kon overnemen. Hoewel ik

ze wel eens anders deed geloven, heb ik veel baat gehad bij hun inspanningen en dank ze voor de prettige samenwerking.

Van alle docenten die een niet te verwaarlozen aandeel hebben gehad in mijn vorming voorafgaande aan mijn promotie-onderzoek, wil ik slechts professor Koomen (U.v.A.) noemen. Hij bracht een beslissende wending in mijn loopbaan teweeg toen hij me uit de bibliotheek sleurde na gehoord te hebben dat ik niet wilde promoveren. Ik zal waarschijnlijk nooit weten hoe belangrijk zijn regelmatige treingesprekken met mijn moeder voor mij zijn geweest.

Tot slot wil ik mijn ouders bedanken voor hun belangstelling, eerlijkheid, en vooral hun relativerend en motiverend vermogen. Door hun cursus 'zitvlees kweken' heb ik ervaren dat je met echte wil en hard werken bijna alles kunt bereiken.

About the author

August 29, 1967	Born in Alkmaar, The Netherlands.
1979-1985	Secondary school (VWO) at the Petrus Canisius College in Alkmaar, The Netherlands.
1985-1986	Chemical Technology study at the Technical Highschool (HTS) in Amsterdam, The Netherlands.
1986-1990	Physical chemistry study at the University of Amsterdam, The Netherlands.
	Graduation report on optically detected magnetic resonance in NV color centers in diamond, under supervision of prof. Dr. M. Glasbeek.
	Graduated with honours.
1990-1995	Applied physics PhD study at the Delft University of Technology, The Netherlands. Under supervision of prof. ir. C.J. Hoogendoorn.
1995-	Research at the Hoogovens Corporate Research Laboratory in IJmuiden, The Netherlands